ACKNOWLEDGMENTS

Any experiment in high energy physics, from its conception to successful completion, necessarily relies upon the contributions of many individuals. I would like to take this opportunity to thank all those whose efforts made this experiment possible. The experiment was performed at the Fermi National Accelerator Laboratory by a collaboration of physicists from the University of Chicago, Harvard University, the University of Illinois, and the University of Oxford. I want to express my gratitude to the members of the collaboration and to the staffs from our home institutions and the Rutherford Laboratory for their invaluable contributions to the experiment. I would also like to thank the Fermilab for the use of their facilities and for their expert help without which the experiment could not have been performed.

I especially want to thank my thesis advisor, Professor Luke W. Mo, for the encouragement and support he has given me throughout my graduate career at the University of Chicago--I have learned a great deal working with him during the past five years. The advice and guidance he has provided in writing this thesis is very much appreciated.

Special thanks must go to Richard M. Fine with whom I have had the pleasure of working during the setup and running of the experiment and with whom I have shared the prime responsibility for the data analysis. His Ph.D. thesis is a companion volume to this present work and describes different but complimentary aspects of the inelastic muon-nucleon scattering experiment.

I am grateful to the staff of the Enrico Fermi Institute Electronics Shop, particularly Thomas A. Nunamaker and Robert M. Norton, for their invaluable help throughout the experiment. The technical support from the Engineering Services and the Central Shop at the University of Chicago is also much appreciated.

I would like to thank Argonne National Laboratory and the staff of the Applied Math Division for the use of their computer facilities and for their expert programming help. They made the task of data analysis a very enjoyable one.

I would also like to express my gratitude to the National Science Foundation for the financial assistance they have provided during my graduate career.

Very special thanks must go to my wife, Cindy, for the encouragement and motivation she has given me throughout my graduate career, and for the excellent job of typing she has done on this manuscript. I would also like to express my sincere gratitude to my parents, Mr. and Mrs. Robert C. Heisterberg, for their support during my college and graduate studies. It is to my wife, Cindy, my father, and my late beloved mother that I dedicate this thesis.

TABLE OF CONTENTS

LIST OF TABLES

LIST OF ILLUSTRATIONS

Figure

CHAPTER I

INTRODUCTION

Electron-nucleon scattering has traditionally provided the best information on the electromagnetic structure of the nucleons, a subject of utmost importance for the understanding of the most basic building blocks of matter.[1] As shown in Figure 1, the basic interaction of the electron and the nucleon is through the exchange of a single virtual photon.[2] Very few other particles make a better probe of nucleon structure. Quantum electrodynamics has been verified experimentally[3] to be valid at distances as small as $\sim 10^{-15}$ cm, and the electron-photon vertex can be regarded as fully understood. The electron can be considered simply as a source of virtual photons to probe the nucleon. Unlike real photons, both the energy and four-momentum transfer of the virtual photon can be varied at will by specifying the angle and energy of the scattered electron in the laboratory. The energy of the virtual photon, ν, is given by the difference of the incident and scattered electron energies

$$\nu = E - E' \quad , \tag{1.1}$$

and q^2, the square of the four-momentum transfer, can be written as

$$q^2 = 2(EE' - PP'\cos\theta - m_e^2) \tag{1.2}$$

where θ is the electron scattering angle. The final state hadronic system which is produced in the interaction can be characterized by its invariant

mass W, whose square is given by

$$W^2 = M^2 + 2M\nu - q^2 \tag{1.3}$$

where M is the mass of the nucleon. (For elastic eN scattering, $q^2 = 2M\nu$, and $W = M$.)

With the virtual photon as a probe, any difference between the measured cross section and that anticipated for a point particle can be unequivocally interpreted as representing the electromagnetic structure of the nucleon. For elastic scattering this deviation from a point cross section is described in terms of the "charge" and "magnetic" form factors, $G_E(q^2)$ and $G_M(q^2)$, for the photon-nucleon vertex.[4] They are empirical functions of q^2 to be determined by experiment. For inelastic scattering the form factors that describe the photon-nucleon vertex can be functions of both q^2 and ν.

Electron-nucleon scattering is much simpler to interpret than say πp scattering. In hadron-hadron collisions there are two unknown vertices, and the quanta exchanged virtually can consist of an entire spectrum of particles. The task of unraveling the information on the structure of the nucleon is much more complex.

The first elastic electron-nucleon scattering experiments, demonstrating the deviation of the cross section from that expected for a point particle and thus measuring the form factors of the nucleon, were carried out by Hofstadter[1] and his collaborators of Stanford. These measurements have since been extended at numerous laboratories. The elastic ep cross section[5] has been measured at values of q^2 up to ~25 $(GeV/c)^2$, and elastic en scattering[6] to q^2 ~6 $(GeV/c)^2$. The results of these experiments can

be summarized by the statement that the elastic form factors, $G_E(q^2)$ and $G_M(q^2)$, for the proton and neutron obey the simple scaling law[7,8]

$$G_E^{\,p}(q^2) = \frac{G_M^{\,p}(q^2)}{2.793} = \frac{G_M^{\,n}(q^2)}{1.91} = \frac{1}{(1 + q^2/0.71)^2}$$

$$G_E^{\,n}(q^2) = 0 \quad . \tag{1.4}$$

The expression $1/(1 + q^2/0.71)$ is called the "dipole form factor," and is purely empirical. This scaling law holds to within 10% over the range of q^2 studied.[9] At the higher values of q^2, only electron-proton scattering data exist and here only from the measurement of the magnetic form factor $G_M^{\,p}(q^2)$, since the electric contribution is small and difficult to measure.

In addition to elastic scattering, inelastic processes also occur in electron-nucleon collisions which result in the production of one or more pions or other particles in the final state. Inelastic electron-nucleon scattering was first studied by Panofsky et al.,[10] also at Stanford. Initially these experiments were aimed at measuring the form factors of each of the πN resonances in a manner similar to what was done for the elastic scattering cross section. The first measurements on the electroproduction of the N^* (1238) were made by Panofsky and Allton.[11] Measurements were extended to other πN resonances such as the N^* (1512), N^* (1688), and N^* (1920). The results of these measurements indicated that the q^2-dependence of the πN resonances was quite similar to the elastic form factors.[12,13]

The breakthrough in inelastic electron-nucleon scattering came in 1968 from an experiment performed at the 20 GeV Stanford Linear Accelerator Center (SLAC).[14,15] It was found that the most exciting physics was not in

the study of the πN resonances, but rather in the continuum part of the inelastic electron scattering spectrum. The continuum cross section, unlike elastic scattering, was found to be varying slowly with q^2 and its value approached that for a point-like particle, as predicted by Bjorken.[16] This marked the beginning of an era of intense study of "deep inelastic" scattering phenomena, and we present a brief review here.

The Inclusive Cross Section

In the first Born approximation, the differential cross section for the scattering of electrons of energy E to a final energy E' through an angle θ is related to the two inelastic form factors W_1 and W_2 for the nucleon[17] by

$$\frac{d^2\sigma}{dq^2 d\nu} = \left(\frac{\pi}{PP'}\right)\frac{2\alpha^2}{q^4}\left(\frac{P'}{P}\right)\left[(2EE' - q^2/2)W_2(q^2,\nu) + (q^2 - 2m_e^2)W_1(q^2,\nu)\right] \quad (1.5)$$

where $\nu = E - E'$, and $q^2 = 2(EE' - PP'\cos\theta - m_e^2)$. Another useful representation, originally due to Hand,[18] is to express the inclusive cross section in terms of the total photo-absorption cross sections for transverse and longitudinal virtual photons:

$$\frac{d^2\sigma}{dq^2 d\nu} = \Gamma_T(q^2,\nu)[\sigma_T(q^2,\nu) + \varepsilon\sigma_L(q^2,\nu)] \quad (1.6)$$

where $\Gamma_T(q^2,\nu)$ is the flux of the virtual photon, σ_T and σ_L the total photo-absorption cross sections for transverse and longitudinally polarized virtual photons, and ε the photon polarization. In the limit of $q^2 \to 0$, the transverse cross section approaches the total photo-absorption cross section $\sigma_{\gamma p}$ for real photons. This offers the possibility of obtaining

information on $\sigma_{\gamma p}$ at high energies by extrapolating the data of electroproduction experiments to the limit of $q^2 = 0$.

The relationship between the two representations is given below:

$$W_1(q^2,\nu) = \frac{K}{4\pi\alpha^2}\,\sigma_T(q^2,\nu) \quad ,$$

$$W_2(q^2,\nu) = \frac{K}{4\pi\alpha^2}\,\frac{q^2}{q^2 + \nu^2}[\sigma_T(q^2,\nu) + \sigma_L(q^2,\nu)] \tag{1.7}$$

where

$$K = \frac{W^2 - M^2}{2M} = \nu - \frac{q^2}{2M} \tag{1.8}$$

is the equivalent real photon energy needed to photoproduce a final hadronic system of invariant mass W. The ratio of the two inelastic form factors W_1 and W_2 can be written as

$$\frac{W_1}{W_2} = \left(1 + \frac{\nu^2}{q^2}\right) \Big/ (1 + R) \tag{1.9}$$

where $R \equiv \sigma_L/\sigma_T$, the ratio of longitudinal to transverse photo-absorption cross sections.

The original experiments at SLAC measured the inclusive cross section for inelastic electron-proton scattering using incident electrons of energy up to 20 GeV. The results can be summarized by plotting the two quantities $2MW_1$ and νW_2 versus the dimensionless variable ω, defined by:

$$\omega = \frac{2M\nu}{q^2} \quad . \tag{1.10}$$

As shown in Figure 2, the data points tended to fall on a universal curve in

ω for all values of q^2 and ν. This agreed with Bjorken's hypothesis.[16] Bjorken originally suggested that, at large values of q^2 and ν, the two structure functions $2MW_1$ and νW_2 should manifest a property of scale invariance. That is, as both q^2 and ν approach ∞, keeping ω finite, the two structure functions should be universal functions of only the dimensionless variable ω:

$$\begin{aligned} 2MW_1(q^2,\nu) &\longrightarrow F_1(\omega) \\ \nu W_2(q^2,\nu) &\longrightarrow F_2(\omega) \end{aligned} \tag{1.11}$$

One of the simplest models put forward to explain the scaling behavior of νW_2 is the parton model, originally proposed by Feynman.[19] Feynman hypothesized that the nucleon consists of a number of elementary, point-like constituents called partons. Each parton carries a fraction x of the nucleon momentum P. The important feature of this model is that the interaction of the virtual photon with the nucleon can be resolved into virtual photon-parton interactions. As shown in Figure 3, the parton model assumes that the virtual photon is absorbed incoherently by a single parton--this is a crucial assumption. The inelastic cross section is then obtained by adding incoherently the cross sections for scattering from each of the individual partons. This immediately yields the large point-like cross sections observed in deep inelastic scattering at SLAC, and the scaling behavior of νW_2. Using this model the two nucleon structure functions, $2MW_1$ and νW_2, can be calculated by simply summing the individual parton contributions weighted appropriately by the parton charge and the probability for finding a parton with fractional momentum x.[20] This leads to the Bjorken scaling relations:

$$2M_1W_1(q^2,\nu) = F_1(x)$$
$$\nu W_2(q^2,\nu) = F_2(x) \qquad (1.12)$$

where $x = 1/\omega$.

It is experimentally known[21] that the ratio $R \equiv \sigma_L/\sigma_T \simeq 0.2$. The smallness of this ratio suggests that partons are spin ½ particles.[22] Thus it is tempting to identify partons with the fractionally charged quarks of Gell-Mann in SU(3) theory.[23] With partons as quarks, the parton come in three varieties and have momentum distributions within the nucleon denoted by u(x), d(x), and s(x). The u, d, and s partons carry quantum numbers identical to the up, down, and strange quarks of Gell-Mann, except that the number of partons is not limited to three for the nucleon. The model does not have to be restricted to just three different types of partons. For example, we can add a charmed[24] parton distribution c(x), or multiply each parton type by the three colors.[25] We can also view the nucleon as consisting of three "valence quarks" as in the three quark-model plus an infinite sea of quark-antiquark pairs.[26]

One of the striking successes of the parton model (with partons as quarks) is the prediction that the ratio of νW_2 for the neutron and proton should approach the value ¼ as $x \to 1$. The observed structure function [i.e., $F_2(x)$] is

$$F_2^{p}(x) = \frac{4}{9}[u(x) + \bar{u}(x)]x + \frac{1}{9}[d(x) + \bar{d}(x)]x + \frac{1}{9}[s(x) + \bar{s}(x)]x \qquad (1.13)$$

for protons, and

$$F_2^{n}(x) = \frac{1}{9}[u(x) + \bar{u}(x)]x + \frac{4}{9}[d(x) + \bar{d}(x)]x + \frac{1}{9}[s(x) + \bar{s}(x)]x \qquad (1.14)$$

for neutrons. As $x \to 1$, if we can neglect the contributions of the d and s quarks (and antiquarks), F_2^n/F_2^p should approach $\frac{1}{4}$.[27] Experimentally, this was found to be a correct prediction.[28]

Electroproduction of Hadrons

One of the most interesting observations on the experimentally measured parton distributions for the proton and neutron is that[29]

$$\int_0^1 \Big[[u(x) + \bar{u}(x)] + [d(x) + \bar{d}(x)] + [s(x) + \bar{s}(x)]\Big] x dx \simeq 0.51 \quad . \qquad (1.15)$$

This integral represents the fraction of the virtual photon energy carried away by the charged partons. The question then immediately arises as to what happened to the missing energy. The most plausible theoretical hypothesis is that the missing energy is carried away by neutral gluons which are the quanta mediating the interaction between quarks.[30] In view of this perplexing situation, one cannot help from thinking that perhaps the answer to understanding the structure of the nucleons lies in the study of the final state hadrons.

The virtual photon makes a good probe for the study of the constituents of the nucleon because it has an energy deficiency, as observed by Chou and Yang.[31] From the simple expression

$$q^2 = |\vec{q}|^2 - \nu^2 > 0 \quad , \qquad (1.16)$$

it is easy to see that in the high q^2 limit the 3-momentum of the virtual photon overwhelms its energy content. In a limiting fragmentation process,[32] the fragmentation of a fast projectile is a gentle process

requiring only an infinitesimal energy transfer and small amount of transverse momentum. However, in deep inelastic electron scattering, the virtual photon cannot fragment into hadrons because of its large energy deficiency. It must first absorb a part of the target and then "pulverize" into hadrons. The remainder of the target then fragments in the usual manner. Another way to visualize the process is that the virtual photon must make a violent collision with the nucleon without transferring much energy to it. The large 3-momentum transferred to the nucleon can eject a parton, which then fragments into ordinary hadrons before it leaves the "nuclear volume." Since there is little energy transfer, the final state hadrons primarily originate from parton fragmentation, rather than energy materialization.

If this picture is indeed correct, we should anticipate approximately the same distribution of hadrons, except for minor details, independent of the type of interaction. This feature can be examined, by comparing the hadron distributions from deep inelastic muon and neutrino scattering, high energy e^+e^- annihilation, and hadron-hadron collisions. The final state hadrons in all different kinds of interactions should simply be the fragmentation products of the outgoing quarks, and we would expect the final state hadron distributions to be universal.[19,32] This will be the main subject of this thesis.

In hadron-hadron collisions, the hypotheses of Limiting Fragmentation[32] and Feynman Scaling[19] make the prediction that the invariant cross section $Ed^3\sigma/d^3\vec{p}$ for the reaction a + b → c + anything should approach a limiting value at high energies (large $\sqrt{s}$), which is finite and independent of s. In other words,

$$\lim_{s\to\infty} E\frac{d^3\sigma}{d^3\vec{p}} = \lim_{s\to\infty} f(p_{\parallel},p_{\perp},s) = f(x_{\parallel},p_{\perp}) \quad . \tag{1.17}$$

Here, $x_{\parallel}$ is the ratio $p_{\parallel}/p_{max}$ with $p_{\parallel}$ being the longitudinal momentum of particle c in the cm-system of particles a and b, $p_{\perp}$ its transverse momentum, and p_{max} its maximum possible momentum in the cm-system. The hypothesis of limiting fragmentation leads to the picture that the fragmentation of the projectile should be independent of the target particle and vice versa, and that the hadron distributions from each should approach a definite limit. If we translate this picture into the rapidity distribution, $d\sigma/dy$, where y is the longitudinal rapidity of particle c,

$$y \equiv \frac{1}{2}\,\ell n\left[\frac{E + p_{\parallel}}{E - p_{\parallel}}\right] \quad , \tag{1.18}$$

then the hypothesis of hadronic scaling states that the height of $d\sigma/dy$ should not change with s. Only its width should increase. This is illustrated in Figure 4. At ISR energies in pp collisions, the experimental data indeed indicates that the height of the rapidity plateau is constant to within ~15%.[33]

This evidence for hadron scaling in hadron-hadron interactions has stimulated much experimental interest in the study of inclusive reactions in electroproduction.[34] For electroproduction we would expect that the hadron distributions in the target fragmentation region to be independent of q^2, the negative mass-squared of the virtual photon. The interesting question, of course, is how do the hadron distributions in the region of photon fragmentation change as we increase q^2.

Other than the parton model and the model of limiting fragmentation, there are also several other interesting models which we would like to understand:

1. Vector Dominance[35] and the Generalized Vector Dominance Model.[36]--In this model, the virtual photon is supposed to turn into neutral vector mesons (ρ^0, ω^0, ϕ^0, ψ^0, . . . , etc.), and the vector meson then interacts elastically with the target nucleon. The features of this model can easily be checked by measuring the decay products of the spectrum of vector mesons.

2. The ρ^+ Dominance Model.--T. D. Lee[37] has proposed a ρ^+ dominance model in which the interaction of the virtual photon with the nucleon can be described by the process

$$\begin{array}{l} \gamma_V + p \rightarrow \rho^+ + n \\ \qquad\quad \llcorner\!\rightarrow \pi^+ \; \pi^0 \\ \qquad\qquad\quad \llcorner\!\rightarrow \gamma\gamma \end{array} \qquad (1.19)$$

This model is beyond the ability of our apparatus because we cannot measure the neutrals with good efficiency.

3. The Regge Pole Model.--The Muller formulation[38] of strong interactions seems to enjoy some quantitative success. It assumes triple Reggeon couplings of the type RRR, PPR, or PPP for inelastic collisions, where R is the Reggeon and P is the Pomeron. It is interesting to see whether this qualitative model can also be applied to virtual photon interactions.

The Study of Deep Inelastic Scattering at Fermilab

With the advent of the 400 GeV proton synchrotron at the Fermi National Accelerator Laboratory, a high energy muon beam of modest intensity could be produced economically.[39] This immediately opened up the opportunity to

extend the study of deep inelastic scattering to an energy of 150 GeV. This energy cannot be easily achieved at electron accelerators because of the heavy losses due to synchrotron radiation.

As far as we know, the muon behaves in every aspect as an electron except for its much larger mass--a mystery yet to be understood. Thus the muon serves as an equally good probe to study nucleon structure. The high energy muons of Fermilab would enable us to explore a (q^2,ν) range unattainable before. The goals of this experiment are essentially threefold and can be summarized as follows:

1) To measure the muon inclusive cross section of the muon energies available at Fermilab and to investigate the behavior of the nucleon structure functions, $2MW_1$ and νW_2 at larger values of ω.
2) To continue the test of Bjorken scaling to higher values of q^2 and ν, and
3) In addition, to study the distributions of the final state hadrons produced in deep inelastic muon scattering.

The specific subject of this thesis is the study of the muo-produced final state hadrons from a deuterium target with 150 GeV incident muons. The major emphasis will be on the hadron distributions, but other topics will also be discussed because of their close relationship.

Chapter II starts with a description of the muon scattering spectrometer and the experiment at Fermilab. Chapter IV describes the analysis of the inclusive muon cross section and presents the results of the deuterium cross section measurement. In Chapter V the nucleon structure function νW_2 is discussed. Finally, the analysis of the final state hadrons and a discussion of the hadron distributions are presented in Chapter VI. Various

technical details concerning the experiment and the data analysis are described in the Appendices.

Fig. 1.--One-photon exchange Feynman diagram for inelastic electron-nucleon scattering.

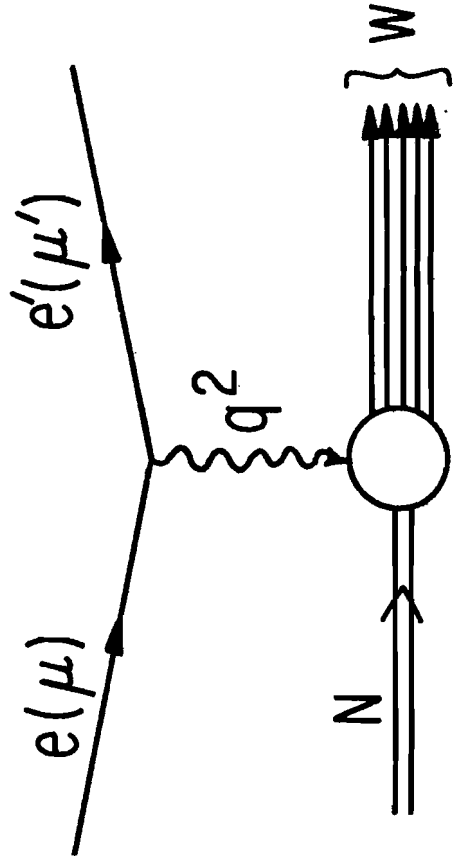
W
e'(μ')
q²
e(μ)
N

Fig. 2.--The inelastic structure functions $2MW_1^p$ and νW_2^p as measured in electron scattering experiments at SLAC.

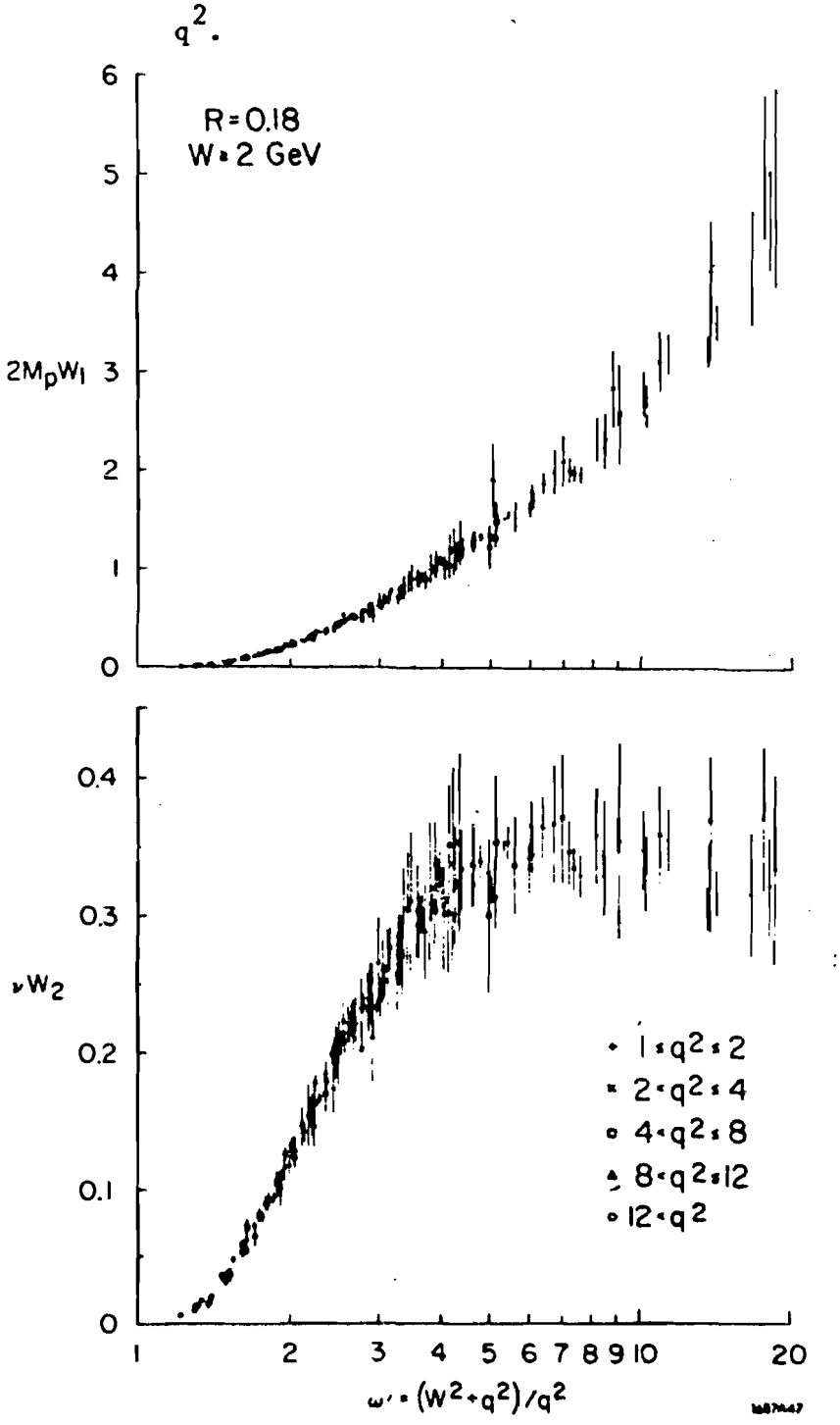
q^2.
R=0.18
W=2 GeV
$2M_pW_1$
νW_2
$1<q^2\leq 2$
$2<q^2\leq 4$
$4<q^2\leq 8$
$8<q^2\leq 12$
$12<q^2$
$\omega' = (W^2+q^2)/q^2$

Fig. 3.--The Feynman diagram for the parton model explanation of inelastic electron-nucleon scattering. In the parton model, the virtual photon is absorbed incoherently by a single parton.

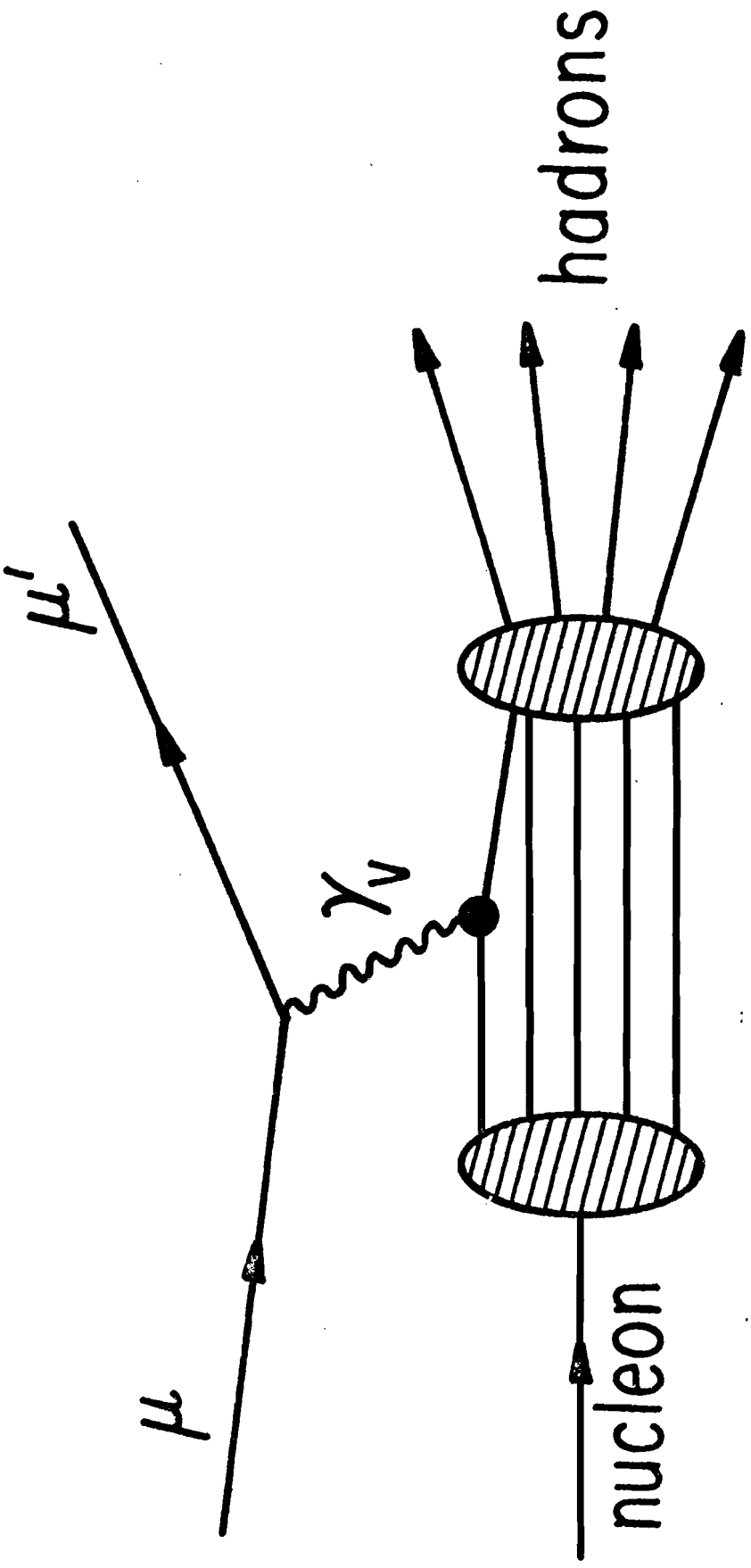
hadrons
μ'
γv
μ
nucleon

Fig. 4.--Schematic diagram showing the s-dependence of the longitudinal rapidity distribution, $d\sigma/dy$. Hadron scaling predicts that the height of the central region plateau should remian constant as s increases.

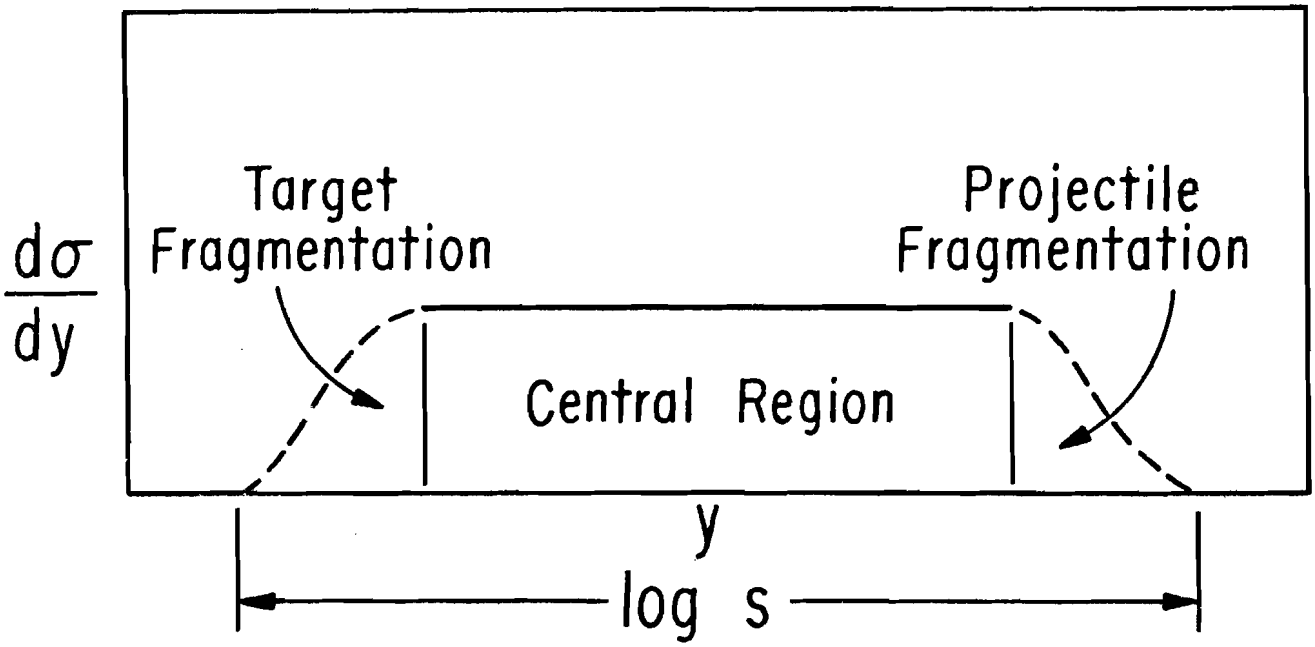
dσ/dy
Target Fragmentation
Projectile Fragmentation
Central Region
y
log s

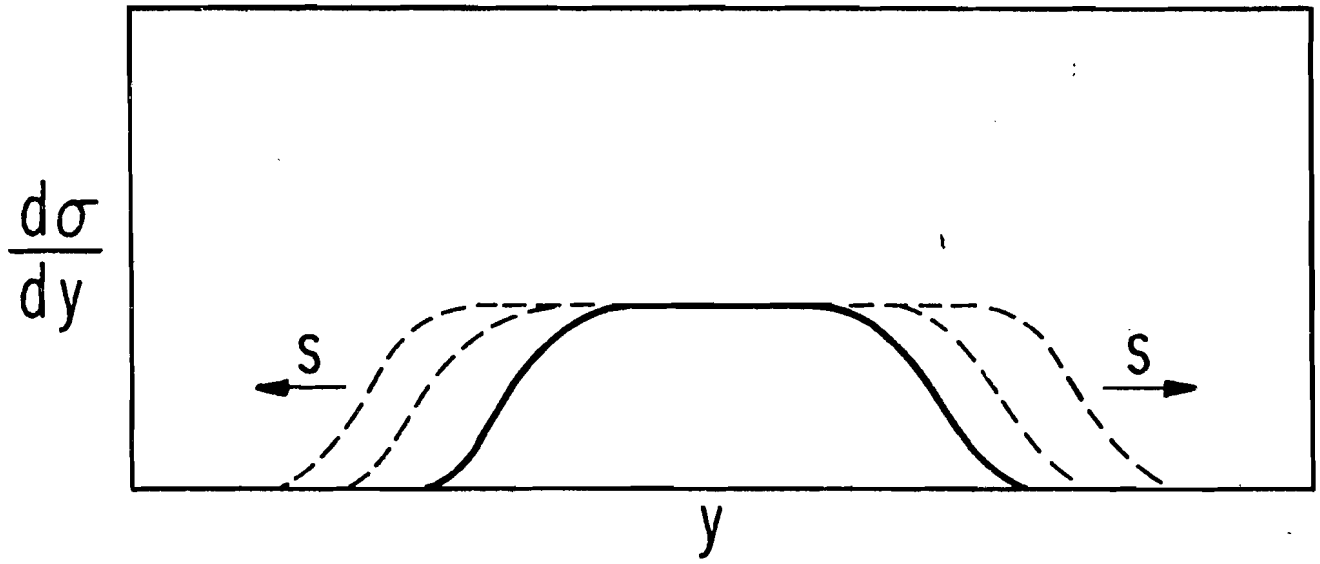
dσ/dy
s
s
y

CHAPTER II

THE EXPERIMENT

Experiment E-98 was proposed in 1970 to study inelastic muon-nucleon scattering at Fermilab. The experiment was a collaboration of physicists from the University of Chicago, Harvard University, and the University of Oxford, formed for the purpose of constructing and operating a Muon Scattering Facility.[40] The group proposed to build a large aperture multi-particle megnatic spectrometer to measure both the inclusive muon cross sections and the final state hadrons produced in inelastic μN processes. The accelerator at Fermilab would extend the energy range of previous deep inelastic scattering experiments by nearly a factor of ten and it was hoped that muon-nucleon scattering at the energies available at Fermilab would reveal new information about the fundamental structure of the nucleons. Also, with a multi-particle detector, the final state hadrons produced in inelastic μN scattering at these energies could be examined.

The construction of the Muon Facility was a major undertaking. It required nearly three years of effort by the three universities and Fermilab to complete. The Chicago Cyclotron at the University of Chicago was dismantled and the 2400-ton magnet moved to Fermilab for use as the analysis magnet. The wire chambers, scintillation counter hodoscopes, and other equipment for the muon spectormeter were built by the three universities at their home institutions and moved to Fermilab for final assembly. The setup and testing of the spectrometer started in late

1973 and data-taking began in March 1974 with 150 GeV muons on a liquid hydrogen target.

This chapter describes the Muon Scattering Facility and Experiment E-98 at Fermilab. The muon spectrometer is described in detail. The experimental trigger and the control system for on-line data acquisition are discussed, and a summary of the data collected during the experiment is presented. Finally, the off-line data analysis of the experiment is outlined.

The Accelerator

The Fermi National Accelerator Laboratory is located at Batavia, Illinois, about 40 miles west of Chicago. The accelerator is a four-stage synchrotron capable of accelerating protons up to energies of 500 GeV. A layout of the accelerator and the experimental areas is shown in Figure 5.

Protons, from ionized hydrogen gas, are first accelerated to 750 KeV by a Cockcroft-Walton generator, and injected into a 145 meter long linear drift-tube accelerator (Linac). The Linac takes the protons from the Cockcroft-Walton, accelerates them to 200 MeV, and injects them into a medium-size synchrotron (Booster) with a radius of 75 meters. In the Booster the protons are accelerated to 8 GeV and injected into the Main Ring at 15 pulses per second. It takes about 13 pulses, or 0.8 seconds, for the Booster to fill the Main Ring. The Main Ring is a larger version of the Booster with a diameter of 2 kilometers, and accelerates the protons to their final energy of up to 400 GeV, and an intensity of up to 2×10^{13} protons per pulse.

At the end of the acceleration period the protons are extracted from the Main Ring and directed to the experimental areas. The extracted proton

beam is split and directed to the experimental areas in the Switchyard, a complicated arrangement of bending and focusing magnets. The protons can be switched left to the Meson Area, or right to the Proton Area, or straight ahead to the Neutrino Area. The Muon Scattering Facility is located in the Neutrino Area, about a mile from the extraction point.

The Muon Beam

A simplified schematic of the muon beam at Fermilab is shown in Figure 6. Figure 7 is a schematic diagram of the beam optics.

Protons from the accelerator strike a 12" aluminum production target (~1 interaction length). The charged pions and kaons produced at the target are first focused into a parallel beam along a 1400' decay pipe by a quadrupole triplet located immediately after the production target. In the decay channel a few percent of the pions and kaons decay to muons and neutrinos. Since the pion decay can only give a maximum transverse momentum of 30 MeV/c to the muon, most of the muons are concentrated in the forward direction. At the end of the decay channel, the charged particles are bent out of the original beam line by a dipole magnet. The decay neutrinos continue in the forward direction to the neutrino experiments.

The decay muons were focused onto the experimental target by three quadrupole doublets and three sets of dipole bending magnets. At the intermediate focal point, approximately 50' of polyethylene (CH_2) was inserted into the beam line to remove the hadrons. The absorber was located at the focal point to reduce the deteriorating effects of multiple Coulomb scattering in the polyethylene. At the focal point, the muon beam had an angular divergence of ~1 mrad. Any additional angle introduced by the multiple scattering in the absorber was small in comparison. The pion

contamination in the muon beam after the hadron absorber was measured to be less than 10^{-6}.

The yield of positive muons at the experimental target was about 10^{-7} per incident primary proton at the production target. For 10^{13} protons, the typical muon intensity was 10^{6} per pulse. For negative muons, the yield was nearly a factor of three lower. The muon beam intensity became optimum for a muon momentum equal to approximately half the momentum of the primary proton beam from the accelerator. The beam had a momentum spread of typically ±2.5% and was confined to an area of ~5" in diameter at the experimental target.

The momentum and direction of the incident muons were measured by six sets of beam multi-wire proportional chambers (BMWPC) and hodoscopes, located before and after the last set of bending magnets. The beam hodoscopes each consisted of eight adjacent counter elements, oriented in either the horizontal or vertical direction. The BMWPC's had a wire spacing of 2 mm and used a shift-register readout. Each beam proportional chamber was combined with a beam hodoscope to measure either the x (horizontal) or y (vertical) position of the muon beam. The incoming muon was measured upstream of the last set of bending magnets by two sets of x-chambers and hodoscopes. After the magnets there were two sets of x-chambers and hodoscopes and two sets of y-chambers and hodoscopes to determine the position of the muon. The momentum of the muon was calculated from the measured bend angle and the known integral $\int B \cdot dl$ of the tagging magnets. The nominal bend angle was 28 mrad in the horizontal plane. The BMWPC's determined the position of the incident muon to within ±1 mm at the experimental target and measured the angle to within ±0.06 mrad. This corresponded to a momentum resolution of ±0.3%.

Typical spatial and angular distributions of the muon beam at the experimental target are shown in Figures 8 and 9, respectively. Figure 10 shows the reconstructed momentum distribution of the muon beam for a nominal beam momentum of 147.22 GeV/c.

The Muon Spectrometer

A schematic of the muon spectrometer at Fermilab is shown in Figure 11. The muon scattering spectrometer is a large acceptance, multi-particle detector, consisting of a liquid hydrogen/deuterium target, a large volume bending magnet for momentum analysis, multi-wire proportional chambers, wire spark chambers with shift-register or magnetostrictive readout, and several banks of scintillation counter hodoscopes. The trigger for the apparatus was defined by a change of direction of the scattered muon from the incident muon beam. Identification of the scattered muon was provided by a 2.44 meter thick steel hadron absorber. In addition to the scattered muon, the charged hadrons produced in the interaction were also detected.

The incident muon beam interacted in a 48" long liquid hydrogen/deuterium target located upstream of the Chicago Cyclotron magnet. Halo muons were vetoed by a large bank of scintillation counters located in front of the target. This veto hodoscope was shielded from backward scattering in the target by a 2'-thick concrete wall. A set of 1m X 1m MWPC's was placed behind the experimental target to measure the forward-going charged particles, and on each side a set of recoil spark chambers and time-of-flight (TOF) system to detect wide angle tracks.

The forward-going charged particles were dispersed horizontally by the 15 kg magnetic field of the Chicago Cyclotron magnet, and measured downstream of the magnet by several sets of wire spark chambers and two x-y hodoscopes. The charged particles were first detected downstream by

sets 2m X 4m and 2m X 6m spark chambers spaced over a distance of approximately 6 meters. Behind this group of chambers there were two banks of scintillation counters, the G hodoscope with horizontal elements, and the H hodoscope with vertical elements, to mask the in-time charged particle tracks found in the spark chambers. The scattered muon was identified by a set of spark chambers and two x-y hodoscopes, the M_v and M_h, located behind the steel absorber. Muons in the unscattered beam were vetoed by the N hodoscope, a set of small horizontal counter elements, also located behind the hadron shield. The scattered muon was defined in the trigger by the M_v, M_h, and N hodoscopes. Hadrons produced in the interaction were stopped by the 2.44 m thick steel absorber.

Although there was no means for specific particle identification in the muon spectrometer, electrons and positrons from μe scattering, π° decays, and photon conversions could be identified by a set of 2m X 4m spark chambers placed behind a 3 radiation length steel plate. Behind a 16 inch thick lead brick wall, there was another set of 2m X 4m spark chambers to measure the neutron-induced cascade showers.

A more detailed description of the elements of the muon spectrometer is given in the following sections. Attention is paid to the specific dimensions, characteristics, operation, and performance of each of the elements.

The Experimental Target

The liquid hydrogen/deuterium target is shown schematically in Figure 12. The liquid hydrogen/deuterium was contained in a 48" long, 7" diameter cylindrical flask made of 14 mil Mylar. The target flask was surrounded and protected by a 10 inch diameter cryostat made of 94 mil aluminum with 32 mil end caps.

The target was cooled by a 50 watt liquid helium refrigerator. Hydrogen/deuterium gas was condensed in the cryostat and allowed to fill the target reservoir. Once the cryostat was cooled to liquid helium temperature, it normally took about thirty hours to condense the 30 liters of liquid necessary to fill the target assembly. There were resistors mounted at the top and bottom of the target flask and in the reservoir to indicate the level of the liquid in the target.

For empty target running, the target assembly was designed to be able to quickly empty the target flask by forcing the liquid up into the reservoir with helium gas, leaving only helium vapor in the flask itself. This would allow the full target running to be interspersed with empty target runs at convenient time intervals. In practice however, this was never accomplished successfully because of operational difficulties. The empty target runs were all taken at the end of the experiment when the target was allowed to warm up and the hydrogen/deuterium gas simply vented to the air.

The Chicago Cyclotron Magnet

The Chicago Cyclotron was dismantled and moved from the University of Chicago as the analysis magnet for the muon spectrometer. The magnet has a pole face diameter of 4.3 meters and the gap was increased to 51 inches for a larger acceptance. During normal running, the magnet was operated at full field (~15 kg at a current of ~4800 amperes) and dissipated approximately 1.8 megawatts of power. The magnet produces a uniform, cylindrically symmetric magnetic field with a central value of 15 kg and has an integral $\int B \cdot dl$ of 74.15 kg-m along its diameter.

The Chicago Cyclotron proved to be an ideal spectrometer magnet because its magnetic field is very uniform and cylindrically symmetric.

It dispersed charged particles in the horizontal direction with very little vertical focusing. The cylindrical symmetry of the magnetic field greatly simplified the pattern recognition and the momentum determination of charged particle tracks upstream and downstream of the magnet. (These will be described in the discussion of the off-line data analysis.)

The magnet pole faces, coils, and yoke were slightly radioactive (~20 mCi) as a result of more than twenty years of cyclotron operation. This radioactivity, mostly soft gamma rays from Co^{60}, increased the dark current of the 1m X 1m MWPC's behind the target, and produced spurious sparks in the 2m X 4m wire spark chambers near the magnet. These spurious sparks complicated the task of pattern recognition in the data analysis.

The Hodoscopes

The scintillation counter hodoscopes in the spectrometer were used to define the trigger for the experiment, and served to mask in-time charged particle tracks in the wire spark chambers. Each counter element, except for the halo veto hodoscope, was latched and recorded on magnetic tape together with the data from the wire chambers and other electronics.

The resolving time of the scintillation counters varied from hodoscope to hodoscope, depending mostly on the length of the counter elements, but was typically 20 nsec. Each of the hodoscopes in the muon spectrometer is briefly described below.

The Beam Hodoscopes

Each multi-wire proportional chamber in the beam momentum tagging system was immediately followed by a scintillation counter hodoscope with either horizontal or vertical elements. As shown in Figure 13, each

hodoscope consisted of eight counters that were 6 inches long, 3/4 inch wide, and 1/4 inch thick. The hodoscope covered the active area of the beam MWPC's and their good time resolution (~8 nsec) helped define the track of the incident muon.

The Halo Veto Hodoscope

The halo veto hodoscope (VH) in front of the target vetoed muons that were outside the muon beam and would accidentally trigger the spectrometer. The hodoscope consisted of 24 counter elements, covering an active area of 3 meters by 5 meters, with a 5 inch diameter hole in the center for the muon beam. In the center there was a small scintillation counter "veto jaw" which helped define the beam. The scintillation counters were shielded from possible backward scattering in the target by a 2 foot thick steel-reinforced concrete wall.

The G and H Hodoscopes

The G and H hodoscopes, illustrated schematically in Figure 14, were located downstream of the Chicago Cyclotron magnet, behind the set of 2m X 6m wire spark chambers. The G hodoscope was constructed of 18 horizontal counter elements, each 3 meters long. The hodoscope covered the entire active area of the 2m X 6m chambers except for a small square in the center for the muon beam. The H hodoscope consisted of 24 vertical counters and covered an area of 2 meters by 4 meters.

The G hodoscope was included in the experimental trigger to help define the scattered muon, and both the G and H hodoscopes were latched and used in the pattern recognition. The H hodoscope proved to be most useful in separating in-time charged hadron tracks from stale halo muons in the downstream spark chambers. The G hodoscope was not very useful

since the counter elements were arranged horizontally, and the Cyclotron magnet dispersed the charged particles along that direction.

The M_v, M_h, and N Hodoscopes

The muon trigger hodoscopes, M_v and M_h, are shown in Figure 15. These two hodoscopes were located behind the 2.44 meter steel hadron absorber, and defined the scattered muon in the experimental trigger. The M_h hodoscope consisted of 20 overlapped vertical counters. The M_v hodoscope was constructed of 22 horizontal counters; a central band of 10 elements that could be adjusted horizontally to change the position and size of the hole for the muon beam; and two sets of six elements above and below this central band. The N hodoscope consisted of 13 overlapped horizontal counters, as shown in Figure 16, and was used to veto muons in the unscattered beam. The position of the N hodoscope could also be adjusted horizontally to cover the hole in the M_v and M_h hodoscopes.

The 1m X 1m MWPC's

There were eight 1m X 1m multi-wire proportional chambers installed behind the experimental target; four x-planes and four y-planes. For the runs in 1975, there was also one x-y chamber located in the center of the Chicago Cyclotron magnet. These chambers were used to detect the forward-going charged particles emerging from the target, and most importantly, to determine the scattering angle of the muon and measure the final state hadrons. When the scattering angle was large, or when there were charged hadrons produced at wide angles, the tracks found in the 1m X 1m MWPC's could be used to locate the vertex of the muon interaction in the target.

The mechanical construction of the MWPC's[41] consisted of an anode wire plane and two cathode wire planes mounted between two rectangular

aluminum frames. The construction is illustrated in Figure 17. The cathode planes were made of silver-plated Be-Cu alloy wires, 4 mil in diameter, with a wire spacing of 1 mm. The tension applied to the cathode wires was very high, 800 grams per wire, to prevent mechanical oscillations, and the aluminum frames had to be prestressed before the wires were applied. The anode or signal wires were made of gold-plated tungsten, 0.8 mil in diameter, and spaced 1.5 mm apart. The tension applied to the anode wires was approximately 70 grams per wire.

Each wire of the cathode plane was soldered to an 18 MΩ resistor on a miniaturized thick-film substrate. The high voltage to the chamber was applied to these resistors to limit the current through the wire during a possible spark breakdown. These resistors also served to decouple the cathode wires. Further protection was provided by an external resistor in series with the high voltage power supply.

The anode and cathode wire planes were tensioned and epoxied to Fiberglas G-10 boards mounted on the aluminum frames, and were separated by 3/16 inch G-10 spacers. The two aluminum frames were bolted together and gas seals, made of laminated Mylar and aluminum foils, 2.5 mil and 0.5 mil in thickness, respectively, were put in place. The gas seals were held down by Lucite strips and a layer of RTV was painted on all edged to prevent possible gas leakage. The G-10 boards glued to the aluminum frames contained the gas manifolds for the flow of gas through the chamber.

The signals on the anode wires were typically a few tens of millivolts with a rise time of less than 50 nsec. To achieve full detection

efficiency, it is necessary to use an amplifier before the discriminator and other stages of readout electronics. The amplifier and associated readout electronics developed for the 1m X 1m MWPC's[41] is described in Appendix 1. The amplified signals from each anode wire were used to trigger a discriminator and the output from the discriminator was latched as a bit in a shift register when an event trigger occurred. The latched shift registers on each chamber were readout by a CAMAC scanning module[42] also described in Appendix 1.

The chambers were normally operated at a high voltage of ~4000 volts. The gas mixture used was 84.6% argon, 15% CO_2, and 0.4% Freon-13B1, although the percentage of CO_2 was not critical. Increasing the percentage of CO_2 in the gas mixture reduces the gas amplification and raises the threshold high voltage plateau curve. It was found experimentally that the chamber operation could be improved and spark breakdown prevented by "ramping" the high voltage applied to the chamber during the beam pulse. While the beam was off, the high voltage applied to the chambers was kept ~300 volts below the plateau curve threshold. A fraction of a second before the beam pulse, the high voltage was increased to its plateau value and maintained for the duration of the pulse.

The shift-register readout for the MWPC's was latched by a "load" signal generated by the master trigger for the experiment. It was found that a gate width of 50 nsec was adequate for achieving near 100% efficiency for all wires, although a gate width of 100 nsec was used. Figure 18 shows the chamber efficiency as a function of the gate width of the latch. Figure 19 is a distribution of the spatial resolution obtained for these chambers. The ratio of one-wire spread events to two-wire spread events was greater than 10.

The Wire Spark Chambers

The wire spark chambers all had a wire spacing of 1 mm. The chambers downstream of the Chicago Cyclotron magnet had the wires arranged into x-, u-, and v-views. The x-wires were vertical; the u- and v-wires made angles of $\pm 7.125^\circ$ (tangents of $\pm 1/8$) with the x-wires. These three small angle stereoscopic views with 1 mm wire spacing combined to give a resolution of ~1 mm in the horizontal x-direction and ~10 mm in the vertical y-direction.

The three sets of 2m X 4m spark chambers immediately downstream of the magnet used a capacitor storage shift register readout developed by T. A. Nunamaker.[43] The other chambers used a conventional magnetostrictive readout. All the chambers were pulsed as parallel plate transmission lines terminated in resistive loads. The type of readout used for the shift register chambers was not affected by magnetic fields and operated with very low spark currents (200 ma flowing for 300 nsec), assuring high multi-spark efficiency. For the magnetostrictive chambers, the threshold for spark detection was approximately 5 amps flowing for 300 nsec.

All the spark chambers were operated with a gas mixture of 90% Ne and 10% He, and used alcohol as a quenching agent. The magnetostrictive chambers had an 8-inch diameter Mylar circle placed between the wire planes to deaden the central beam region.

The 2m X 4m Shift-Register Chambers

The 2m X 4m shift-register chambers had the advantage that, unlike magnetostrictive delay line chambers, they could be operated in a magnetic field. The spark information is held on individual wire capacitors until the electrical pulsing noise has subsided, and then parallel loaded into shift registers located directly on the chamber. The shift registers are

then serially readout by the same CAMAC scanning module used for the 1m X 1m MWPC's. The readout is described in detail in Appendix 1.

The mechanical construction of the chambers[44] is illustrated in Figure 20. Altogether there were 12 wire planes arranged into three modules. As shown, a module consisted of two spark gaps (four wire planes) mounted on each side of a 2m X 4m rectangular frame made of extruded aluminum channel. In addition to providing the support for the wire planes, the aluminum channel frame served as the intake and exhaust gas manifolds for the chamber. The construction techniques used were new for wire chambers of this size. The wires were first wound on a compact drum and glued to support strips. The wires were then removed from the drum, stretched over the chamber, and epoxied to Fiberglas G-10 boards mounted on the frame. The wire planes were made of 3 mil silver-plated Be-Cu alloy with a wire spacing of 1 mm. The wires on the low voltage (L.V.) plane were vertical, perpendicular to the 4m side of the chamber. The high voltage (H.V.) wires were slanted at an angle whose tangent was 1/8 with respect to the vertical direction. These two wire planes give a stereo image with 1 mm horizontal and 8 mm vertical resolution. The separation between the L.V. and H.V. wire planes was 3/8 inch.

The two chamber gaps were separated by a Mylar laminated aluminum foil mounted in the center of the aluminum frame. This foil was not a gas seal but served to optically decouple the two gaps and provided a dc clearing field to sweep away ionized particles. The chamber was sealed with two foils mounted on the outside of the chamber and held in place with Lucite strips. All edges were painted with RTV to prevent gas leakage.

The pulsing of the chamber is illustrated in Figure 21. The H.V. pulse was provided by a simple three electrode, nitrogen pressurized spark

gap with a 25,000 pF charging capacitor. The H.V. pulse was fed to the chamber by an aluminum bus bar, which ran the 4m length of the chamber and was terminated in a 3.1 Ω resistive load. One chamber gap presents a capacitative load of about 8,000 pF to the pulser. Diodes were mounted on the high voltage pulse bar in series with the 3.1 Ω termination resistance. They maintained a positive dc fast clearing field between the wire planes while passing the negative polarity high voltage pulse. After the chamber is pulsed, the pulser recharging current produces a large positive voltage across the chamber. This acts as a fast pulsed clearing field. The pulse shape produced across the chamber is shown schematically in Figure 22. A dc clearing field of ~100 volts on the H.V. wire plane and ~600 volts on the inner aluminum foil was also applied. The recharging time of the chambers was ~5 msec. This allowed a maximum pulsing rate of about 50 Hz. All of the chambers were powered by a single high voltage power supply. The typical operating voltage on the chamber was ~4 kV.

The gas used in the chambers was a mixture of 90% Ne and 10% He, with approximately 0.2% 1-propyl alcohol to promote spark quenching. The alcohol concentration was controlled by bubbling a fixed proportion of the input gas through alcohol held at a stable temperature. Each chamber required a gas flow of about 10 cm^3/min to maintain a stable, low-oxygen gas mixture. The maximum permissible oxygen level was approximately 600 ppm O_2.

The Magnetostrictive Chambers[45]

Each magnetostrictive chamber was constructed of two wire planes wound on a 1/2 inch thick Fiberglas G-10 frame with aluminum angles on each side for support. The wires were either vertical or slanted at tangents of ±1/8 with respect to the vertical direction and were spaced 1 mm apart. The

chambers were sealed with Mylar laminated aluminum foils that also served as the electrodes for a dc clearing field. Each chamber had an 8 inch diameter Mylar circle glued between the wire planes to deaden the central beam region. The chambers used 90% Ne and 10% He gas mixture with alcohol added to promote spark quenching and were typically operated at a high voltage of ~6 kV. For additional support, the chambers were stacked and bolted together in compact modules of three to four chambers.

Both the low voltage and high voltage wire planes of each chamber were readout using a conventional magnetostrictive delay line. There were fiducial wires at the ends of each chamber to provide two reference pulses on the magnetostrictive wands. One problem with the magnetostrictive wands was that the propogation velocity was a function of temperature. This caused the position of the fiducial pulses to wander. Their position could change by as much as 3 cm over a period of a few hours and they had to be closely monitored in the data analysis. A small shift in position severely affected the alignment of the downstream chambers. Otherwise, these chambers performed well throughout the experiment. The following paragraphs briefly describe the various sets of magnetostrictive chambers used in the muon spectrometer.

The 2m X 6m chambers formed a module of 3x-, 3u-, and 2v-wire planes. These eight wire planes were used in conjunction with the twelve 2m X 4m shift-register planes to measure the tracks and determine the momentum of charged particles downstream of the Chicago Cyclotron magnet.

There was a set of four 2m X 4m magnetostrictive chambers located behind the 2 inch thick steel wall. Electrons, positrons, and photons would shower in the 3 r.l. steel plate and produce a dense cluster of sparks in these chambers around the track found in the spark chambers in front of the steel converter.

There were three 2m X 4m chambers installed behind a 16 inch thick lead brick wall (~70 radiation lengths) with the intention of measuring the neutron-induced cascade showers. After looking at the on-line event display, it was felt that the chance of success in neutron detection was remote. No attempt was made to use these chambers in the data analysis.

The muon chambers were located behind the 2.44 meter steel hadron absorber. These four magnetostrictive chambers were used to identify the scattered muon. Identification of the muon was complicated by multiple Coulomb scattering and showers in the steel.

The Recoil and TOF System

On each side of the target there was a set of four 2m X 4m magnetostrictive chambers and a set of scintillation counters to detect recoil particles. The chambers had wires oriented in either the x- or y-direction. The scintillation counters measured the velocity of a particle by time-of-flight and, in conjunction with the pulse height from the counters, could separate pions from protons up to a momentum of 500 MeV/c.

The recoil and TOF system was moved to Fermilab from a μp scattering experiment[46] at Brookhaven National Laboratory. These chambers failed to work properly during most of the experiment. Neither the data collected from the chambers nor the counter TOF information was used in the data analysis.

Experimental Trigger

The trigger for the muon scattering experiment was an extremely simple one. The trigger was basically the requirement that an incoming muon scatter by a large enough angle or lose enough energy to fire an element of the

muon hodoscope located behind the 2.44 meter steel wall. As shown schematically in Figure 23, the trigger signal was provided by the logic requirement

$$B*\bar{N}*M*G \quad .$$

Each of the four inputs to the trigger logic is briefly described below:

1) B is formed by an incident beam particle passing through trigger counters, T_1, T_{1A}, T_2, and T_3 in the muon beam line. The veto counters, VS, ensure that the incoming muon pass cleanly through the apertures of the tagging magnets, and the halo veto counters, VH, reject in-time muons outside the beam region from triggering the spectrometer. The additional requirement that the two beam hodoscopes, B_5 and B_6, just before the target have at most one struck element reduced the number of spurious triggers due to upstream interactions of the muon beam.

2) $\bar{N}$ required that the triggering muon had lost sufficient energy or scattered by a large enough angle to miss the beam veto hodoscope N, located behind the steel hadron absorber.

3) M was the requirement that the triggering particle penetrate the 2.44 meter steel absorber and fire an element of either the M_v or M_h hodoscope.

4) G ensured that the scattered muon also fired an element of the G hodoscope located in front of the hadron absorber.

It should be noted that the (q^2,ν) limit of the experiment could be varied by changing the size and position of the N hodoscope, or by the removal of M elements in the median plane. Removal of elements in the central band of the muon trigger hodoscope corresponds to the requirement that the vertical scattering angle of the muon be larger than some minimal

angle. This eliminates the high trigger rate caused by low q^2 events. Since the muon beam intensity was only 10^6 muons/pulse, it was not necessary to exclude this central band. With this central band included in the trigger, μe scattering events comprised approximately 16% of the total triggers. These events could be easily rejected in the data analysis.

About 10% of the event triggers were accidental coincidences. The accidental trigger rates were monitored by a set of scalers that measured the random coincidences of $B*\bar{N}*M*G$ with one or more of the inputs delayed. Interactions of the muon beam upstream in the tagging magnets, in the beam trigger counters and hodoscopes, and in the aluminum walls of the target accounted for a sizeable fraction of the experimental trigger rate. These were measured during empty target runs. During the LD_2 runs in 1974, the ratio of the trigger rates for target full to target empty was close to 1. The typical trigger rate for a full LD_2 target run was ~8/pulse for a muon beam intensity of ~5 X 10^5 muons/pulse.

The On-line Control System

The primary function of the on-line computer control system was to collect data for the experiment and record it on magnetic tape. The major elements of the system were an XDS Sigma-3 computer, an experimental control panel, a CAMAC data acquisition system, and the on-line program. These are described in detail in Appendix 2.

In addition to its main task of data acquisition, the on-line control system served to monitor the performance of the muon spectrometer and provided the basic control for the experiment. No physics calculations were done on-line. The control system was designed to provide a great deal of flexibility and a minimum of confusion for the experimenter. There were

only four buttons to push to control the experiment and the on-line program could be tailored to one's specific needs by means of a panel of thirty-two sense switches.

The vast amount of electronics in the muon spectrometer was interfaced to the Sigma-3 computer through the use of a CAMAC data acquisition system. The CAMAC system provided a convenient standard for integrating the many different pieces of equipment in the muon spectrometer, and could easily incorporate the addition of a new piece of electronics. The prime merit of the Sigma-3 computer was its hardware priority interrupt structure. This allowed the on-line program to respond to event triggers at the highest priority level, reading the event data from the CAMAC system and logging it on magnetic tape, while monitoring the performance of the spectrometer and performing basic control functions at lower levels. A small sample of the event triggers recorded on magnetic tape were examined by the on-line program to ensure that the spectrometer was functioning properly.

The Collection of Data

Experiment E-98 at Fermilab conducted two major periods of data-taking with liquid hydrogen and liquid deuterium targets. The data collected during these two periods is summarized below:

Period	Muon Energy	Useful Muon Intensity	Target	# Triggers
March-July 1974	150 GeV	~5 X 10^5/pulse	LH_2	~242 K
March-July 1974	150 GeV	~5 X 10^5/pulse	LD_2	~256 K
December-February 1975	150 GeV	~5 X 10^5/pulse	LH_2	~355 K
December-February 1975	100 GeV	~5 X 10^5/pulse	LH_2	~360 K

This data was collected in approximately 1000 hours of running time.

Each major period of data-taking was divided up into short runs, each a few hours long. The length of each run was in general determined by the amount of time it took to fill one magnetic tape with data (~5000 events). In too many instances, a run was prematurely terminated because of equipment failure in the muon spectrometer, a beam line magnet tripping off, or loss of beam in the accelerator. Rarely, however, was the experiment down for more than a few hours.

The full target runs were interspersed with runs for various types of studies. Some data was taken using a beam trigger for studies of the beam distribution and reconstruction efficiency. Also, a few runs were taken using a muon halo trigger. The muon halo illuminated the apparatus rather uniformly and these runs were intended for checking the alignment of the chambers and hodoscopes in the spectrometer, although they did not turn out to be as useful as thought. The empty target runs were taken at the end of each major running period because of operational difficulties with the target.

Off-line Data Analysis

The off-line data analysis was performed on computers in the Applied Math Division of Argonne National Laboratory (ANL). The major software development was done on an IBM 360/75 computer using an interactive time-sharing option (TSO). The processing and reduction of most of the experimental data was performed on an IBM 370/195 computer with 4 million bytes of memory. The data analysis was carried out in three separate phases which are briefly described below.

In the first phase, the "raw" data tapes written by the on-line program were processed and checked for errors. The hodoscope information was unpacked

and the wire chamber addresses were converted into spatial spark coordinates. The wire chambers were checked for missing fiducials and any errors in hodoscope positions or chamber alignment were corrected. Once the muon spectrometer was properly aligned, the tracks were found in the wire chambers. The pattern recognition took an average of 0.2 seconds per event on the IBM 370/195 computer, which made this phase of the analysis the most time consuming (more than 90% of the total computer time was spent in the pattern recognition). After the tracks had been found in the wire chambers, a summary containing the decoded hodoscope information and reconstructed tracks was written on magnetic tape. All the tracks in the wire chambers were recorded--no selections were made on the tracks found.

In the second phase of the analysis, the in-time particle tracks were identified and stale out-of-time tracks rejected. Most important was the identification of the scattered muon from among the tracks found in the downstream spark chambers. If the scattered muon could not be found the event was rejected. The momenta of the scattered muon and all the tracks identified as in-time hadrons were calculated, and the event was classified accordingly as a nuclear scatter, μe event, or radiative tail event, etc.

In the third phase the kinematics of each scattering event were calculated and cross sections tabulated. The measured cross sections were corrected for the geometrical acceptance, efficiencies, and dead-time of the apparatus, and the radiative corrections were applied. Finally, a subtraction for the empty target background, evaluated in the same manner, was made. More details will be discussed in the following chapters.

Fig. 5.--Layout of the Fermi National Accelerator Laboratory, showing the 500 GeV synchrotron and experimental areas.

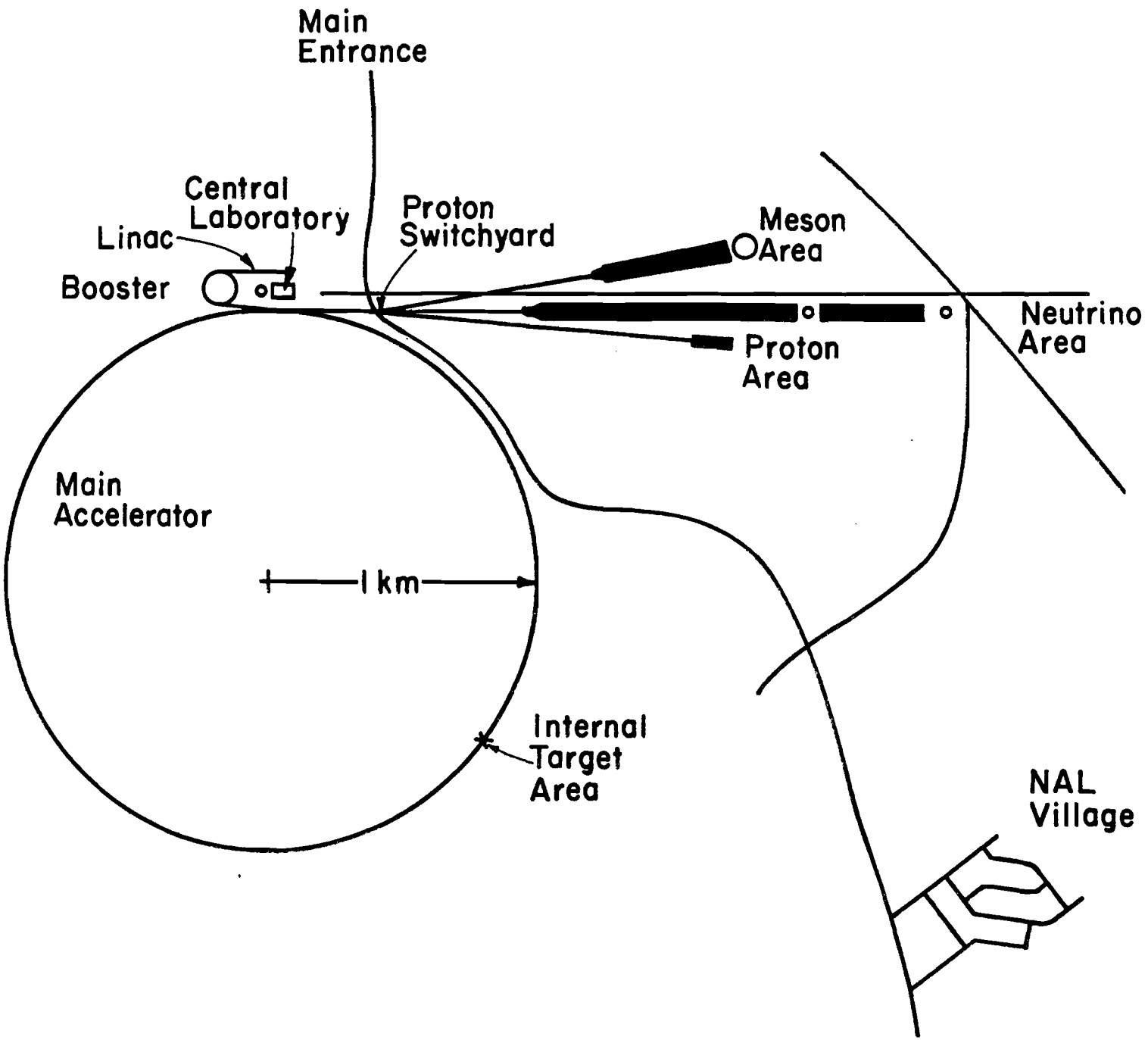
Main
Entrance
Central
Laboratory
Linac
Booster
Proton
Switchyard
Meson
Area
Neutrino
Area
Proton
Area
Main
Accelerator
1 km
Internal
Target
Area
NAL
Village

Fig. 6.--Schematic layout of the muon beam at Fermilab.

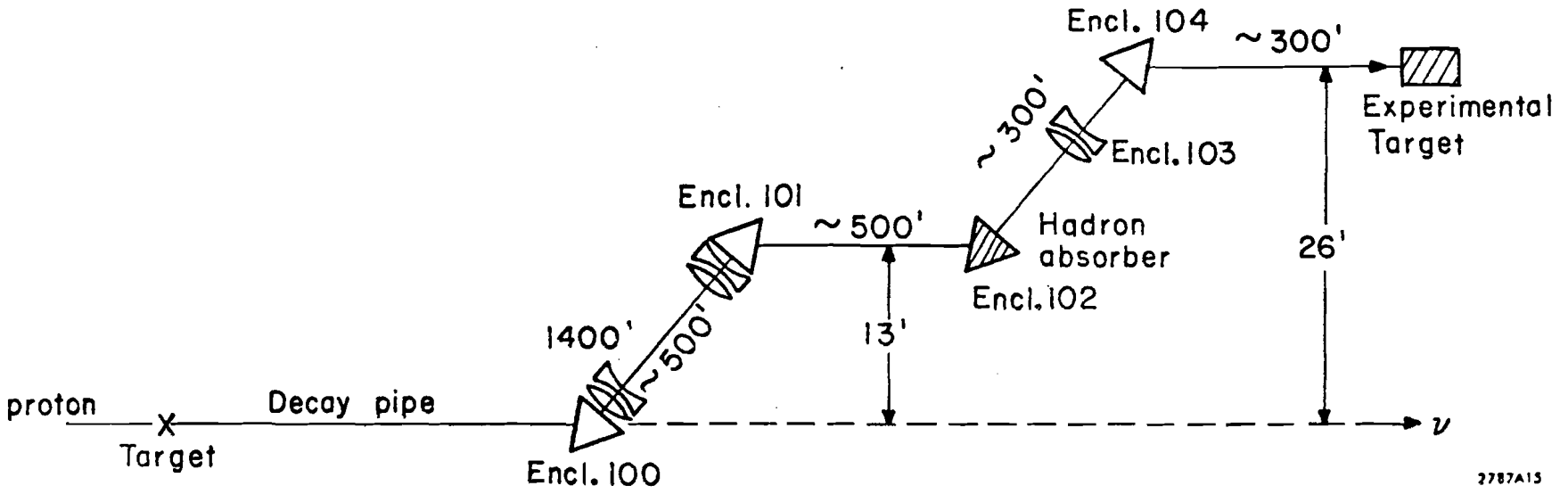
Encl. 104
~300'
Experimental Target
~300'
Encl. 103
Encl. 101
~500'
Hadron absorber
Encl. 102
26'
1400'
~500'
13'
proton
Decay pipe
Target
Encl. 100
ν
2787A15

Fig. 7.--Schematic of the muon beam optics.

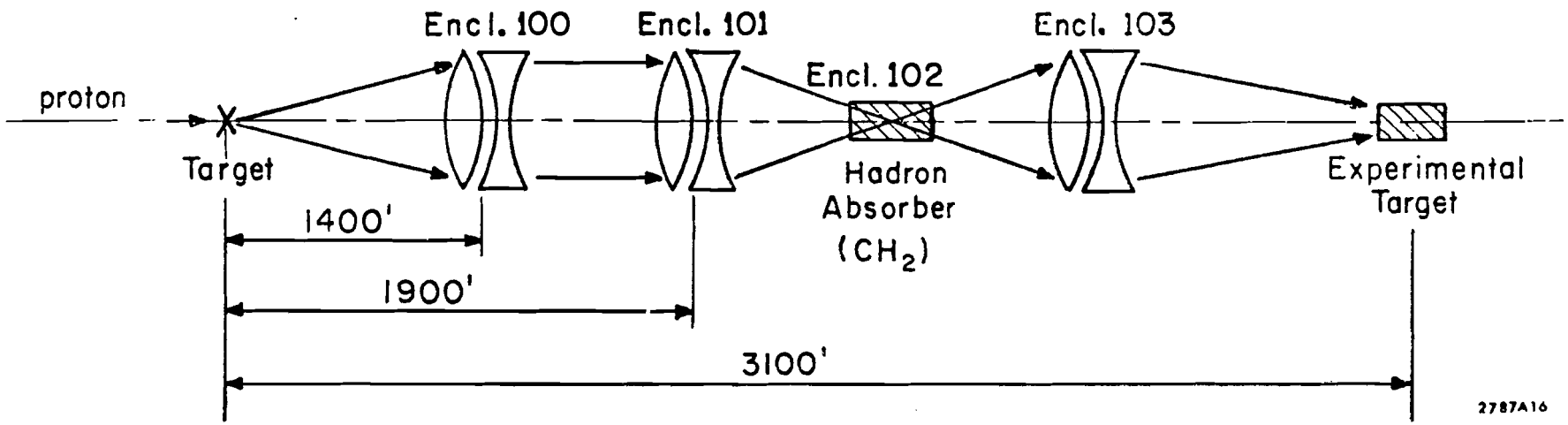
Encl. 100
Encl. 101
Encl. 103
Encl. 102
proton
Target
Hadron
Absorber
(CH_2)
Experimental
Target
1400'
1900'
3100'
2787A16

Fig. 8.--Spatial distributions of the muon beam at the experimental target, reconstructed from tracks in the beam multiwire proportional chambers.

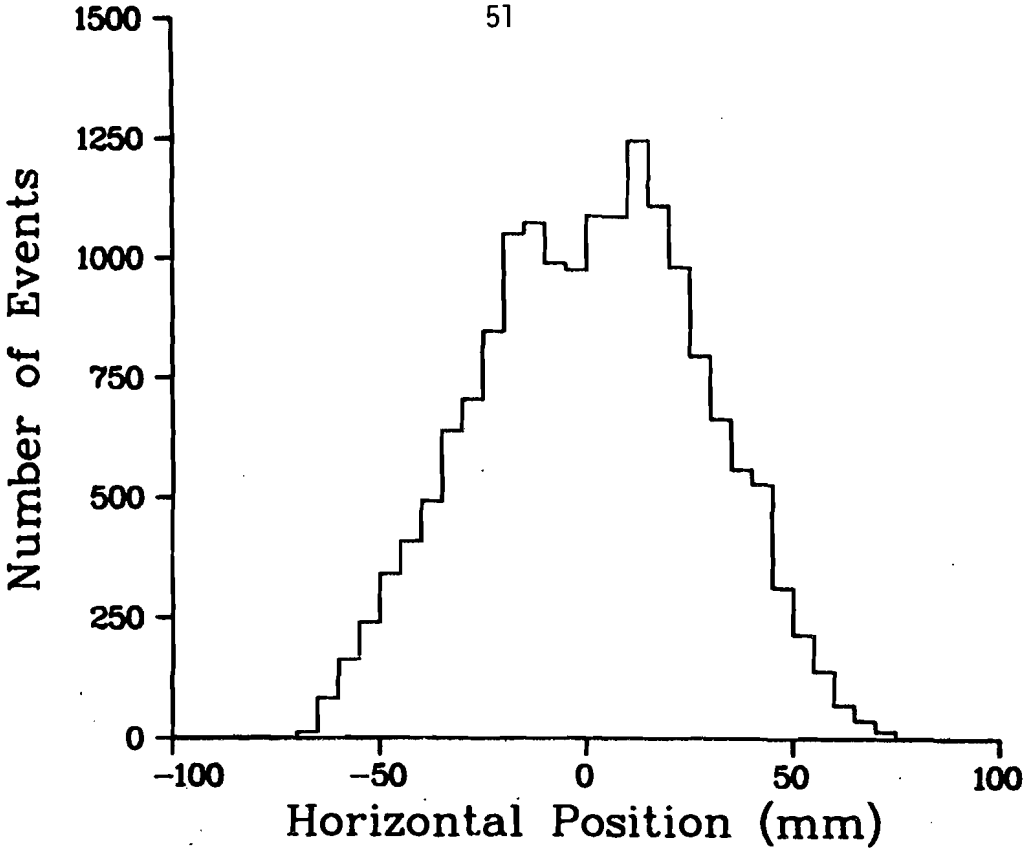
1500
1250
1000
750
500
250
0
Number of Events
-100
-50
0
50
100
Horizontal Position (mm)

(a)

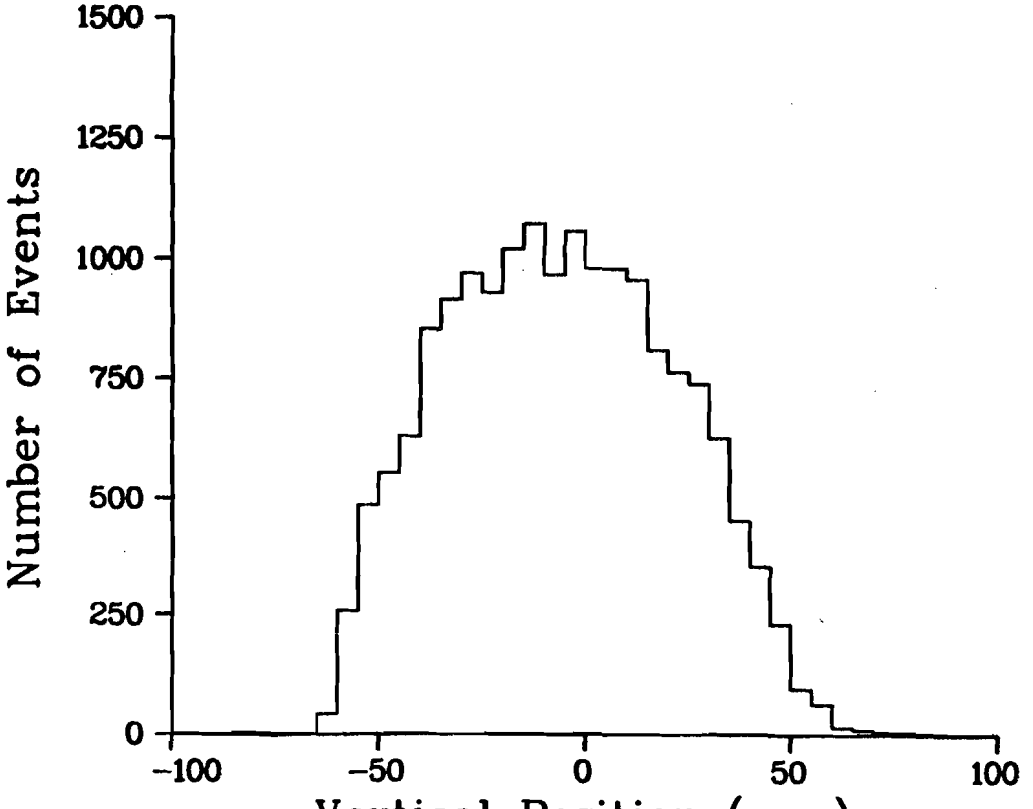
1500
1250
1000
750
500
250
0
Number of Events
-100
-50
0
50
100
Vertical Position (mm)

(b)

Fig. 9.--Angular distributions of the muon beam at the experimental target, reconstructed from tracks in the beam multiwire proportional chambers.

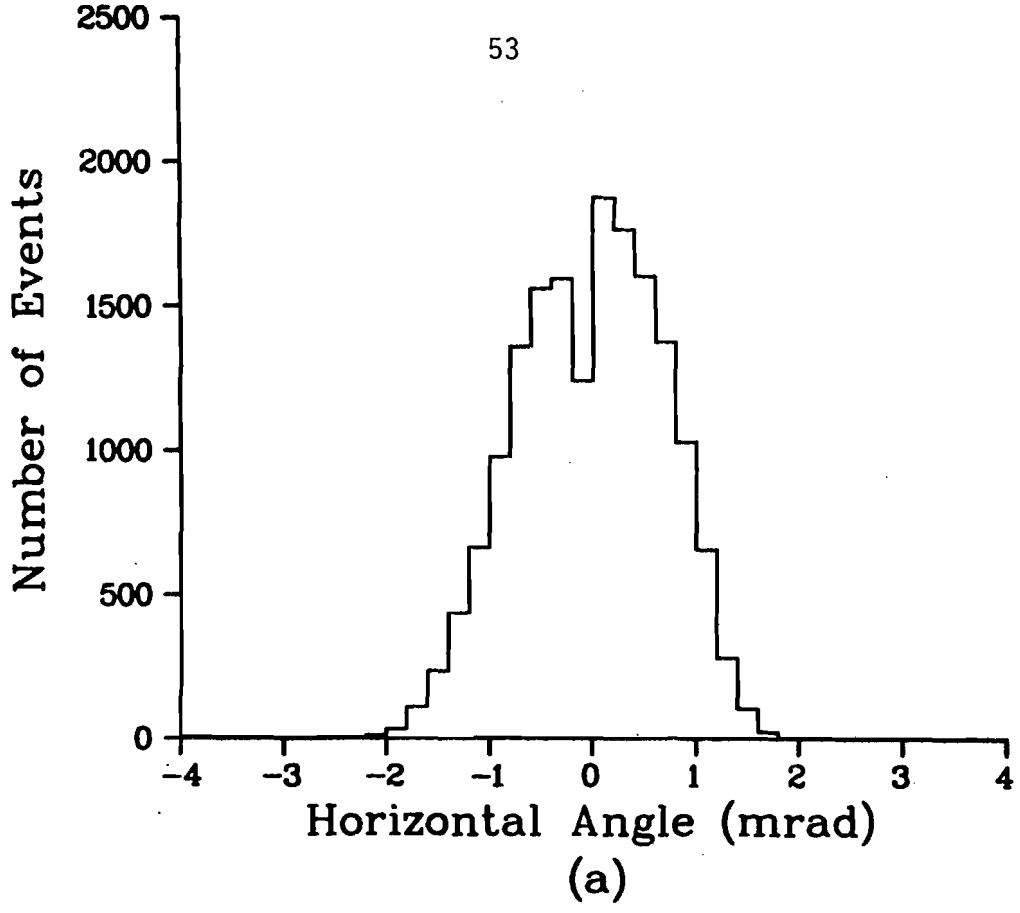
Number of Events
2500
2000
1500
1000
500
0
−4
−3
−2
−1
0
1
2
3
4
Horizontal Angle (mrad)

(a)

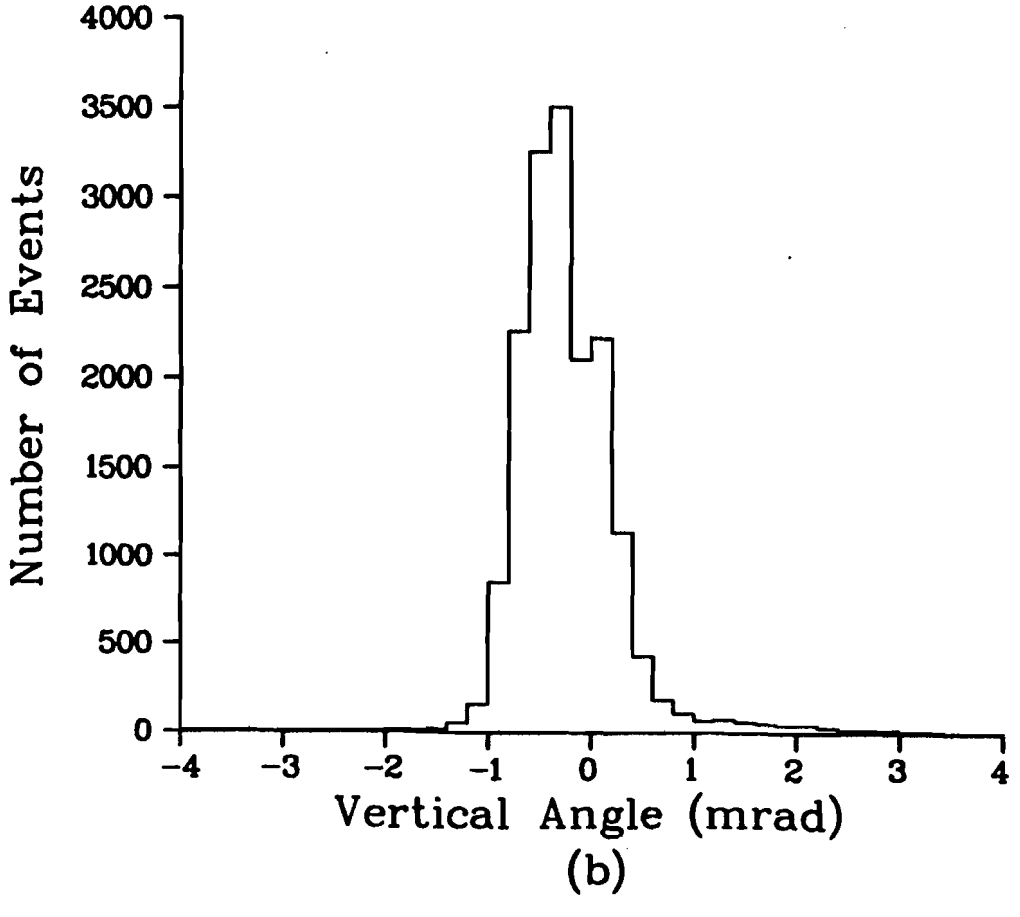
Number of Events
4000
3500
3000
2500
2000
1500
1000
500
0
−4
−3
−2
−1
0
1
2
3
4
Vertical Angle (mrad)

(b)

Fig. 10.--Typical reconstructed momentum distribution of the muon beam for a nominal momentum of 147.22 GeV/c.

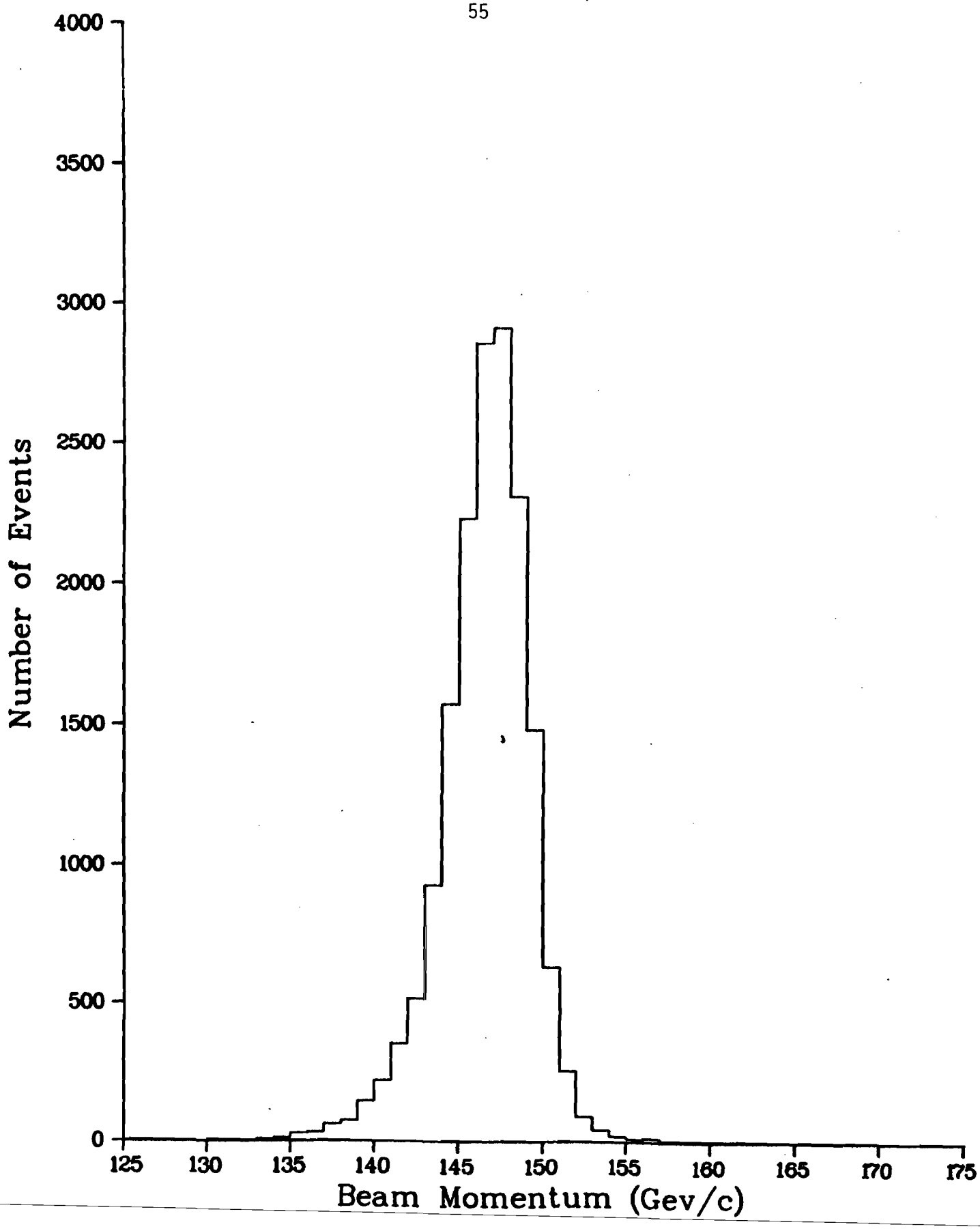
4000
3500
3000
2500
2000
1500
1000
500
0
Number of Events
125
130
135
140
145
150
155
160
165
170
175
Beam Momentum (Gev/c)

Fig. 11.--Schematic layout of the muon scattering spectrometer at Fermilab, built by a Chicago-Harvard-Illinois-Oxford collaboration.

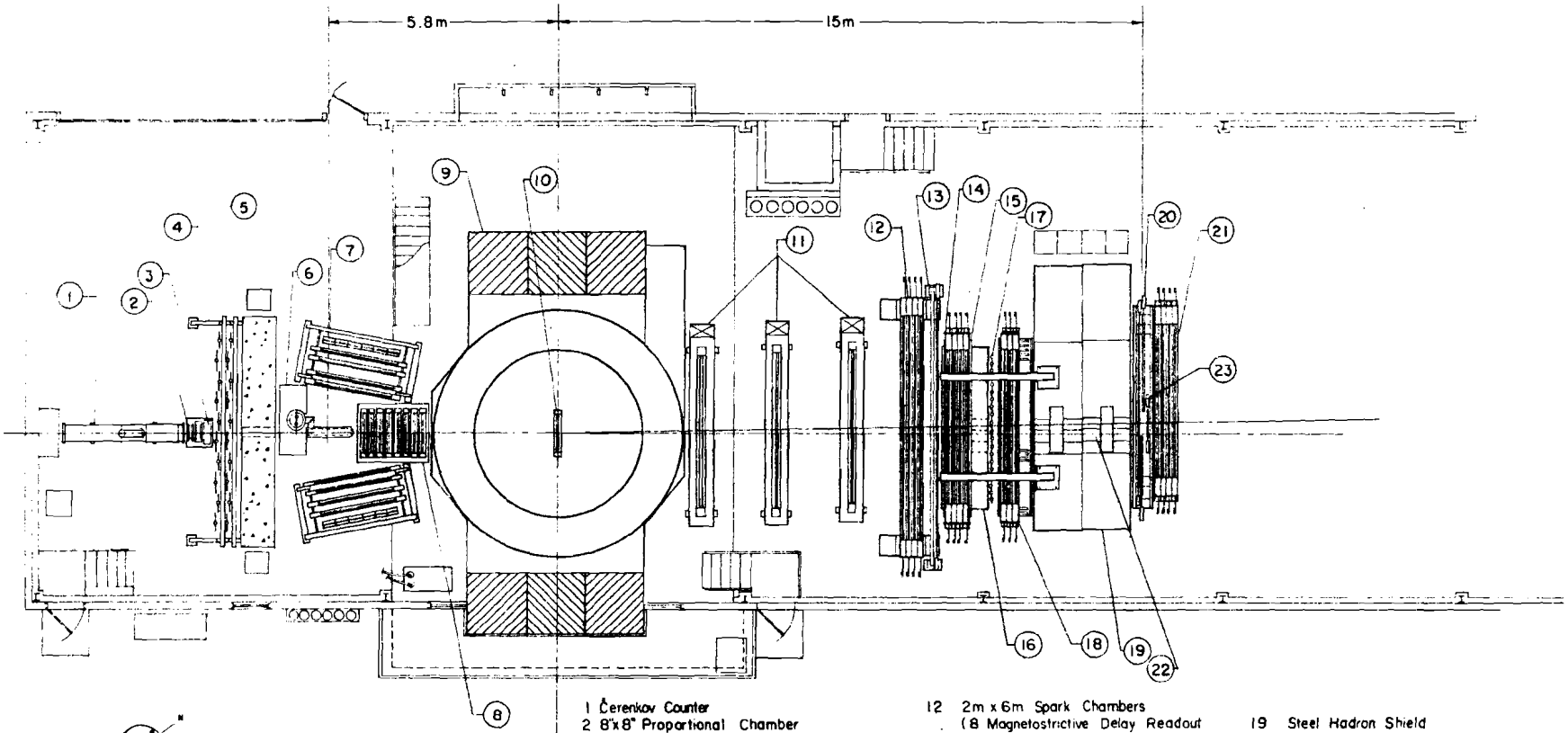

N (project)

0 1 10

Scale in Feet

1 Čerenkov Counter
2 8"x8" Proportional Chamber
3 Hodoscope
4 Halo Veto Counter
5 Backward Scattering Shield
6 Liquid H_2 Target (1m Long)
7 Spark Chambers & Time of Flight System
8 8 - 1m x 1m Proportional Chambers
9 Cyclotron Magnet (4.3m dia. Poletip)
10 1m x 1m Proportional Chamber
11 3-2m x 4m Spark Chamber
4 Shift Readout Planes/Chamber
12 2m x 6m Spark Chambers
(8 Magnetostrictive Delay Readout Planes)
13 2m x 6m G Hodoscope
14 2m x 6m x 2" Steel Plate
15 2m x 4m Spark Chambers
(8 Magnetostrictive Delay Line Readout Planes)
16 2m x 4m x 40.6cm Pb Absorber
17 2m x 4m H Hodoscope
18 2m x 4m Spark Chambers
(6 Magnetostrictive Delay Line Readout Planes)
19 Steel Hadron Shield
20 2m x 4m M Hodoscope
21 2m x 4m Spark Chambers
(8 Magnetostrictive Delay Line Readout Planes)
22 Removable Shutters
23 N Hodoscope

μ-p INELASTIC SCATTERING EXPERIMENT AT N.A.L.

Fig. 12.--Schematic diagram of the liquid hydrogen/deuterium target.

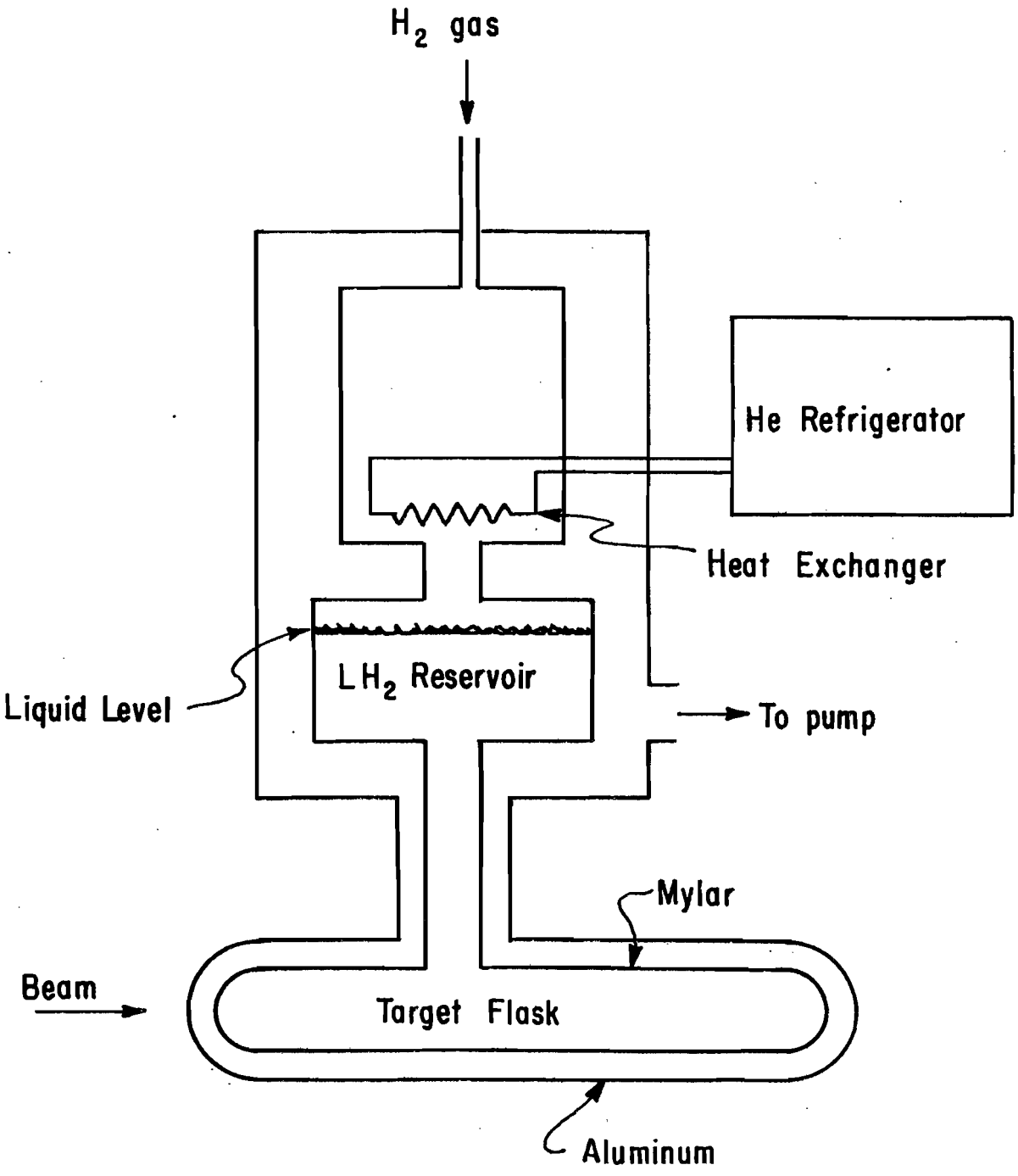
H_2 gas
He Refrigerator
Heat Exchanger
LH_2 Reservoir
Liquid Level
To pump
Mylar
Beam
Target Flask
Aluminum

Fig. 13.--Drawing of the beam hodoscopes.

Beam Hodoscopes

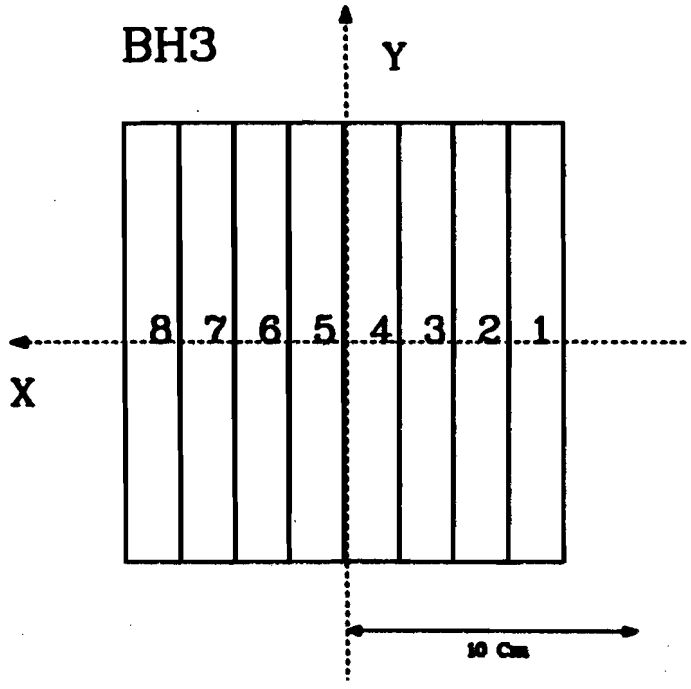

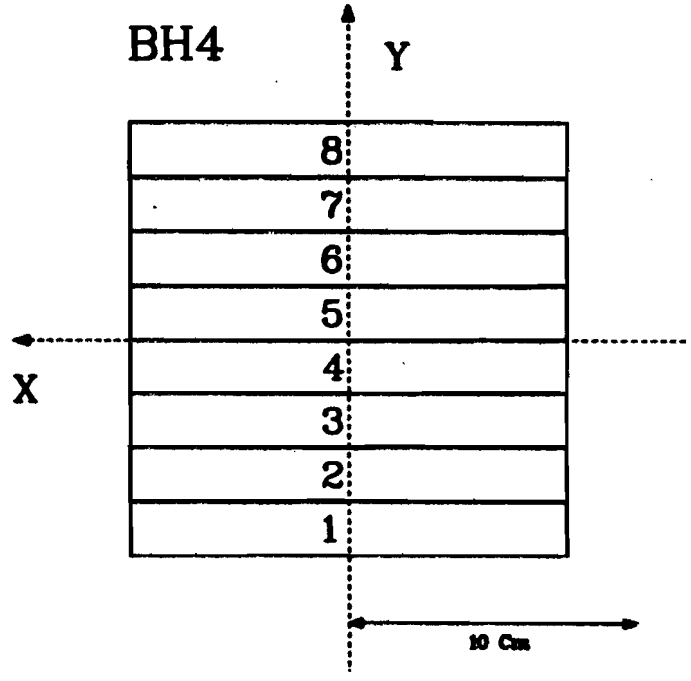

Fig. 14.--Layout of the G and H hodoscopes.

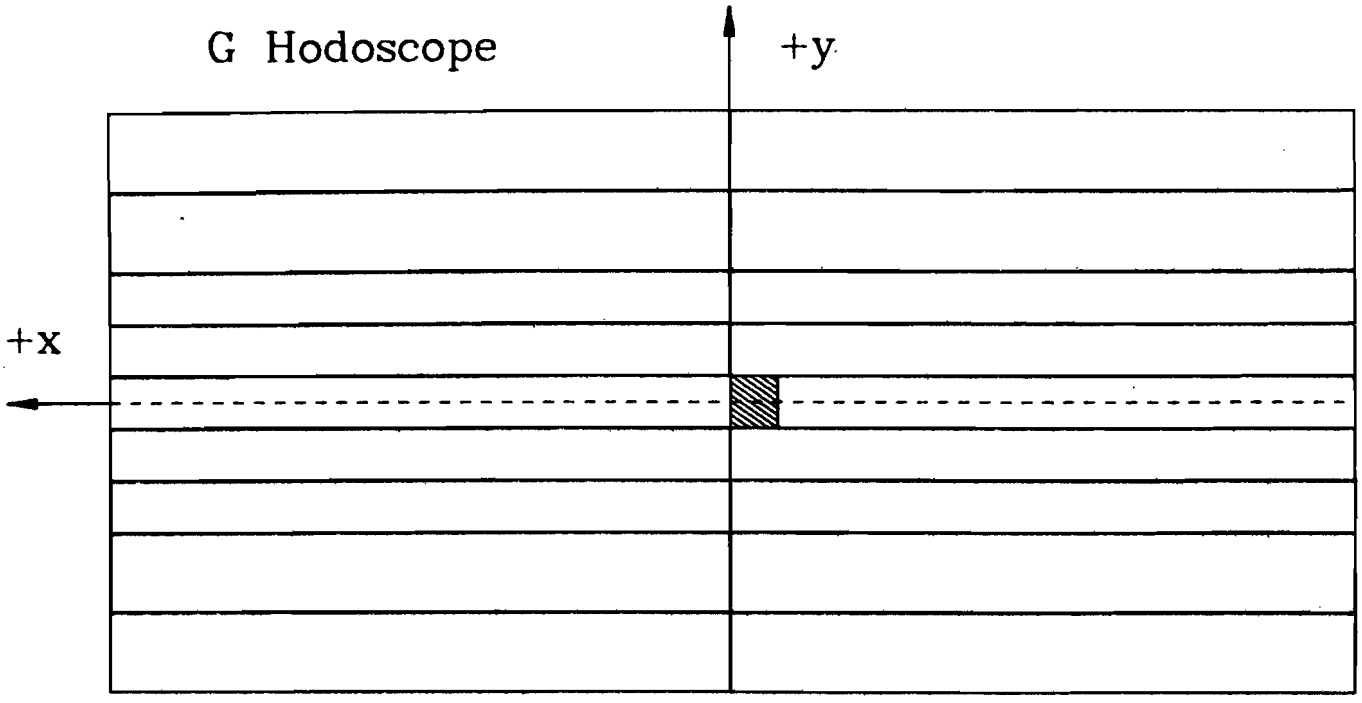
G Hodoscope
+y
+x

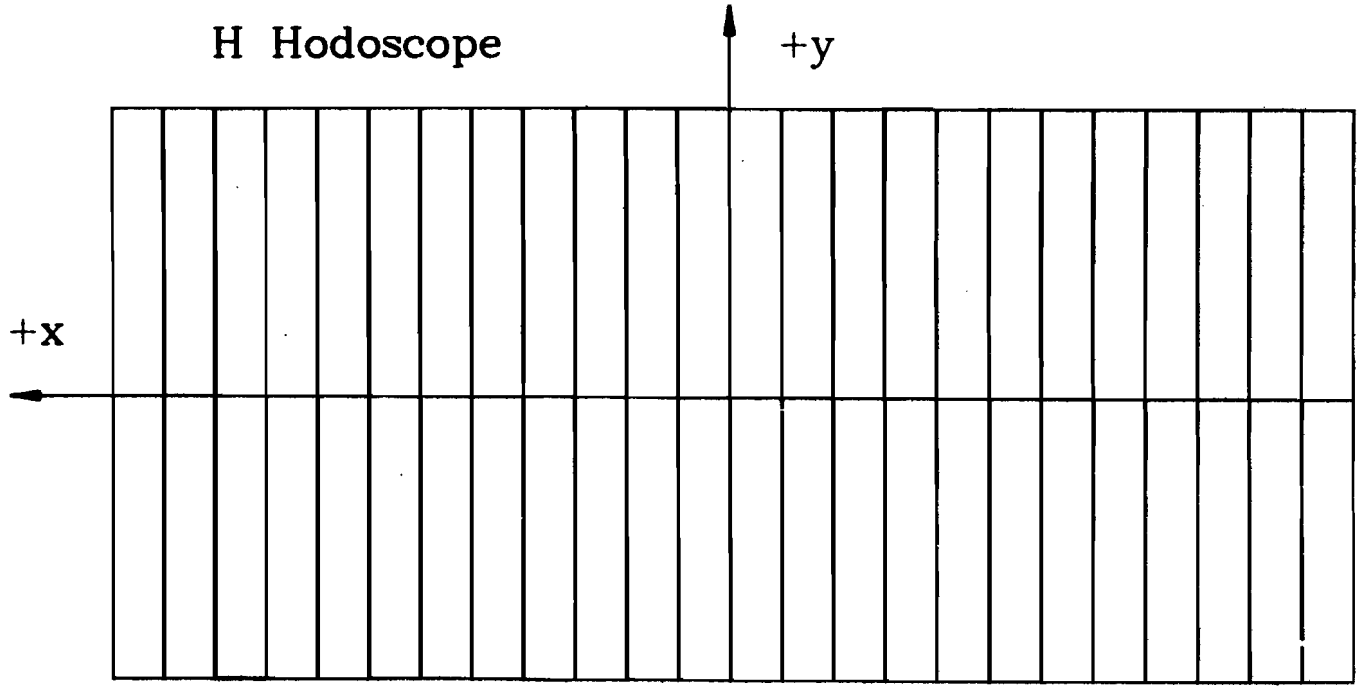
H Hodoscope
+y
+x

Fig. 15.--Schematic drawing of the muon trigger hodoscopes M_v and M_h.

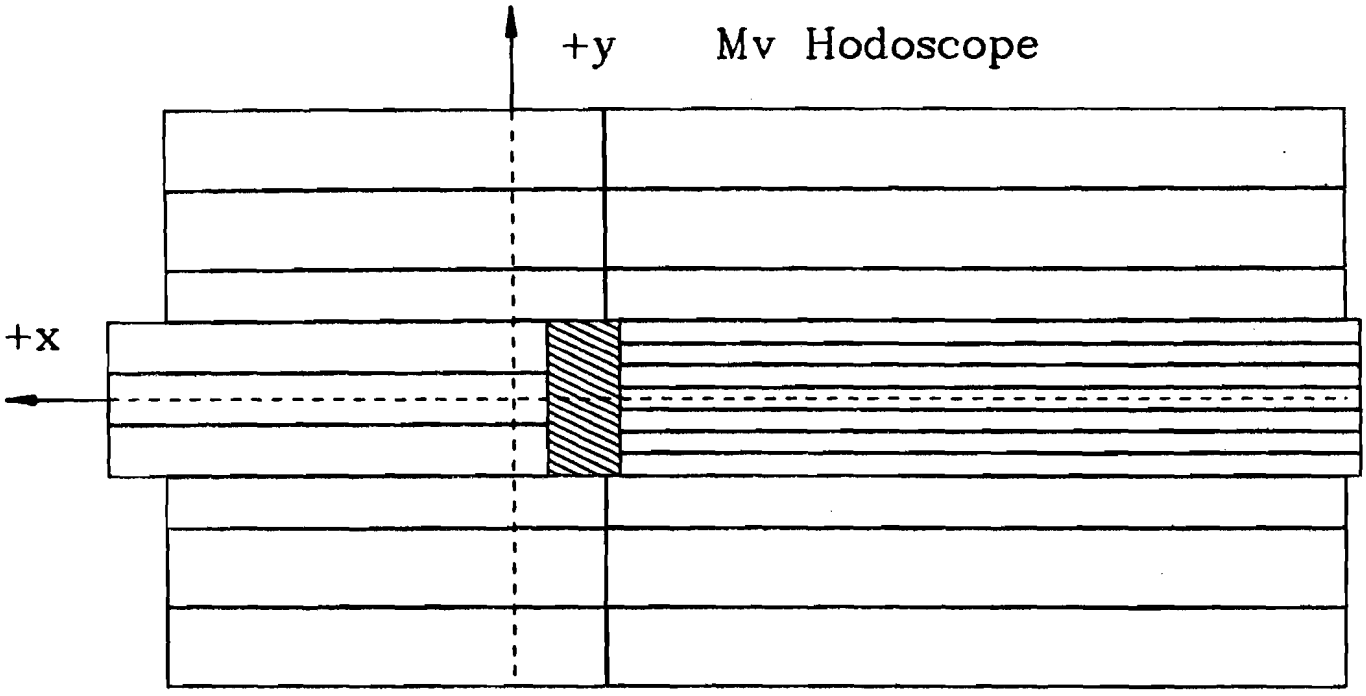
+y
Mv Hodoscope
+x

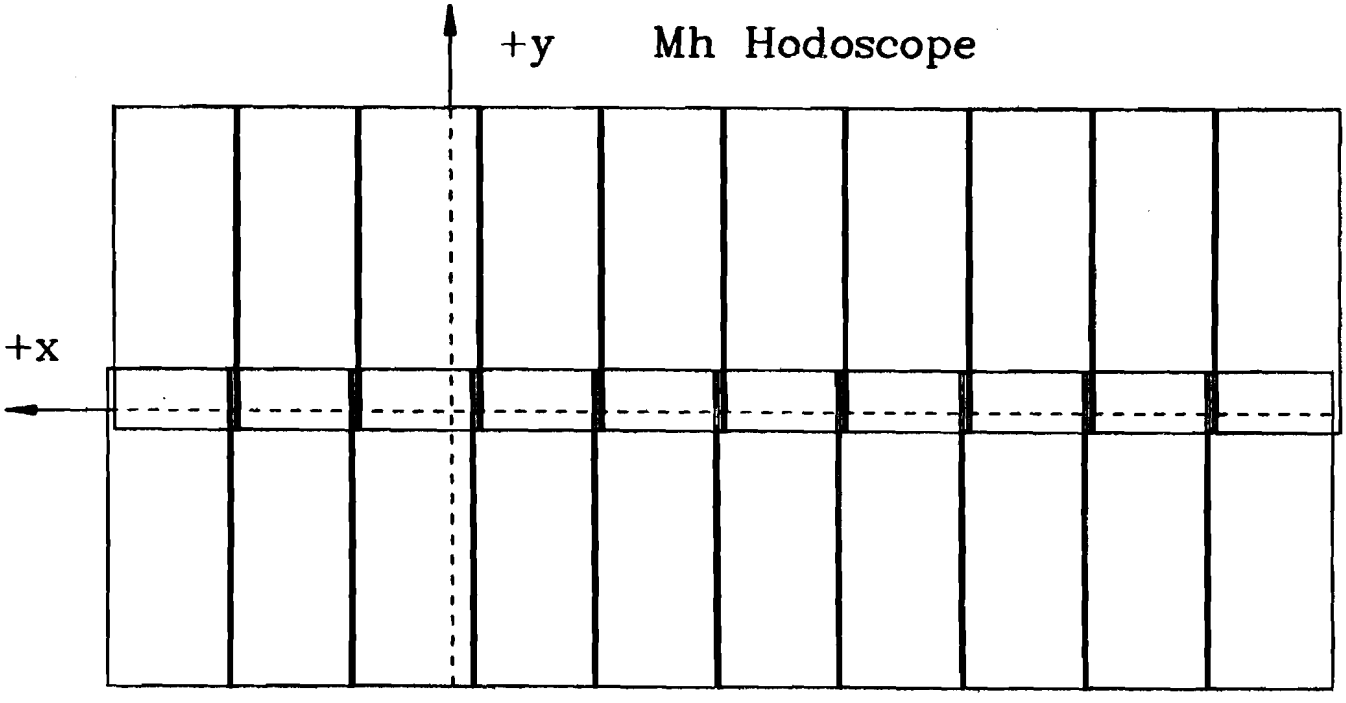
+y
Mh Hodoscope
+x

Fig. 16.--Drawing of the N beam veto hodoscope showing overlapping counter elements.

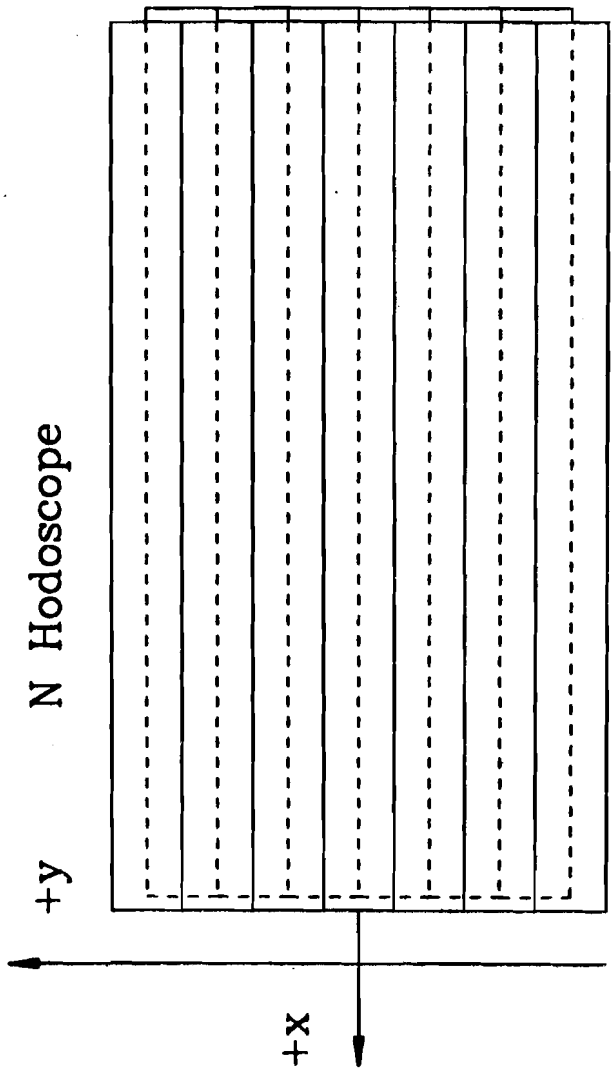
N Hodoscope
+y
+x

Fig. 17.--A schematic of the mechanical construction of the 1m X 1m MWPC's.

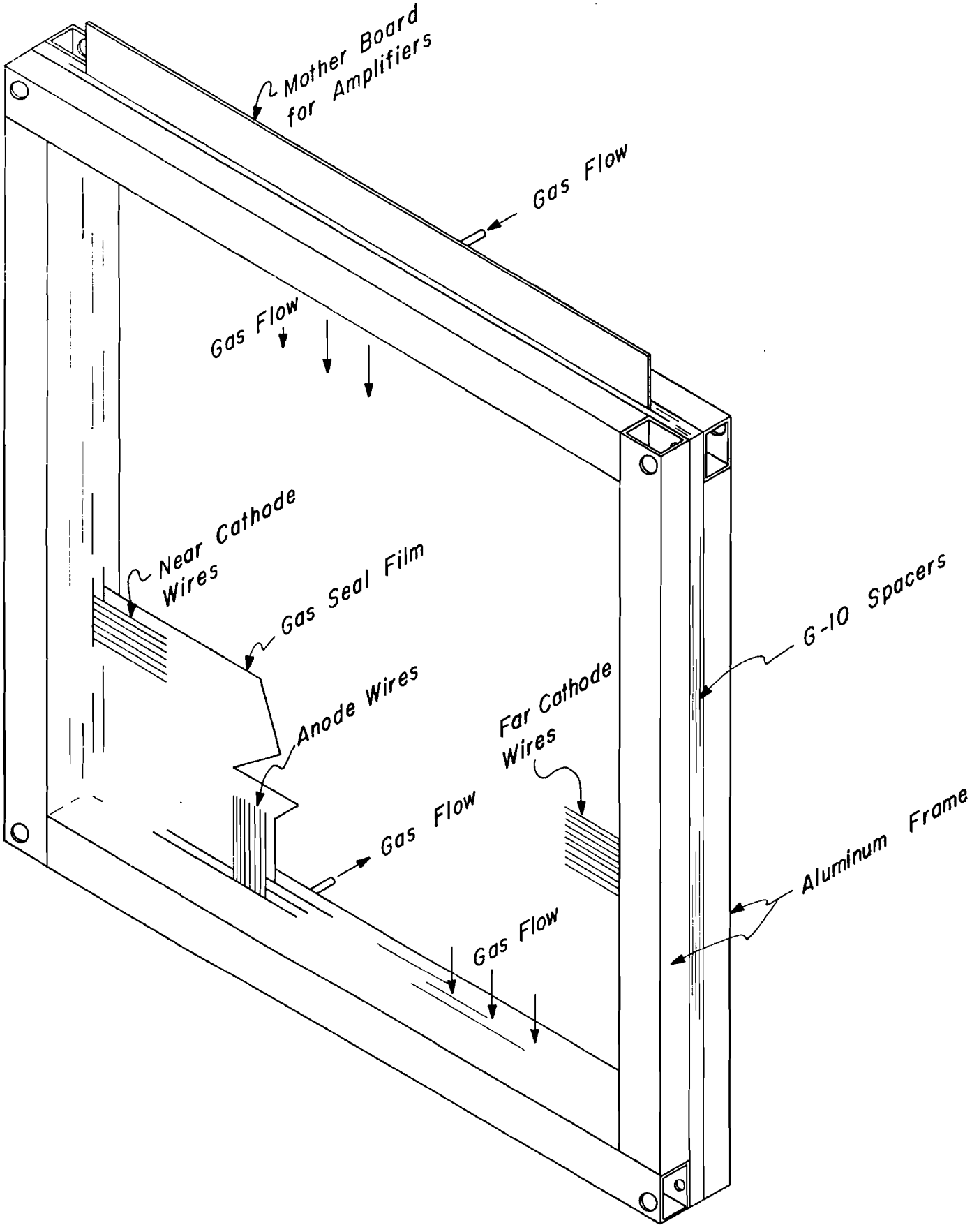
Mother Board for Amplifiers
Gas Flow
Gas Flow
Near Cathode Wires
Gas Seal Film
G-10 Spacers
Anode Wires
Far Cathode Wires
Gas Flow
Aluminum Frame
Gas Flow

Fig. 18.--A typical efficiency curve of a 1m X 1m MWPC as a function of the gate width at the latch.

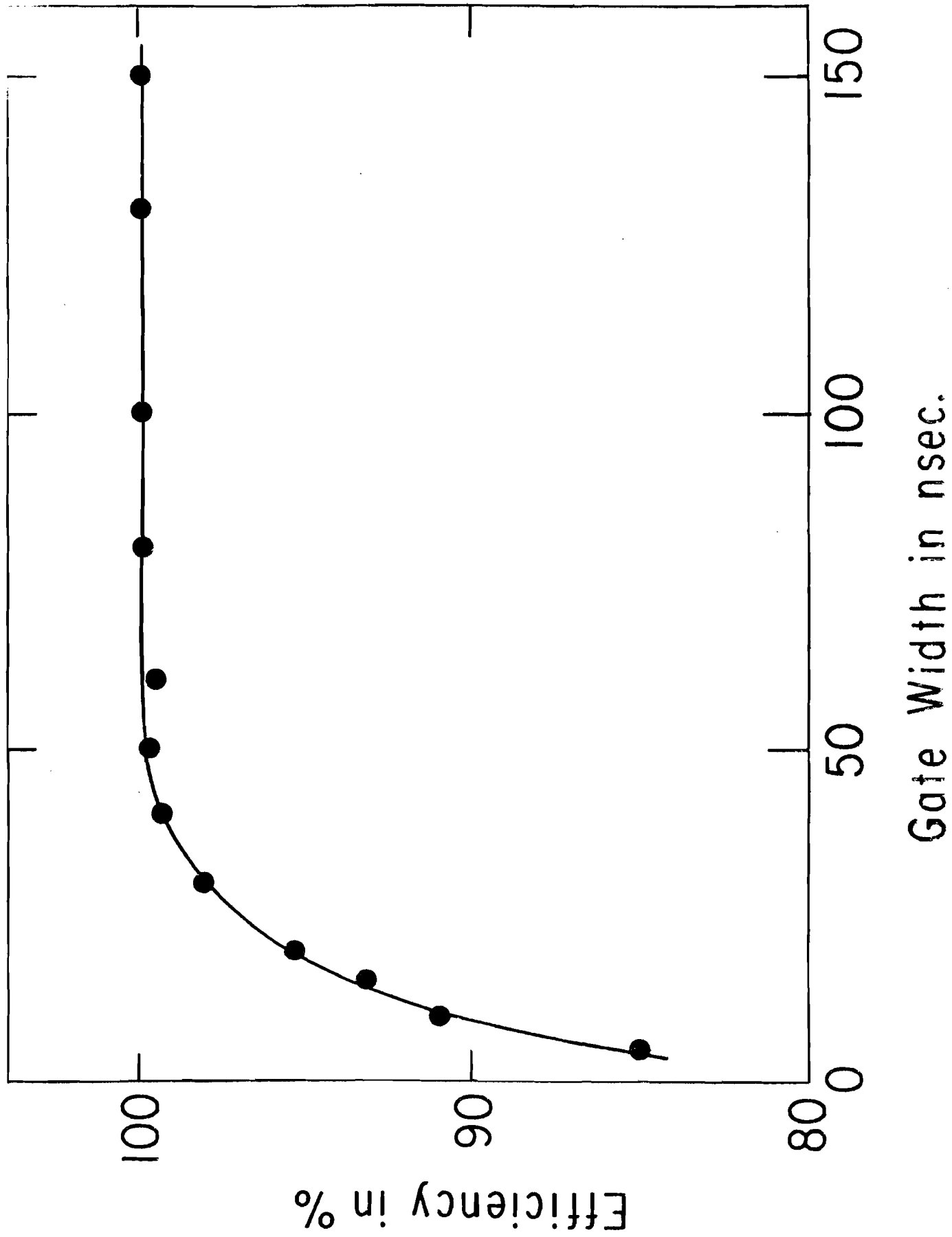
Efficiency in %
100
90
80
0
50
100
150
Gate Width in nsec.

Fig. 19.--Spatial resolution of a 1m X 1m MWPC. The anode wire spacing is 1.5 mm.

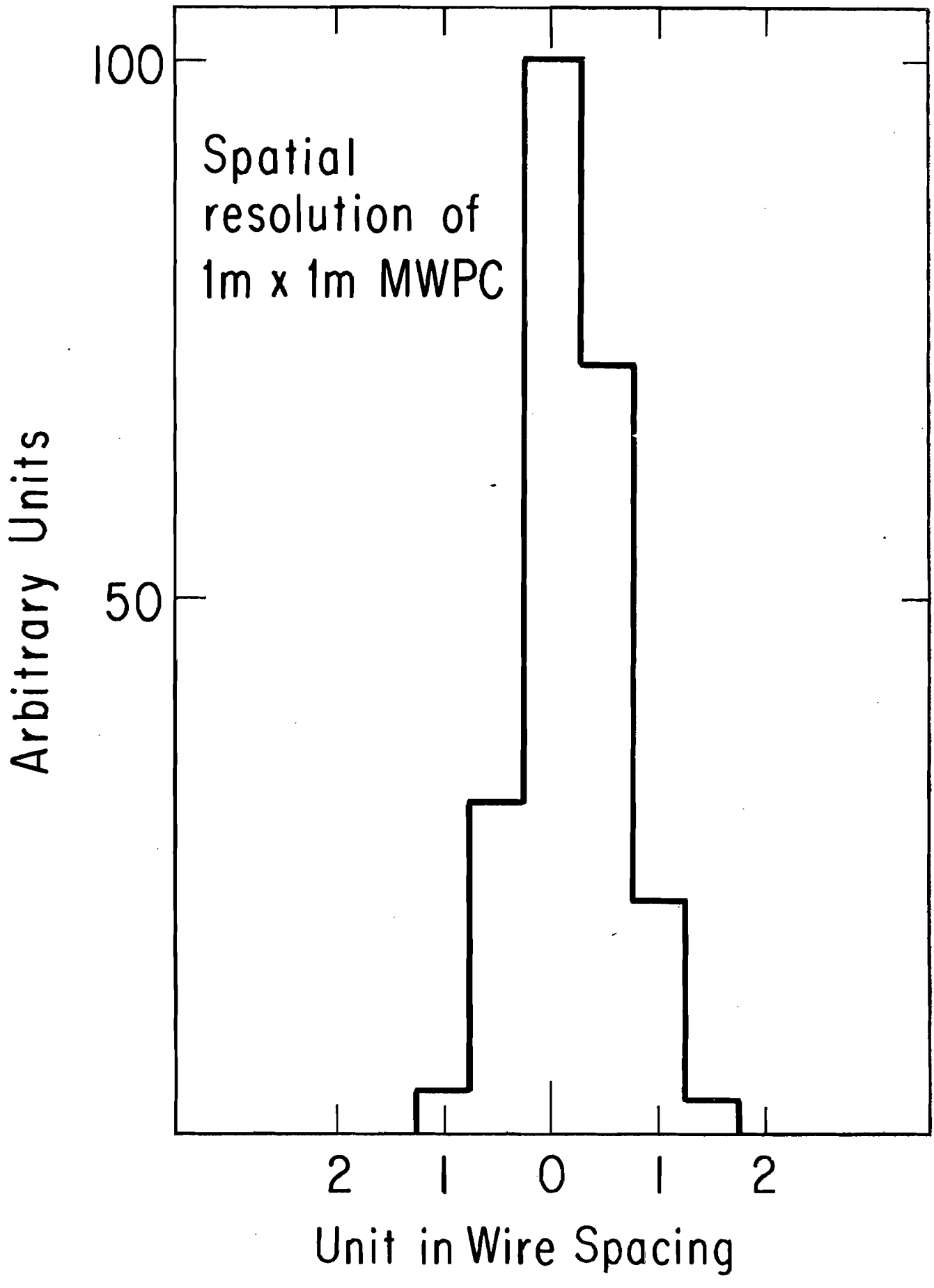
100
50
Arbitrary Units
Spatial
resolution of
1m x 1m MWPC
2
1
0
1
2
Unit in Wire Spacing

Fig. 20.--Overview of the construction of the 2m X 4m shift-register wire spark chambers.

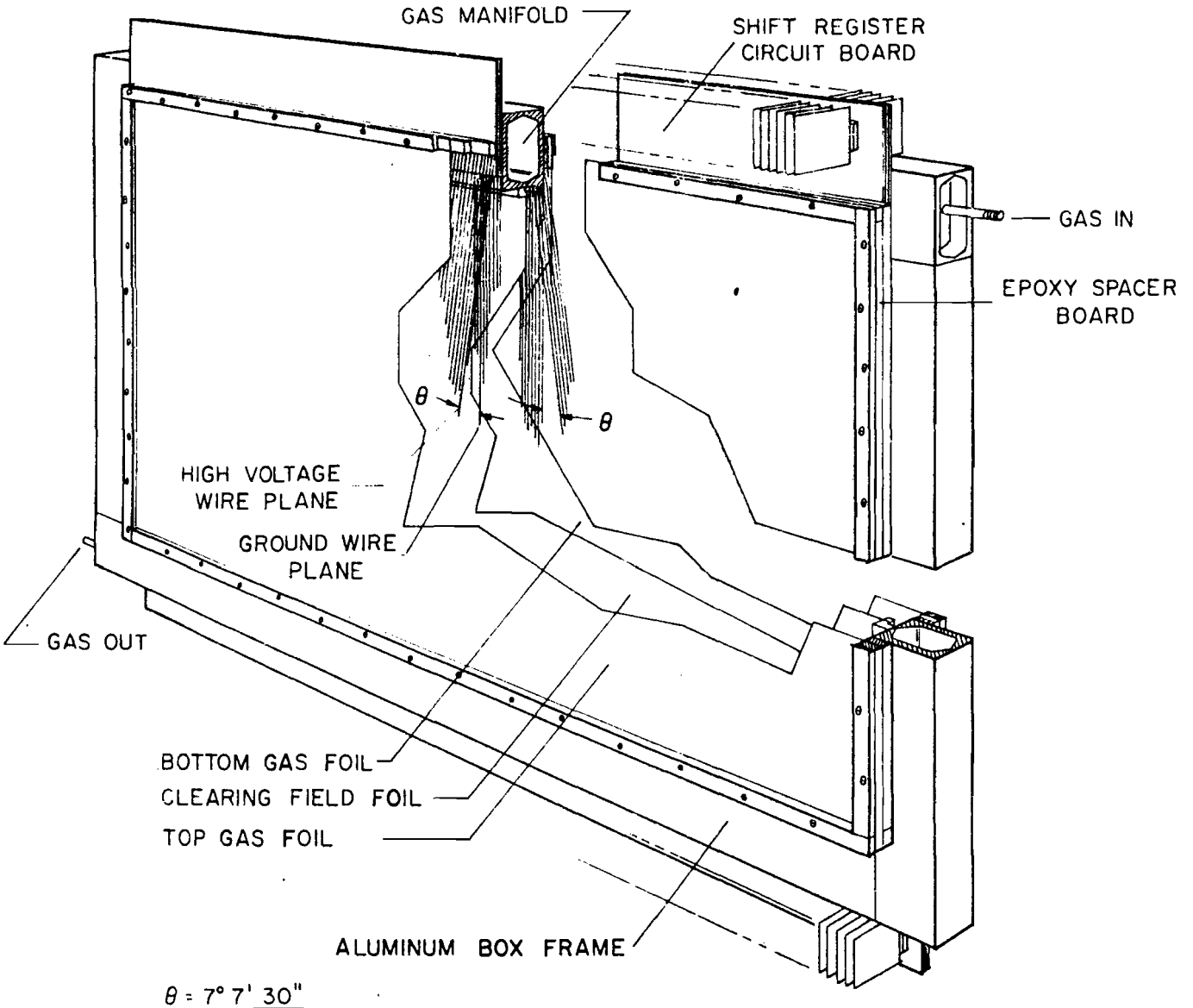
GAS MANIFOLD
SHIFT REGISTER
CIRCUIT BOARD
GAS IN
EPOXY SPACER
BOARD
θ
θ
HIGH VOLTAGE
WIRE PLANE
GROUND WIRE
PLANE
GAS OUT
BOTTOM GAS FOIL
CLEARING FIELD FOIL
TOP GAS FOIL
ALUMINUM BOX FRAME

$\theta = 7° 7' 30''$

Fig. 21.--Schematic of the pulsing arrangement for the 2m X 4m shift-register wire spark chambers.

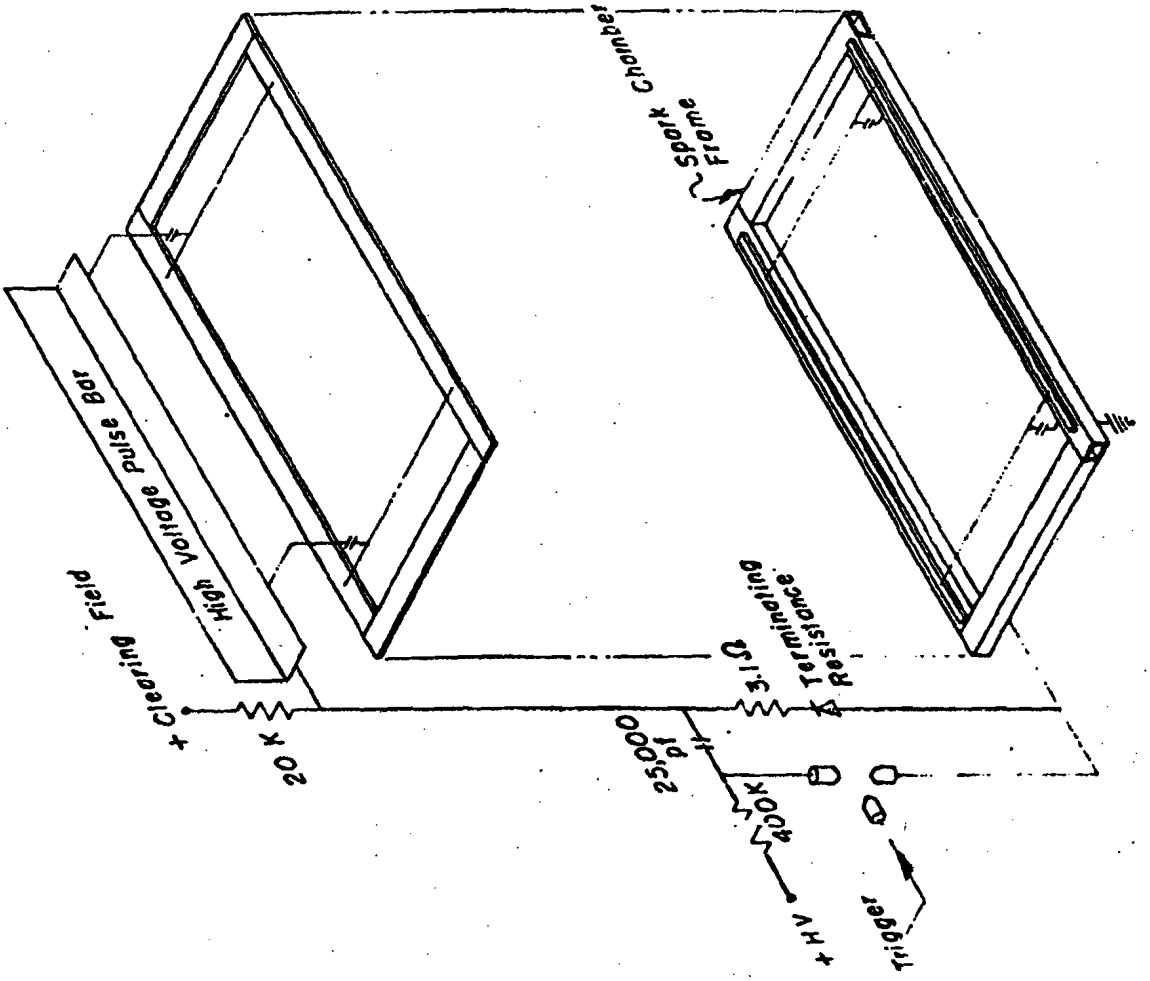
Spark Chamber
Spark Frame
High Voltage Pulse Bar
+ Clearing Field
20 K
25,000 pf
3.1 Ω
Terminating Resistance
400 K
+ HV
Trigger

Fig. 22.--Drawing of the high voltage pulse on the 2m X 4m shift-register wire spark chamber.

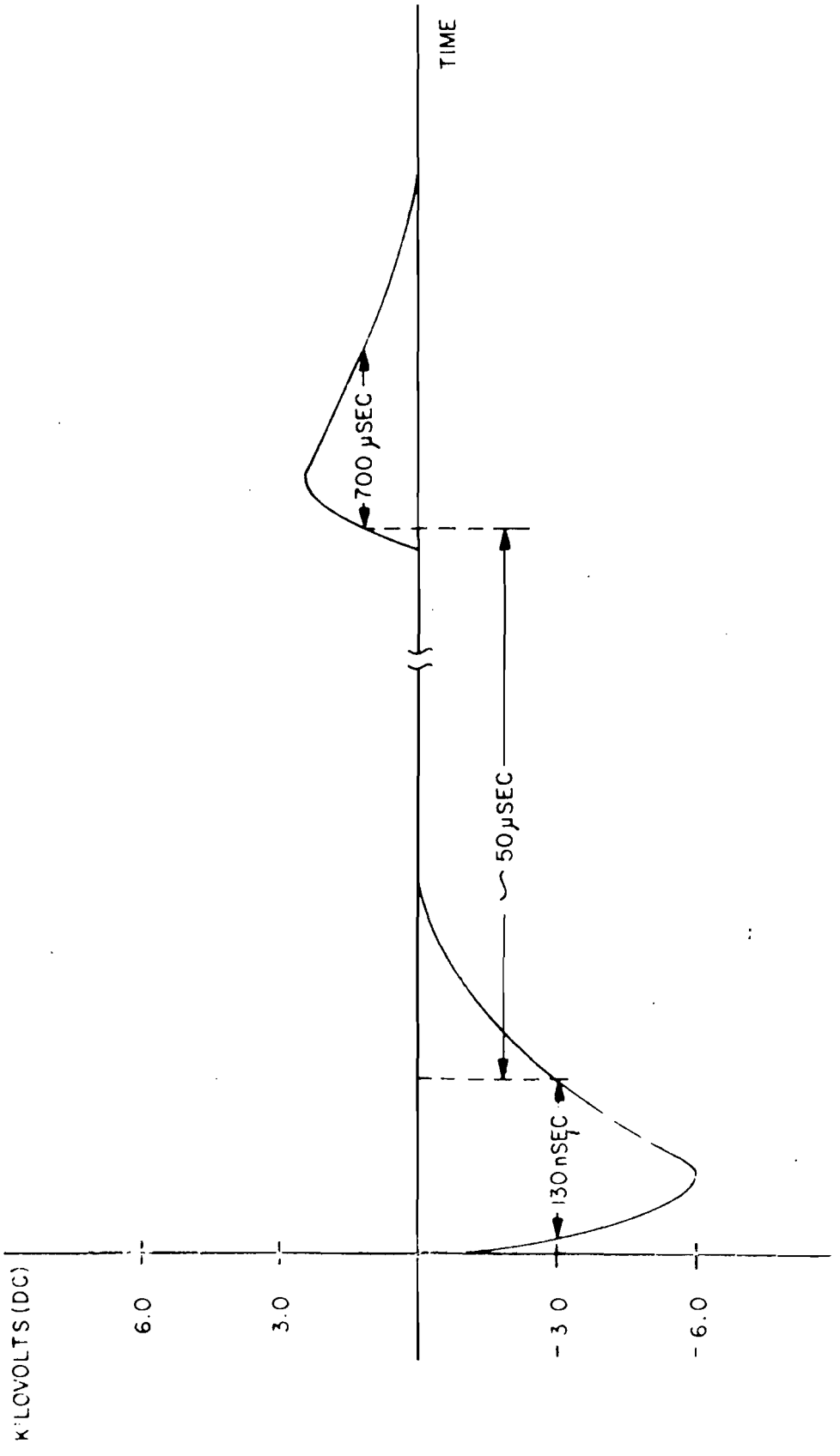
TIME
700 μSEC
~ 50μSEC
130 nSEC
KILOVOLTS (DC)
6.0
3.0
-3.0
-6.0

Fig. 23.--Block diagram of the experimental trigger for the muon spectrometer.

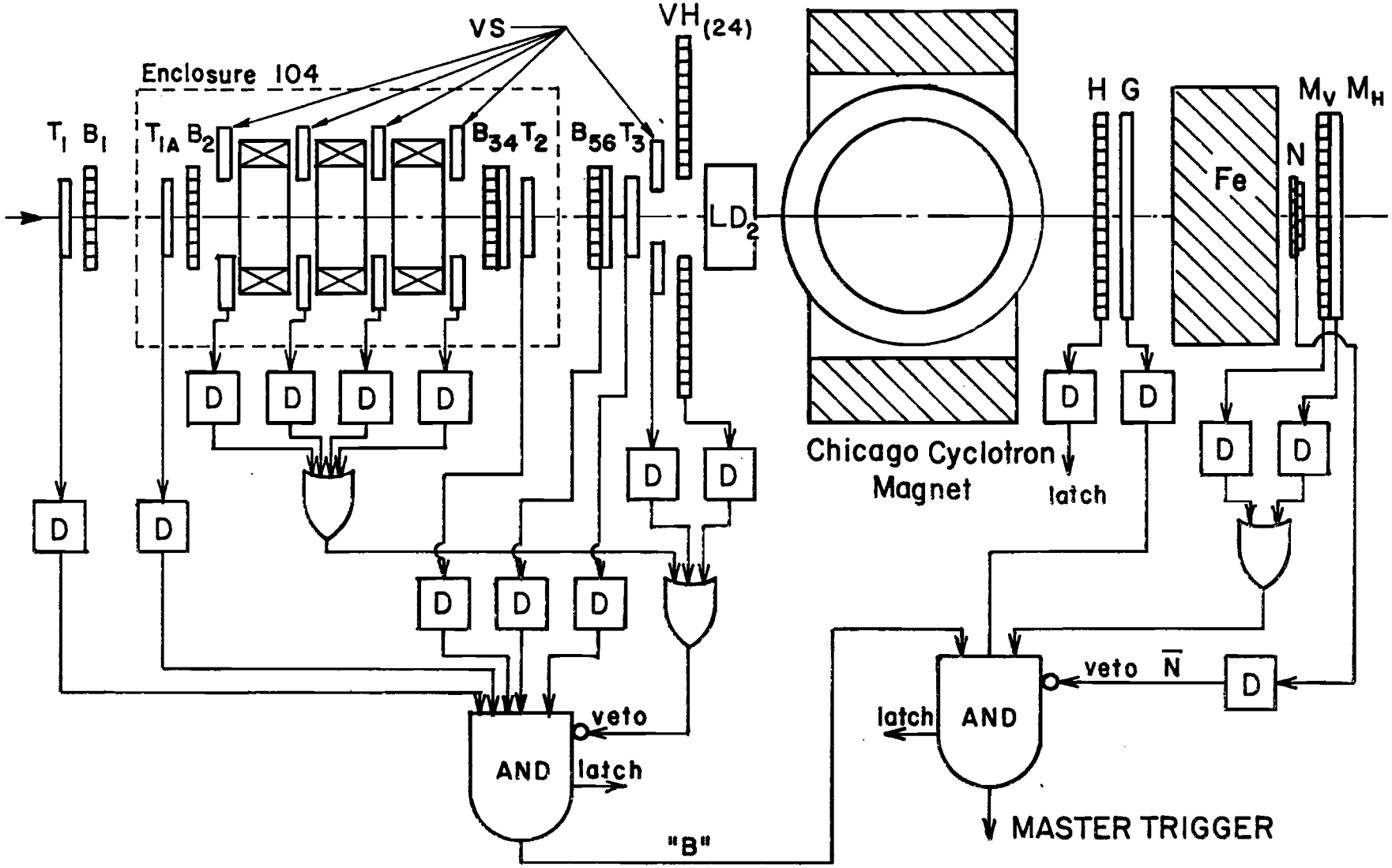
VS
VH(24)
Enclosure 104
T1 B1
T1A B2
B34 T2
B56 T3
LD2
H G
Fe
N
MV MH
D
Chicago Cyclotron Magnet
latch
veto
AND
latch
veto N̄
latch
AND
MASTER TRIGGER
"B"

CHAPTER III

EVENT RECONSTRUCTION

The first task of the off-line data analysis is event reconstruction. For a wire chamber experiment this task is complicated by the fact that the track information from the event is degenerated into a finite set of sparks. For a large aperture multi-particle detector, such as the muon spectrometer, the reconstruction of scattering events can be quite complex. It was not uncommon to have more than ten charged particle tracks in the wire chambers. The reconstruction problem was further complicated by the presence of spurious sparks and inefficiencies in the chambers, and by the fact that the charged particle trajectories are bent by the magnetic field of the Cyclotron magnet.

In this chapter, we describe how we solved the problems of pattern recognition and momentum determination in the muon spectrometer. The criteria used for particle identification and the general classification of the different types of scattering events are also discussed.

Pattern Recognition

Pattern recognition for the muon experiment was divided into three parts. The first task was to find the incoming muon track in the beam MWPC's and hodoscopes before and after the momentum tagging magnets. The second task was to find the tracks of the scattered muon and the charged hadrons in the 1m X 1m MWPC's located behind the target. And finally, the tracks were found in the spark chambers downstream of the Cyclotron magnet.

The task of pattern recognition was often confused by upstream interactions of the muon beam, electromagnetic showers in the target, and multiple Coulomb scattering and showers in the steel hadron absorber. Accidental triggers could produce events that were totally "unintelligible." Track finding in the downstream spark chambers was complicated by the presence of spurious sparks from the Cyclotron radioactivity, stale beam tracks, halo muons, and the long memory time of the chambers (1-3 μsec). These out-of-time tracks could be eliminated to a great extent by "linking through the magnet" to tracks in the 1m X 1m MWPC's because of their much better time resolution. The counter hodoscopes also proved to be useful in filtering out stale tracks. By requiring that the downstream tracks fire at least one hodoscope element, most of the out-of-time tracks could be rejected.

The following paragraphs describe the methods of track finding in the three sections of the spectrometer and the techniques of magnet linkage and counter masking for the downstream spark chambers. First however, we briefly discuss the procedures used for chamber alignment.

Chamber Alignment

To ensure that the wire chambers were properly positioned for each run, a portion of each raw data tape was first checked for alignment and any errors in chamber position corrected. This pre-processing task was necessary because the positions of the fiducials in the magnetostrictive delay line chambers could change from run to run. About 500 events on each tape were analyzed and the tracks found in the different sections of the spectrometer were checked for consistency. The positions for the magnetostrictive delay line chamber fiducials were adjusted and any discrepancy in wand propagation velocity was corrected. Once the spectrometer was properly aligned,

a corrected set of chamber positions and alignment specifications was retained. The data tape was rewound, and the analysis began with these new specifications. The fiducials of the magnetostrictive delay line chambers were checked and corrected event by event through the entire tape.

Beam Reconstruction

The track of the incoming muon was measured by six sets of MWPC's and beam hodoscopes located before and after the momentum tagging magnets. The geometry of the beam tagging system is shown schematically in Figure 24. Each beam chamber was immediately followed by a scintillation counter hodoscope (eight counter elements) in a single module to measure the beam position in either the x (horizontal) or y (vertical) direction.

The wires fired in the MWPC's were first masked by the struck hodoscope elements in that module to see if they were in-time. If a hodoscope element was set without an accompanying wire set in the MWPC, the center of the counter was used as the position of the muon in that module. Using the center of a beam hodoscope element was not a serious compromise in resolution because of the large distances between modules. The width of each hodoscope element was 3/4 inch and the typical distance between modules was ~300 feet. Using the center of the hodoscope element corresponded to a maximum error of ~0.3 mrad in angle.

All possible tracks before and after the tagging magnets were formed from the sets of "hits" (struck wire or hodoscope element) in each module. Some combinations were rejected by demanding that the reconstructed tracks pass through the beam trigger counters and the apertures of the beam line magnets. The tracks downstream of the tagging magnets were required to pass through the hole in the center of the halo veto hodoscope (VH) and strike

the target. In the x-view the tracks upstream and downstream of the tagging magnets were required to "link" (i.e., have the same intercept) in the tagging magnet bend plane. Tracks that failed to link were rejected. This requirement was extremely powerful in eliminating false tracks. The distribution of track linkage in the tagging magnet bend plane is shown in Figure 25.

The reconstruction of the incoming muon was complicated by multiple tracks and inefficiencies in the beam MWPC's. Spikes in the beam spill structure could produce more than one muon track in the multi-wire proportional chambers. These could mostly be eliminated by masking the MWPC's with the beam hodoscopes. A more serious problem was that the muon beam could "scrape" in the tagging magnets or interact in the beam trigger counters and hodoscopes to produce multiple tracks in the beam line. One of the more annoying problems of beam reconstruction was μe scattering in the beam hodoscopes downstream of the tagging magnets. Both the muon and electron remained in the beam line to strike the target. If the interaction occurred upstream, both particles were swept out of the beam line by the tagging magnets.

In a small fraction of the events the incoming muon could not be identified. For these events the decision was postponed until more information was available from the tracks in the 1m X 1m MWPC's after the target. If the ambiguities could not be resolved the event was rejected. The typical reconstruction efficiency was about 85%.

Downstream Pattern Recognition

The track finding in the wire spark chambers downstream of the Chicago Cyclotron magnet was the most complicated and time-consuming of all the

pattern recognition. There were a total of 42 wire planes arranged into three small angle stereo x-, u-, and v-views. The u- and v-wires made angles of ±7.125° (tangents of ±1/8) with the vertical x-wires. There were typically ten tracks in these chambers and each wire plane had an average of 20-30 sparks.

The decision was made to only do track finding in the 2m X 4m and 2m X 6m spark chambers immediately behind the magnet. Tracks in the muon chambers behind the hadron absorber were often confused by multiple Coulomb scattering and showers in the steel. Consequently, it was not always possible to find the muon tracks in these chambers. Track finding in the photon and neutron chambers was also ruled out due to the same problems of showers and multiple Coulomb scattering in the steel plate and lead wall in front of these chambers.

For the 20 x-, u-, and v-wire planes in the 2m X 4m and 2m X 6m chambers, the track finding was done separately in the x-view and in a composite "u" view. Since there were not enough wire planes in either the u- or v-view to ensure a successful independent search (there were nine x-, six u-, and five v-planes), the planes in the v-view were combined with the u-planes to form a composite "u" view of 11 wire planes. The spark coordinates in the v-view were rotated about each track found in the x-view to give the coordinates in the composite "u" view.

The methods of track finding in the x-view and in the composite "u" view were identical. First an arbitrary pair of reference wire planes is chosen. One spark from each reference plane is selected and a straight line is connected between the two sparks. The line is extended to the next plane and if a spark falls within calculated error, the line is refit including this new point. This procedure is continued until all the wire

planes in the view have been interrogated. The search process is then repeated several times with different pairs of initial reference planes. Finally the tracks found in each search process are compared and the common ones regarded as the genuine particle tracks. The "efficiency" of this search method was very high. Identical tracks were typically found in 80% of the individual searches. This provided ample redundancy in the pattern recognition to compensate for any chamber inefficiencies. Once the tracks were found in these two views, the individual x-, u-, and v-spark coordinates of a track were fitted by the method of least squares to form a three-dimensional track.

The downstream pattern recognition was complicated by a number of problems, and we simply list them below:

1) The positions of the fiducials in the magnetostrictive chambers had a tendency to wander throughout a run. This shifting of the fiducials caused an excessive amount of work in trying to maintain proper chamber alignment. This problem was handled by processing the first 500 events of each run to find the correct starting position of the fiducials, and then correcting for the fiducial shifts event by event.

2) There were often stale beam tracks and out-of-time halo muons in the wire spark chambers. The 2m X 4m shift-register chambers were not deadened in the central beam region and saw the full unscattered muon beam. The chambers close to the magnet contained spurious sparks due to the radioactivity of the Cyclotron magnet. These extra sparks added additional burden to the pattern recognition.

3) The 2m X 6m magnetostrictive chambers were deadened in the central beam region so that they did not see the unscattered muon beam. However,

this created another problem. Oftentimes the scattered muon or one of the forward-going hadrons passed through the deadener and was undetected by these chambers. This left only the twelve 2m X 4m shift-register wire planes to measure the charged particle tracks near the beam region. The pattern recognition near the beam region was more difficult because of the large number of sparks.

Track Finding in the 1m X 1m MWPC's

The eight 1m X 1m MWPC's were placed directly behind the target and spaced over a distance of about two meters in a yxyxyxyx arrangement. The tracks were found in the x- and y-views separately in a manner similar to the downstream pattern recognition. Here however, the x- and y-views are orthogonal and there was no correlation between the two views to resolve the classical x-y ambiguity. During the LD_2 running in 1974, an attempt was made to correlate the x- and y-views by rotating one of the y-chambers to a tangent of 1/8 from the horizontal. This third view would provide the necessary information to resolve the x-y ambiguity. The attempt turned out to be unnecessary because we were able to correlate all the tracks by simply demanding linkage through the magnet. We also realized that all four y-planes were necessary for efficient track finding. The rotated plane was restored to its original position for the subsequent LH_2 running. To supplement the planes in each view, a fictitious plane was constructed in the center of the Cyclotron magnet using the intercepts of the downstream tracks. This greatly improved the efficiency of the 1m X 1m MWPC pattern recognition by adding another plane to the search. This fictitious plane was only used to aid the search algorithm and was not included in the least-squares fit of the track. For the LH_2 runs in 1975, an x-y chamber was installed in the

center of the magnet. Its better resolution along the y-direction helped to improve the efficiency of pattern recognition and magnet linkage.

The 1m X 1m MWPC's had the advantage of good time resolution (~100 nsec). They did not suffer nearly the problems of stale out-of-time beam tracks and halo muons that complicated the downstream pattern recognition. However, there could be electromagnetic showers in these chambers since the target represented ~1/8 of a radiation length. When electromagnetic showers occurred, there could be too many tracks in these chambers to do the pattern recognition.

The tracks found in the 1m X 1m MWPC's were used to determine the angles of the scattered muon and the hadrons. The muon was identified in the downstream spark chambers and the corresponding track in the MWPC's determined by "linking" the downstream tracks through the magnet. (See the following section for a description of magnet linkage.) In events where the muon scattering angle was large or there were charged hadrons produced at large angles, the tracks in the MWPC's could be used to determine the vertex of the muon interaction. In most cases, however, the scattering angle was too small to determine the position of the vertex to better than the length of the target along the beam direction.

Magnet Linkage

One nice feature about the Chicago Cyclotron magnet is that its magnetic field is cylindrically symmetric in azimuthal angle ϕ about a vertical axis in the center. This means that a charged particle's angular momentum J_ϕ about this axis will be conserved. This follows most easily from Lagrange's equation:

$$\frac{d}{dt}\left(\frac{\partial L}{\partial \dot{\phi}}\right) - \frac{\partial L}{\partial \phi} = 0 \quad . \tag{3.1}$$

Since the lagrangian for the Cyclotron magnet is cyclic in the variable ϕ, then

$$\frac{d}{dt}\left(\frac{\partial L}{\partial \dot{\phi}}\right) = 0 \quad , \tag{3.2}$$

i.e., J_ϕ = constant. Since the magnetic field also conserves the particle's linear momentum p, this implies that the impact parameter b of the particle, defined in the usual sense as the distance of closest approach to the center of the magnet, will remain constant.

Thus, in the horizontal x-view or bending view of the Cyclotron magnet the tracks found downstream in the spark chambers should have the same impact parameter b with respect to the center of the magnet as the tracks found in the 1m X 1m MWPC's. In the y-view, the tracks upstream and downstream of the magnet should have the same slope and intercept at the center. This is illustrated in Figure 26.

By demanding "linkage" through the magnet in the x- and y-views, most of the stale tracks could be eliminated because of their random orientation. The good time resolution of the 1m X 1m MWPC's also helped, particularly for those near the beam region. Figure 27a shows a distribution of the linkage in impact parameter in the x-view for tracks upstream and downstream tracks of the Cyclotron magnet. Figure 27b shows the difference in slope for upstream and downstream tracks in the x-view for zero magnetic field. Figures 28a and 28b show the linkage in intercept and slope in the y-view. The typical linkage efficiency for downstream tracks was ~90% in the x-view and ~75% in the y-view. The y-linkage efficiency was slightly lower because

of the rotated y-plane in the 1m X 1m MWPC's and because of the poorer y-resolution of tracks downstream.

Counter Masking

The G and H hodoscopes in front of the hadron absorber, and the M_v and M_h hodoscopes behind the hadron absorber, were also useful in filtering out stale tracks. The H and M_h hodoscopes were particularly useful for this purpose since their counter elements were arranged vertically and the Cyclotron magnet dispersed particles horizontally. Each track found in the downstream spark chambers was tested to see if it was masked by a struck hodoscope element. For the M_v and M_h hodoscopes behind the hadron shield, the tracks were tested for a struck hodoscope element within the multiple Coulomb scattering cone around the track. By requiring at least one struck hodoscope element, most stale tracks could be rejected.

The counter-masking of downstream tracks was not perfect. There were inefficiencies caused by holes in the hodoscopes for the muon beam, and by cracks between adjacent non-overlapping elements. Also, more than one track could pass through the same hodoscope element. When this happened, the struck hodoscope could not distinguish which track was in-time. This was especially a problem for the central elements of the G and M_v hodoscopes. Because of the high trigger rate of μe scattering and low q^2 nuclear events, these elements were fired almost every trigger.

Momentum Determination

Once the tracks had been found in the downstream spark chambers and in the 1m X 1m MWPC's behind the target, their momenta were calculated. The calculation was greatly simplified by the uniformity and cylindrical symmetry of the magnetic field of the Chicago Cyclotron. The circular pole faces of

the magnet have a diameter of 4.3 meters and are separated by a gap of 51 inches. The magnetic field has a central value of 15 kG when operated at 1.8 Mw of power, and is symmetric in azimuthal angle about a vertical axis in the center of the magnet. The magnetic field is vertical and has almost no radial component. Figure 29a shows the measured vertical magnetic field as a function of radial position, and Figure 29b shows the radial component at the center of the magnet as a function of vertical position.

The momentum of charged particles could be calculated with good accuracy by using a hard-edged model approximation for the magnetic field. The magnet was approximated by a cylindrically symmetric field of uniform strength B_0 = 15 kG and effective radius R_0 = 2.47 meters. B_0 and R_0 were determined from measurements of the integrals[47]

$$\int B \cdot d\ell = 2B_0R_0 = 74.15 \text{ kG - m} \tag{3.3}$$

and

$$R_0 \equiv \frac{\int r\frac{\partial B_y}{\partial r}\, d\ell}{\int \frac{\partial B_y}{\partial r}\, d\ell} = 2.47 \text{ meters} \tag{3.4}$$

With a hard-edged model, the calculation of charged particle momenta can be reduced to an analytic expression. The time-consuming procedure of tracing the particle orbits through the magnet by numerical integration was avoided. The procedure used to calculate the momentum of charged particles is illustrated in Figure 30. The magnet is centered at x = y = z = 0 in the coordinate system. The magnetic field is in the vertical y-direction. For a particle of charge e and momentum $\vec{p}$ parallel to the z-axis, the initial trajectory outside the magnet is given by

$$x_i = a_i + m_i z = b \tag{3.5}$$

where b is the particle's impact parameter with respect to the center of the magnet, defined in the usual sense as the distance of closest approach. Inside the magnet, the particle follows a circular path with radius of curvature ρ given by:

$$\rho = \frac{p}{\frac{e}{c}B} = \frac{p}{0.03B} \tag{3.6}$$

where ρ is in meters, p in GeV/c and B in kG. As illustrated in Figure 30a, the magnet deflects the charged particle by an angle θ given by

$$\tan\frac{\theta}{2} = \frac{\sqrt{R^2 - b^2}}{\rho + b} \quad . \tag{3.7}$$

The momentum p of the charged particle can then be expressed in terms of the angle θ and the impact parameter b:

$$= 0.03B\left[\frac{\sqrt{R^2 - b^2}}{\tan\theta/2} - b\right] \quad . \tag{3.8}$$

If the initial trajectory of the particle is at an angle θ_i with respect to the z-axis,

$$x_i = a_i + m_i z = a_i + z\tan\theta_i \quad , \tag{3.9}$$

we can use the cylindrical symmetry of the magnetic field to obtain the solution. We rotate the coordinate system by an angle θ_i around the y-axis to a new set of axes x' and z', and shown in Figure 30b. In this new coordinate system, the incident particle is parallel to the z'-axis with impact parameter $b = a_i\cos\theta_i$. Since the magnetic field is unchanged by such a

rotation, the solution for the momentum is given by

$$\rho = 0.03B\left[\frac{\sqrt{R^2 - b^2}}{\tan(\theta_f - \theta_i)/2} - b\right] \qquad (3.10)$$

with

$$b = a_i \cos\theta_i = a_f \cos\theta_f \quad . \qquad (3.11)$$

The tracks in the 1m X 1m MWPC's were used to specify the initial particle trajectories before entering the magnetic field, and the tracks downstream determined the angle of deflection. A particle path through the magnetic field was determined by linking the upstream and downstream tracks.

Particle and Event Identification

After the momenta of the charged particles had been calculated, they were classified as muons, electrons, or hadrons. As illustrated in Figure 31, the different particle types could be identified by their behavior in the various converters and absorbers in the muon spectrometer. Electrons, positrons, and photons could be identified by showers produced in the 3 r.l. steel radiator. Muons were perhaps the easiest to identify by their ability to penetrate the 2.44 meter steel absorber.

The criteria used to identify each type of particle and the general classification of events into nuclear scatters, μe events, and radiative tail events from elastic μN scattering are described below. Figures 32-37 are examples of the different types of scattering events.

Muons

Muons had the unique ability to penetrate the hadron absorber; this fact, of course, was used to define the trigger for the experiment. In

passing through the hadron absorber, the scattered muon could change direction due to multiple Coulomb scattering. Because of this, all particle trajectories in front of the hadron absorber were determined independently of the muon chambers. Muons were identified from among the downstream tracks by projecting each track into the muon chambers and counting the number of sparks within a multiple Coulomb scattering cone around the track. The angular width of this cone was determined by the thickness of the Pb-wall and the hadron absorber t in radiation lengths (~210 r.l.) and the momentum of the particle p as measured by the tracks in the 1m X 1m MWPC's and spark chambers in front of the hadron absorber:

$$\langle\theta\rangle = \frac{21}{p}\sqrt{t} \qquad (3.12)$$

where p is in GeV/c and $\langle\theta\rangle$ is given in milliradians. For a 10 GeV muon, this cone could cover an area as large as 20 cm in diameter at the muon chambers. By looking for clusters of sparks in the muon chambers within a multiple scattering cone around the track, the problems of track finding behind the hadron absorber were avoided.

Stale beam tracks and halo muons were eliminated by demanding that there be a fired element of M_v or M_h within the multiple Coulomb scattering cone. If an in-time muon could not be identified, the event was rejected. In about 2% of the triggers there was more than one in-time muon in the muon chambers and the scattered muon could not be identified. These events were also rejected.

Electrons (Positrons)

The primary sources of electrons and positrons in the muon spectrometer were from μe scattering, π° decays, and photon conversions. The μe events

comprised about 16% of the experimental triggers. For this reason it was important to be able to identify electrons so that μe events could be separated from low q^2 nuclear scatters.

Electrons (positrons) were identified in a set of magnetostrictive spark chambers located behind a 2 ft thick steel plate (~3 r.l.). Showers in the steel plate induced dense clusters of sparks in these chambers. Electrons and positrons were identified in the photon chambers by counting the number of sparks within a cone around the track found in the spark chambers in front of the steel plate.

The μe events were identified by having only one other in-time track in the downstream spark chambers besides the scattered muon. The particle was required to be negatively charged and satisfy the electron shower criteria in the photon chambers. Even though μe events are due to elastic scattering, one cannot take advantage of energy conservation to identify them because of the radiative effects. Figures 32 and 33 are examples of μe scattering events.

Photons

Although photons were not identified explicitly, it should be mentioned how they affected the data analysis. Photons of course do not leave tracks in the 2m X 4m and 2m X 6m spark chambers immediately behind the magnet, but they do induce showers in the photon chambers located behind the 3 r.l. steel plate in the same way as electrons and positrons. In principle they could be identified by the same procedure of counting sparks, but no attempt to do so was made. There was no viable means to measure the photon energies.

A large number of the experimental triggers were nuclear scatters belonging to the category of elastic radiative tail events. They were

characterized by a single scattered muon and a photon along either the incoming or scattered muon direction. These events were included in the category of nuclear scattering to allow the radiative corrections to be properly applied to the measured cross sections according to our procedure. Figures 34 and 35 are examples of radiative tail events.

Hadrons

The charged particle tracks identified as hadrons in the muon spectrometer contained a few percent contamination of electrons and positrons that could not be eliminated by hardware requirements. These could be rejected by demanding the scattering event to have q^2 greater than 0.3 $(GeV/c)^2$. Since there was no facility in the muon spectrometer to measure the hadron mass, we could not separate pions, kaons, etc. Depending on the physics results desired, they were assumed to be pions or kaons in the data analysis.

In principle, the total energy of the forward-going charged hadrons must be less than or equal to the energy loss ν of the muon. This is particularly true for the muon experiment in view of the fact that the energies of photons and neutral particles are not measured. Charged particles produced in the backward hemisphere in the center of mass could not be dedetected, and forward-going charged particles with less than ~8 GeV/c momentum were swept out by the Cyclotron magnet. The total energy spectrum of the detected hadrons plus scattered muon did exhibit the correct shape; a peak at the incident muon energy followed by a rising low energy tail as anticipated from the radiative corrections. However, on the high energy side a few percent of the events violated energy conservation. These originated mostly from stale tracks in the beam region which were misidentified as genuine hadrons. These events could be excluded from hadron studies

and did not affect the muon inclusive cross sections. Figures 36 and 37 are examples of inelastic muon scattering events with several charged hadrons in the final state.

Resolution in q^2 and ν

The accuracy to which we can determine q^2 and ν depends on the basic resolution of the muon spectrometer and our ability to measure p, the momentum of the incident muon, and determine the momentum p' and angle θ of the scattered muon.

The uncertainty in the incident muon momentum was determined by the spatial resolution of the beam MWPC's and hodoscopes and the uncertainty in the field integral $I = \int B \cdot d\ell$ of the three tagging magnets in the muon beam line. Using the 2 mm wire spacing of the beam chambers determines the bend angle of the incoming muon to ~±0.05 mrad. With a nominal bend angle in the tagging magnets of 28 mrad, and assuming that the field integral was known to ~0.2%, this corresponds to a momentum resolution of

$$\frac{\delta p}{p} = \left[\left(\frac{\delta\theta}{\theta}\right)^2 + \left(\frac{\delta I}{I}\right)^2\right]^{\frac{1}{2}}$$

$$= \left[\left(\frac{.05}{28}\right)^2 + (.002)^2\right]^{\frac{1}{2}} \qquad (3.13)$$

$$\simeq 0.3\%$$

or

$$\delta p \simeq \pm 0.5 \text{ GeV/c} \qquad (3.14)$$

for 150 GeV muons. If the incoming muon tracks were measured using only the beam hodoscope elements, then

$$\delta p \simeq 2.5 \text{ GeV/c} \quad . \qquad (3.15)$$

The resolution of the apparatus in measuring p' and θ for the scattered muon was basically determined by the combined angular resolution $\delta\theta$ of the 1m X 1m MWPC's behind the target and the 2m X 4m and 2m X 6m wire spark chambers downstream of the Chicago Cyclotron magnet. For an apparatus in which the momentum of a charged particle is determined by its angle of deflection θ in a magnetic field, the momentum resolution deteriorates with increasing momentum p, i.e.,

$$\frac{\delta p}{p} \propto p\delta\theta \quad . \tag{3.16}$$

For the muon experiment, $\delta\theta$ was ~0.5 mrad. Thus for a scattered muon of 50 GeV/c momentum, the momentum resolution was about ±2.5% or ±1.25 GeV/c.

Figures 38 and 39 show a rough calculation of the resolution of the muon spectrometer in q^2 and ν for an incident beam momentum of 150 GeV/c.

Fig. 24.--Schematic drawing of the beam momentum tagging system. In the horizontal direction (x-view), the incoming muon is measured before and after the tagging magnets by two sets of multiwire proportional chambers (2 mm wire spacing) and scintillation counter hodoscopes (8 elements). In the vertical direction (y-view), the muon is measured by two sets of MWPC's and hodoscopes located downstream of the tagging magnets. The nominal bend angle is 28 mrad in the horizontal plane.

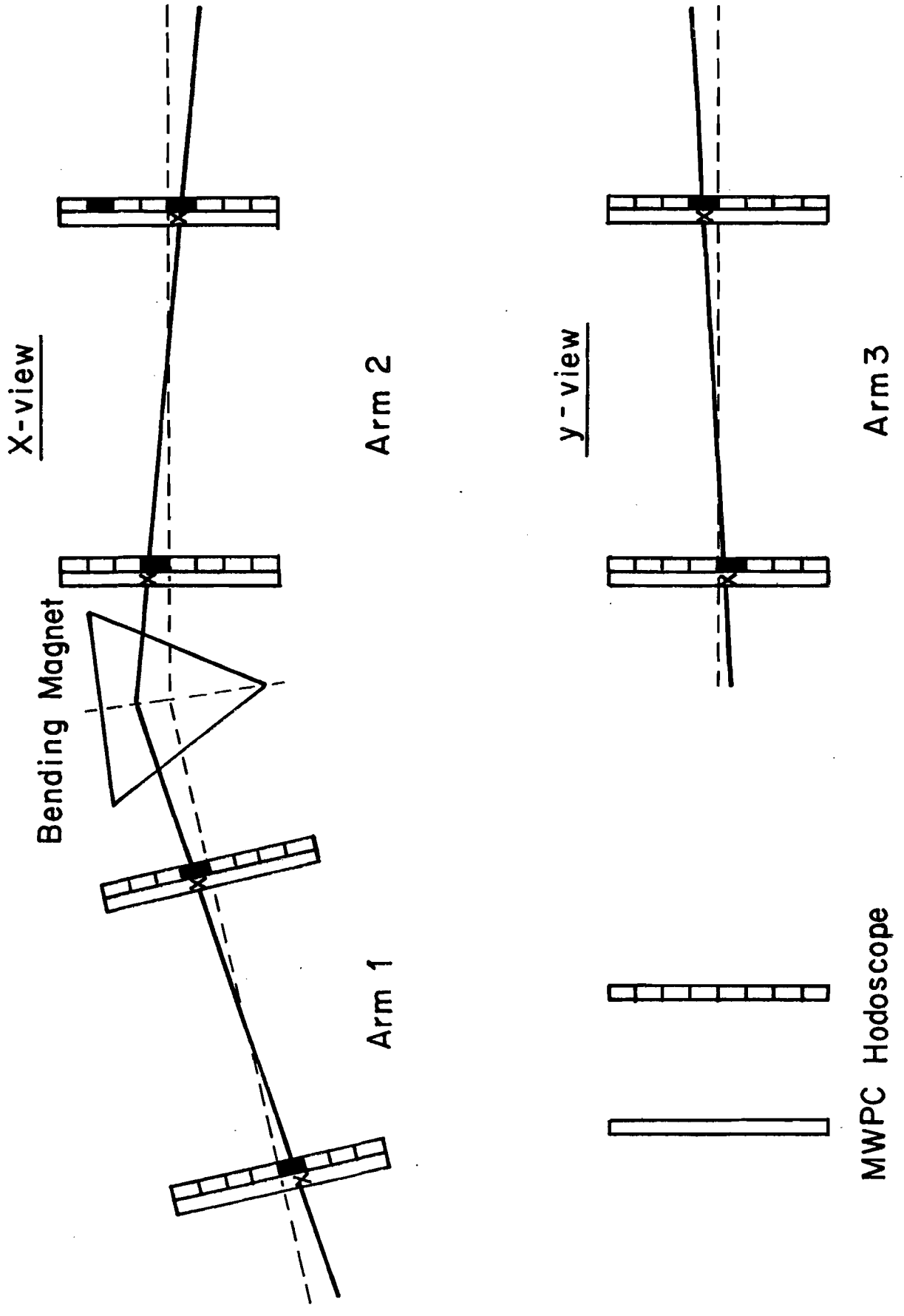
X-view
y-view
Arm 1
Arm 2
Arm 3
Bending Magnet
MWPC Hodoscope

Fig. 25.--Linkage of tracks upstream and downstream of the beam momentum tagging magnets. The distribution is a plot of the difference in intercepts at the bend plane of the magnets.

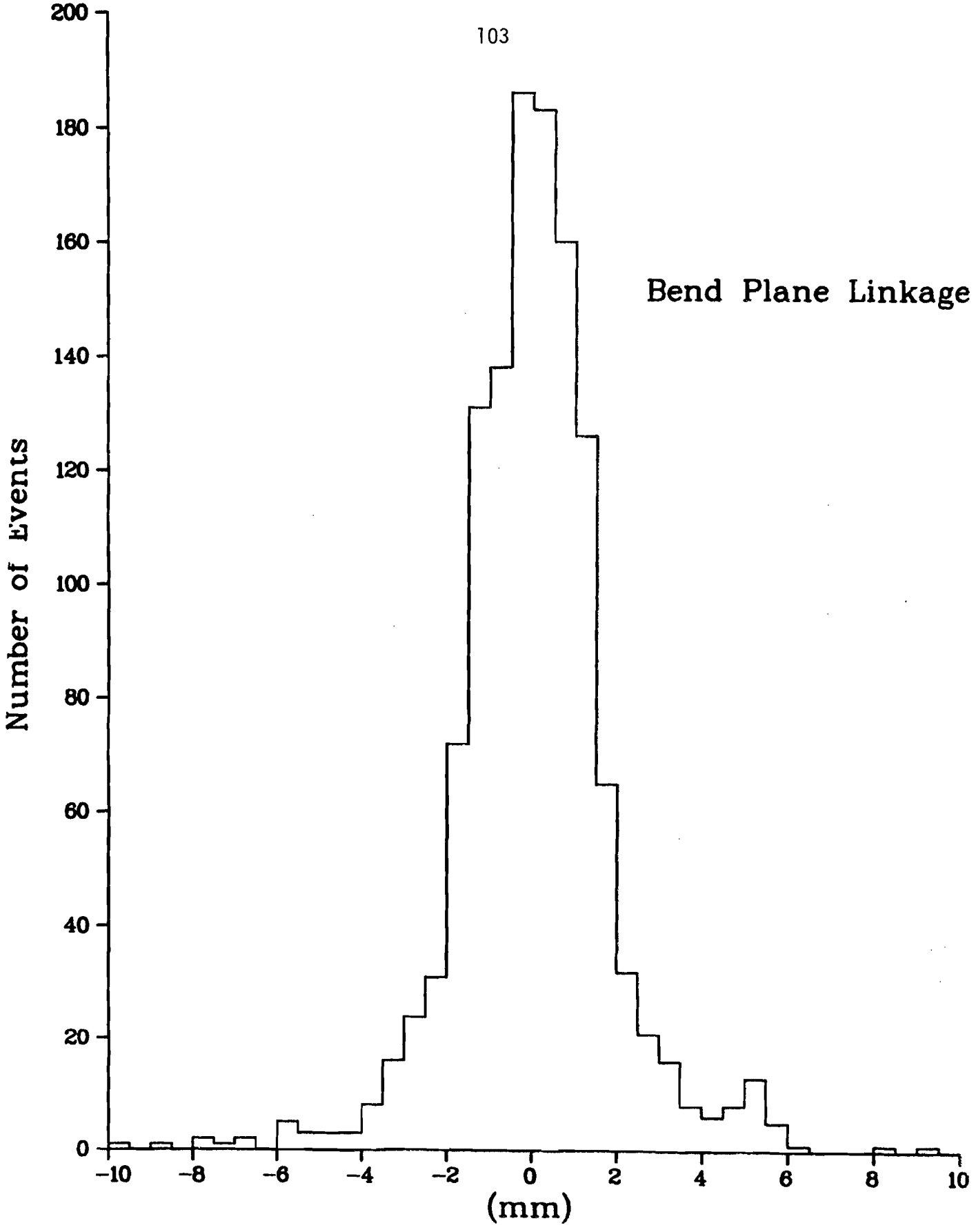
Bend Plane Linkage
Number of Events
200
180
160
140
120
100
80
60
40
20
0
-10
-8
-6
-4
-2
0
2
4
6
8
10
(mm)

Fig. 26.--Illustration of the technique of linking tracks found in the 1m X 1m MWPC's through the Cyclotron magnet to tracks in the downstream spark chambers. In the bending view, tracks upstream and downstream are required to have the same impact parameter with respect to the center of the magnet. In the non-bending view, tracks are matched in slope and intercept.

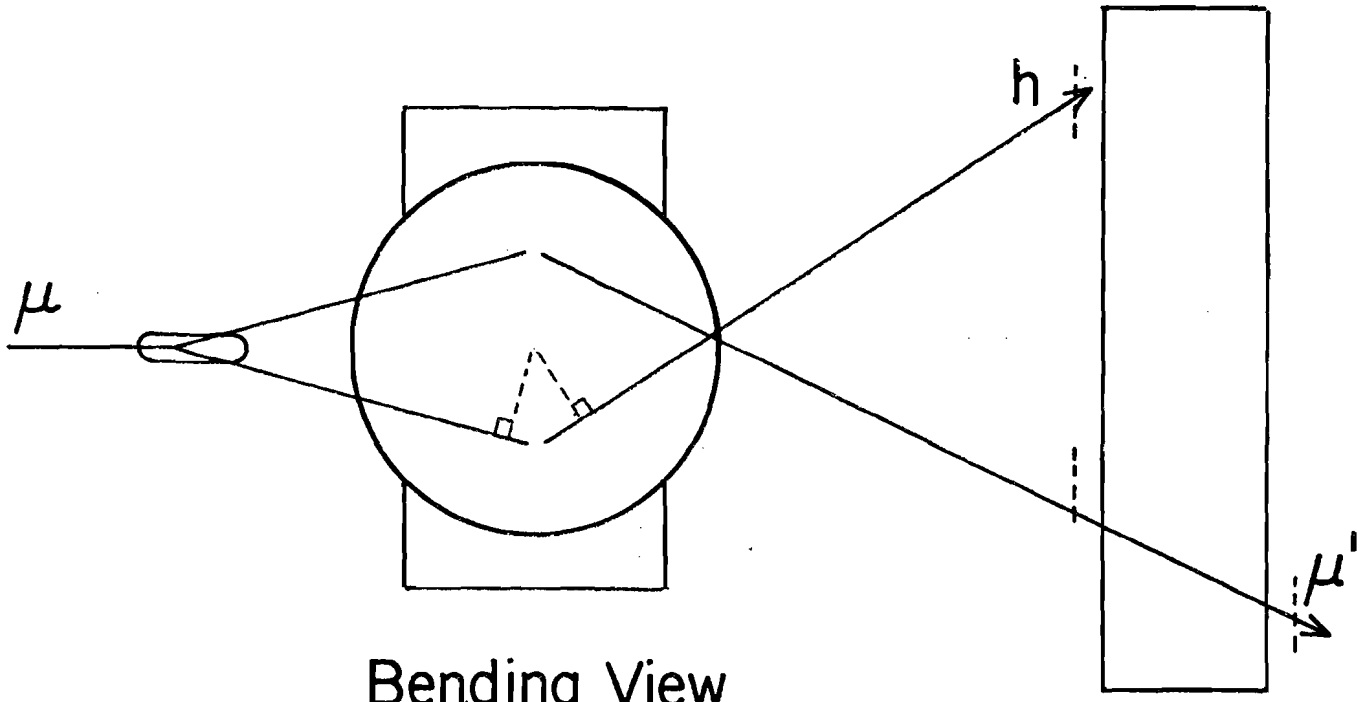

Bending View

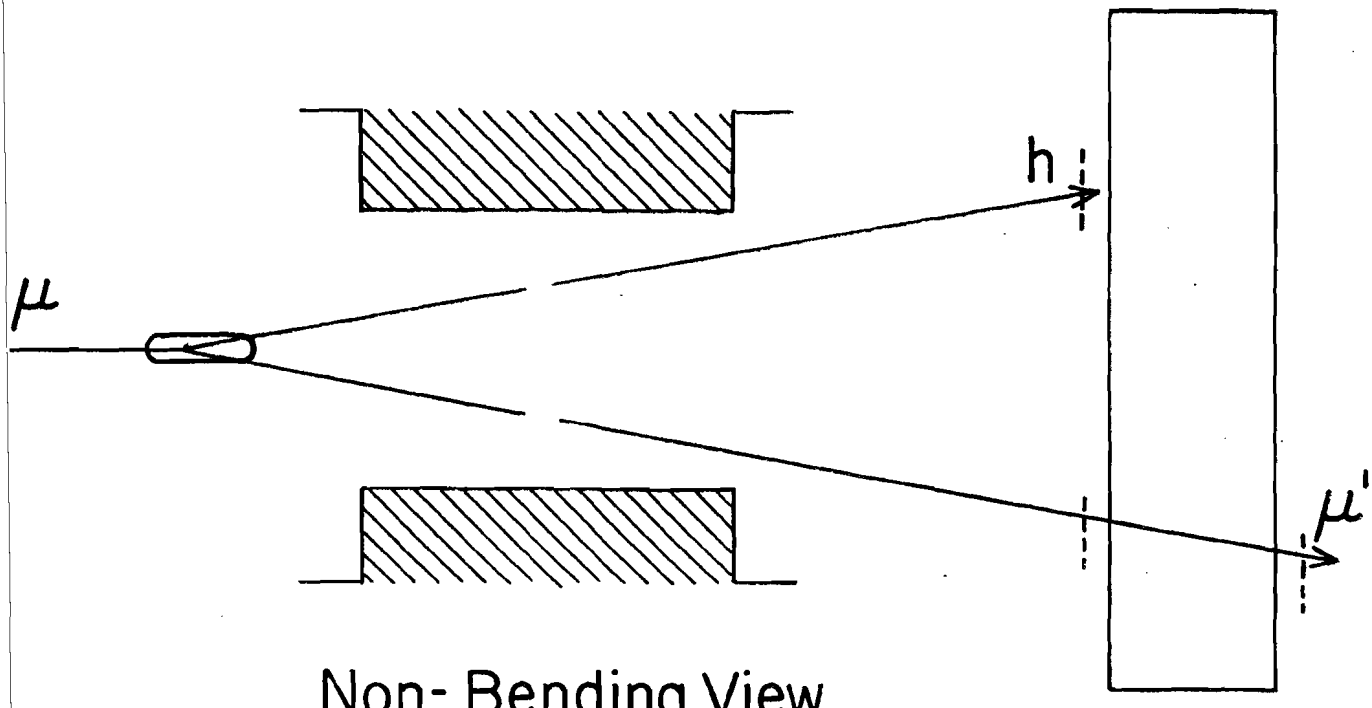

Non- Bending View

Fig. 27.--Distributions of track linkage through the Cyclotron magnet in the x-view: (a) The difference in impact parameters. (b) The difference in slopes for zero magnetic field.

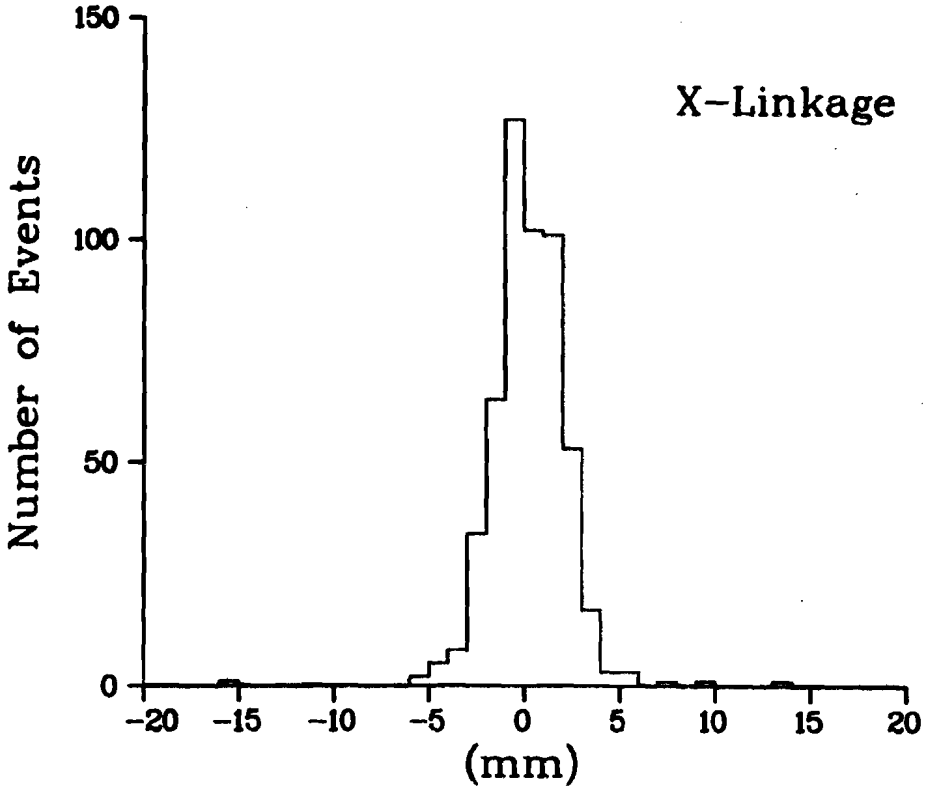
X–Linkage
Number of Events
150
100
50
0
−20 −15 −10 −5 0 5 10 15 20
(mm)

(a)

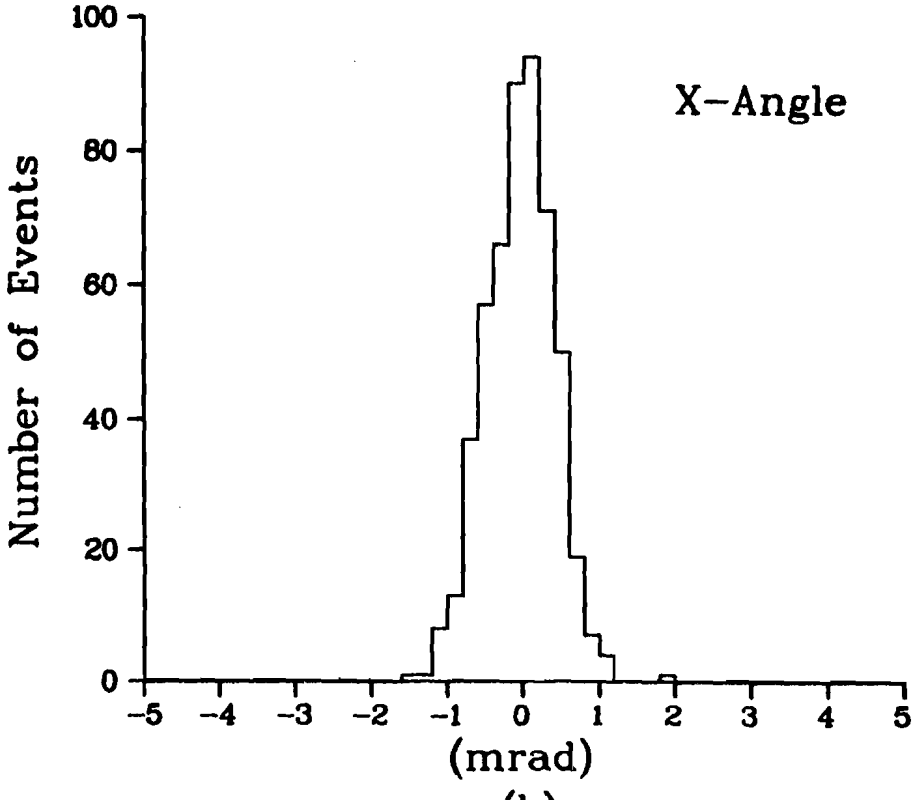
X–Angle
Number of Events
100
80
60
40
20
0
−5 −4 −3 −2 −1 0 1 2 3 4 5
(mrad)

(b)

Fig. 28.--Distributions of track linkage through the Cyclotron magnet in the y-view: (a) The difference in intercepts at the center of the magnet. (b) The difference in slopes.

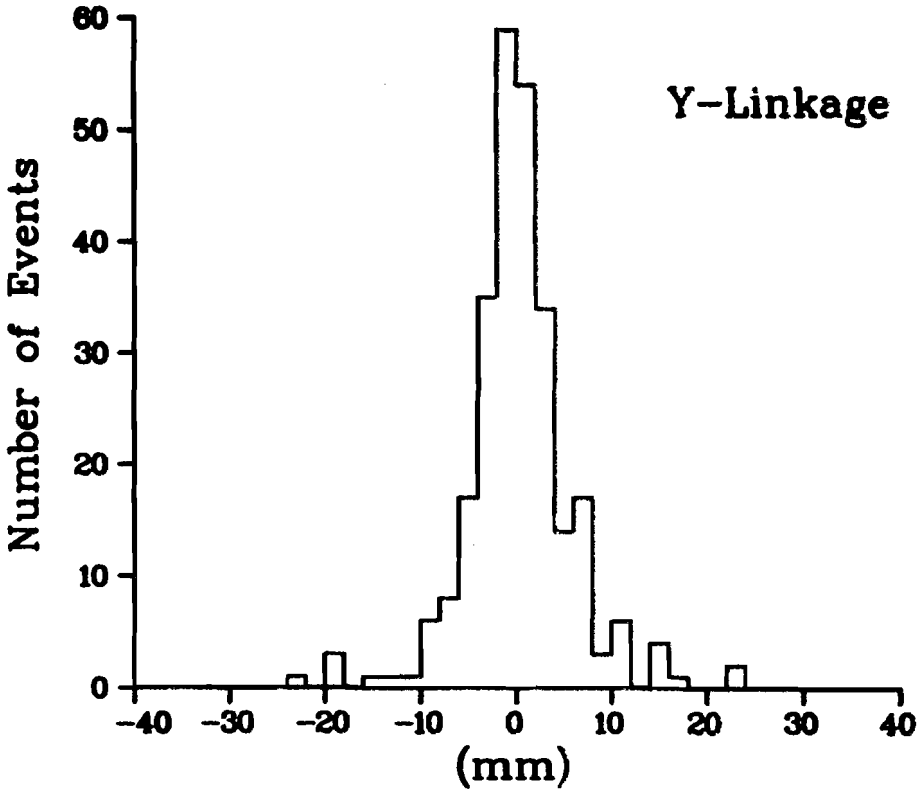
Y-Linkage
Number of Events
60
50
40
30
20
10
0
-40
-30
-20
-10
0
10
20
30
40
(mm)

(a)

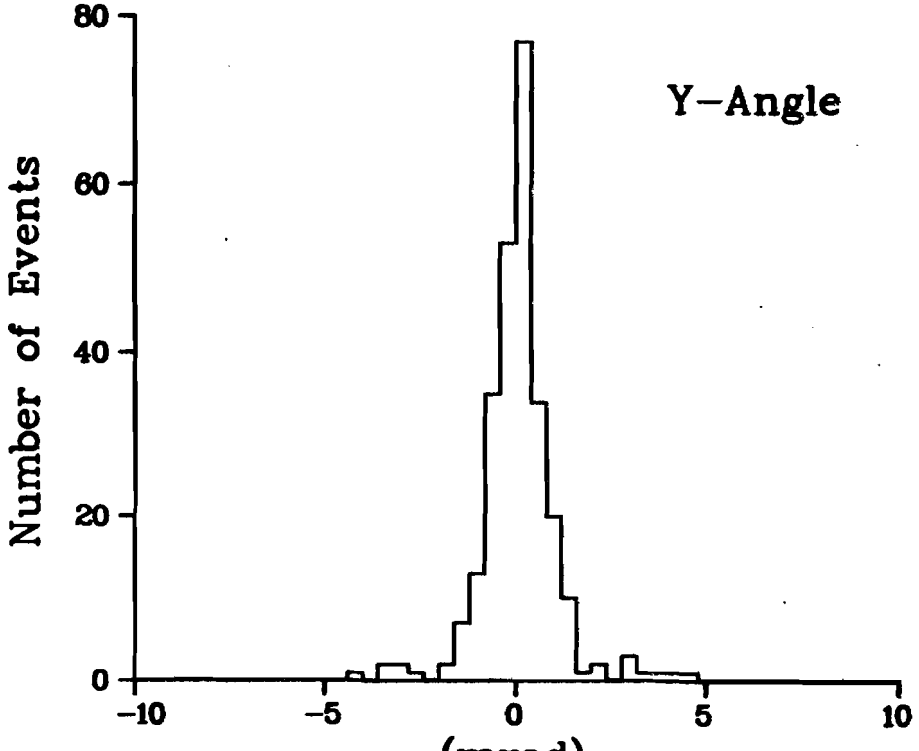
Y-Angle
Number of Events
80
60
40
20
0
-10
-5
0
5
10
(mrad)

(b)

Fig. 29.--Plots of the vertical and radial components of the magnetic field of the Chicago Cyclotron magnet: (a) The vertical magnetic field as a function of radial position. For the calculation of charged particle momentum, a hard-edge model with an effective radius of 2.47 m and uniform field of 15 kG was used. (b) The radial magnetic field as a function of vertical position, measured at the center of the magnet.

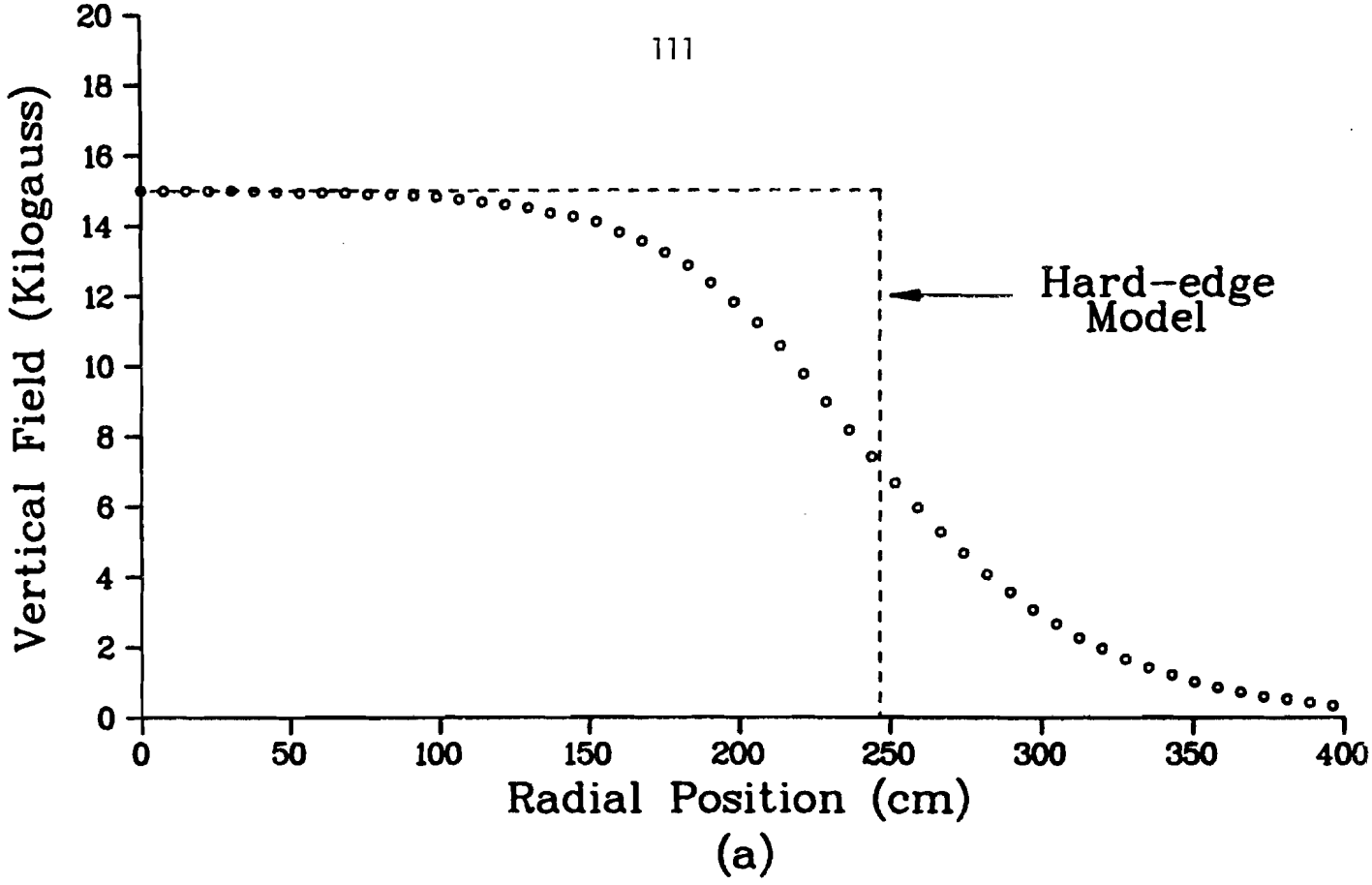
Vertical Field (Kilogauss)
Hard-edge Model
Radial Position (cm)

(a)

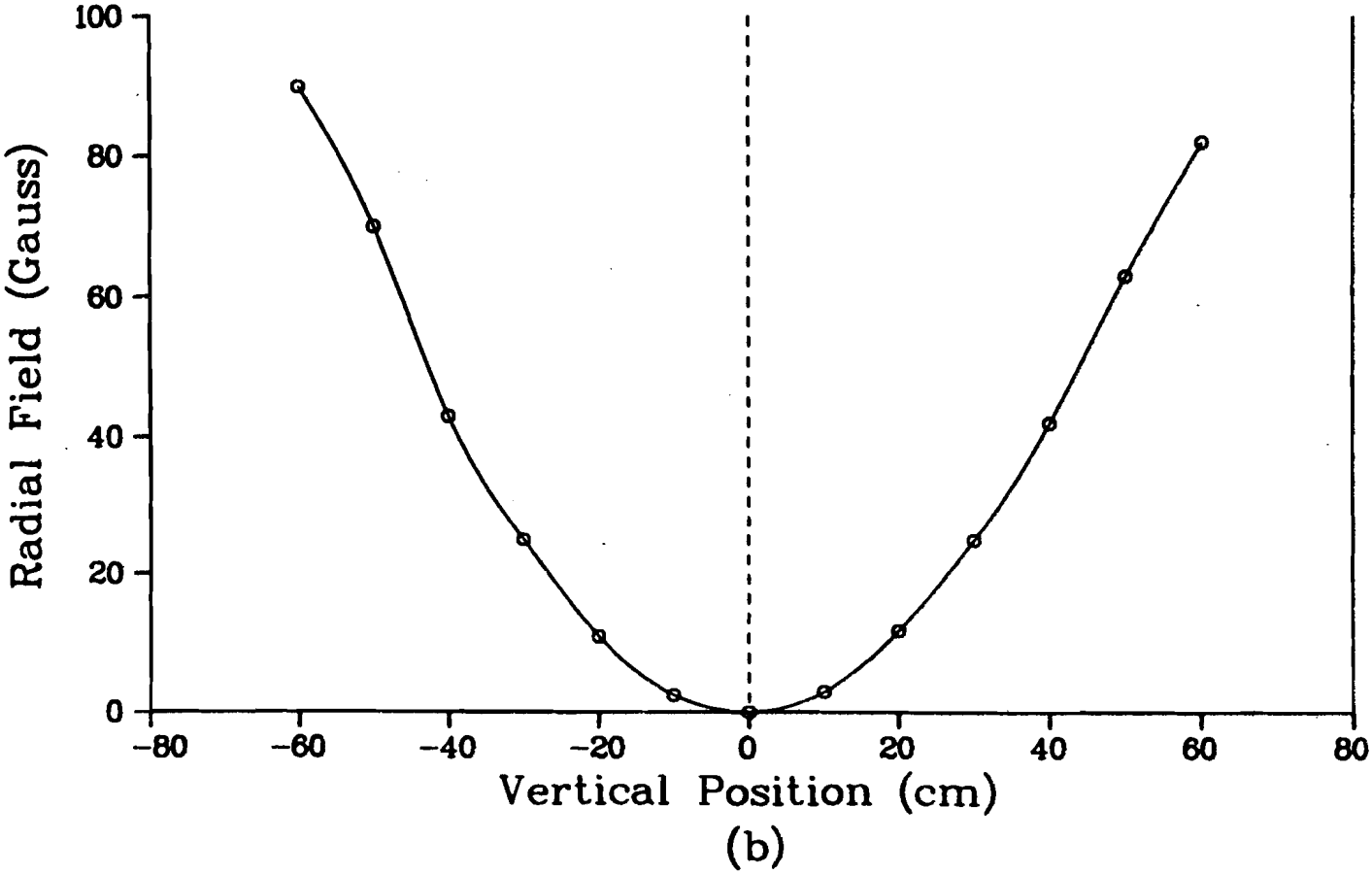
Radial Field (Gauss)
Vertical Position (cm)

(b)

Fig. 30.--The geometry for momentum calculation using a cylindrically symmetric, uniform magnetic field of radius R: (a) The charged particle is initially parallel to z-axis with impact parameter b. The angle of deflection is θ. (b) The charged particle is initially at an angle θ_i with respect to z-axis.

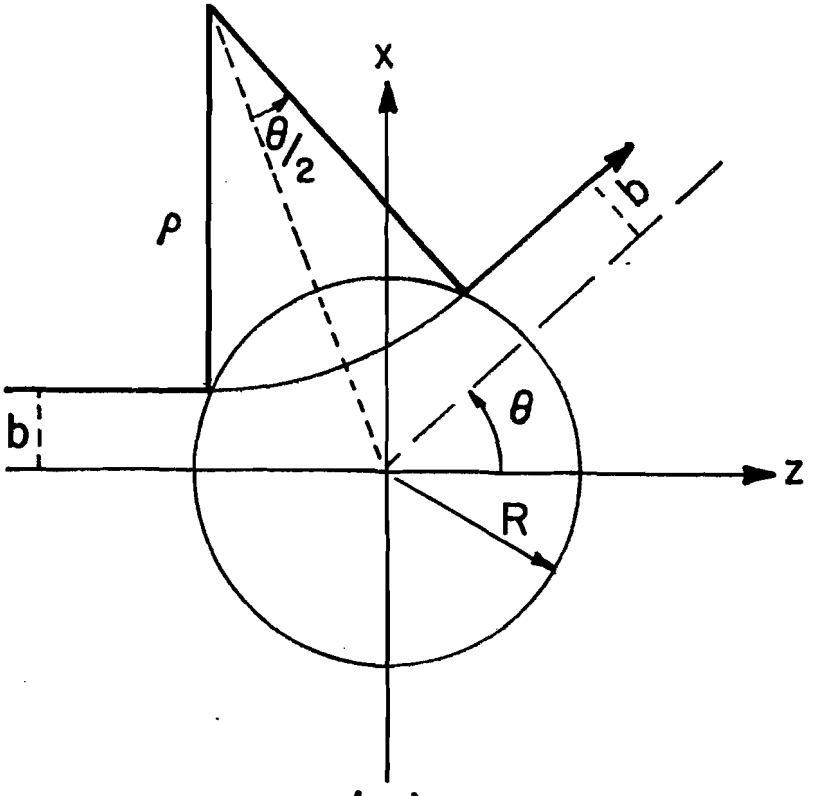

(a)

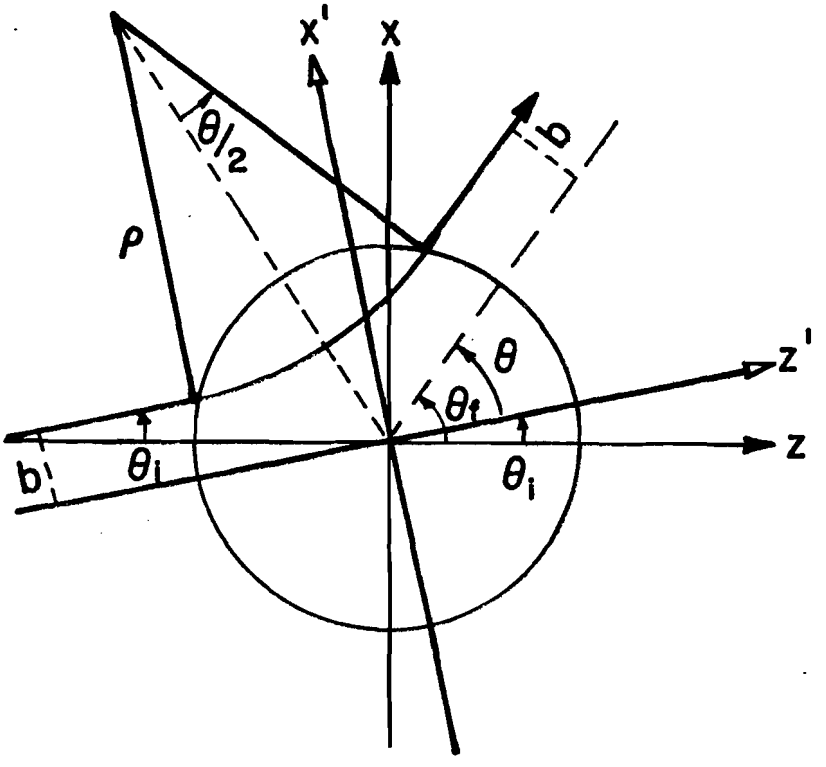

(b)

Fig. 31.--Simplified drawing of the muon scattering spectrometer. Upstream of the Cyclotron magnet, halo muons are vetoed by a large hodoscope wall located in front of the liquid hydrogen/deuterium target. Forward-going charged particles are measured by a set of 1m X 1m MWPC's located behind the target. Downstream of the magnet, charged particles are detected by sets of 2m X 4m and 2m X 6m wire spark chambers. The scattered muon is identified by its ability to penetrate the 8' steel wall and fire elements of the muon trigger hodoscopes. Electrons, positrons, and photons can be identified by showers produced in a set of wire spark chambers located behind a 3 r.l. steel plate.

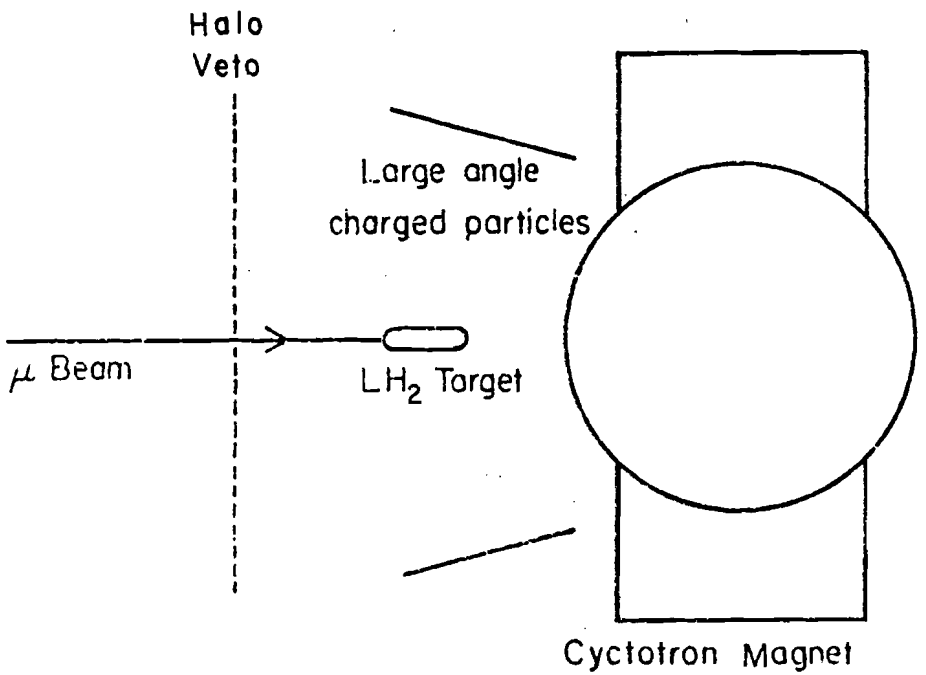
Halo
Veto
Large angle
charged particles
μ Beam
LH2 Target
Cyctotron Magnet

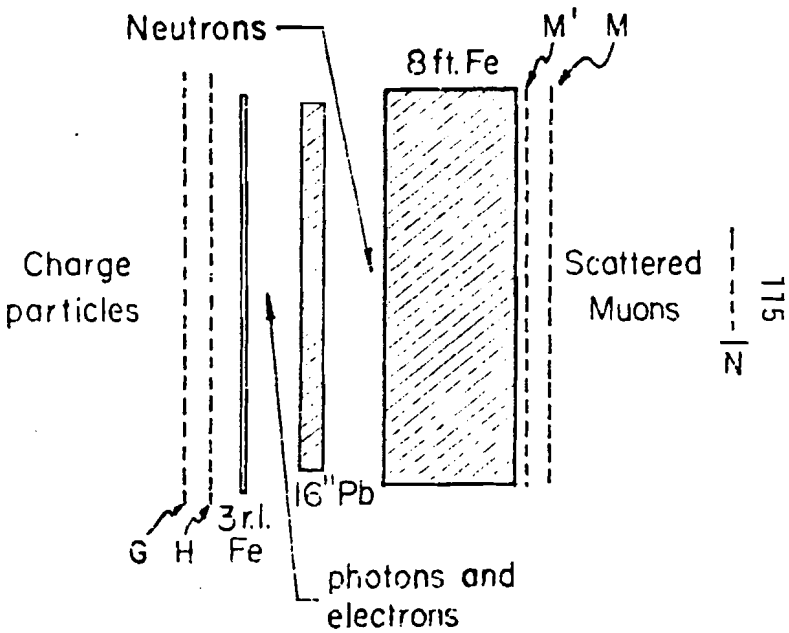
Neutrons
M' M
8ft. Fe
Charge
particles
Scattered
Muons
16" Pb
G H
3r.l.
Fe
photons and
electrons

Fig. 32.--Example of a μe scattering event. The scattered muon, μ_1, fires elements of the muon trigger hodoscopes (indicated by dotted lines), and registers in the wire spark chambers behind the steel hadron absorber. The electron e_3 fires elements of the G and H hodoscopes in front of the hadron absorber and showers in the 3 r.l. steel plate, producing a dense cluster of sparks in the wire spark chambers. The scattering angle of the muon in the experimental target is extremely small. Both the scattered muon and the electron appear as a single track in the 1m X 1m MWPC's behind the target.

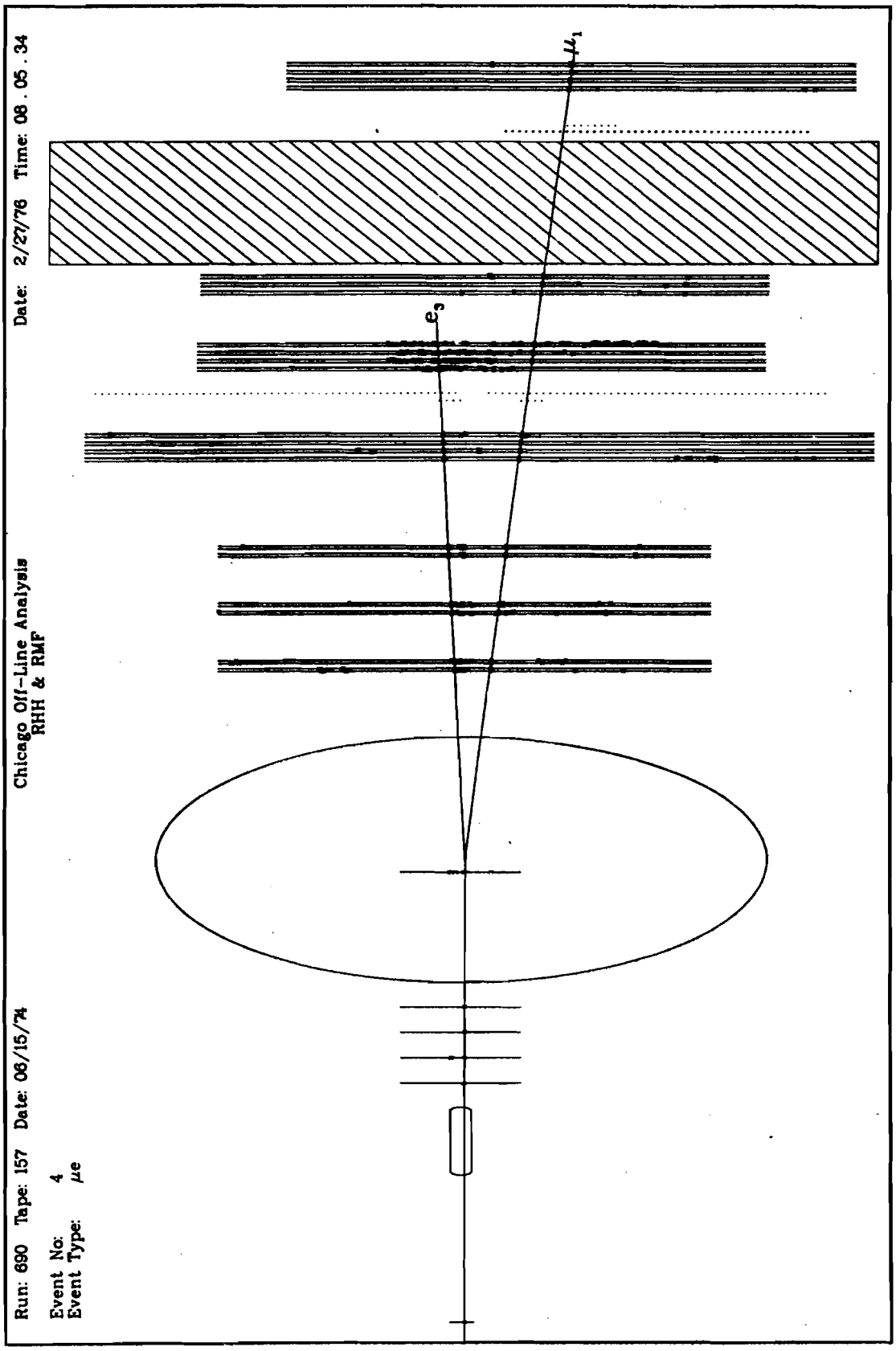
Run: 690 Tape: 157 Date: 06/15/74
Event No: 4
Event Type: μe
Chicago Off-Line Analysis
RHH & RMF
Date: 2/27/76 Time: 08.05.34
μ_1
e_3

Fig. 33.--Another example of a μe scattering event. In this event, the scattered muon and electron are separated in the 1m X 1m MWPC's behind the target and the linkage to the individual downstream tracks of the center of the magnet can be seen. Notice the stale tracks in the central beam region of the wire spark chambers. These extra tracks can especially be a problem in identifying the scattered muon in wire spark chambers behind the hadron absorber because of multiple Coulomb scattering and showers in the steel.

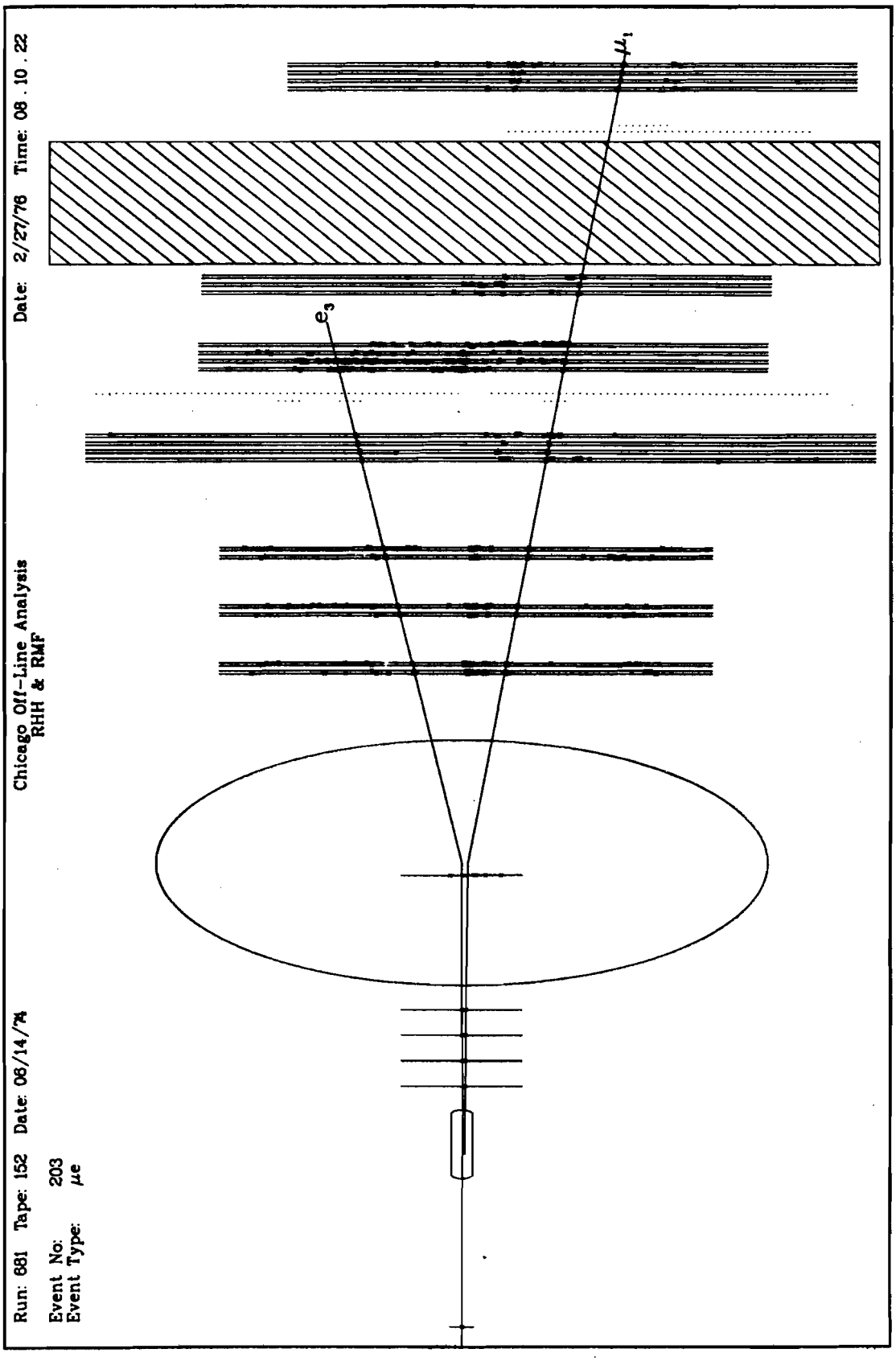
Chicago Off-Line Analysis
RHH & RMF
Run: 681 Tape: 152 Date: 06/14/74
Event No: 203
Event Type: μe
Date: 2/27/76 Time: 08.10.22
μ_1
e_3

Fig. 34.--Example of a radiative tail event in which the muon has emitted a high energy photon before or after scattering from the target nucleon. The radiated photon appears as a shower of sparks in the wire spark chambers located behind the 3 r.l. steel plate. These radiative tail events are included in the category of nuclear scatters (μN events) and a radiative correction applied to the data. There is no viable means to measure the energy of the radiated photon.

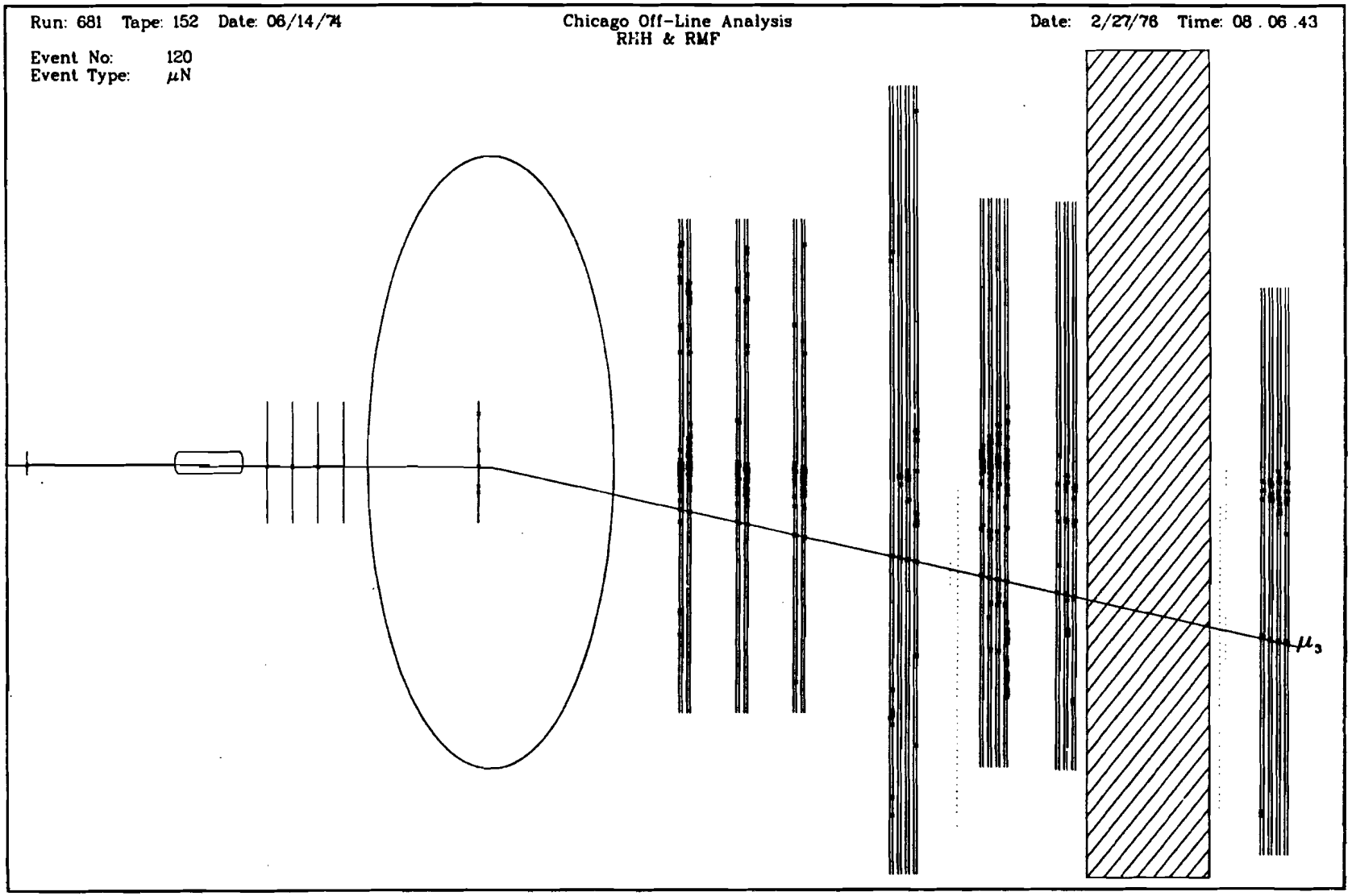
Run: 681 Tape: 152 Date: 06/14/74
Chicago Off-Line Analysis
RHH & RMF
Date: 2/27/76 Time: 08 . 06 .43
Event No: 120
Event Type: μN
μ3

Fig. 35.--Another example of an elastic scattering event accompanied by the emission of a high energy photon. Notice the large scattering angle of the muon in the target with no evidence for any other charged particle tracks in the 1m X 1m MWPC's.

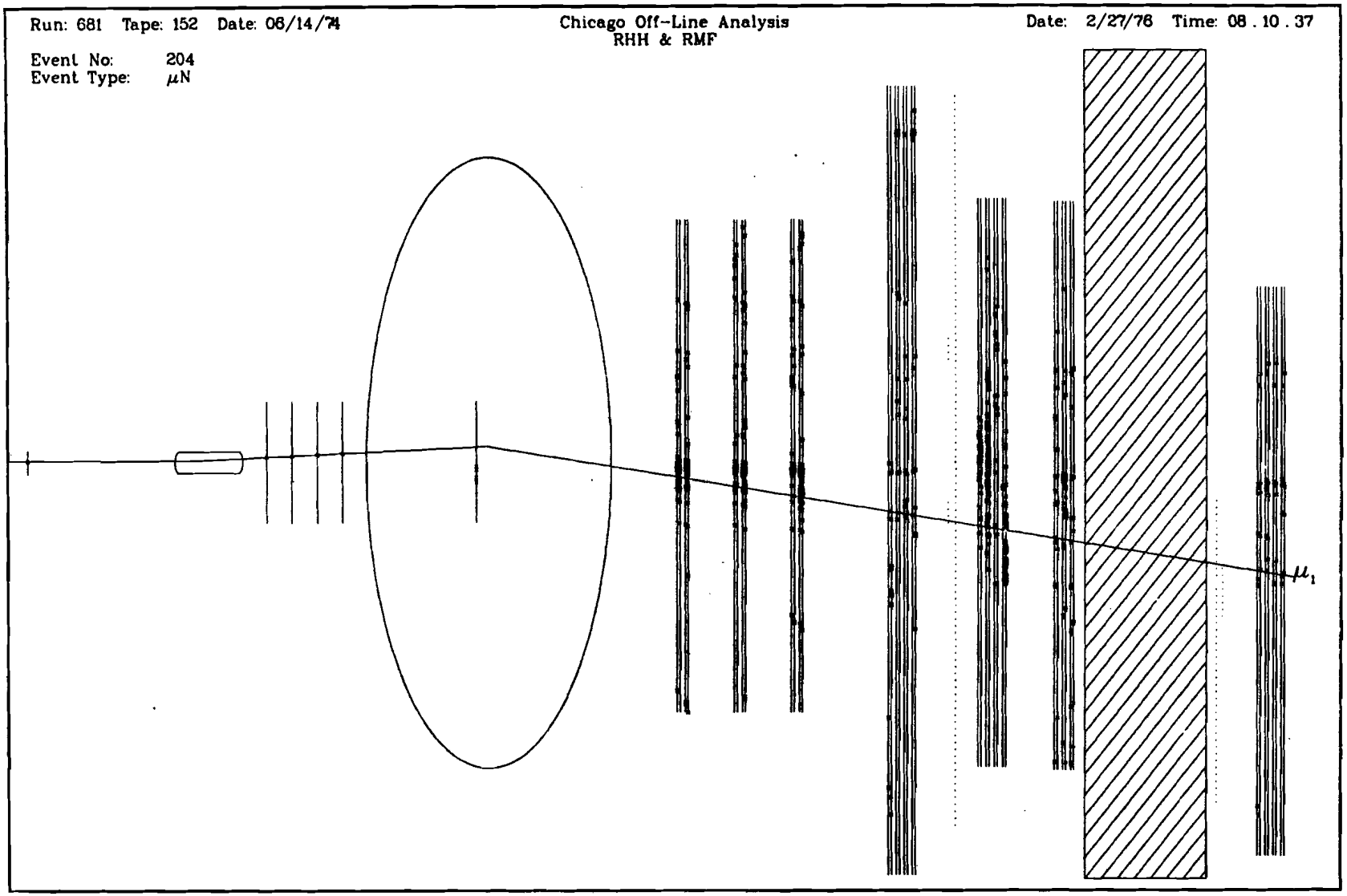
Run: 681 Tape: 152 Date: 06/14/74
Chicago Off-Line Analysis
RHH & RMF
Date: 2/27/76 Time: 08 . 10 . 37
Event No: 204
Event Type: μN
μ1

Fig. 36.--Example of an inelastic scattering event with several charged hadrons in the final state. The vertex of the interaction in the experimental target can clearly be seen. Notice the linkage of tracks found in the downstream spark chambers with tracks found in the 1m X 1m MWPC's behind the target. The linkage requirement is a powerful technique in eliminating stale out-of-time tracks. Two of the charged hadrons produced in the interaction have low momentum and are swept out by the magnetic field of the Chicago Cyclotron.

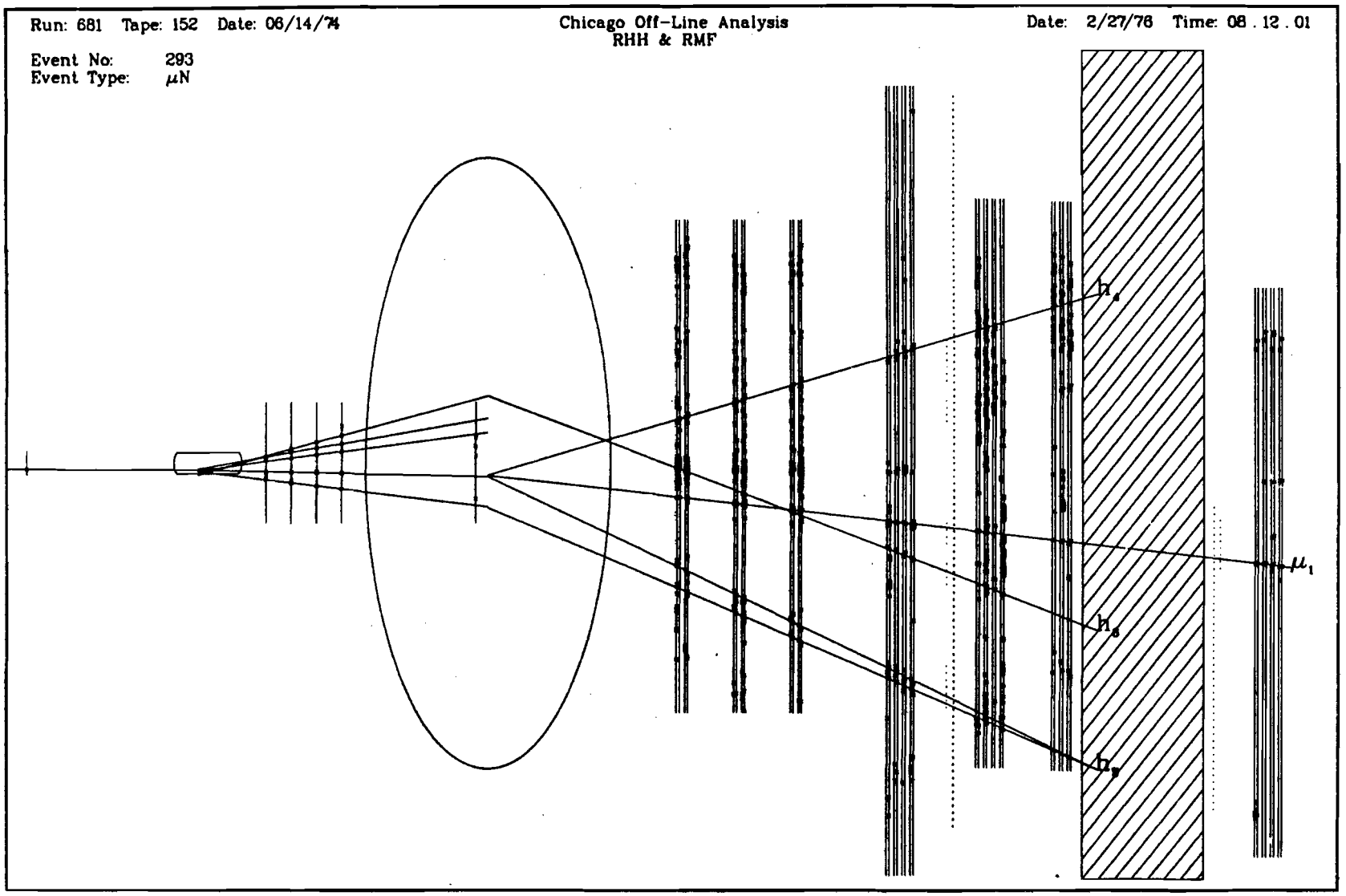
Run: 681 Tape: 152 Date: 06/14/74
Chicago Off-Line Analysis
RHH & RMF
Date: 2/27/76 Time: 08 . 12 . 01
Event No: 293
Event Type: μN
h1
μ1
h2
h3

Fig. 37.--Another example of an inelastic scattering event. In this event the muon scatters by a large angle in the experiment target and is then deflected back through the central beam region of the downstream spark chambers by the Cyclotron magnet. The pattern recognition of these types of scattering events is particularly difficult to handle because of the large number of sparks in the central beam region. Notice that the scattered muon μ_6 does not produce a clearly defined track in the wire spark chambers behind the hadron absorber. Multiple Coulomb scattering and showers in the steel often make track finding in these chambers impossible. There are also a large number of stale tracks from the unscattered beam.

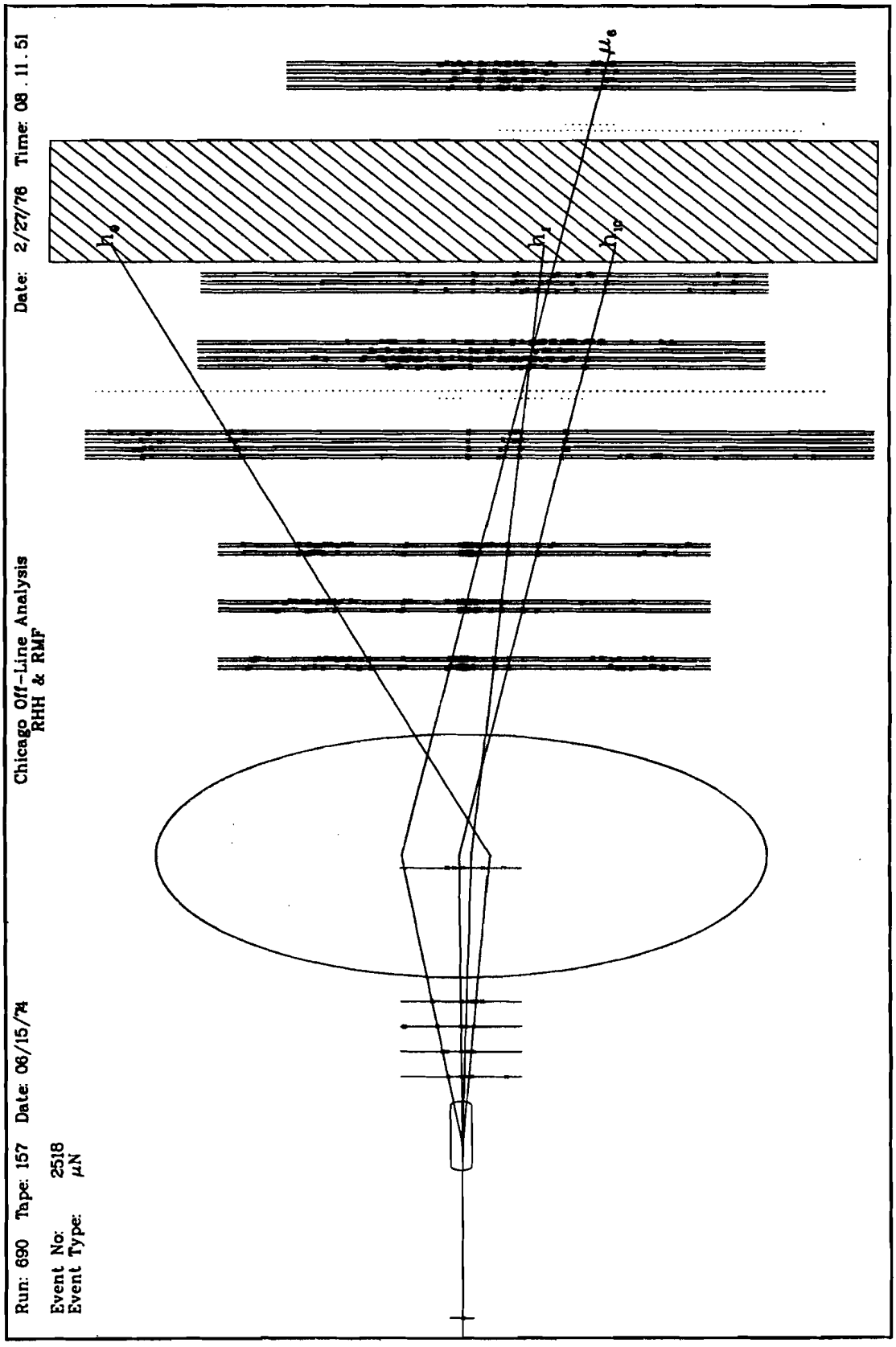
Chicago Off-Line Analysis
RHH & RMF
Run: 690 Tape: 157 Date: 06/15/74
Event No: 2518
Event Type: μN
Date: 2/27/76 Time: 08.11.51
h_0
h_1
h_{15}
μ_6

Fig. 38.--A two-dimensional plot of the resolution of the muon spectrometer in determining ν, the energy loss of the muon. The ratio $d\nu/\nu$ is plotted as a function of ν and q^2.

q^2 (Gev/c)^2													Values x 10^{-3}		
24·0	25·0		254	132	81	53	36	26	18	13	9	7	5	4	3	
23·0	24·0		254	132	81	53	36	26	18	13	9	7	5	4	3	
22·0	23·0		254	132	81	53	36	26	18	13	9	7	5	4	3	
21·0	22·0		254	132	81	53	36	26	18	13	9	7	5	4	3	
20·0	21·0		254	132	81	53	36	26	18	13	9	7	5	4	3	
19·0	20·0		254	132	81	53	36	26	18	13	9	7	5	4	3	
18·0	19·0		254	132	81	53	36	26	18	13	9	7	5	4	3	
17·0	18·0		254	132	81	53	36	26	18	13	9	7	5	4	3	
16·0	17·0		254	132	81	53	36	26	18	13	9	7	5	4	3	
15·0	16·0		254	132	81	53	36	26	18	13	9	7	5	4	3	
14·0	15·0		254	132	81	53	36	26	18	13	9	7	5	4	3	
13·0	14·0		254	132	81	53	36	26	18	13	9	7	5	4	3	
12·0	13·0		254	132	81	53	36	26	18	13	9	7	5	4	3	
11·0	12·0		254	132	81	53	36	26	18	13	9	7	5	4	3	
10·0	11·0		254	132	81	53	36	26	18	13	9	7	5	4	3	
9·0	10·0		254	132	81	53	36	26	18	13	9	7	5	4	3	
8·0	9·0		254	132	81	53	36	26	18	13	9	7	5	4	3	
7·0	8·0	872	254	132	81	53	36	26	18	13	9	7	5	4	3	
6·0	7·0	872	254	132	81	53	36	26	18	13	9	7	5	4	3	
5·0	6·0	872	254	132	81	53	36	26	18	13	9	7	5	4	3	
4·0	5·0	872	254	132	81	53	36	26	18	13	9	7	5	4	3	
3·0	4·0	872	254	132	81	53	36	26	18	13	9	7	5	4	3	
2·0	3·0	872	254	132	81	53	36	26	18	13	9	7	5	4	3	
1·0	2·0	872	254	132	81	53	36	26	18	13	9	7	5	4	3	
0·0	1·0	872	254	132	81	53	36	26	18	13	9	7	5	4	3	
ν (Gev)		0	10	20	30	40	50	60	70	80	90	100	110	120	130	140
		10	20	30	40	50	60	70	80	90	100	110	120	130	140	150

Fig. 39.--A two-dimensional plot of the resolution of the muon spectrometer in determining q^2, the four-momentum transfer-squared of the virtual photon. The ratio $\delta q^2/q^2$ is plotted as a function of ν and q^2.

q^2 $(Gev/c)^2$													Values x 10^{-3}		
24·0	25·0		43	41	38	36	34	32	29	27	25	22	20	17	14	
23·0	24·0		43	41	39	37	34	32	30	28	25	23	20	17	14	
22·0	23·0		44	42	39	37	35	33	30	28	25	23	20	18	15	
21·0	22·0		44	42	40	38	35	33	31	28	26	23	21	18	15	
20·0	21·0		45	43	40	38	36	34	31	29	26	24	21	18	15	
19·0	20·0		46	43	41	39	36	34	32	29	27	24	21	18	15	
18·0	19·0		46	44	42	39	37	35	32	30	27	25	22	19	15	
17·0	18·0		47	45	43	40	38	35	33	30	28	25	22	19	16	
16·0	17·0		48	46	43	41	39	36	34	31	28	26	23	19	16	
15·0	16·0		49	47	44	42	39	37	34	32	29	26	23	20	16	
14·0	15·0		50	48	45	43	40	38	35	33	30	27	24	20	16	
13·0	14·0		51	49	46	44	41	39	36	33	31	28	24	21	17	
12·0	13·0		53	50	48	45	43	40	37	34	31	28	25	21	17	
11·0	12·0		54	52	49	47	44	41	38	36	33	29	26	22	17	
10·0	11·0		56	54	51	48	46	43	40	37	34	30	27	23	18	
9·0	10·0		58	56	53	50	47	45	42	38	35	32	28	24	19	
8·0	9·0		61	58	55	52	50	47	43	40	37	33	29	25	19	
7·0	8·0	67	64	61	58	55	52	49	46	42	39	35	31	26	20	
6·0	7·0	71	68	65	62	59	55	52	49	45	41	37	33	27	21	
5·0	6·0	76	73	69	66	63	60	56	52	48	44	40	35	29	23	
4·0	5·0	82	79	76	72	69	65	61	57	53	49	44	38	32	24	
3·0	4·0	92	88	85	81	77	73	69	64	60	54	49	43	36	27	
2·0	3·0	107	103	99	94	90	85	80	75	70	64	57	50	42	31	
1·0	2·0	138	131	125	120	114	108	103	95	89	81	73	63	52	38	
0·0	1·0	232	222	213	203	194	185	175	162	151	137	123	106	88	59	
ν (Gev)		0 10	10 20	20 30	30 40	40 50	50 60	60 70	70 80	80 90	90 100	100 110	110 120	120 130	130 140	140 150

CHAPTER IV

INCLUSIVE MUON CROSS SECTION

The muon inclusive cross section can be calculated in a straightforward manner once the tasks of pattern recognition, momentum determination, and particle identification have been done. We need only to determine the momenta of the incoming and scattered muon and the muon scattering angle. Various corrections, such as acceptance, efficiency, radiative corrections, etc., have to be applied. In this chapter, we describe the detailed procedures used to evaluate the muon cross section and discuss the various corrections applied to the data. Results on the measured muon cross section for the deuterium data are presented. Discussion of the structure function νW_2, and comparison with theoretical models will be presented in Chapter V.

Evaluation Procedure

For each muon-nucleon scattering event, the kinematics were calculated and the event binned versus the kinematic variables, q^2 and ν. The muon inclusive cross section for each (q^2,ν) bin was evaluated by summing over all the scattered muons in the bin, according to the following relation:

$$\frac{d^2\sigma}{dq^2 d\nu} = \frac{N_{Bin}(q^2,\nu)}{N_\mu N_T (\Delta q^2 \Delta\nu)} C(q^2,\nu) \qquad (4.1)$$

where

$N_{Bin}(q^2,\nu)$ is the number of scattered muons in the $(\Delta q^2 \Delta\nu)$ bin centered at (q^2,ν);

N_μ is the total number of incident muons;

N_T is the number of target nucleons/cm^2; and,

$C(q^2,\nu)$ is a factor to take into account several corrections to the measured inclusive muon cross section:

1. Beam Selection
2. Track Finding Efficiency
3. Magnet Linkage
4. Counter Efficiency
5. Dead-time Corrections
6. Acceptance Calculation
7. Radiative Corrections .

Each of these corrections to the inclusive muon cross section is discussed in the following sections.

Beam Selection

In order to evaluate the muon cross section, we must be able to reconstruct the incoming muon track. In calculating the kinematics of a scattering event, it is important to know both the position and angle of the incoming muon at the experimental target. Because of chamber inefficiencies, it was not always possible to reconstruct the incoming muon track. To facilitate the data analysis, we demanded that the incoming muon satisfy a number of stringent requirements.

The reconstructed tracks of the incoming muon before and after the tagging magnets were required to "link" in the bend plane of the magnet and any tracks which did not pass cleanly through the apertures of the beam line magnets or the hole in the halo veto hodoscope were rejected. Also the muon beam was restricted to a 5 inch diameter circle at the experimental target

to eliminate possible interactions in the aluminum walls of the target. We required that the incident muon fire elements of the two beam hodoscopes, B_5 and B_6, in front of the target and also register in the MWPC's associated with each hodoscope. This determined the position of the muon interaction within the target to ±1 mm in both the x- and y-directions and reduced the uncertainty in the direction of the incoming muon to less than ±0.3 mrad. Events with multiple muons in the beam line were also eliminated to reduce the possible confusion.

This pre-selection of triggers simplified the data analysis since it was found that multiple-muon tracks were often associated with non-analyzable events in the muon spectrometer. To correct for this beam selection procedure, the muon inclusive cross section was multiplied by a factor of $1/\eta_B$ where η_B was the fraction of triggers selected for analysis. η_B was typically 70%.

Track Finding, Linkage, and Counter Efficiencies

The efficiency of the pattern recognition was evaluated by visually scanning computer-generated pictures of scattering events. From these pictures the track finding efficiency was estimated to be better than 99% and no correction to the cross section was applied.

The downstream tracks of the scattered muon and hadrons were required to link through the magnet in both the x- and y-views to tracks in the 1m X 1m MWPC's. This requirement was important to eliminate stale out-of-time tracks in the wire spark chambers and gave more reliable measurements of the muon scattering angle and the angles of the final state hadrons. Because of this restriction, the muon cross section was corrected for the combined x-y linkage efficiency for upstream and downstream tracks. This efficiency was typically 70%.

The scattered muon was also required to fire elements of the G and H hodoscope and the M_v and M_h hodoscope. This more stringent requirement on the scattered muon led to a correction factor of approximately 1.1.

Dead-time Correction

For a period of ~50 msec after an event, the master event trigger logic was gated off to allow the spark chamber pulsers to recharge and to read the event data and record it on magnetic tape. Actually, only ~10 msec were needed to recharge the 2m X 4m shift-register chamber pulsers, and somewhat longer for the magnetostrictive delay line chambers. Reading out of the wire chambers and fast electronics took about 35 msec. During this time the spectrometer was unable to accept another trigger and a dead-time correction had to be applied to the muon cross section.

The dead-time of the apparatus was measured by using two scalers, S_1 and S_2, before and after the master event gate. The placement of these two scalers in the trigger logic is shown in Figure 103 in Appendix 2. S_1 recorded the total number of event triggers. S_2 was only incremented for event triggers accepted by the apparatus. Thus, the dead-time was simply $(S_1-S_2)/S_1$. Typically, the dead-time correction was ~1.4.

Acceptance Calculations

To account for those events which failed to trigger the apparatus because of the finite size of the trigger counters, the muon cross section had to be corrected for the acceptance of the spectrometer, $A_\mu(q^2,\nu)$, at each value of q^2 and ν. The calculation of the spectrometer acceptance for the scattered muon is in principle a straightforward geometical problem. The complication came from the spatial and momentum distribution of the muon

beam, the finite size of the target, the arrangement of the beam veto hodoscope, and multiple Coulomb scattering in the steel hadron absorber. Because of the finite size of the muon beam and length of the liquid hydrogen/deuterium target, the acceptance for the scattered muon was a function of the position of the muon interaction inside the target volume. Any change in the lateral (x,y) or longitudinal (z) position of the interaction vertex would affect the position where the scattered muon struck the muon trigger hodoscopes. Multiple Coulomb scattering and showers produced in the hadron absorber could also affect the acceptance. For low ν, low q^2 events the showers produced by the scattered muon could veto the event by firing an element of the beam veto hodoscope. In order to avoid inadvertent systematic errors and the problem of muon induced showers in the vicinity of the beam veto hodoscope, events were rejected in the kinematic region where the acceptance was less than 10%.

A further complication was caused by Čerenkov light produced in the plastic light pipes of the beam veto hodoscope. If the scattered muon passed through one of the light pipes, the Čerenkov light could falsely veto the event. The effect can be seen by looking at the distribution of scattered muons across the muon hodoscope in the vicinity of the beam veto, as shown in Figure 40. The dip near the edge of the N hodoscope is caused by events being vetoed by Čerenkov light in the thick part of the light pipes near the phototubes. The muon acceptance was corrected for this effect by assigning a veto efficiency to each of the light pipes.

The spectrometer acceptance for the scattered muon was calculated using two different methods described below. Both calculations yielded similar results.

Pre-calculated Acceptance

In this method the spectrometer acceptance is pre-calculated as a function of ν and q^2 for the scattered muon and stored in a two-dimensional (ν,q^2) lookup table. Then for each scattering event the muon acceptance, $A_\mu(\nu,q^2)$, is evaluated by performing a two-dimensional interpolation in and q^2 from the pre-calculated table of acceptances.

For each value of ν and q^2 in the table, the muon acceptance is calculated by making the following set of assumptions: (1) the interaction vertex of the muon is at the center of the target, (2) no multiple Coulomb scattering in the hadron absorber, and (3) no scattered muon induced showers. For each (ν,q^2) value, the scattering angle θ of the muon is calculated and momentum vector of the scattered muon is rotated in azimuthal angle ϕ around the direction of the incident beam in 10^3 steps. As illustrated in Figure 41, the rotated cone of the scattered muon is traced through the magnetic field of the Chicago Cyclotron to the muon trigger hodoscopes. For each value of azimuthal angle ϕ, the trajectory of the scattered muon downstream of the Cyclotron magnet is calculated using a hard-edged model for the magnetic field. The muon acceptance is defined as the fraction of the cone that is accepted by the trigger hodoscopes and not vetoed by the beam veto hodoscope. This procedure is quite straightforward but tedious. Figures 42-45 illustrate this procedure for several different values of ν and q^2. The muon acceptance for two different ranges of ν and q^2 are shown in Figures 46 and 47. In Figure 46, note the region of low ν and low q^2 which is excluded by the beam veto hodoscope. For ν values less than 90 GeV, the beam veto effectively limits scattering events to q^2 values greater than 2 $(GeV/c)^2$.

Event-by-Event Acceptance

This method differs from the one described above in that the muon acceptance is calculated event-by-event for each scattered muon. Once the scattered muon is found, its momentum vector is rotated around the direction of the incident muon and traced through the Cyclotron magnet to the muon hodoscopes. This procedure has the advantage that it automatically folds in proper distributions of the beam momentum and vertex position. Muon induced showers are not considered. The boundary of the acceptance is again defined by the muon hodoscopes and beam veto.

Muon Acceptance in q^2 and ν

The kinematic region in q^2 and ν available to the muon experiment for 150 GeV incident muons is shown in Figure 48. Except for the small shaded area excluded by the beam veto hodoscope, the entire range of q^2 from q^2_{min} up to more than 50 $(GeV/c)^2$, and ν from 10 to 130 GeV could be reached. The acceptance of the apparatus is illustrated by the contour lines of constant acceptance in the figure. In ω the region extends from the elastic scattering peak at $\omega = 1$ to values of $\omega = \sim 1000$ for small values of q^2 in the deep inelastic region for ν between 90 and 130 GeV. It should be noted that for ω values greater than about 60, the kinematics and spectrometer acceptance limit the data to ranges of q^2 which become rapidly narrower and progressively lower as ω increases. This can be seen by extending in ν along lines of constant ω. For an ω value of 100, the q^2 range is about 1 to 3 $(GeV/c)^2$.

Radiative Corrections

The radiative corrections complicate the measurement of the muon inclusive cross section. Theoretically, we are interested in studying the process in which the muon interacts with the nucleon through the exchange

a single virtual photon, as shown by the first diagram in Figure 49. In reality, however, this scattering process is always accompanied by the emission of real photons. As shown in Figure 49, the measured cross section is a sum of the two processes (a) and (b), in which the muon radiates a photon before or after scattering from the target nucleon.

An important feature of these radiative processes is that they change the values of q^2 and ν, the square of the four-momentum and the energy transferred to the nucleon. In muon or electron scattering experiments, q^2 and ν are determined by measuring the momentum and angle of the scattered muon (or electron). As shown in Figure 50, if the muon emits a photon, the actual values of q^2 and ν transferred to the nucleon are changed from their apparent values. Moreover, since the γNW vertex has a q^{-N} dependence (for elastic scattering N = 4), the emission of photons can change the cross section for scattering considerably, particularly for process (a). These radiative processes must be taken into account if one hopes to extract information about the structure of the nucleons.

For elastic scattering from nucleons, the radiative corrections are well understood and straightforward once the instrumentation resolution is known.[48] The radiative corrections to the elastic cross section depend on the energy resolution ΔE of the experimental apparatus. As the energy resolution becomes smaller, more scattering events are excluded from the elastic peak due to energy loss from photon emission, and the radiative corrections to the cross section become larger.

The radiative corrections for inelastic scattering are more complicated than for the elastic scattering case. First, there is a contribution to the measured muon cross section from the "radiative tail" of elastic scattering. These elastic scattering events appear to be inelastic scatters

because of the emission of a photon. Second, the measured cross section at a given kinematic point contains contributions from inelastic scattering at lower incident energies and higher outgoing energies because of photon emission by the incident or scattered muon. This is illustrated in Figure 50. The inelastic cross section at a point (E_s, E_p), for fixed scattering angle θ, contains contributions from the entire shaded kinematic region. For the purpose of convenience in calculation, a peaking approximation[49] was used to avoid a two-dimensional integration. The peaking approximation corresponds to only considering the contributions from the two strips of width Δ. The horizontal strip represents the contribution from the high energy photons emitted before scattering, and the vertical strip contains the contribution from the high energy photons emitted after scattering.

The procedure used for calculating the radiative corrections was essentially the same as that described by Mo and Tsai.[50] However, because of a lack of data at many incident energies, the radiative corrections could not be done numerically by the model-independent unfolding technique suggested. Instead, the well-established inelastic structure functions measured at SLAC were used as an input model to calculate the theoretical cross section as well as the cross section including radiative corrections. In other words, for a given (q^2,ν) point, the input model was used to calculate the ratio $\delta_R(q^2,\nu)$ defined by:

$$\delta_R(q^2,\nu) = \frac{\sigma_{Theory}}{\sigma_{Experimental}} \quad . \tag{4.4}$$

For protons,

$$\delta_R{}^P(q^2,\nu) = \frac{\sigma^P_{Inelastic}}{\sigma^P_{Inelastic\ Radiated} + \sigma^P_{Elastic\ Tail}} \quad , \tag{4.5}$$

where $\sigma^{P}_{Inelastic}$ is the theoretical inelastic cross section calculated using the input model, $\sigma^{P}_{Inelastic\ Radiated}$ is the inelastic cross section including radiative corrections, and $\sigma^{P}_{Elastic\ Tail}$ is the contribution from the radiative tail of elastic μp scattering. Figures 51 and 52 show the calculated values of $\delta_R{}^{P}$ as a function of q^2 and ν for an incident muon energy of 150 GeV. The largest correction is in the high ν region. For deuterons,

$$\delta_R{}^{D}(q^2,\nu) = \frac{\sigma^{D}_{Inelastic}}{\sigma^{D}_{Inelastic\ Radiated} + \sigma^{D}_{Quasi\text{-}elastic\ Tail} + \sigma^{D}_{Elastic\ Tail}} , \quad (4.6)$$

where $\sigma^{D}_{Inelastic}$ is the theoretical inelastic cross section and $\sigma^{D}_{Inelastic\ Radiated}$ is the inelastic cross section including radiative corrections. $\sigma^{D}_{Elastic\ Tail}$ is the contribution to the measured cross section from the radiative tail of elastic dueteron scattering, $\mu + D \rightarrow \mu' + D$. In calculating $\sigma^{D}_{Elastic\ Tail}$, the elastic form factors of the deuteron were calculated in the impulse approximation using a phenomenological model for the deuteron wave function. $\sigma^{D}_{Quasi\text{-}elastic\ Tail}$ is the radiative tail from quasi-elastic μD scattering, $\mu + D \rightarrow \mu' + p + n$, in which the deuteron breaks up into its constituent proton and neutron. These calculations are discussed in Appendix 4. Figures 53 and 54 show the calculated values of $\delta_R{}^{D}(q^2,\nu)$ as a function of q^2 and ν for 150 GeV incident muons.

Using the calculated values for $\delta_R(q^2,\nu)$, the muon cross section is then simply given by the product of the experimentally measured cross section and δ_R:

$$\frac{d^2\sigma}{dq^2 d\nu} = \left(\frac{d^2\sigma}{dq^2 d\nu}\right)^{measured} \times \delta_R(q^2,\nu) \quad . \quad (4.7)$$

The radiatively corrected cross section was then compared with the input model. If necessary, the model was adjusted and the radiative correction procedure iterated until the input model agreed with the final result.

As a last remark, the radiative corrections (associated with scattering) for muons is only about a factor of 5 less than that for electrons, since their ratio is proportional to

$$\frac{\ell n(q^2/m_\mu{}^2)}{\ell n(q^2/m_e{}^2)} \quad . \tag{4.8}$$

However, the cross section for real bremsstrahlung is different by a factor of 40,000 ($m_\mu{}^2/m_e{}^2$). For muon scattering, the real bremsstrahlung can be ignored. If electrons were used, the experiment would have been impossible with a 48 inch long liquid hydrogen/deuterium target.

The radiative corrections and the procedures used in calculating $\delta_R(q^2,\nu)$ are described in more detail in Appendix 5.

Results on the Muon Inclusive Cross Section

We end this chapter by presenting the results on the muon inclusive cross section, $d^2\sigma/dq^2d\nu$, for 147.22 GeV/c positive muons on deuterium. The measurement of the cross section was made with a total of 2.36×10^{10} incident muons. The empty target background subtraction was made with a total of 1.42×10^9 incident muons.

Figures 55 and 56 show the number of scattering events collected as a function of q^2 and ν. Two different ranges of q^2 are shown. Figures 57 and 58 show the measured cross section, $d^2\sigma/dq^2d\nu$. Values of the cross section are only presented for q^2 values up to 15 (GeV/c) because of the limited statistics for larger values of q^2.

Discussion of these results will be presented in the next chapter in terms of the nucleon structure function νW_2.

Fig. 40.--The distribution of scattered muons across the muon hodoscope in the vicinity of the beam veto. The dip near the edge of the N hodoscope caused Čerenkov light in the plastic light guides vetoing scattered muons can clearly be seen. The correction for this effect was less than 3% for the worst possible case.

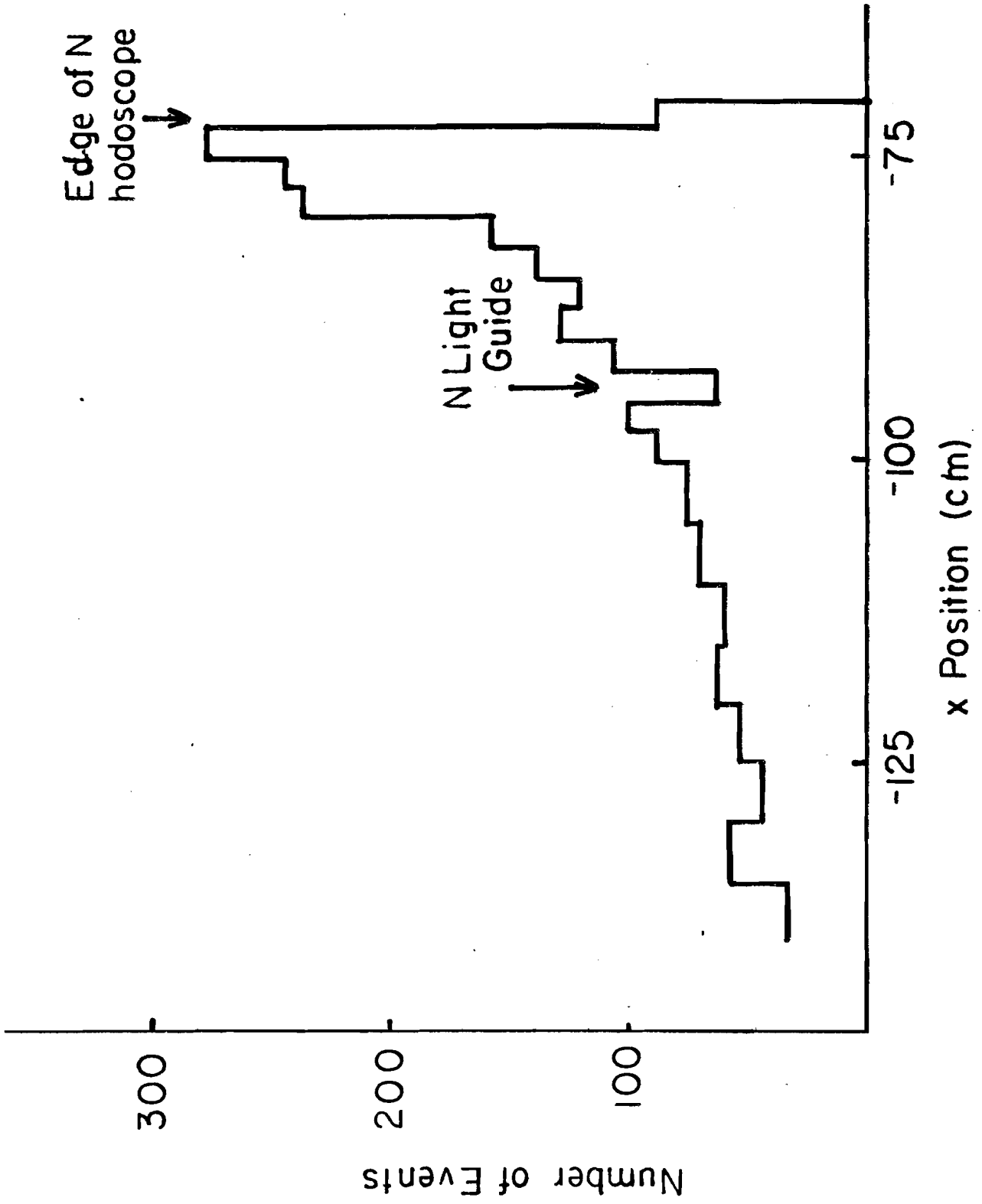
Edge of N hodoscope
N Light Guide
Number of Events
300
200
100
-75
-100
-125
x Position (cm)

Fig. 41.--Illustration of the method of calculating the acceptance of the scattered muon, μ', for a given value of q^2 and ν. The momentum vector of the scattered muon was rotated in a cone around the direction of the incoming muon and traced through the Cyclotron magnet to the muon hodoscope in 10^3 steps. The acceptance is defined as the fraction of the projected cone which intersects the muon hodoscope and is not vetoed by the N hodoscope.

ACCEPTANCE

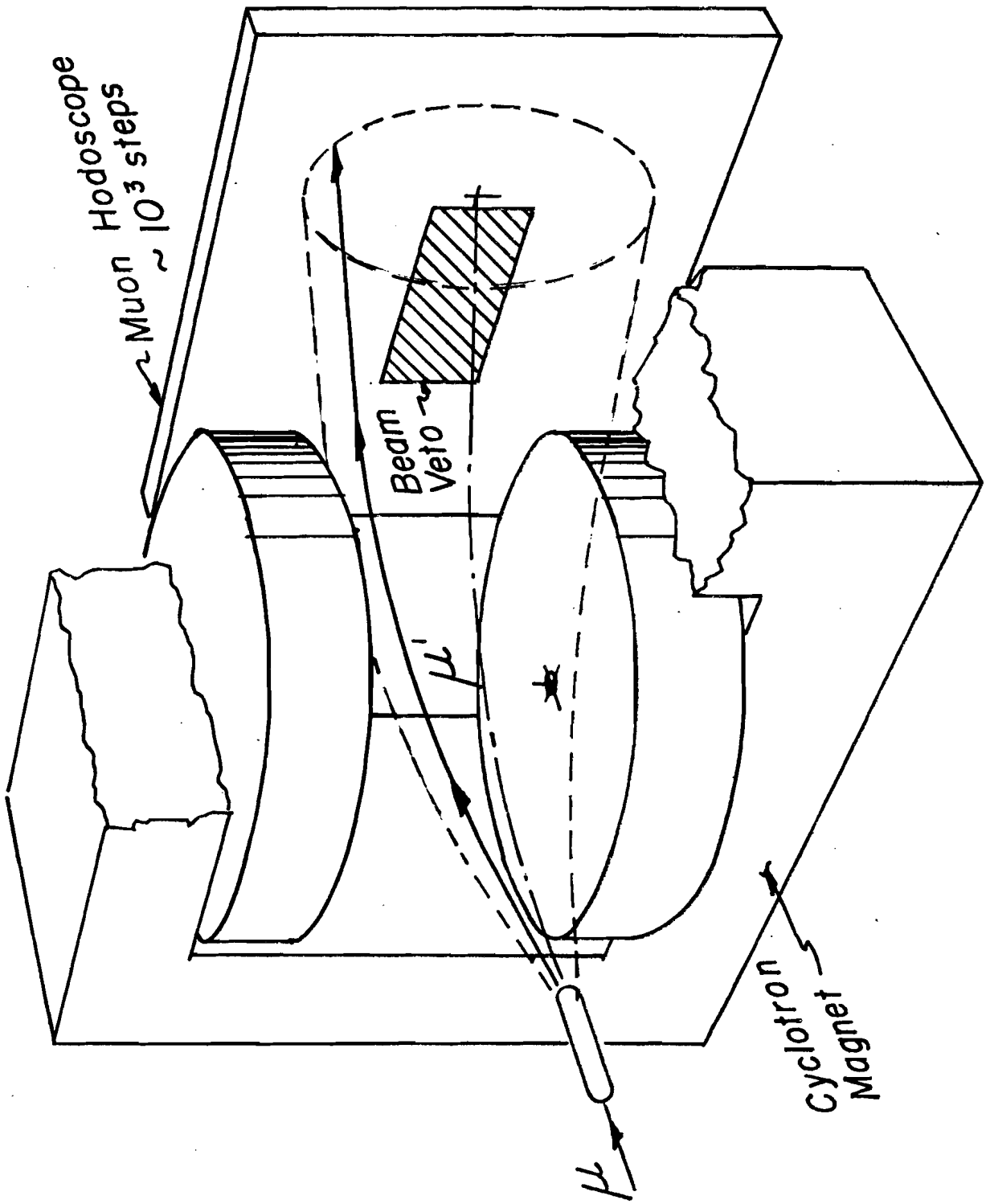

Fig. 42.--Projected muon acceptance cones for $q^2 = 1$ $(GeV/c)^2$ and $100 \leq \nu \leq 130$ GeV.

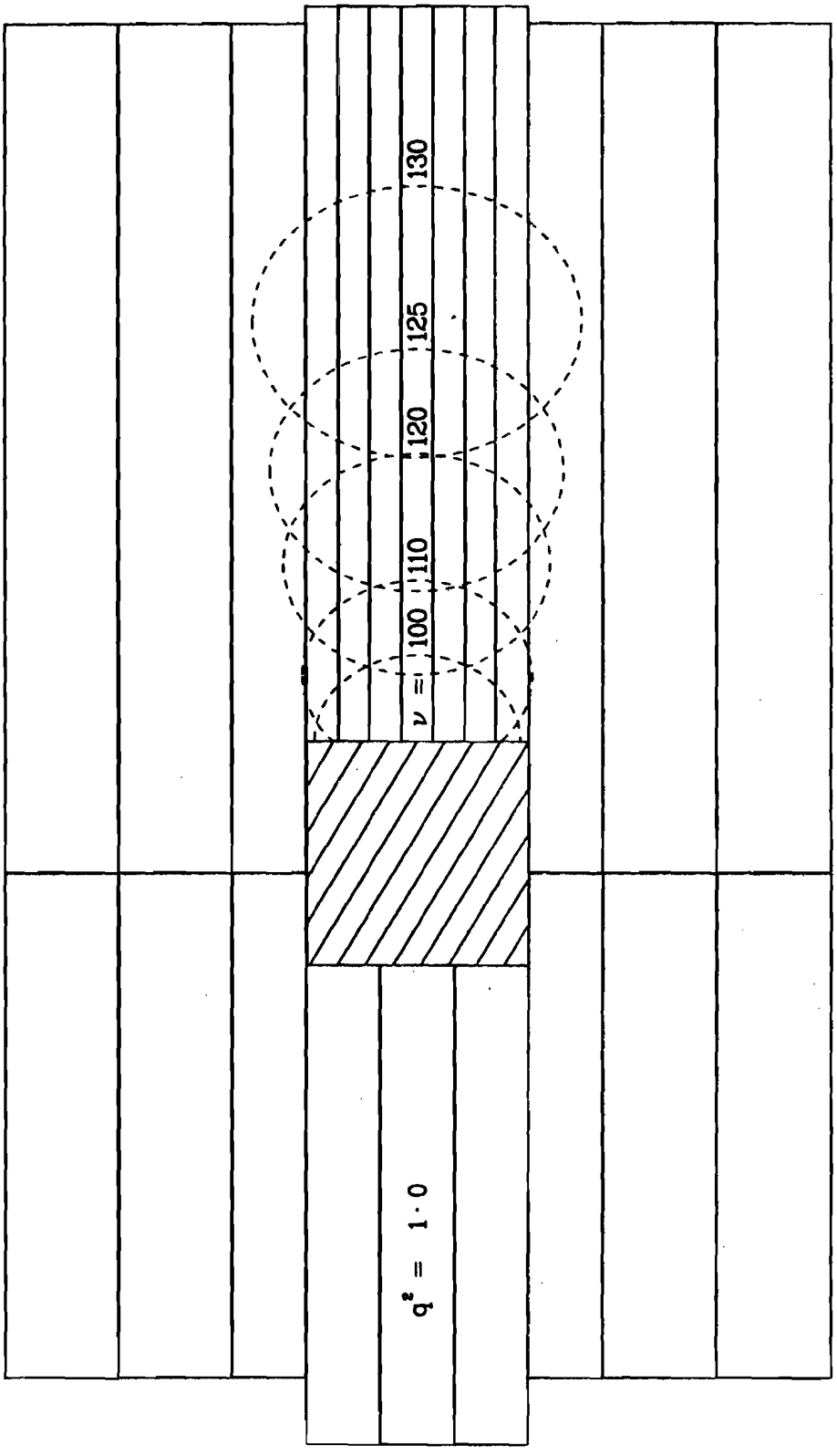
130
125
120
110
100
ν =
$q^2 = 1 \cdot 0$

Fig. 43.--Projected muon acceptance cones for $q^2 = 2$ $(GeV/c)^2$ and $110 \leq \nu \leq 130$ GeV.

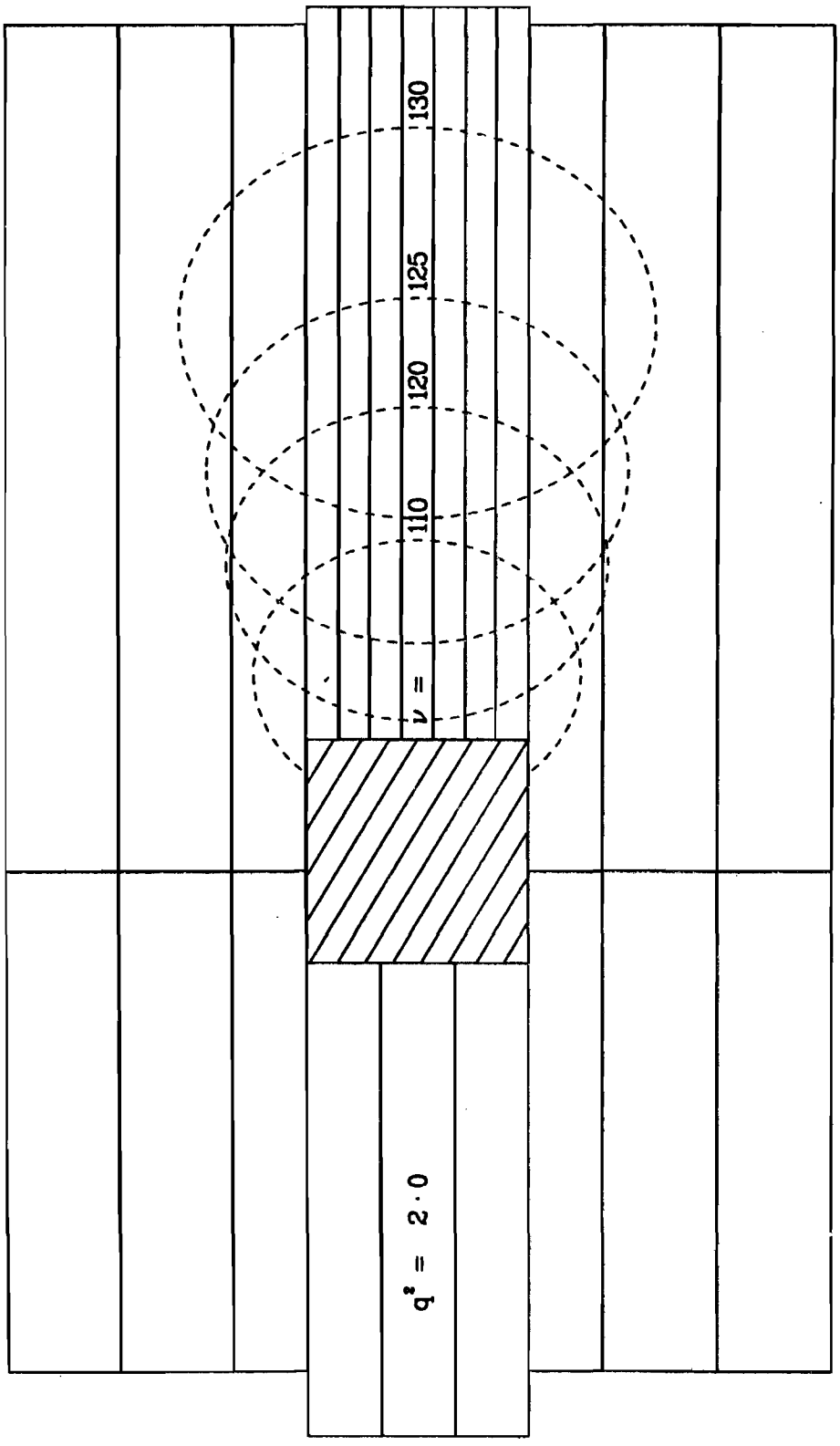
130
125
120
110
ν =
q² = 2·0

Fig. 44.--Projected muon acceptance cones for $q^2 = 5$ (GeV/c)^2 and $80 \leq \nu \leq 125$ GeV.

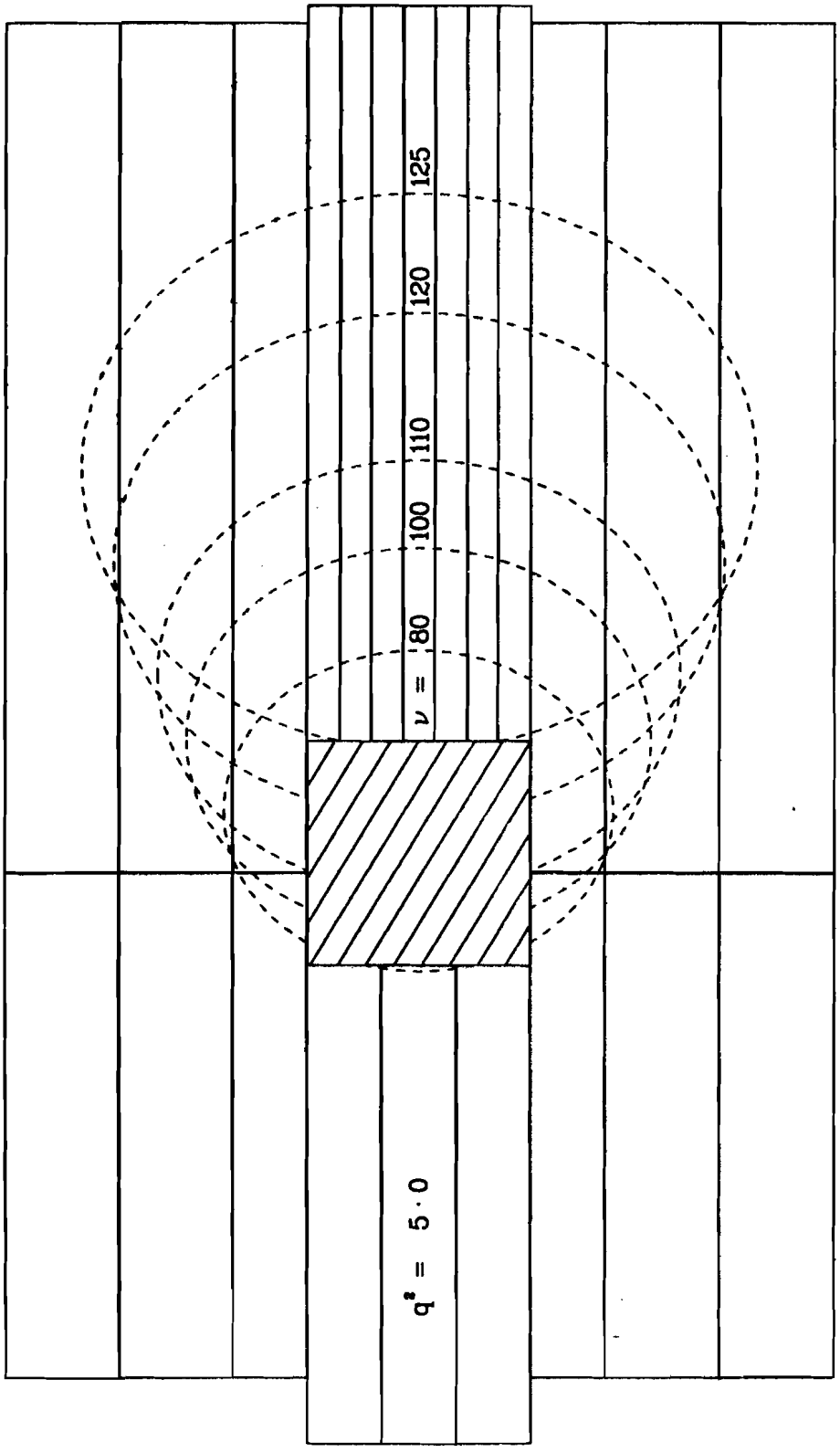
125
120
110
100
80
ν =
q² = 5·0

Fig. 45.--Projected muon acceptance cones for $q^2 = 10$ $(GeV/c)^2$ and $60 \leq \nu \leq 125$ GeV.

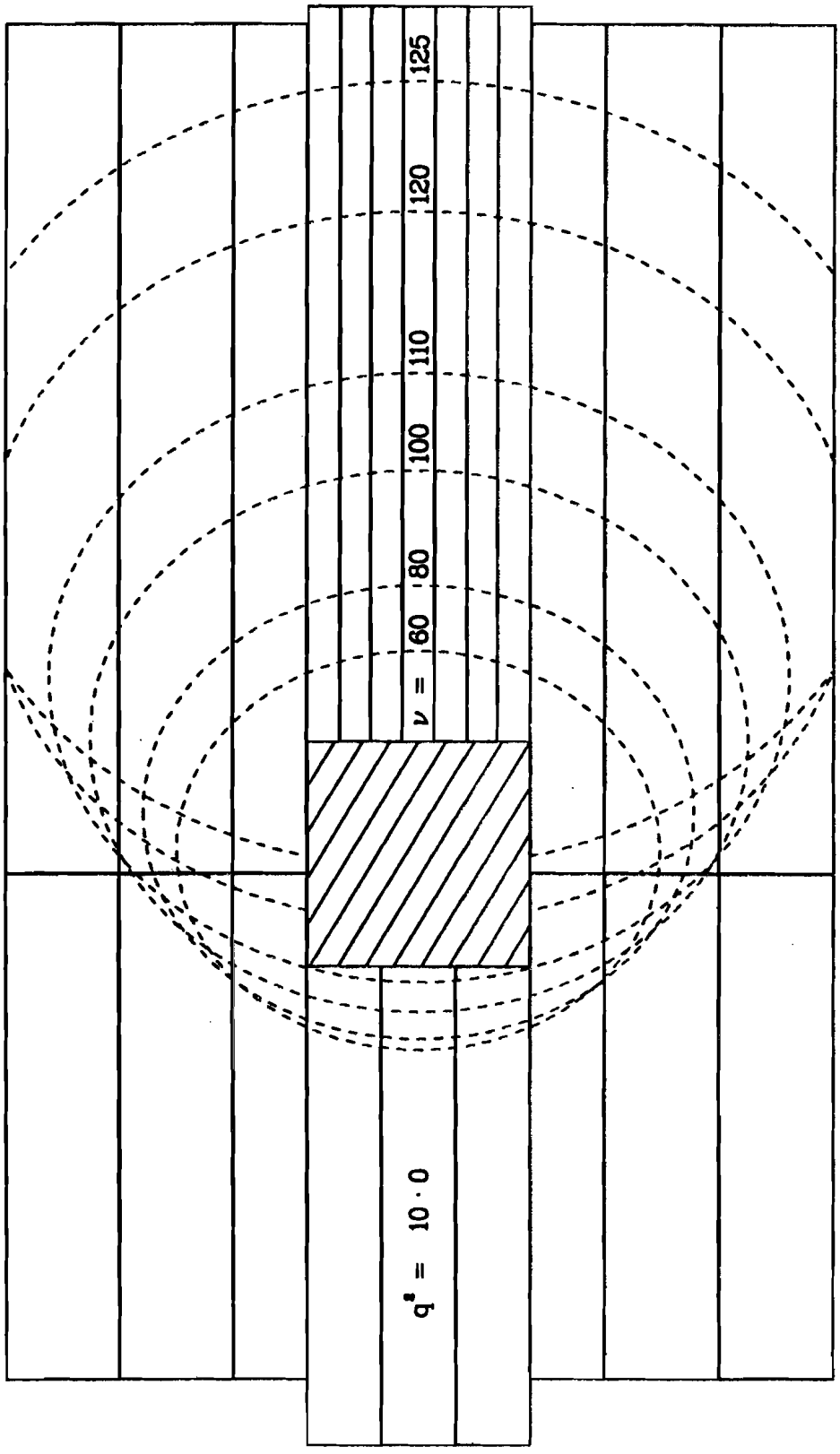
125
120
110
100
80
60
ν =
q* = 10·0

Fig. 46.--Values of the muon acceptance as a function of q^2 and ν for $0 \leq q^2 \leq 5.0$ $(GeV/c)^2$ and $0 \leq \nu \leq 150$ GeV. For ν values less than 90 GeV and for q^2 less than about 2 $(GeV/c)^2$, the scattered muons are vetoed by the N hodoscope.

q^2 (Gev/c)^2	A_μ												Values x 10^{-3}	
4·8 5·0	400	640	668	689	718	892	942	910	818	829	848	868	964	379
4·6 4·8	368	616	649	673	707	861	917	886	809	825	844	865	963	411
4·4 4·6	341	586	625	651	667	824	888	858	802	821	840	862	962	440
4·2 4·4	320	540	587	625	637	783	859	820	796	816	836	859	964	452
4·0 4·2	313	493	544	590	607	733	822	782	790	810	832	854	969	461
3·8 4·0	337	459	500	537	572	670	766	758	784	805	827	850	980	478
3·6 3·8	384	438	458	471	529	593	695	746	777	799	822	846	994	504
3·4 3·6	422	420	418	407	477	508	624	735	769	792	816	842	1000	527
3·2 3·4	404	396	390	376	409	405	583	713	759	785	810	836	1000	530
3·0 3·2	368	367	362	348	336	311	539	688	749	776	803	830	1000	530
2·8 3·0	328	331	329	314	263	242	481	661	739	766	795	823	1000	530
2·6 2·8	270	287	286	265	203	211	370	623	725	756	786	813	1000	531
2·4 2·6	199	217	233	182	171	197	270	564	702	743	776	803	1000	532
2·2 2·4	155	139	114	114	148	177	215	474	667	728	763	797	1000	534
2·0 2·2	128	69	10	37	115	151	178	403	589	708	749	797	1000	536
1·8 2·0	83				59	117	157	360	516	685	731	809	1000	537
1·6 1·8						50	118	296	495	622	708	837	1000	539
1·4 1·6							31	196	454	569	673	873	1000	543
1·2 1·4								15	388	550	657	901	1000	545
1·0 1·2									249	521	643	952	1000	549
0·8 1·0									204	406	619	1000	1000	555
0·6 0·8									120	395	627	1000	1000	565
0·4 0·6									24	373	653	1000	1000	609
0·2 0·4										335	705	1000	1000	703
0·0 0·2										157	1000	1000	1000	
ν (Gev)	0 10	10 20	20 30	30 40	40 50	50 60	60 70	70 80	80 90	90 100	100 110	110 120	120 130	130 140	140 150

Fig. 47.--Values of the muon acceptance, $A_\mu(q^2,\nu)$, for $0 \leq q^2 \leq 25$ $(GeV/c)^2$ and $0 \leq \nu \leq 150$ GeV for 150 GeV incident muons.

q^2 (Gev/c)^2	A_μ												Values x 10^{-3}	
24·0 25·0		889	1000	1000	1000	994	969	869	737	628	540	455	177	99
23·0 24·0		1000	1000	1000	1000	1000	984	906	769	649	556	465	182	97
22·0 23·0		1000	1000	1000	1000	1000	993	940	805	673	572	478	189	99
21·0 22·0		1000	1000	1000	1000	1000	997	970	842	703	591	492	200	102
20·0 21·0		1000	1000	1000	1000	1000	1000	992	882	740	612	508	217	106
19·0 20·0		1000	1000	1000	1000	1000	1000	1000	927	791	636	525	247	107
18·0 19·0		1000	1000	1000	1000	1000	1000	1000	970	850	665	543	282	110
17·0 18·0		1000	1000	1000	1000	1000	1000	1000	994	893	701	565	301	127
16·0 17·0		1000	1000	1000	1000	1000	1000	1000	1000	922	745	590	305	154
15·0 16·0		1000	1000	1000	1000	1000	1000	1000	1000	954	798	617	313	171
14·0 15·0		1000	1000	1000	1000	1000	1000	1000	1000	987	858	650	333	177
13·0 14·0		999	1000	1000	1000	1000	1000	1000	1000	1000	922	708	386	183
12·0 13·0		991	1000	1000	1000	1000	1000	1000	1000	1000	979	782	466	191
11·0 12·0		971	999	1000	1000	1000	1000	1000	1000	1000	1000	823	527	201
10·0 11·0		935	987	1000	1000	1000	1000	1000	1000	1000	1000	831	569	212
9·0 10·0		879	953	998	1000	1000	1000	1000	1000	1000	985	851	626	226
8·0 9·0		810	897	980	1000	1000	1000	1000	1000	1000	947	885	703	242
7·0 8·0	534	769	838	911	995	1000	1000	1000	1000	965	908	898	786	262
6·0 7·0	507	747	778	803	960	999	1000	998	991	887	876	889	867	289
5·0 6·0	457	696	715	729	853	956	984	961	884	841	857	876	942	322
4·0 5·0	341	586	625	651	667	824	888	858	802	821	840	862	962	440
3·0 4·0	422	420	418	407	477	508	624	735	769	792	816	842	1000	527
2·0 3·0	199	217	233	182	171	197	270	564	702	743	776	803	1000	532
1·0 2·0							31	196	454	569	673	873	1000	543
0·0 1·0									24	373	653	1000	1000	609

ν (Gev)	0	10	20	30	40	50	60	70	80	90	100	110	120	130	140
	10	20	30	40	50	60	70	80	90	100	110	120	130	140	150

Fig. 48.--Plot of the kinematic region in q^2 and ν covered by this experiment for an incident energy of 150 GeV. Contours of constant muon acceptance are shown.

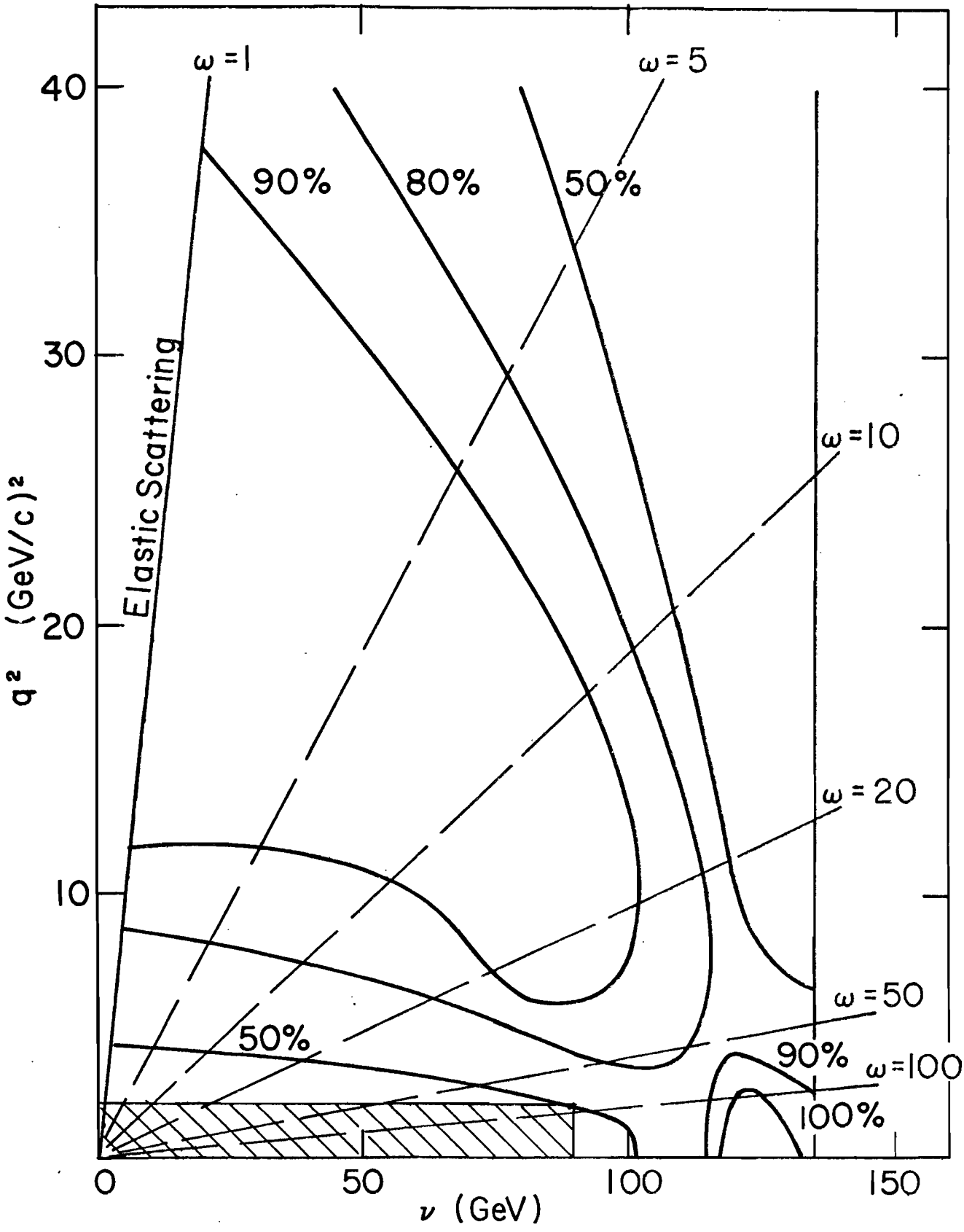
ω = 1
ω = 5
90%
80%
50%
Elastic Scattering
ω = 10
ω = 20
ω = 50
50%
90%
ω = 100
100%
40
30
20
10
0
50
100
150
q² (GeV/c)²
ν (GeV)

Fig. 49.--Radiative corrections to muon-nucleon scattering. The top diagram illustrates the scattering process we are interested in studying. The muon can, however, emit high-energy photons before (a) or after (b) scattering from the nucleon.

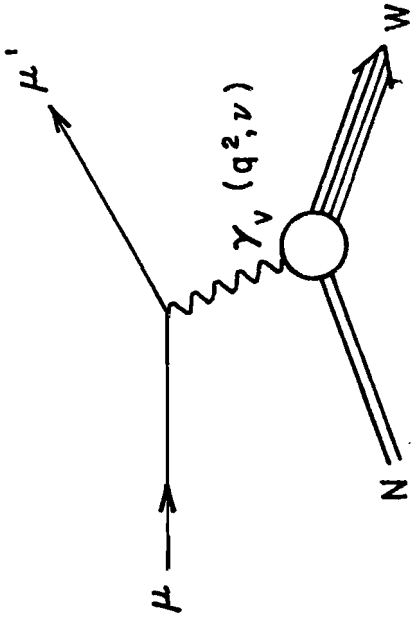
μ'
γ_ν (q², ν)
W
N
μ

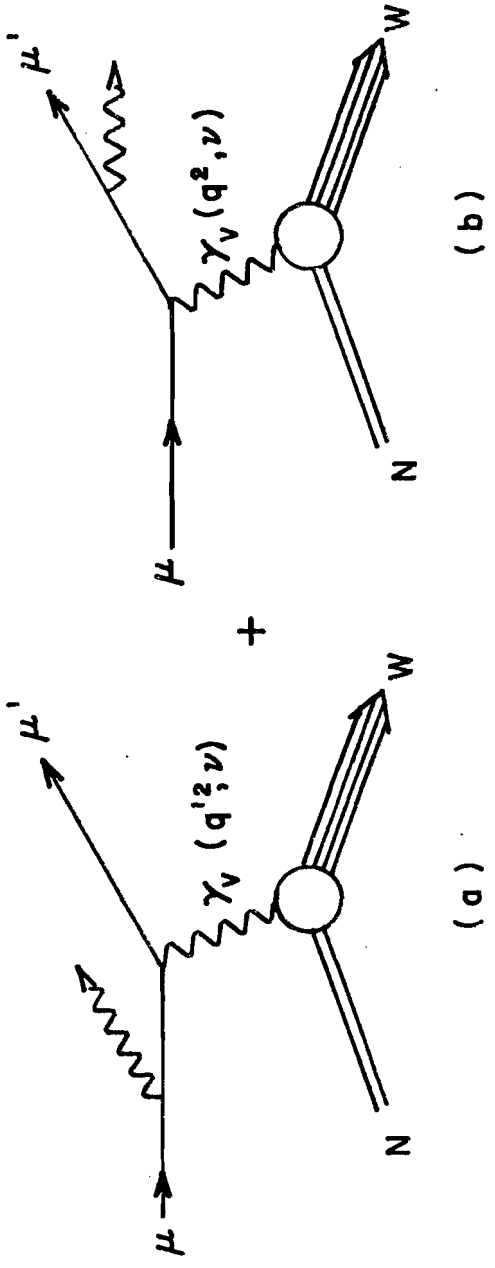
μ'
γ_ν (q², ν)
W
N
μ
+
μ'
γ_ν (q'², ν)
W
N
μ
(b)
(a)

Fig. 50.--The radiative correction triangle for inelastic muon nucleon-scattering. The cross section at the point (E_s, E_p) contains radiative contributions from the entire shaded region. The horizontal strip corresponds to radiation before the scattering (a). The vertical strip corresponds to radiation after the scattering (b). The interior of the triangle corresponds to radiation both before and after the scattering. The effects of radiations are roughly equivalent to those produced by two radiators, one placed before (a) and one placed after (b) the scattering.

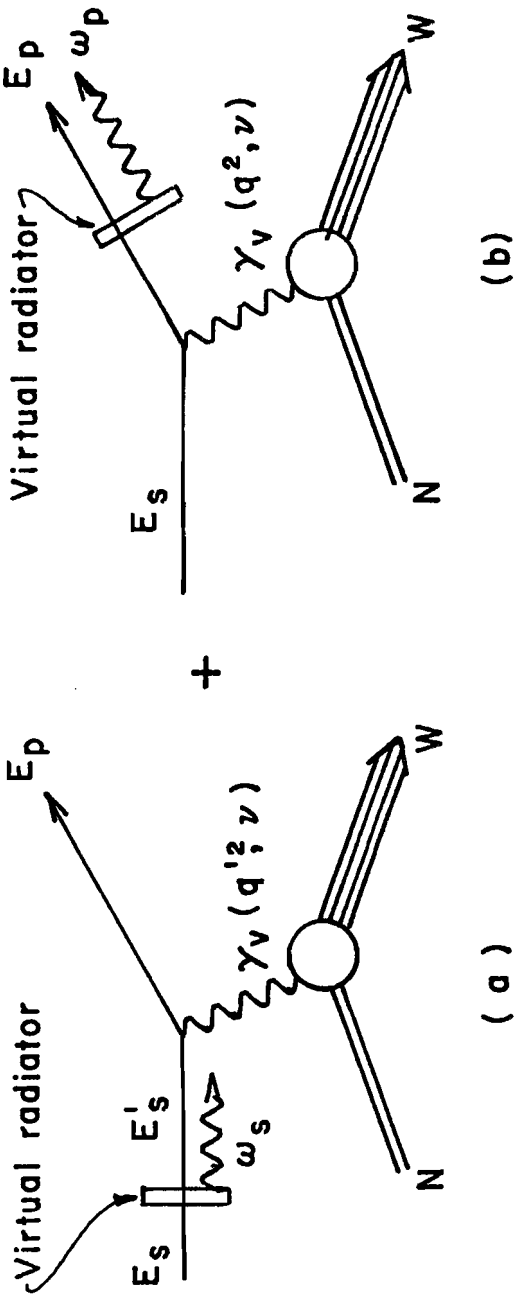
Virtual radiator
E_s
E'_s
ω_s
E_p
$\gamma_v\ (q'^2, \nu)$
W
N
(a)
+
Virtual radiator
E_s
E_p
ω_p
$\gamma_v\ (q^2, \nu)$
W
N
(b)

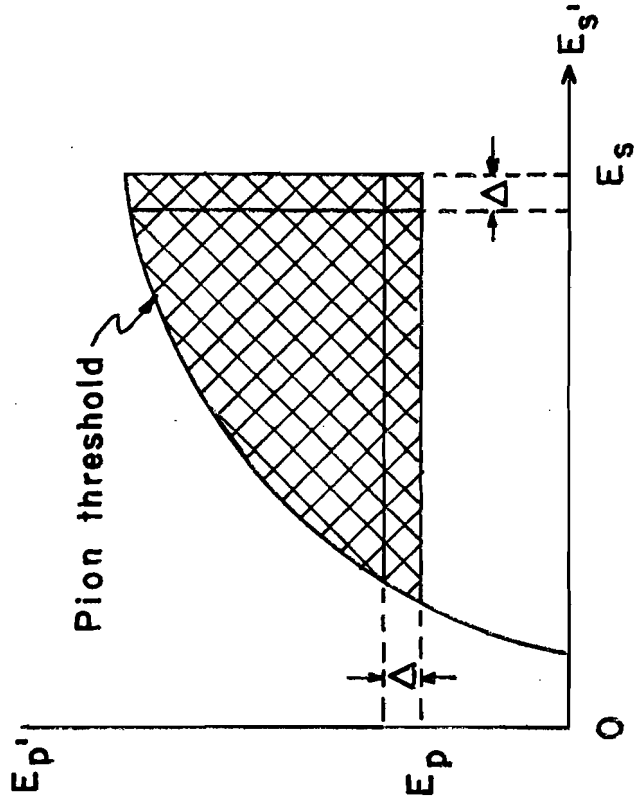
Pion threshold
$E_{p'}$
E_p
$E_{s'}$
E_s
Δ
Δ
0

Fig. 51.--The proton radiative correction factor $\delta_R{}^p(q^2,\nu)$ in the kinematic range $0 \leq \nu \leq 150$ GeV and $0 \leq q^2 \leq 5$ $(\text{GeV/c})^2$.

q^2 (Gev/c)^2		δ_R^P												Values x 10^{-2}		
4·8	5·0	110	102	99	97	96	94	93	91	89	86	81	75	65	49	
4·6	4·8	110	102	99	97	96	94	93	91	88	85	81	75	65	49	
4·4	4·6	109	102	99	97	96	94	92	91	88	85	81	74	65	49	
4·2	4·4	109	102	99	97	95	94	92	90	88	85	81	74	64	48	
4·0	4·2	109	102	99	97	95	94	92	90	88	85	80	74	64	48	
3·8	4·0	108	102	99	97	95	94	92	90	88	85	80	74	64	48	
3·6	3·8	108	101	99	97	95	94	92	90	88	84	80	73	64	48	
3·4	3·6	108	101	98	96	95	93	92	90	87	84	80	73	63	48	
3·2	3·4	107	101	98	96	95	93	92	90	87	84	79	73	63	47	
3·0	3·2	107	101	98	96	95	93	91	89	87	84	79	73	63	47	
2·8	3·0	107	100	98	96	95	93	91	89	87	84	79	72	63	47	
2·6	2·8	106	100	98	96	94	93	91	89	87	83	79	72	62	47	
2·4	2·6	106	100	97	96	94	93	91	89	86	83	78	72	62	47	
2·2	2·4	105	100	97	96	94	93	91	89	86	83	78	71	62	46	
2·0	2·2	105	99	97	95	94	92	91	89	86	82	78	71	61	46	
1·8	2·0	104	99	97	95	94	92	90	88	86	82	77	71	61	46	
1·6	1·8	104	99	97	95	93	92	90	88	85	82	76	70	61	46	
1·4	1·6	103	98	96	95	93	92	90	88	85	81	76	70	60	45	
1·2	1·4	103	98	96	94	93	91	90	87	85	81	76	68	60	45	
1·0	1·2	102	98	96	94	93	91	89	87	84	80	75	67	59	44	
0·8	1·0	101	97	95	94	92	91	89	87	84	80	74	67	55	44	
0·6	0·8	100	97	95	93	92	90	88	86	83	79	73	65	53	42	
0·4	0·6	99	96	94	93	91	90	88	85	82	77	72	63	50	30	
0·2	0·4	97	94	93	92	90	88	86	83	79	74	67	58	44	26	
0·0	0·2	94	92	90	89	86	83	80	75	69	62	52	41	30		
ν (Gev)		0	10	20	30	40	50	60	70	80	90	100	110	120	130	140
		10	20	30	40	50	60	70	80	90	100	110	120	130	140	150

Fig. 52.--The proton radiative correction factor $\delta_R^p(q^2,\nu)$ in the kinematic range $0 \leq \nu \leq 150$ GeV and $0 \leq q^2 \leq 25$ $(GeV/c)^2$.

q^2 (Gev/c)^2	δ_R^P												Values x 10^{-2}		
24·0 25·0		116	108	105	102	100	99	97	96	94	91	87	81	67	
23·0 24·0			108	104	102	100	99	97	95	94	91	87	80	66	
22·0 23·0			108	104	102	100	98	97	95	93	91	87	80	66	
21·0 22·0		113	107	104	102	100	98	97	95	93	90	86	79	65	
20·0 21·0		113	107	104	101	100	98	96	95	93	90	86	79	64	
19·0 20·0		112	106	103	101	99	98	96	94	92	90	85	78	63	
18·0 19·0		111	106	103	101	99	97	96	94	92	89	85	78	62	
17·0 18·0		111	106	103	101	99	97	96	94	92	89	84	77	62	
16·0 17·0		110	105	102	100	99	97	95	94	91	88	84	76	61	
15·0 16·0		110	105	102	100	98	97	95	93	91	88	83	76	60	
14·0 15·0		109	104	102	100	98	96	95	93	91	88	83	75	59	
13·0 14·0		108	104	101	99	98	96	95	93	90	87	82	74	58	
12·0 13·0		108	104	101	99	97	96	94	92	90	87	82	73	57	
11·0 12·0		107	103	101	99	97	96	94	92	90	86	81	72	56	
10·0 11·0		107	103	100	98	97	95	94	92	89	86	80	71	55	
9·0 10·0		106	102	100	98	96	95	93	91	89	85	80	71	54	
8·0 9·0		105	102	99	98	96	94	93	91	88	84	79	69	53	
7·0 8·0		105	101	99	97	96	94	92	90	88	84	78	68	52	
6·0 7·0		104	101	98	97	95	94	92	90	87	83	77	67	51	
5·0 6·0	111	103	100	98	96	95	93	91	89	86	82	76	66	50	
4·0 5·0	109	102	99	97	96	94	92	91	88	85	81	74	65	49	
3·0 4·0	108	101	98	96	95	93	92	90	87	84	80	73	63	48	
2·0 3·0	106	100	97	96	94	93	91	89	86	83	78	72	62	47	
1·0 2·0	103	98	96	95	93	92	90	88	85	81	76	70	60	45	
0·0 1·0	99	96	94	93	91	90	88	85	82	77	72	63	50	30	
ν (Gev)	0	10	20	30	40	50	60	70	80	90	100	110	120	130	140
	10	20	30	40	50	60	70	80	90	100	110	120	130	140	150

Fig. 53.--The deuteron radiative correction factor $\delta_R{}^D(q^2,\nu)$ in the kinematic range $0 \leq \nu \leq 150$ GeV and $0 \leq q^2 \leq 5$ $(\text{GeV}/c)^2$.

q^2 (Gev/c)^2		δ_R^D												Values x 10^{-2}		
4·8	5·0	110	103	100	98	96	95	93	92	90	87	83	77	68	53	
4·6	4·8	110	103	100	98	96	95	93	91	89	87	83	77	68	52	
4·4	4·6	109	102	99	98	96	95	93	91	89	86	83	77	68	52	
4·2	4·4	109	102	99	97	96	94	93	91	89	86	82	77	67	52	
4·0	4·2	109	102	99	97	96	94	93	91	89	86	82	76	67	52	
3·8	4·0	108	102	99	97	96	94	93	91	89	86	82	76	67	52	
3·6	3·8	108	102	99	97	96	94	93	91	89	86	82	76	67	51	
3·4	3·6	108	101	99	97	95	94	92	91	88	86	82	76	66	51	
3·2	3·4	107	101	99	97	95	94	92	91	88	85	82	75	66	51	
3·0	3·2	107	101	98	97	95	94	92	90	88	85	81	75	66	51	
2·8	3·0	107	101	98	96	95	94	92	90	88	85	81	75	66	51	
2·6	2·8	106	101	98	96	95	93	92	90	88	84	81	75	65	50	
2·4	2·6	106	100	98	96	95	93	92	90	88	84	81	74	65	50	
2·2	2·4	106	100	98	96	95	93	92	90	87	84	80	74	65	50	
2·0	2·2	105	100	97	96	94	93	91	89	87	83	80	74	64	50	
1·8	2·0	105	99	97	96	94	93	91	89	87	84	79	73	64	49	
1·6	1·8	104	99	97	95	94	93	91	89	87	83	79	73	64	49	
1·4	1·6	104	99	97	95	94	92	91	89	86	83	78	73	63	49	
1·2	1·4	103	98	96	95	94	92	91	89	86	83	78	71	63	48	
1·0	1·2	102	98	96	95	93	92	90	88	86	82	77	70	62	47	
0·8	1·0	102	98	96	94	93	92	90	88	85	82	77	69	57	46	
0·6	0·8	101	97	95	94	93	91	90	87	85	81	76	68	56	44	
0·4	0·6	100	96	95	94	92	91	89	87	84	80	74	65	52	31	
0·2	0·4	98	96	94	93	91	90	88	85	81	76	70	60	46	26	
0·0	0·2	96	94	93	91	89	86	82	77	71	63	54	42	30		

ν (Gev)															
0	10	20	30	40	50	60	70	80	90	100	110	120	130	140	
10	20	30	40	50	60	70	80	90	100	110	120	130	140	150	

Fig. 54.--The deuteron radiative correction factor $\delta_R{}^D(q^2,\nu)$ in the kinematic range $0 \leq \nu \leq 150$ GeV and $0 \leq q^2 \leq 25$ $(\text{GeV}/c)^2$.

q^2 (Gev/c)^2	δ_R^D												Values x 10^{-2}		
24·0 25·0		116	108	105	103	101	99	98	96	95	92	89	83	71	
23·0 24·0			108	105	102	101	99	98	96	94	92	89	83	70	
22·0 23·0			108	104	102	100	99	97	96	94	92	88	82	69	
21·0 22·0		113	107	104	102	100	99	97	96	94	91	88	82	69	
20·0 21·0		113	107	104	102	100	98	97	95	94	91	88	81	68	
19·0 20·0		112	107	104	101	100	98	97	95	93	91	87	81	67	
18·0 19·0		111	106	103	101	99	98	96	95	93	91	87	80	66	
17·0 18·0		111	106	103	101	99	98	96	95	93	90	86	80	65	
16·0 17·0		110	105	103	101	99	97	96	94	92	90	86	79	65	
15·0 16·0		110	105	102	100	99	97	96	94	92	89	85	78	64	
14·0 15·0		109	105	102	100	98	97	95	94	92	89	85	77	63	
13·0 14·0		109	104	102	100	98	97	95	93	91	89	84	77	62	
12·0 13·0		108	104	101	99	98	96	95	93	91	88	84	76	61	
11·0 12·0		108	103	101	99	98	96	95	93	91	88	83	75	60	
10·0 11·0		107	103	101	99	97	96	94	92	90	87	82	74	59	
9·0 10·0		106	103	100	98	97	95	94	92	90	87	82	73	58	
8·0 9·0		106	102	100	98	96	95	93	92	89	86	81	72	57	
7·0 8·0		105	102	99	98	96	95	93	91	89	85	80	71	56	
6·0 7·0		104	101	99	97	96	94	93	91	88	84	79	70	55	
5·0 6·0	111	103	100	98	97	95	94	92	90	87	84	78	69	53	
4·0 5·0	109	102	99	98	96	95	93	91	89	86	83	77	68	52	
3·0 4·0	108	101	99	97	95	94	92	91	88	86	82	76	66	51	
2·0 3·0	106	100	98	96	95	93	92	90	88	84	81	74	65	50	
1·0 2·0	104	99	97	95	94	92	91	89	86	83	78	73	63	49	
0·0 1·0	100	96	95	94	92	91	89	87	84	80	74	65	52	31	
ν (Gev)	0	10	20	30	40	50	60	70	80	90	100	110	120	130	140
	10	20	30	40	50	60	70	80	90	100	110	120	130	140	150

Fig. 55.--The numbers of muon-nucleon scattering events as a function of ν and q^2 in the kinematic range $0 \leq \nu \leq 130$ GeV and $0 \leq q^2 \leq 5$ $(\text{GeV}/c)^2$.

q^2 (GeV/c)^2		Events											Values x 10^0
4·8	5·0	11	10	10	5	3	3	6	2	4	2	1	2
4·6	4·8	13	19	4	3	6	9	2	4	1	2	2	3
4·4	4·6	17	11	7	6	7	6	6	3	4	5		2
4·2	4·4	20	15	10	3	3	2	3	4	1	2	3	2
4·0	4·2	13	9	6	5	8	7	4	1	4	6	4	2
3·8	4·0	14	9	8	4	13	10	4	7		2	3	6
3·6	3·8	21	9	5	9	3	10	7	3	8	5	2	4
3·4	3·6	24	13	8	5	13	7	5	5	7	6	4	4
3·2	3·4	20	10	14	3	5	3	4	9	3	8	5	1
3·0	3·2	17	7	12	9	5	10	7	8	6	5	3	5
2·8	3·0	17	10	9	3	11	4	4	6	9	7	5	7
2·6	2·8	25	11	6	7	3	3	7	9	4	4	9	6
2·4	2·6	16	11	4	3	4	4	5	5	9	9	2	8
2·2	2·4	17	4	4	4	5	5	9	8	5	8	6	14
2·0	2·2	8			4	3	10	6	7	6	10	9	10
1·8	2·0					1	6	3	11	9	9	9	16
1·6	1·8					1	6	12	11	8	14	20	23
1·4	1·6							2	10	12	17	20	24
1·2	1·4							2	12	18	26	36	32
1·0	1·2								15	23	27	36	52
0·8	1·0									31	38	70	60
0·6	0·8									44	80	92	94
0·4	0·6									84	156	197	177
0·2	0·4									265	519	687	590
0·0	0·2									1181	3941	3955	2556

ν (GeV)	0	10	20	30	40	50	60	70	80	90	100	110	120	130	140
	10	20	30	40	50	60	70	80	90	100	110	120	130	140	150

Fig. 56.--The numbers of muon-nucleon scattering events as a function of ν and q^2 in the kinematic range $0 \leq \nu \leq 130$ GeV and $0 \leq q^2 \leq 25$ $(\text{GeV}/c)^2$.

q^2 $(GeV/c)^2$	Events													Values x 10^0
24·0 25·0			1	1		1	2							
23·0 24·0			2	1		2	2		1					
22·0 23·0			1	2		2								
21·0 22·0			1	2	2	3		1	1					
20·0 21·0		1	4			1	1	1	1					
19·0 20·0		2	1	1		1	1	2		2	2			
18·0 19·0		1	2	1	4	2	1	2		2				
17·0 18·0		4	3	4	1			4	1	2		1		
16·0 17·0		3	6	4	2	3	1	1	1	4	1			
15·0 16·0		3	3	5	1	3	1	5	3	1	2		1	
14·0 15·0		6	5	5	6	3	2	2	3	3	1	2		
13·0 14·0		3	6	3	2	5	2	3	1	3	1	1		
12·0 13·0		11	7	8	10	6	4	4	2	1	2	1		
11·0 12·0		9	17	8	8	5	3	4	1	1	3	1		
10·0 11·0		4	21	8	6	4	7	3	2	3	3	1	1	
9·0 10·0		28	17	16	6	6	4	7		6	1	2		
8·0 9·0		33	22	25	13	13	8	12	4	3	6	4		
7·0 8·0		34	22	26	19	14	15	6	11	5	5	2	4	
6·0 7·0		37	30	27	25	16	10	7	7	6	6	7	1	
5·0 6·0		52	41	26	31	26	11	14	9	10	9	12	8	
4·0 5·0		74	64	37	22	27	27	21	14	14	17	10	11	
3·0 4·0		96	48	47	30	39	40	27	32	24	26	17	20	
2·0 3·0		83	36	23	21	26	26	31	35	33	38	31	45	
1·0 2·0						2	12	19	59	70	93	121	147	
0·0 1·0										1605	4734	5001	3477	
ν (GeV)	0	10	20	30	40	50	60	70	80	90	100	110	120	130	140
	10	20	30	40	50	60	70	80	90	100	110	120	130	140	150

Fig. 57.--The muon inclusive cross section $d^2\sigma/dq^2d\nu$ for deuterium in the kinematic region $0 \leq \nu \leq 130$ GeV and $0 \leq q^2 \leq 5$ $(GeV/c)^2$, before empty target subtraction.

q^2 (GeV/c)^2		$d^2\sigma/dq^2d\nu$												Values x 10^0	
4·8	5·0	248	241	224	95	45	53	87	38	59	28	11	21		
4·6	4·8	366	429	91	69	101	141	33	66	14	32	30	32		
4·4	4·6	439	282	151	120	124	105	91	46	65	74		22		
4·2	4·4	556	404	229	75	58	38	55	72	23	35	42	23		
4·0	4·2	407	255	151	115	166	121	65	17	57	87	46	22		
3·8	4·0	484	254	226	96	294	180	74	110		42	38	58		
3·6	3·8	765	298	181	243	74	223	139	50	138	73	29	38		
3·4	3·6	888	499	271	158	354	154	96	81	114	93	61	46		
3·2	3·4	758	369	596	112	185	68	76	159	55	125	70	10		
3·0	3·2	726	291	534	399	248	267	145	137	93	79	49	44		
2·8	3·0									152	108	62	69		
2·6	2·8									65	63	142	59		
2·4	2·6									148	142	23	79		
2·2	2·4									83	144	86	132		
2·0	2·2									112	160	119	102		
1·8	2·0									169	150	130	156		
1·6	1·8									165	239	262	227		
1·4	1·6									275	315	251	242		
1·2	1·4									390	465	433	319		
1·0	1·2									549	495	432	485		
0·8	1·0									959	712	777	530		
0·6	0·8									1319	1474	968	810		
0·4	0·6									2682	2628	2002	1417		
0·2	0·4									9414	7469	6215	4026		
0·0	0·2									40069	42615	33101	23261		
ν (GeV)		0	10	20	30	40	50	60	70	80	90	100	110	120	130	140
		10	20	30	40	50	60	70	80	90	100	110	120	130	140	150

Fig. 58.--The muon inclusive cross section $d^2\sigma/dq^2d\nu$ for deuterium in the kinematic region $0 \leq \nu \leq 130$ GeV and $0 \leq q^2 \leq 25$ $(GeV/c)^2$, before empty target subtraction.

q^2 (GeV/c)^2	$d^2\sigma/dq^2d\nu$														Values x 10^0
24·0 25·0															
23·0 24·0															
22·0 23·0															
21·0 22·0															
20·0 21·0															
19·0 20·0															
18·0 19·0															
17·0 18·0															
16·0 17·0															
15·0 16·0															
14·0 15·0		22	19	16	18	10	5	5	9						
13·0 14·0		10	19	10	9	15	6	9	3						
12·0 13·0		35	23	24	30	16	12	11	5						
11·0 12·0		33	55	26	21	15	11	12	3						
10·0 11·0		15	64	23	20	13	21	8	5						
9·0 10·0		107	56	45	19	17	10	21		16	2	6			
8·0 9·0		131	80	79	41	37	23	34	11	9	15	12			
7·0 8·0		137	83	89	54	42	44	17	30	13	14	6	11		
6·0 7·0		159	127	100	81	49	27	19	18	17	16	18	2		
5·0 6·0		247	177	106	110	77	31	40	26	31	29	30	18		
4·0 5·0		403	322	169	95	99	92	66	48	43	51	26	24		
3·0 4·0		720	340	358	199	230	177	105	107	80	82	49	39		
2·0 3·0										112	123	86	88		
1·0 2·0										310	333	302	286		
0·0 1·0										10544	10272	7792	4988		
ν (GeV)	0	10	20	30	40	50	60	70	80	90	100	110	120	130	140
	10	20	30	40	50	60	70	80	90	100	110	120	130	140	150

CHAPTER V

NUCLEON STRUCTURE FUNCTION νW_2

In this chapter we discuss the method used to extract the nucleon structure function νW_2 from the muon inclusive cross section, and present measurements for the kinematic ranges $0.2 \lesssim q^2 \lesssim 50$ $(GeV/c)^2$ and $10 \lesssim \nu \lesssim 130$ GeV, obtained by scattering 147 GeV positive muons inelastically from a deuterium target. Some of the results of these measurements have already been reported.[51]

After a discussion of the extraction procedure, the results on νW_2 from deuterium are presented and compared with recent measurements at Fermilab with 56 GeV and 150 GeV muons scattering from an iron target[52] and with lower energy electron scattering results from SLAC.[53] The results are discussed with regard to a test of Bjorken scaling, and the q^2-dependence of νW_2 is examined for possible patterns of scaling violation. The behavior of νW_2 as a function of ω is investigated, with particular emphasis on the large ω region ($\omega \geq 60$) which has not been explored by previous experiments. Several theoretical models which are relevant to the subject are discussed.

Extraction of νW_2

At the present time, the muon experiment has only taken deuterium data at one incident energy; namely, 147 GeV. We cannot do a complete separation of the two inelastic nucleon form factors W_1 and W_2. The separation of both W_1 and W_2 at a given (q^2,ν) value requires the measurement of the differential

cross section for at least two different incident energies, or equivalently, two different scattering angles. In order to extract a value for νW_2 from the measurement of the cross section at a single incident energy, some assumption about W_1 must be made.

In the first Born approximation, the differential cross section for the scattering of muons of energy E to a final energy E' through an angle θ is related to the two inelastic form factors W_1 and W_2 by[17]

$$\frac{d^2\sigma}{dq^2 d\nu} = \left(\frac{\pi}{PP'}\right) \frac{2\alpha^2}{q^4} \left(\frac{P'}{P}\right) \left[(2EE' - q^2/2)W_2(q^2,\nu) + (q^2 - 2m_\mu{}^2)W_1(q^2,\nu)\right] , \quad (5.1)$$

where $\nu = E - E'$, $q^2 = 2(EE' - PP'\cos\theta - m_\mu{}^2)$. The ratio of the inelastic form factors can be expressed as

$$\frac{W_1}{W_2} = (1 + \frac{\nu^2}{q^2})/(1 + R) \quad , \quad (5.2)$$

where $R \equiv \sigma_L/\sigma_T$ is the ratio of the longitudinal to transverse virtual photoabsorption cross sections.[18] Using these relations, the nucleon structure function νW_2 can be calculated from the following expression:

$$\nu W_2(q^2,\nu) = \frac{\nu \frac{d^2\sigma}{dq^2 d\nu}}{\left(\frac{\pi}{PP'}\right) \frac{2\alpha^2}{q^4} \left(\frac{P'}{P}\right) \left[(2EE' - q^2/2) + (q^2 - 2m_\mu{}^2) \frac{(1 + \frac{\nu^2}{q^2})}{1 + R}\right]} \quad . \quad (5.3)$$

To evaluate this expression and extract a value for νW_2 from the measured cross section, we have assumed R = 0.18. This value of R is taken from lower energy electron scattering measurements where W_1 and W_2 have been

separated.[54] These measurements are consistant with R being a constant, although some dependence of q^2 and ν is not ruled out. Assumptions about the value of R, however, do not affect the value of νW_2 significantly. At incident energies of 150 GeV, the W_1 term only contributes about 10% to the muon cross section in the large ω region. Changing the value of R by a factor of two only affects νW_2 by 15%.

It should be mentioned that when studying the behavior of νW_2 as a function of ω and q^2, νW_2 was evaluated event by event directly in terms of ω and q^2, rather than ν and q^2. For a fixed range of ω, νW_2 is quite sensitive to kinematic boundaries imposed in q^2 and ν.

The results on the measurement of νW_2^D from deuterium, binned as a function of ν and q^2 are presented in Figure 59. The number of scattering events in each (q^2,ν) bin is shown in Figure 60. Since we have not completed the analysis of the data taken on hydrogen, we make no attempt here to separate νW_2^D into individual contributions from νW_2^p for the proton and νW_2^n for the neutron. Results on the nucleon structure function νW_2 are presented per nucleon; that is, simply dividing νW_2^D by two.

No corrections for Fermi motion were made. These corrections to νW_2 are only important for values of ω near 1. In the large ω region with which we are mainly concerned, the scattering from deuterium is approximately the sum of scattering from the proton and the neutron. Fermi motion corrections are less than a few percent.[55]

Also, no Glauber corrections[56] were applied to the deuterium data. Previous electron scattering experiments have shown no evidence for a shadowing effect. This is very strange, since shadowing of nucleons has been observed in experiments studying the absorption of real photons in heavy nuclei.

Theories like Vector Meson Dominance (VMD) have predicted[35] that shadowing should also occur for virtual photons in electron and muon scattering experiments. Recently, in a low q^2 electron scattering experiment at Cornell,[57] some shadowing (~10%) was seen in a number of heavy nuclei (carbon, aluminum, copper, and tantalum) for $q^2 \leq 0.1$ $(GeV/c)^2$, but there was no evidence for shadowing at higher q^2. From these results, one can take the view that there is little shadowing at any value of q^2, or that there is a rapid dependence of q^2 between 0 and 0.1 $(GeV/c)^2$. With either alternative, the Glauber correction for deuterium is negligible.

Patterns of Scaling Violation

We begin by discussing the results on the q^2-dependence of νW_2. Bjorken[16] originally suggested that for large values of ν and q^2, νW_2 should have the universal form

$$\nu W_2(q^2,\nu) = F_2(\omega) \quad , \tag{5.4}$$

where $\omega = 2M\nu/q^2$. $F_2(\omega)$ is a universal function in the sense that it only depends on the ratio of ν and q^2, but not on ν and q^2 separately. This predicted scaling behavior of the nucleon structure functions has been verified in electron scattering experiments at SLAC.[53] Measurements at SLAC energies indicate approximate scaling for $q^2 \geq 1.2$ $(GeV/c)^2$. The experimental observation of the large, almost point-like, cross sections in electron scattering has prompted much discussion on constituent models of the nucleon, notably the parton model. However, theoretical attempts to justify this physically appealing interpretation of incoherent scattering off point-like constituents of the nucleon have been difficult. In view of the situation, two important questions come to mind for the present muon experiment at Fermilab. First,

will the scaling behavior of νW_2 persist at the higher energies at Fermilab? And, at what values of q^2 and ν? Secondly, if Bjorken scaling does hold, does it hold in the strict sense, or will patterns of scaling violation emerge?

We first look at the q^2-dependence of νW_2 for fixed values of ω. Figure 61 shows νW_2 (q^2,ω) per nucleon as a function of q^2 for various ranges of ω. The most prominent feature of the data is that there is no large violation of scaling. At an incident energy of 150 GeV, and over a greatly extended kinematic range in ω and q^2, the nucleons still exhibit the large point-like cross sections seen at lower energies and there is approximate scaling behavior of the structure functions. However, νW_2 does show some systematic q^2-dependence and we are interested in the finer deviations from strict scaling behavior. The results indicate that νW_2 is a decreasing function of q^2 for ω less than about 5, it remains fairly constant at $\omega \simeq 5$, and becomes an increasing function of q^2 for $\omega > 5$. As shown in Figure 62, this systematic change of the q^2-dependence as a function of ω agrees with recent measurements of νW_2 by Chang et al.,[52] made with muons scattering from an iron target at Fermilab. Although this experiment does not measure $\nu W_2(q^2,\omega)$ directly, the information on the (q^2,ω) dependences has been extracted from Monte Carlo calculations. The results also agree with the SLAC measurements of νW_2 at lower energy,[53] as shown in Figure 63. This observed pattern of scaling violation is in accord with the predictions of field theoretical calculations.[58] The pattern disagrees with that predicted by various modified parton models.[59] These models predict similar q^2-dependence for all ranges of ω.

To parameterize the q^2-dependence of νW_2, we have fitted the data to the form

$$\nu W_2(q^2,\omega) = \nu W_2(q_0^2,\omega)\left[1 + a\ell n\left(\frac{q^2}{q_0^2}\right)\ell n\left(\frac{\omega}{\omega_0}\right)\right] \quad . \qquad (5.5)$$

The results obtained are given in Table 1. For a fit to all the data in the ranges $2 \leq q^2 \leq 50$ $(GeV/c)^2$ and $3 \leq \omega \leq 80$, we find $a = 0.16 \pm 0.04$ with a χ^2 of 25.1 for 21 degrees of freedom with $\omega_0 = 6$ and $q_0^2 = 3$ $(GeV/c)^2$ fixed. This parameterization is essentially the same as that used by Chang et al.[52] for muon scattering from an iron target. They found $a = 0.099 \pm 0.018$ for data in the range $3 \leq \omega \leq 50$, $1 \leq q^2 \leq 50$ $(GeV/c)^2$.

There have been many discussions on which variable is the correct one to use to study the scaling question. The original scaling variable of Bjorken, $\omega = 2M\nu/q^2$, has been supplemented by several others,[60] based on various reasons, to salvage the scaling of data measured at low energy electron accelerators. For our experiment, because of the fact that ν is large, these variables all approach the Bjorken scaling variable ω to within a few percent. Different choices of scaling variables do not affect our results significantly, but they do make a big difference for results obtained at lower energy.

The Structure Function νW_2 Versus ω

Since the amount of observed scaling violation is small, it is appropriate to average over the q^2 range and to plot νW_2 as a function of ω. The main feature of approximate scaling holds to within 20-30% over the measured range of q^2. In Figure 64, we plot νW_2 averaged over the appropriate q^2 range versus ω. All but the last three data points at high ω have average q^2 values above 1 $(GeV/c)^2$, which is approximately the scaling region for νW_2 measured at SLAC energies. For values of ω larger than 240, the

average q^2 is less that 1 $(GeV/c)^2$. The values of νW_2, along with the q^2 ranges, are given in Table 2. Figure 65 shows νW_2 plotted as a function of the Feynman scaling variable $x = 1/\omega$.

For ω values less than about 60, where we overlap with lower energy experiments at SLAC, the results on νW_2 are in good agreement with previous measurements. νW_2 rises quickly from zero at $\omega = 1$ to approximately 0.32 at $\omega \simeq 5$, and remains essentially constant out to an ω value of approximately 60. For ω values greater than 60, our results show that νW_2 is decreasing as a function of ω.

The behavior of νW_2 in the large ω (equivalently small x) region is of great physics interest. It notably provides information on the anti-quark distributions, $\bar{q}(x)$, inside the nucleon. As it stands at this time, this muon scattering experiment is the only one which can provide such information. One can always argue that the average q^2 is not high enough in the large ω region. This defect can only be remedied by doing the experiment at higher incident energies. It should be pointed out that the average q^2 value at $\omega = 200$ is 1 $(GeV/c)^2$. The value of νW_2 is only 0.22 at this point, considerably lower than that anticipated from the SLAC measurement.

There are a number of theoretical models which make predictions about the shape of νW_2, particularly its behavior at large ω, or in the small x region. We briefly mention a few.

The Kuti-Weisskopf Model

In a model proposed by Kuti and Weisskopf,[26] the physical nucleon is composed of three valence quarks (qqq) which contribute all of the nucleon's quantum numbers, and a core of "sea" of quark-antiquark pairs ($q\bar{q}$) and neutral gluons. The interaction amplitude of the virtual photon with the

valence quarks is assumed to be of the Regge type and is interpreted as the nondiffractive part of the cross section. The scattering amplitude from the core is assumed to be of the Pomeron type and is interpreted as the diffractive component of the cross section. The interaction between the quarks is mediated by neutral gluons. As mentioned in Chapter I, neutral gluons are necessary to account for the energy of the virtual photon not carried away by the charged constituents of the nucleon. There is only one adjustable constant in this model, which determines the ratio of the number of gluons to quark-antiquark pairs in the core. This ratio was determined by comparison with electron scattering data on νW_2 for $x \geq 0.1$. At the time, no data for x values less than 0.1 was available. Figure 66 shows such a fit. It is important to note that the Kuti-Weisskopf model predicts that νW_2 should decrease for $x \leq 0.1$, which is in qualitative agreement with the data from our muon experiment. It is also interesting to notice the relative contributions to νW_2 from the valence quarks and the sea of quark-antiquark pairs. At x values near 1, the main contribution to νW_2 is from the three valence quarks, and the contribution from the sea is small. As $x \to 0$, however, the contribution of the valence quarks vanishes, and νW_2 is dominated by diffractive scattering from the sea. This is one of the reasons why the behavior of νW_2 at small x is interesting. We are measuring the contribution of the sea of quark-antiquark pairs.

Modified Kuti-Weisskopf Models

One of the objections to the simple Kuti-Weisskopf model is that it fails to predict the correct ratio of the neutron and proton structure functions as x approaches 1. In particular, Kuti and Weisskopf assume identical momentum distributions for the u-type and d-type valence quarks. This leads

to a prediction of 2/3 for the ratio $\nu W_2^n/\nu W_2^p$ as $x \to 1$, whereas experimentally it is known[28] to approach the value 1/4. McElhaney and Tuan[61] have proposed a modified version of the Kuti-Weisskopf model which assumes different momentum distributions for the valence quarks. By modifying the momentum distribution of the d-type valence quark so that it vanishes as $x \to 1$, they find that they can accommodate a value of 1/4 for the ratio $\nu W_2^n/\nu W_2^p$ at $x = 1$, and not change any of the qualitative predictions of the model. In particular, νW_2 should still exhibit a decrease at small x values.

Model of Alterelli, Cabibbo, Maiani, and Petronzio

Another model, suggested by Alterelli, Cabibbo, Maiani, and Petronzio,[62] is quite similar to that of Kuti and Weisskopf. An interesting feature is that each of the three constituent quarks, which make up the nucleon, is itself a complex object, made up of point-like partons and neutral gluons. The structure functions of the nucleon thus result from two factors, one determined by the momentum distributions of the three constituent quarks, the other being the structure function of the constituents themselves. Their calculation, using a complicated $SU(6)_W \otimes O(3)$ theory, also indicates the observed decreasing behavior of νW_2 at small x, as shown in Figure 67.

Parton Model Fit to νW_2

Several other authors have proposed quark-parton models assuming different momentum distributions for the valence quarks and quark-antiquark pairs in the sea. Barger, Weiler, and Phillips,[63] using a modified Kuti-Weisskopf model, have taken our measurements of νW_2 from deuterium and determined the relative valence and sea contributions. The results of the fit are shown in Figure 68. They find that the sea contribution is small, which simply reflects the fact that νW_2 is decreasing at large ω. As we

shall see in the next section, the small sea contribution observed in the muon experiment is consistent with a small or zero sea component observed in recent neutrino scattering experiments at Fermilab.

One remark should be made with regard to the specific forms of the momentum distributions of the constituent quarks used in the different models. It should be remembered that many possibilities exist that can fit the available data on νW_2 equally well. Even with the constraints imposed by the numerous quark sum rules, many models can reproduce the observed shape of νW_2 and accommodate a value of 1/4 for the ratio $\nu W^n/\nu W_2^p$ as $x \to 1$. We adopt a "realistic" point of view and regard the various models as convenient numerical representations of the data. They rarely lead to any deep understanding beyond the original ideas of the quark-parton model.

Comparison with Neutrino Scattering

The weak interactions provide an alternate and complimentary way to probe the structure of the nucleon through the study of inelastic nuetrino-nucleon scattering at high energies. The cross section for inelastic neutrino-nucleon scattering is given by an expression analogous to that for inelastic muon scattering, except for two important differences: First, in the neutrino-nucleon interaction there are axial as well as vector current contributions. This leads to a description of inelastic neutrino scattering in terms of three structure functions, as compared with two for the electromagnetic interaction. Secondly, the factor of $1/q^4$ from the virtual photon propogator in the expression for the muon cross section is absent in the expression for the neutrino scattering cross section. Hence, the fraction of high q^2 events compared to the total cross section will be larger than in electron or muon scattering.

Within the framework of the parton model, the neutrino is assumed to scatter incoherently from the individual partons, analogous to the virtual photon in electron or muon scattering. This leads to similar predictions of Bjorken scaling for the three structure functions that describe the neutrino-nucleon vertex. These three structure functions can be expressed in terms of the parton momentum distributions of the nucleon, u(x), d(x), etc., and compared with results obtained in electron or muon scattering experiments.

Figure 69 shows results from a recent neutrino scattering experiment at Fermilab.[64] We observe that the data indicate a shape similar to that observed in our muon experiment. The structure function is decreasing when x becomes smaller. The curves are a parton model fit to the data by Barger.[65] The solid line represents a valence only solution, with zero sea contribution. The dashed line corresponds to a valence plus sea solution. We see that the neutrino scattering data is consistent with a small or zero sea component, in qualitative agreement with our results.

Regge Pole Model

Regge theory can also yield the observed decrease of νW_2 at large ω. This is accomplished by the addition of a fixed pole at J = 0 in the forward Compton scattering amplitude for virtual photons in describing the deep inelastic scattering process.[66]

In Regge theory the total photoabsorption cross section $\sigma_{\gamma p}$ for real photons is considered to be described in terms of the pomeron P, and the ordinary Regge trajectories f,A_2 with intercepts at t = 0 of approximately 0.57. This predicts an energy dependence of the form[67]

$$\sigma_{\gamma p}(K) = c_1 + \frac{c_2}{\sqrt{K}} \quad , \tag{5.6}$$

where K is the photon energy. As shown in Figure 70, this is in reasonable agreement with the observed high energy behavior. A fit to the experimental data yield a value of c_1 = 89.0 μb for the pomeron contribution, and c_2 = 93.2 μb-GeV$^{\frac{1}{2}}$ for the f,A_2 trajectories. Evidence for a fixed pole with $\alpha(o) \sim -\frac{1}{2}$ has come from a detailed analysis of the forward Compton amplitude by Damashek and Gilman.[68] They concluded that a fixed pole (i.e., a pole whose trajectory $\alpha(t)$ is independent of t) was needed in the real part of the Compton amplitude to get agreement between the observed γp cross section and forward dispersion relations for Compton scattering. Since such a fixed pole term exists in the on-mass-shell Compton amplitude, it is not improbable that there is also a J = 0 fixed pole in the off-mass-shell amplitude. The implications of this additional fixed pole in the Compton amplitude for $q^2 \neq 0$ has been investigated by Cheng and Tung,[69] and also Close and Gunion.[70] The application to νW_2 presented here is that due to Close and Gunion. They suggest an expression for νW_2 of the form

$$\nu W_2(\omega) = a + b\omega^{-1/2} + c\omega^{-3/2} \quad , \tag{5.7}$$

where the $\omega^{-3/2}$ term is due to the inclusion of a fixed pole. A fit to electron scattering data is shown in Figure 71, and yields a = 0.12, b = 0.462, and c = 4.02. The implications of this result are significant. For ω values less than 10, there are important contributions to νW_2 from terms other than those arising from the leading Regge singularities. The pomeron contributes only a relatively small part. Consequently νW_2 must decrease significantly from its measured value of ω = 10 as $\omega \to \infty$. This, of course, is what we observe. In a theory given by Harari,[71] the deep inelastic scattering process is assumed to be dominated by the pomeron contribution. It yields a

constant νW_2 for all values of ω, and thus contradicts our result.

Heavy Quarks and Color Brightening

Several authors[72] have suggested that we might begin to see evidence for heavy quarks or other new degrees of freedom, such as color, at Fermilab energies. Evidence for heavy quarks would appear as an enhancement in νW_2 at large ω as the threshold for their excitation was crossed. Needless to say, we have seen no indication in our data of such an effect. Evidence for the excitation of color, or color brightening, would be a more subtle effect--a general increase in νW_2 above the color threshold. Pati and Salam[72] have suggested that this would be a 10-20% effect.

Approach to Scaling

Since the nucleon structure function νW_2 does not strictly observe Bjorken scaling, it becomes difficult to express νW_2 as simple functions of ω, q^2, ν, etc. One important aspect of the structure function is its behavior in low q^2 region. It is interesting to see how νW_2 approaches its scaling behavior as q^2 is increased. We would also like to see how well this region can be described by vector meson dominance[35] or the generalized vector dominance model.[36]

In the SLAC electron scattering experiments, νW_2 is observed to reach a constant plateau at a q^2 value of approximately 1.2 $(GeV/c)^2$. This is illustrated in Figure 72, where νW_2 is plotted as a function of q^2 for all values of ω. A similar plot for our muon experiment is shown in Figure 73, for data in the deep inelastic region $90 \leq \nu \leq 130$ GeV. At Fermilab energies, the onset of scaling occurs at a higher q^2 value of approximately 3.5 $(GeV/c)^2$. Figure 74 shows νW_2 measured with muons scattering from an iron target at

Fermilab.[73] These results also indicate an onset of scaling at a q^2 value between 3 and 4 $(GeV/c)^2$, in agreement with our result.

Apparently we are observing a ν-dependence in the way νW_2 approaches its scaling behavior. In both the experiments at SLAC and at Fermilab, the values of νW_2 were extracted assuming the same value of 0.18 for R. The major difference is in the value of ν, which is nearly a factor of ten higher at Fermilab. As ν increases, the approach to scaling is slower, and the onset of Bjorken scaling shifts toward higher values of q^2.

The vector meson or generalized vector dominance models are expected to describe the nucleon structure function in the low q^2 region. In a specific calculation, given by Devenish and Schildknecht,[74] νW_2 is expressed as:

$$\nu W_2(q^2,\nu) = \frac{\nu K}{4\pi^2\alpha} \frac{q^2}{q^2+\nu^2} \frac{\bar{m}^2}{(q^2+\bar{m}^2)} \sigma_{\gamma_N}(K)(1+R) \quad , \qquad (5.8)$$

where $\sigma_{\gamma_N}(K)$ is the total photoabsorption cross section for real photons of energy K, and $\bar{m}$, an adjustable parameter in the model. For a fit to the SLAC electron data, $\bar{m}^2 = 0.61\ m_\rho{}^2$. Figure 75 shows a comparison of our muon scattering data in the high ν region, $90 \leq \nu \leq 130$ GeV, with this particular model.

TABLE 1

FITS OF THE q^2-DEPENDENCE OF νW_2

(TO THE FORM

$$\nu W_2(q^2,\omega) = \nu W_2(q_o{}^2,\omega)\left[1 + a\ \ell n\left(\frac{q^2}{q_o^2}\right)\ell n\left(\frac{\omega}{\omega_o}\right)\right]$$

WITH $\omega_o = 6$ and $q_o{}^2 = 3$ $(GeV/c)^2$ FIXED)

$\langle\omega\rangle$	ω Range	a
2.0	1 - 3	0.27 ± 0.09
4.0	3 - 5	-0.06 ± -0.26
8.0	5 - 11	0.34 ± 0.23
23.0	11 - 35	0.22 ± 0.07
57.5	35 - 80	0.10 ± 0.09
120.0	80 - 160	0.12 ± 0.06
200.0	160 - 240	0.13 ± 0.10
320.0	240 - 400	0.07 ± 0.07
500.0	400 - 600	0.21 ± 0.29
800.0	600 - 1000	0.02 ± 0.15
41.5	3 - 80	0.15 ± 0.04

TABLE 2

νW_2 FROM DEUTERIUM FOR 150 GeV INCIDENT MUONS

$\langle\omega\rangle$	ω Range	q^2 Range $(GeV/c)^2$	νW_2 (per nucleon)
1.5	1 - 2	4 - 50	.08 ± .01
2.5	2 - 3	3 - 50	.16 ± .02
3.5	3 - 4	2 - 50	.21 ± .02
4.5	4 - 5	2 - 50	.29 ± .02
6.0	5 - 7	2 - 30	.33 ± .02
8.0	7 - 9	2 - 30	.32 ± .02
10.0	9 - 11	2 - 15	.33 ± .02
12.5	11 - 14	2 - 15	.34 ± .02
17.0	14 - 20	2 - 15	.32 ± .02
27.5	20 - 35	2 - 10	.29 ± .01
40.0	35 - 45	2 - 6	.30 ± .03
52.5	45 - 60	2 - 6	.30 ± .02
70.0	60 - 80	2 - 4	.29 ± .02
100.0	80 - 120	1 - 3	.25 ± .02
140.0	120 - 160	1 - 2	.24 ± .03
200.0	160 - 240	0.8 - 1.4	.21 ± .03
320.0	240 - 400	0.4 - 1.0	.21 ± .01
500.0	400 - 600	0.3 - 0.6	.16 ± .02
800.0	600 - 1000	0.2 - 0.5	.12 ± .02

Fig. 59.--Measured values of the structure function νW_2^D versus q^2 and ν before empty target subtraction. All other corrections have been applied.

q^2 $(GeV/c)^2$	νW_2^D													Values x 10^{-3}	
48·0 50·0															
46·0 48·0				930					3951						
44·0 46·0								2778							
42·0 44·0									3194						
40·0 42·0				552			1751								
38·0 40·0									2414						
36·0 38·0				366				1242							
34·0 36·0			373	411											
32·0 34·0				260				1083	1506						
30·0 32·0			148			515	523	917	1397			2610			
28·0 30·0				422	580	420	435	1766	3671						
26·0 28·0				203	249	922	1176	1353		1153	1342				
24·0 26·0			245	147	426	631	679			909		1659	5138		
22·0 24·0			287	408		972	668		464						
20·0 22·0		71	445	235	408	806	261	727	724						
18·0 20·0		128	190	190	567	462	405	923		1552	1271				
16·0 18·0		248	468	569	374	433	145	969	449	1633	371	669			
14·0 16·0		225	344	608	551	652	334	1121	174	930	794	767	1651		
12·0 14·0		222	408	457	715	795	552	788	360	699	468	660			
10·0 12·0		179	796	494	592	526	729	617	263	473	873	326	206		
8·0 10·0		633	617	841	531	652	512	1048	231	718	541	650			
6·0 8·0		472	546	751	760	672	707	414	739	511	588	515	374		
4·0 6·0		482	668	571	611	654	561	611	501	645	750	657	560		
2·0 4·0		508	412	532	529	810	727	541	616	573	690	526	545		
0·0 2·0						53	294	248	480	455	525	528	509		
ν (GeV)	0 10	10 20	20 30	30 40	40 50	50 60	60 70	70 80	80 90	90 100	100 110	110 120	120 130	130 140	140 150

Fig. 60.--The numbers of muon-nucleon scattering events as a function of ν and q^2 in the kinematic range $0 \leq \nu \leq 130$ GeV and $0 \leq q^2 \leq 50$ $(GeV/c)^2$.

q^2 (GeV/c)^2	Events												Values x 10^0		
48·0 50·0															
46·0 48·0				1					1						
44·0 46·0								1							
42·0 44·0									1						
40·0 42·0				1			1								
38·0 40·0									1						
36·0 38·0				1				1							
34·0 36·0			1	1											
32·0 34·0				1				1	1						
30·0 32·0			1			1	1	1	1			1			
28·0 30·0				2	2	1	1	2	3						
26·0 28·0				1	1	2	2	2		1	1				
24·0 26·0			2	1	2	2	2			1		1	1		
22·0 24·0			3	3		4	2		1						
20·0 22·0		1	5	2	2	4	1	2	2						
18·0 20·0		3	3	2	4	3	2	4		4	2				
16·0 18·0		7	9	8	3	3	1	5	2	6	1	1			
14·0 16·0		9	8	10	7	6	3	7	6	4	3	2	1		
12·0 14·0		14	13	11	12	11	6	7	3	4	3	2			
10·0 12·0		13	38	16	14	9	10	7	3	4	6	2	1		
8·0 10·0		61	39	41	19	19	12	19	4	9	7	6			
6·0 8·0		71	52	53	44	30	25	13	18	11	11	9	5		
4·0 6·0		126	105	63	53	53	38	35	23	24	26	22	19		
2·0 4·0		179	84	70	51	65	66	58	67	57	64	48	65		
0·0 2·0						2	12	19	59	1675	4827	5122	3624		
ν (GeV)	0 10	10 20	20 30	30 40	40 50	50 60	60 70	70 80	80 90	90 100	100 110	110 120	120 130	130 140	140 150

Fig. 61.--The q^2-dependence of νW_2 for several different ranges of ω.

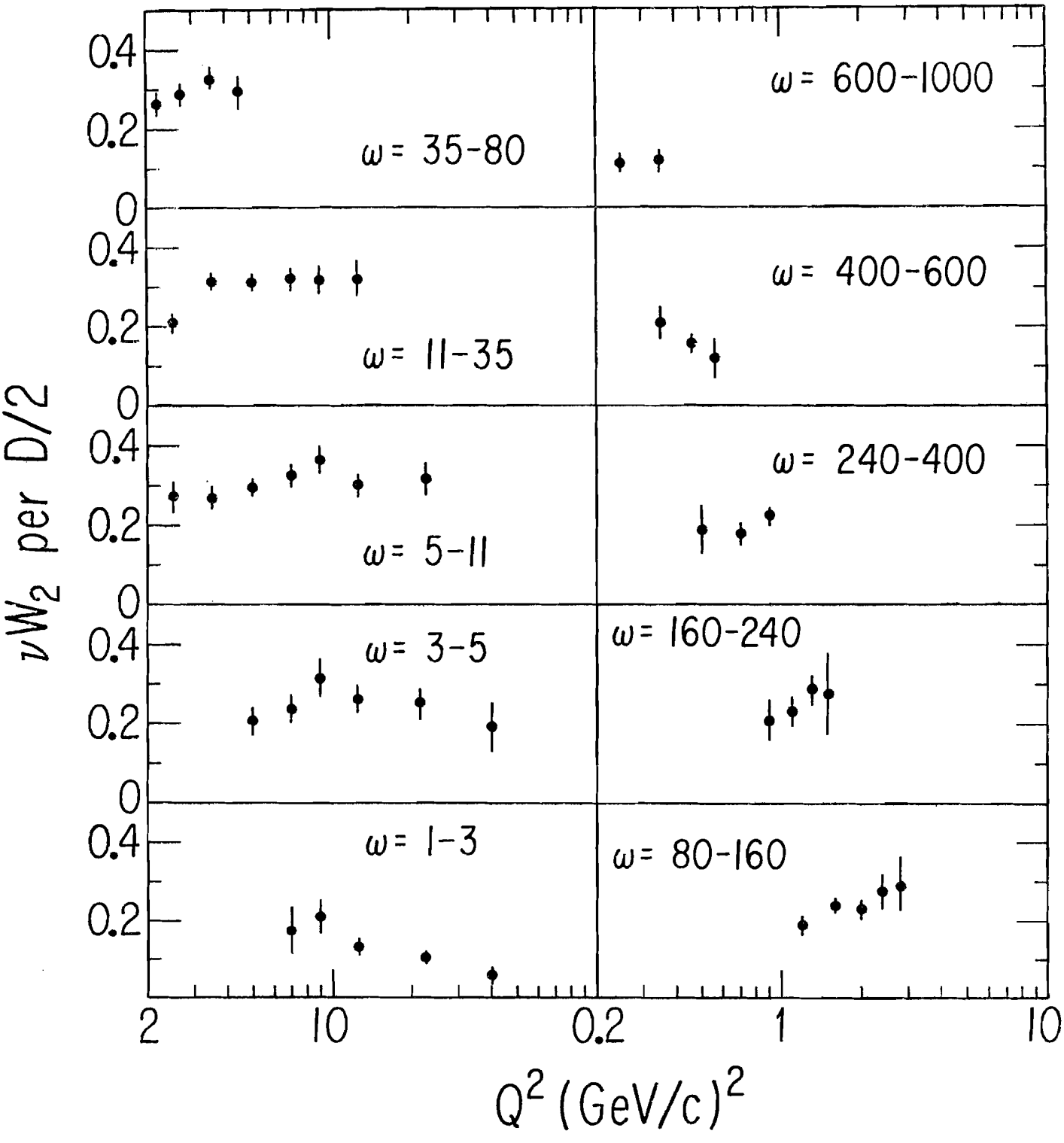
0.4
0.2
0
ω = 35-80
ω = 600-1000
ω = 11-35
ω = 400-600
ω = 5-11
ω = 240-400
ω = 3-5
ω = 160-240
ω = 1-3
ω = 80-160
νW2 per D/2
2
10
0.2
1
10
Q2 (GeV/c)2

Fig. 62.--νW_2 as a function of q^2 measured with muons scattering from an iron target at Fermilab.[52] The ratio of observed to simulated event rate is plotted versus q^2 for eight ranges of ω.

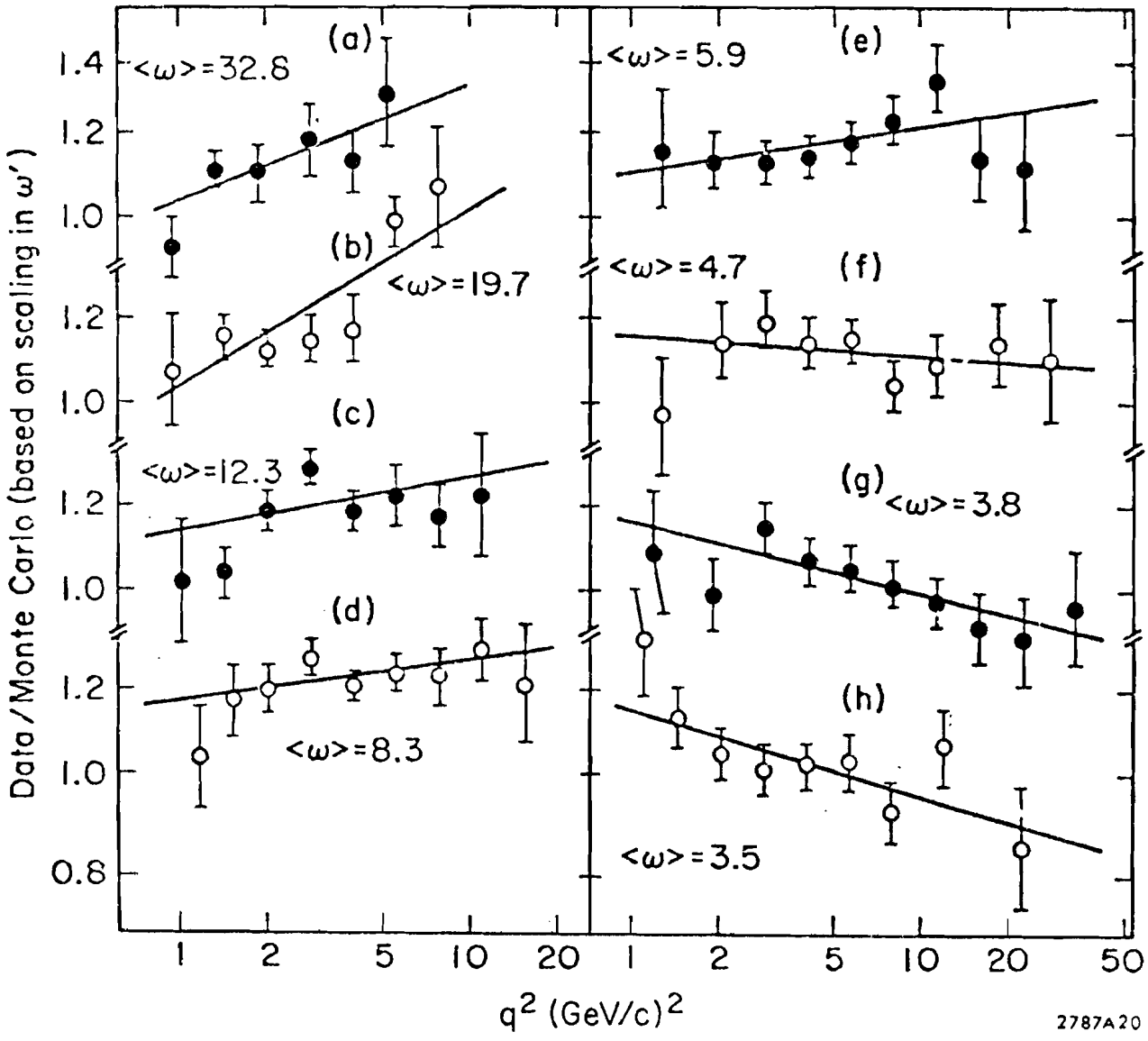
(a)
<ω>=32.8
(b)
<ω>=19.7
(c)
<ω>=12.3
(d)
<ω>=8.3
(e)
<ω>=5.9
(f)
<ω>=4.7
(g)
<ω>=3.8
(h)
<ω>=3.5
Data/Monte Carlo (based on scaling in ω')
q² (GeV/c)²
2787A20

Fig. 63.--The q^2-dependence of the two nucleon structure functions νW_2^p and $2MW_1^p$ for several values of ω, as measured in ep scattering at SLAC.

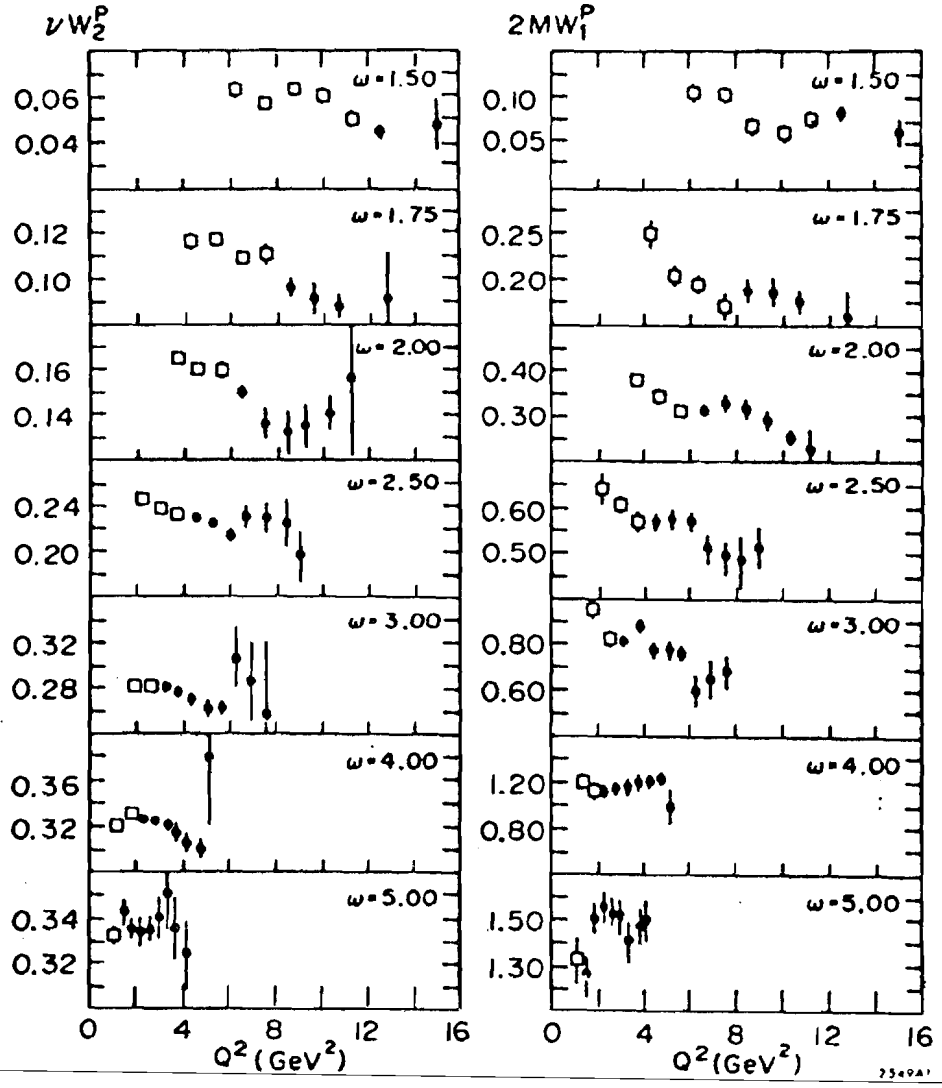
νW2P
2MW1P
ω=1.50
ω=1.75
ω=2.00
ω=2.50
ω=3.00
ω=4.00
ω=5.00
0.06
0.04
0.12
0.10
0.16
0.14
0.24
0.20
0.32
0.28
0.36
0.32
0.34
0.32
0.10
0.05
0.25
0.20
0.40
0.30
0.60
0.50
0.80
0.60
1.20
0.80
1.50
1.30
0
4
8
12
16
Q2 (GeV2)
Q2(GeV2)

Fig. 64.--νW_2 as a function of the Bjorken scaling variable ω. The three data points plotted with open circles have average q^2 values less than 1 $(GeV/c)^2$.

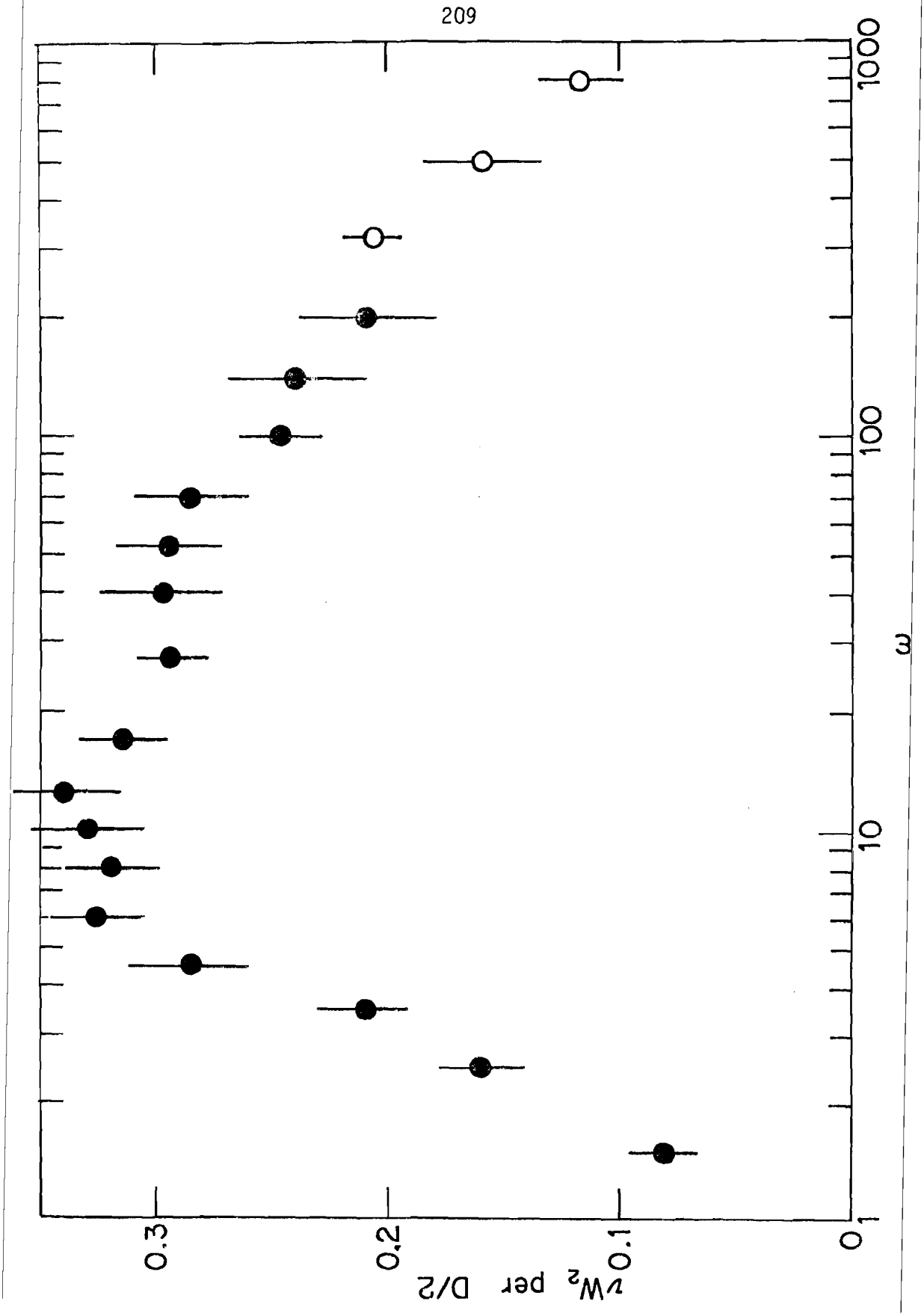
0.3
0.2
0.1
0
1000
100
10
1
ω
νW_2 per D/2

Fig. 65.--νW_2 as a function of the Feynman scaling variable $x = 1/\omega$.

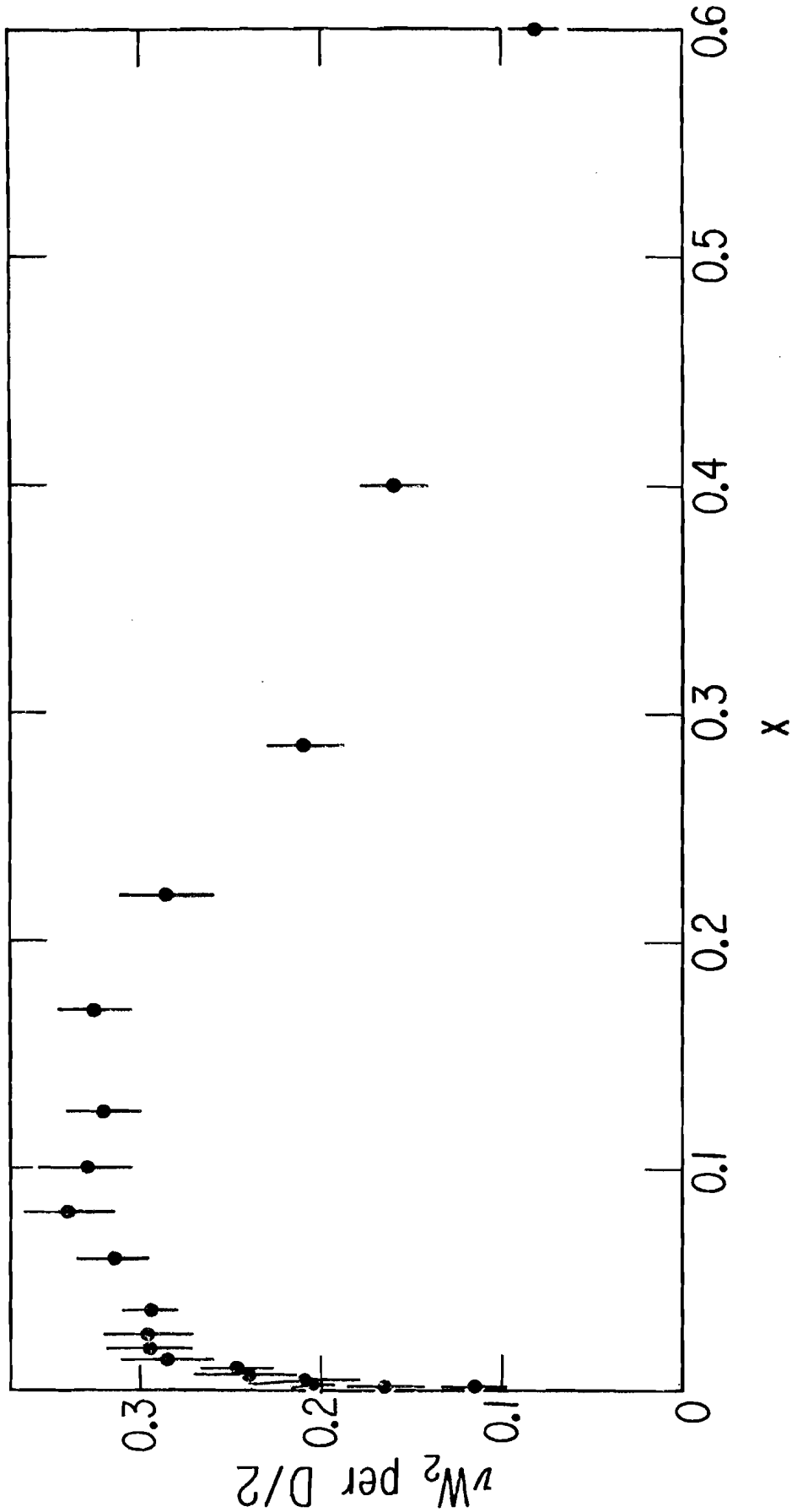
0.6
0.5
0.4
0.3
0.2
0.1
0
x
0.3
0.2
0.1
νW_2 per D/2

Fig. 66.--The predicted behavior of νW_2 as a function of x' in the Kuti-Weisskopf model. The model is fitted to electron scattering data from SLAC.

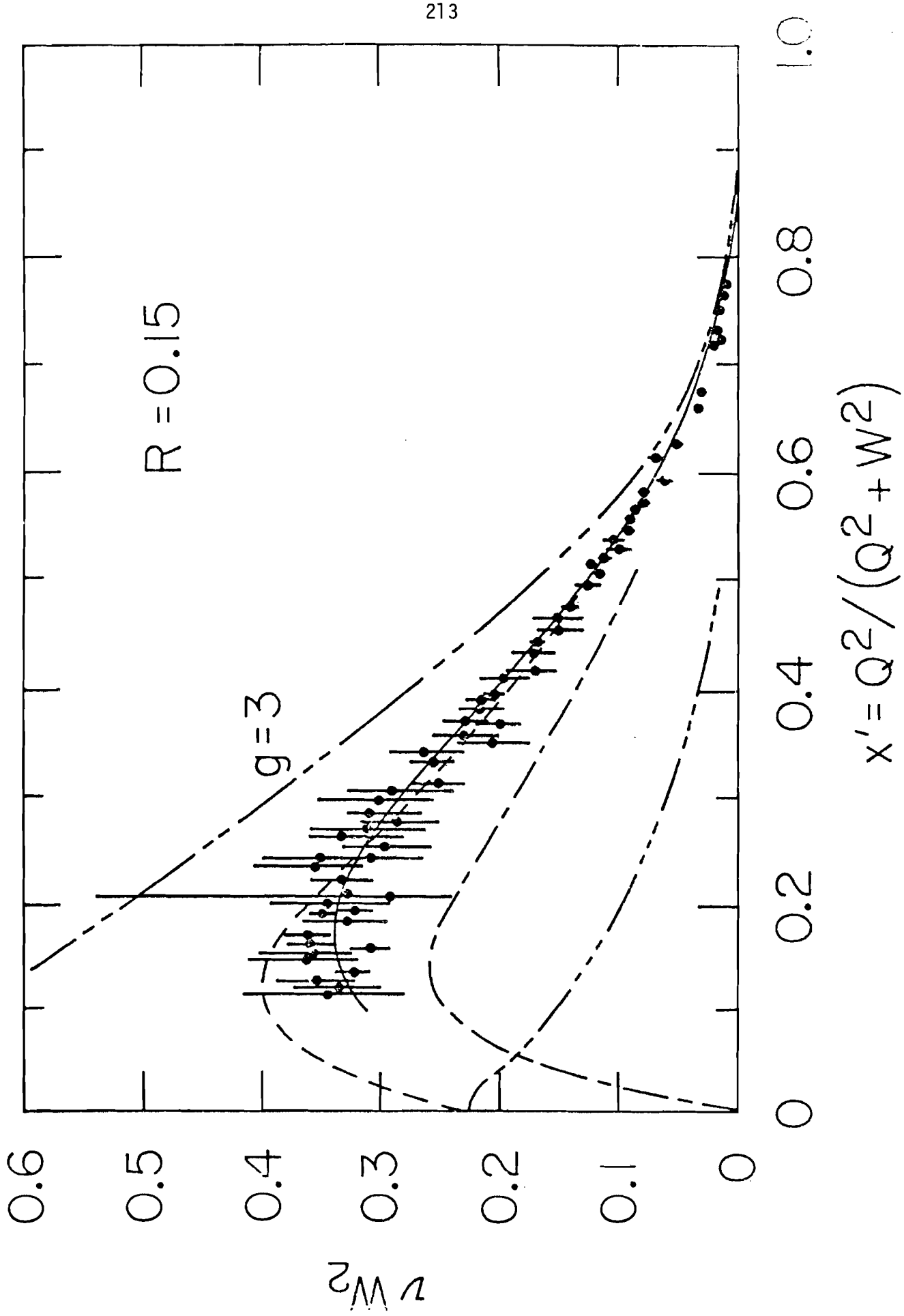
R=0.15
g=3
νW_2
$x' = Q^2/(Q^2+W^2)$
0
0.1
0.2
0.3
0.4
0.5
0.6
0.2
0.4
0.6
0.8
1.0

Fig. 67.--νW_2 as a function of x in the model of Alterelli, Cabbibo, Maiani, and Petronzio. In the model, each of the three constituent quarks, which make up the nucleon, is itself a complex object, made up of point-like partons and neutral gluons.

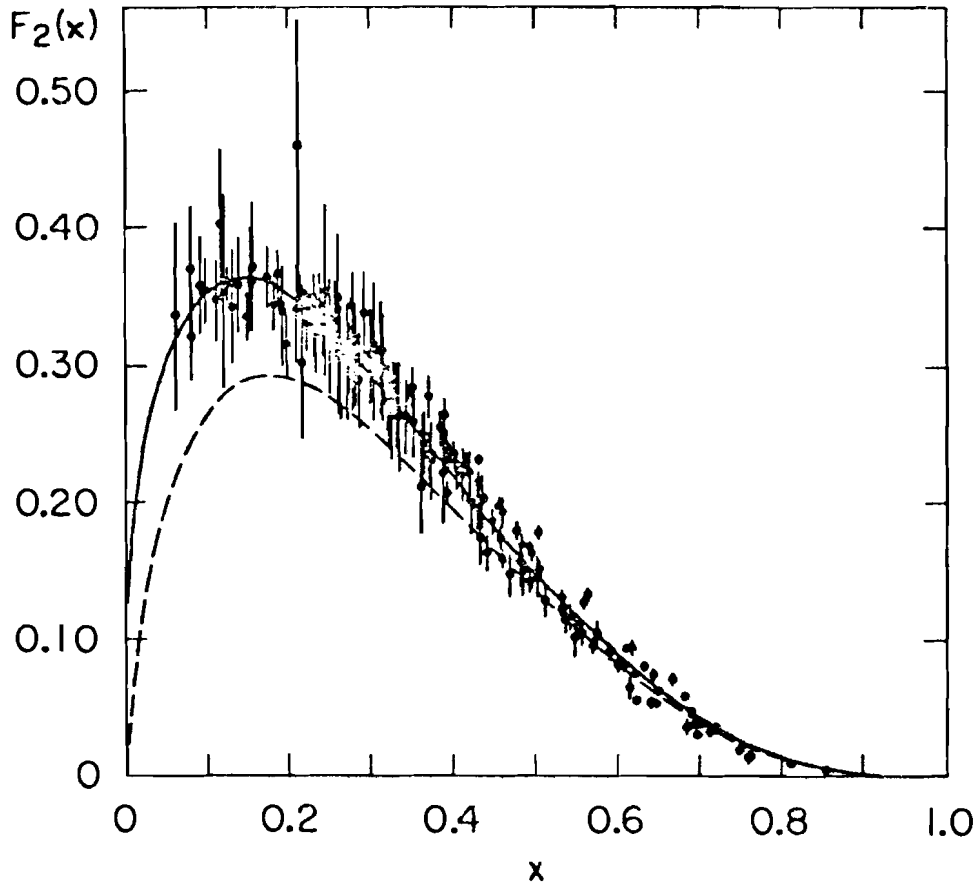
$F_2(x)$
0.50
0.40
0.30
0.20
0.10
0
0
0.2
0.4
0.6
0.8
1.0
x

Fig. 68.--A parton model fit to νW_2 from deuterium by Barger, showing the relative contributions of the valence quarks and the sea of quark-antiquark pairs.

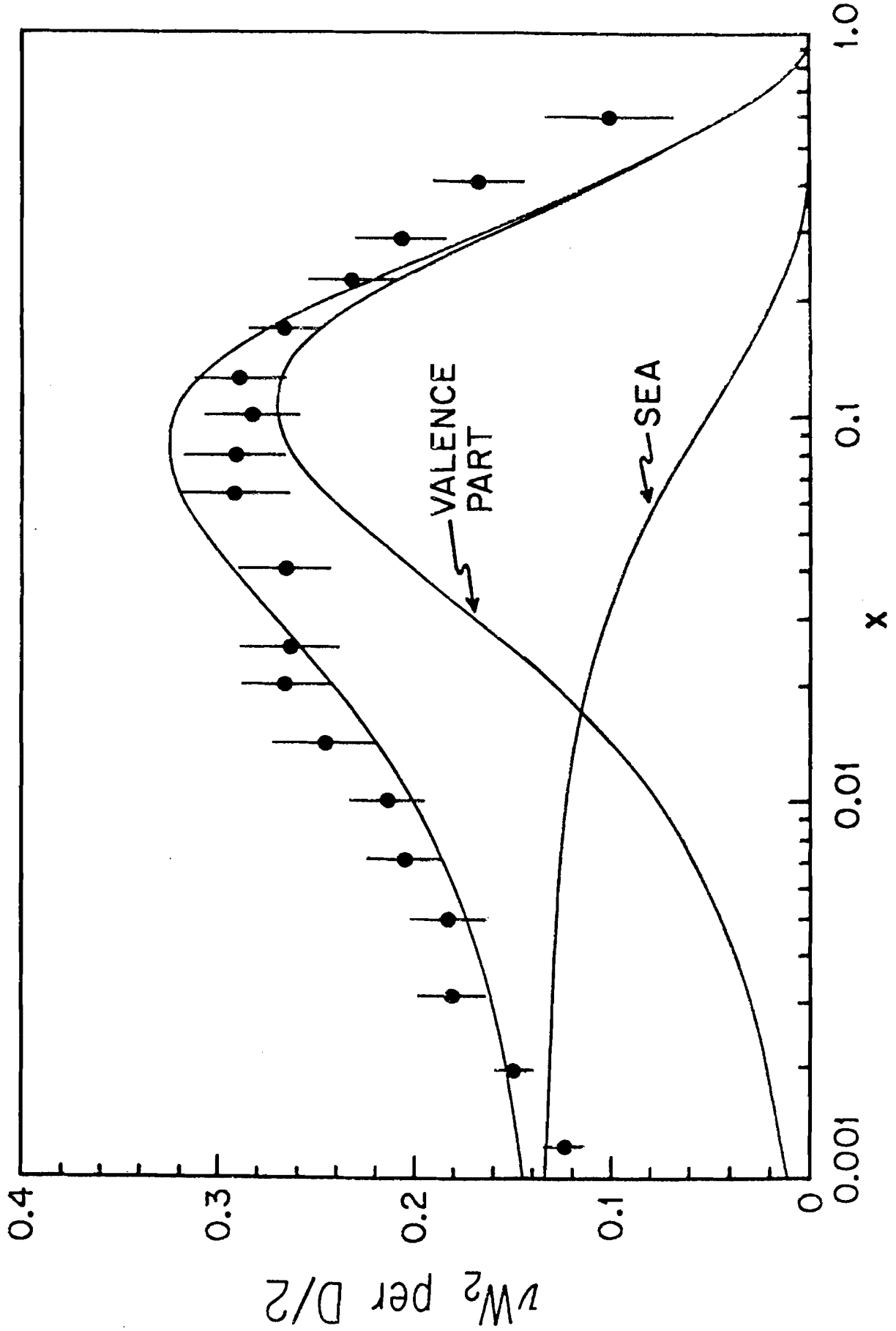
νW_2 per D/2
0.4
0.3
0.2
0.1
0
0.001
0.01
0.1
1.0
x
VALENCE PART
SEA

Fig. 69.--A parton model fit to recent neutrino scattering data from Fermilab.

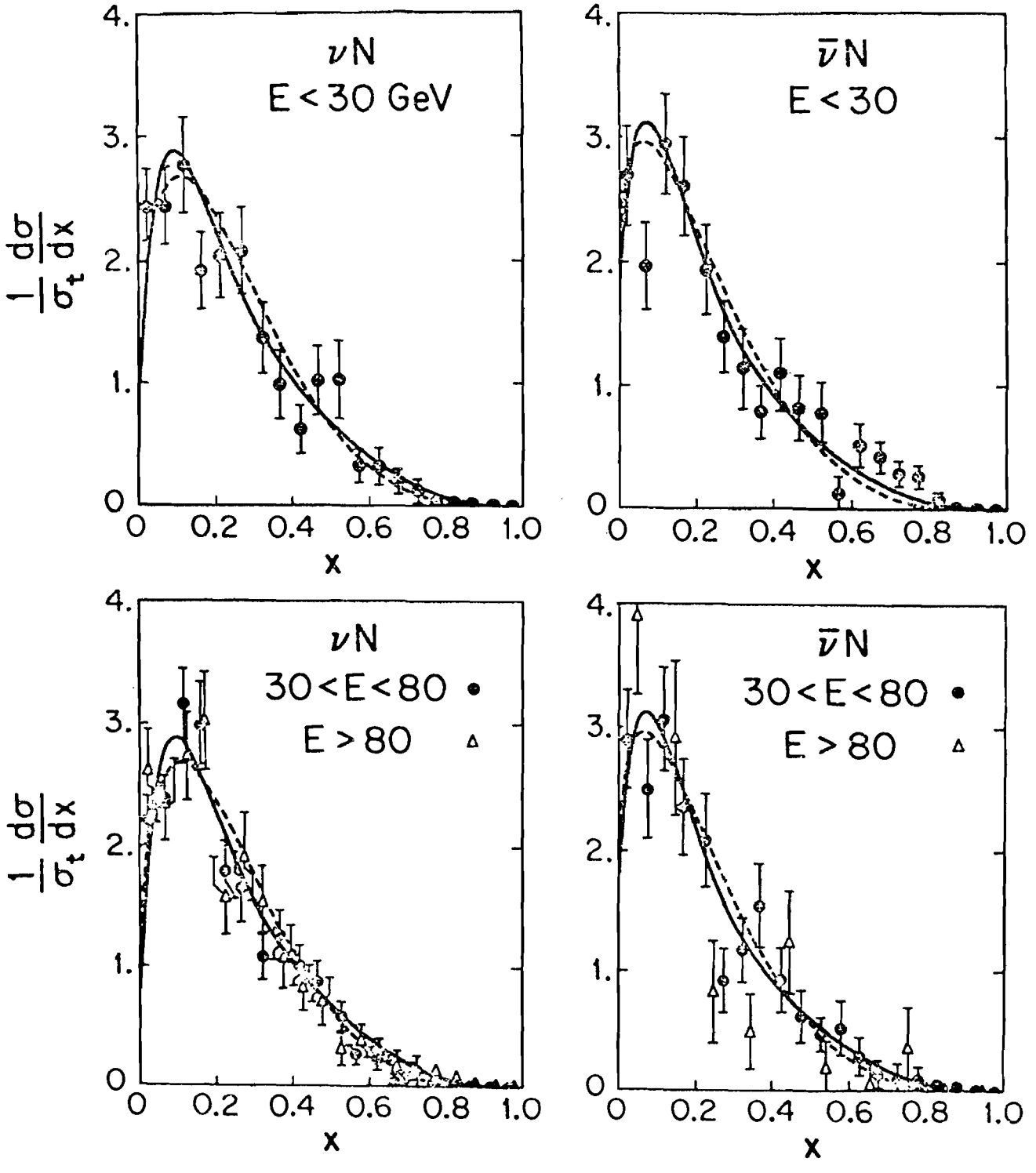
νN
E < 30 GeV
ν̄N
E < 30
νN
30 < E < 80 •
E > 80 △
ν̄N
30 < E < 80 •
E > 80 △
1/σt dσ/dx
x
0
0.2
0.4
0.6
0.8
1.0
1.
2.
3.
4.

Fig. 70.--The total photoabsorption cross section for protons, $\sigma_{\gamma p}(K)$, as a function of the photon energy, K. The solid line is a Regge model fit including the pomeron, P, and the ordinary Regge trajectories f,A_2.

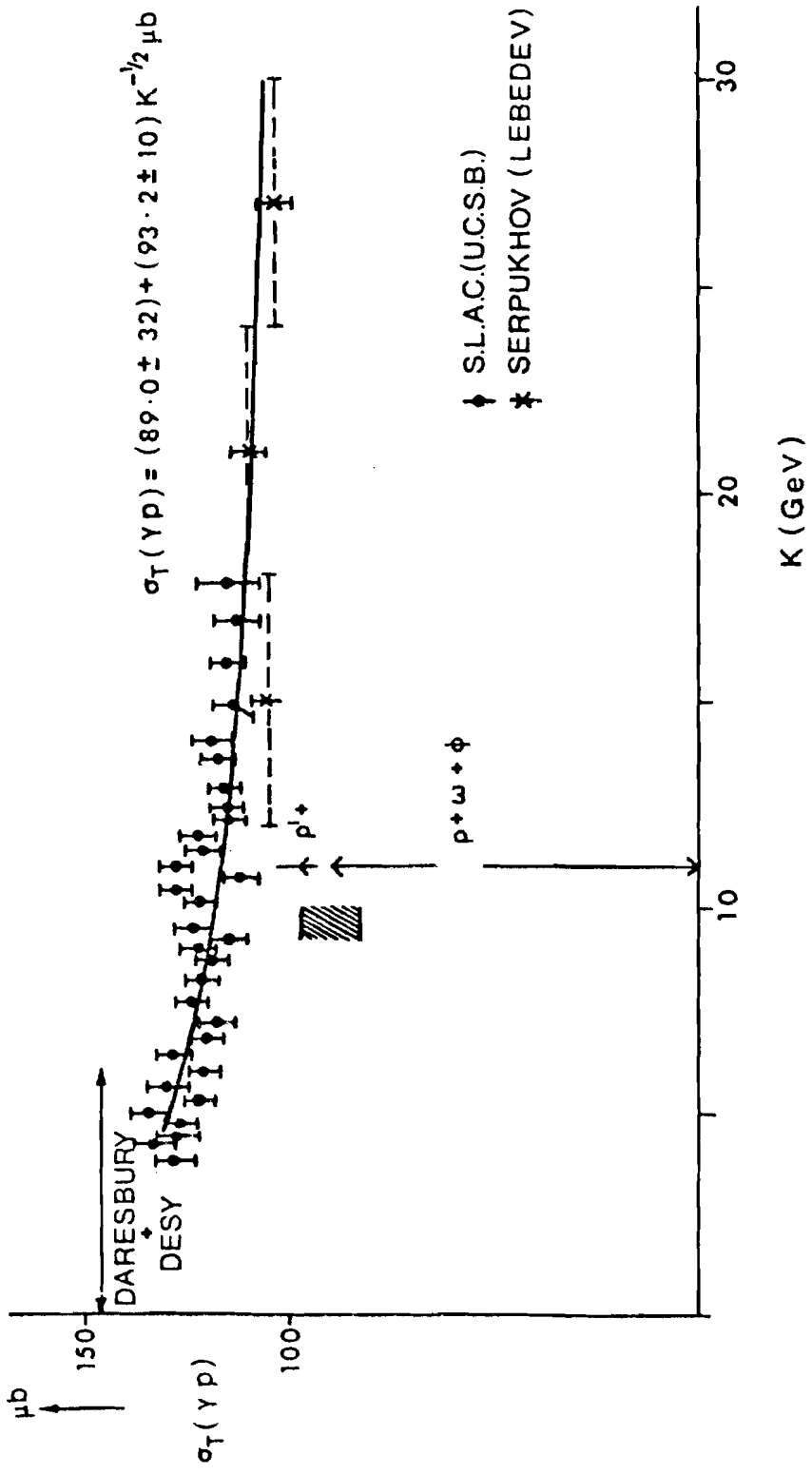
$\sigma_T(\gamma p) = (89.0 \pm 32) + (93.2 \pm 10)\, K^{-1/2}\ \mu b$
S.L.A.C.(U.C.S.B.)
SERPUKHOV (LEBEDEV)
DARESBURY
DESY
ρ'
$\rho + \omega + \phi$
$\sigma_T(\gamma p)$
μb
150
100
10
20
30
K (GeV)

Fig. 71.--A Regge model fit to νW_2 including a fixed pole in the forward Compton scattering amplitude. The data is from electron scattering experiments at SLAC.

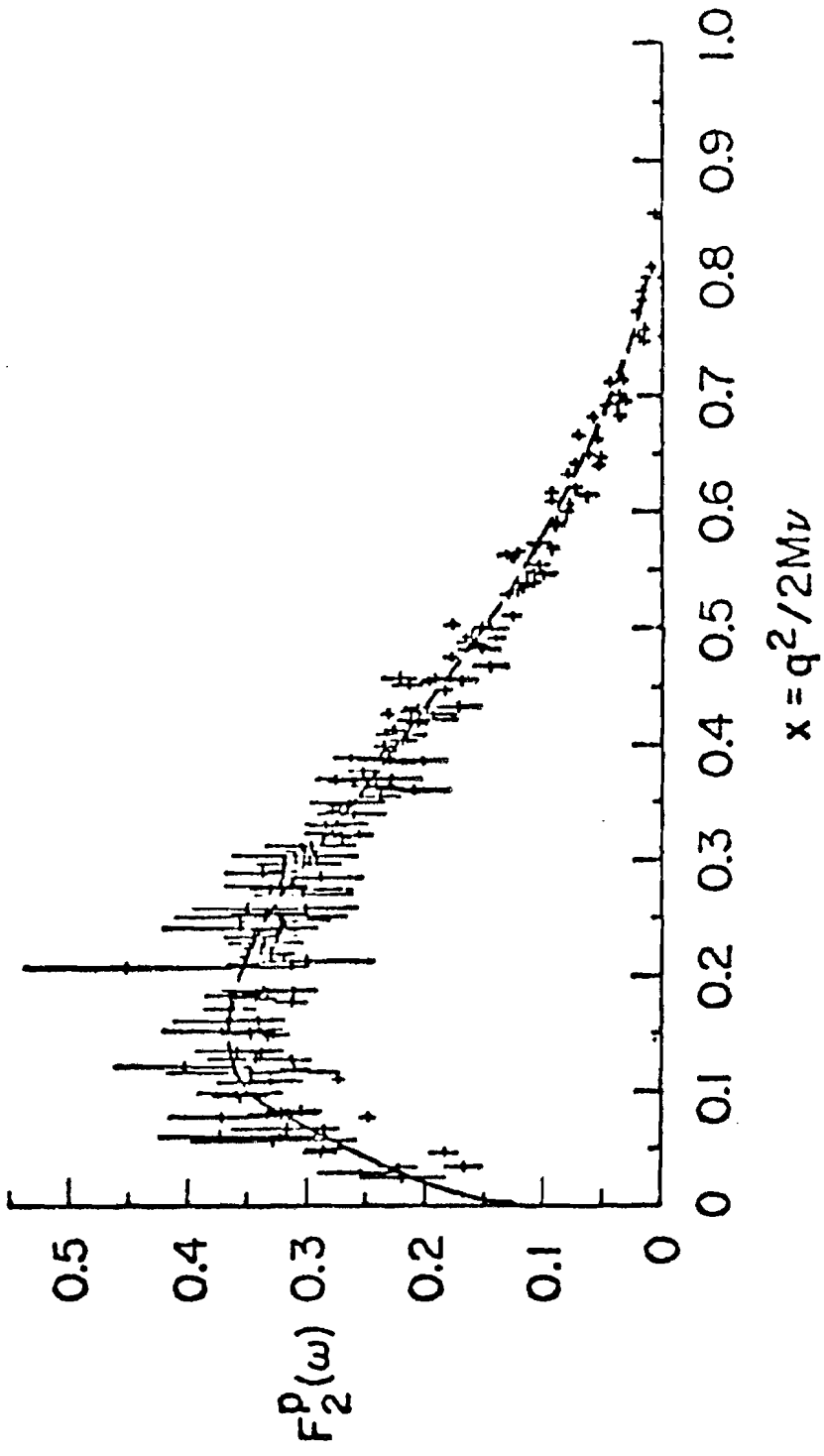
0.5
0.4
0.3
0.2
0.1
0
$F_2^p(\omega)$
0
0.1
0.2
0.3
0.4
0.5
0.6
0.7
0.8
0.9
1.0
$x = q^2/2M\nu$

Fig. 72.--νW_2 as a function of q^2 for all values of ω, as measured in electron scattering at SLAC.

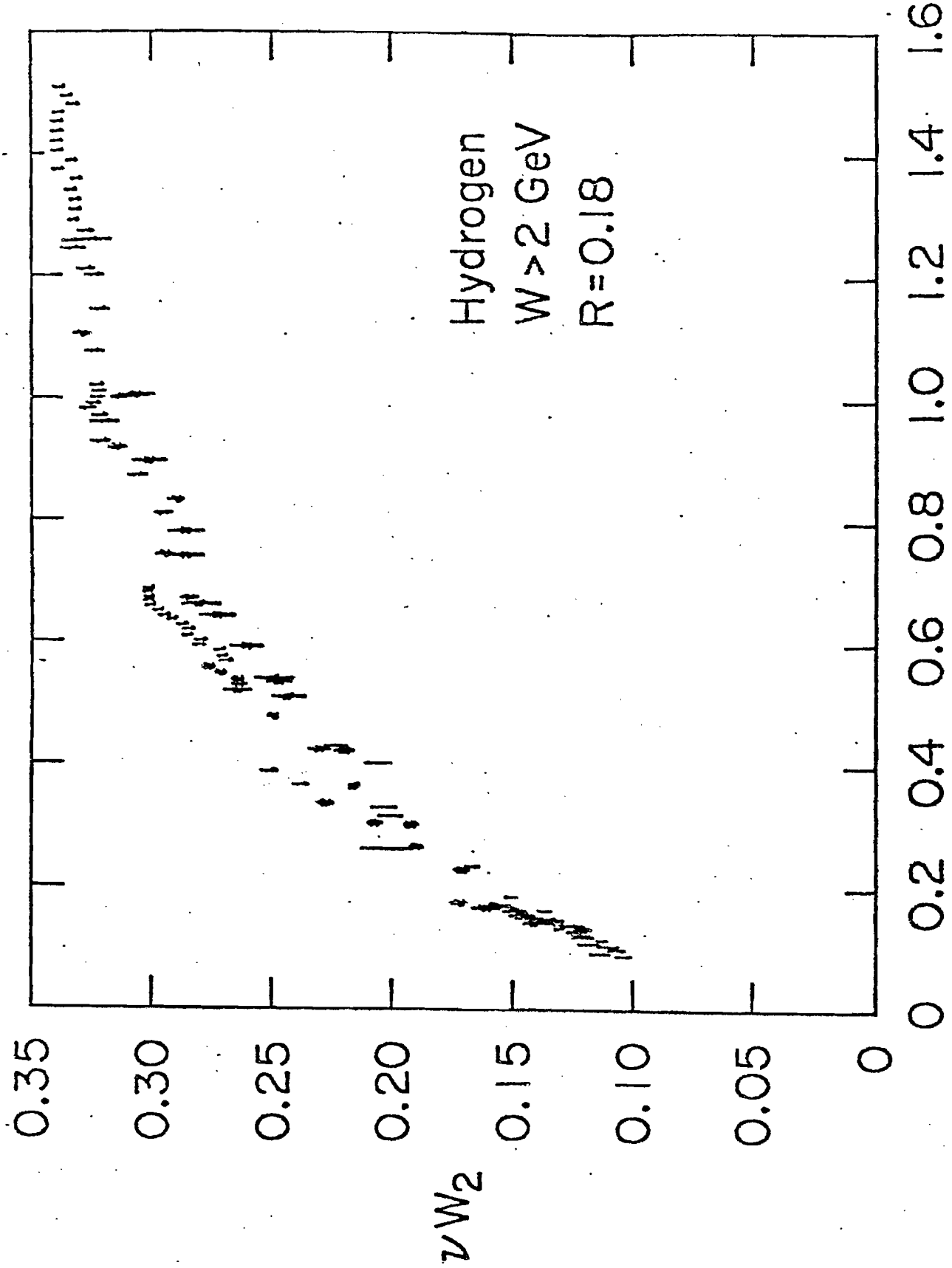
Hydrogen
W > 2 GeV
R=0.18
νW2
q2 (GeV/c)2
0.35
0.30
0.25
0.20
0.15
0.10
0.05
0
0.2
0.4
0.6
0.8
1.0
1.2
1.4
1.6

Fig. 73.--νW_2 as a function of q^2 for data in the deep inelastic region, $90 \leq \nu \leq 130$ GeV.

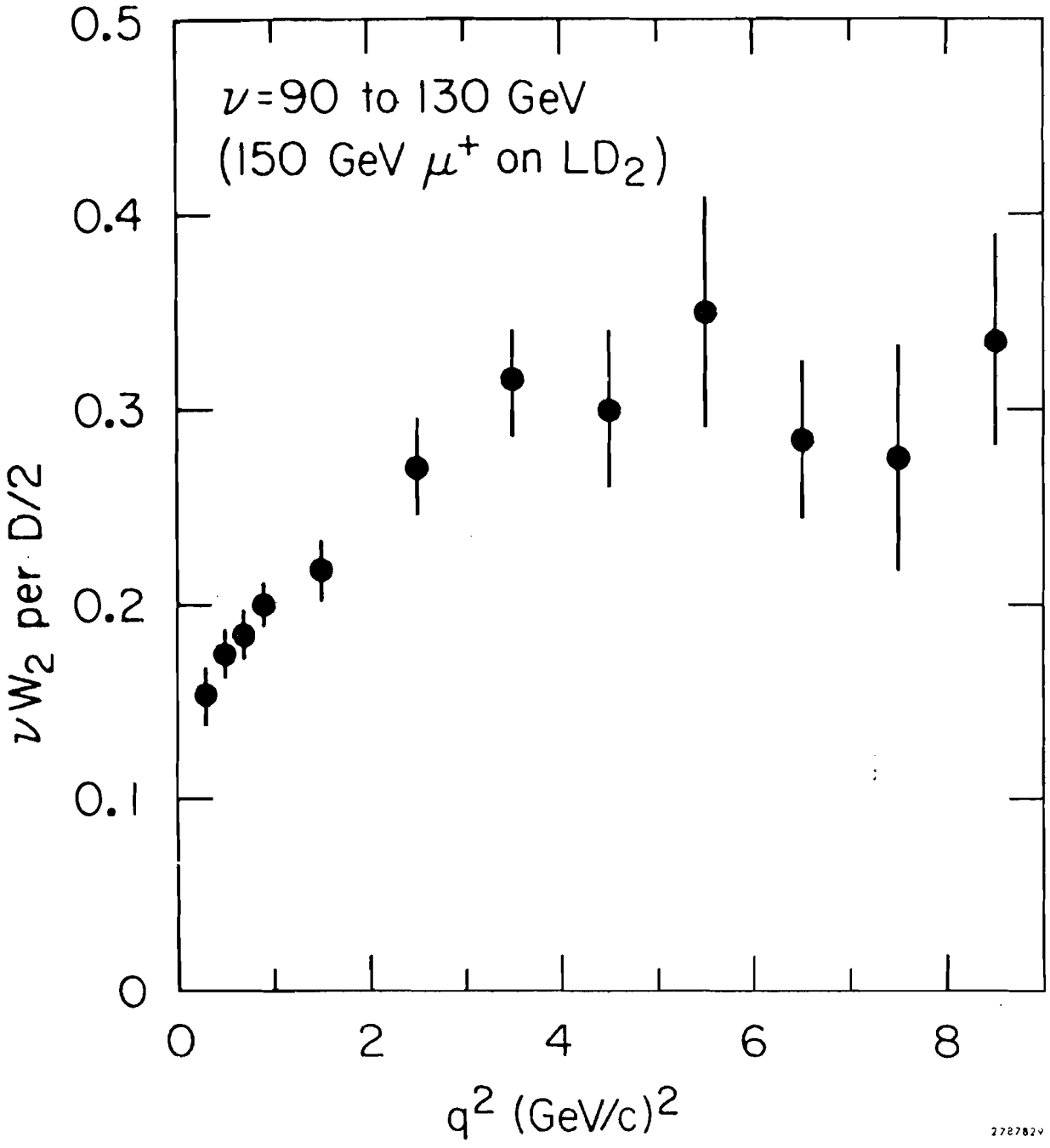
0.5
0.4
0.3
0.2
0.1
0
ν=90 to 130 GeV
(150 GeV μ^+ on LD_2)
νW_2 per D/2
0
2
4
6
8
q^2 (GeV/c)^2
2787B2v

Fig. 74.--νW_2 as a function of q^2 for all values of ω, as measured with muons scattering from an iron target at Fermilab.

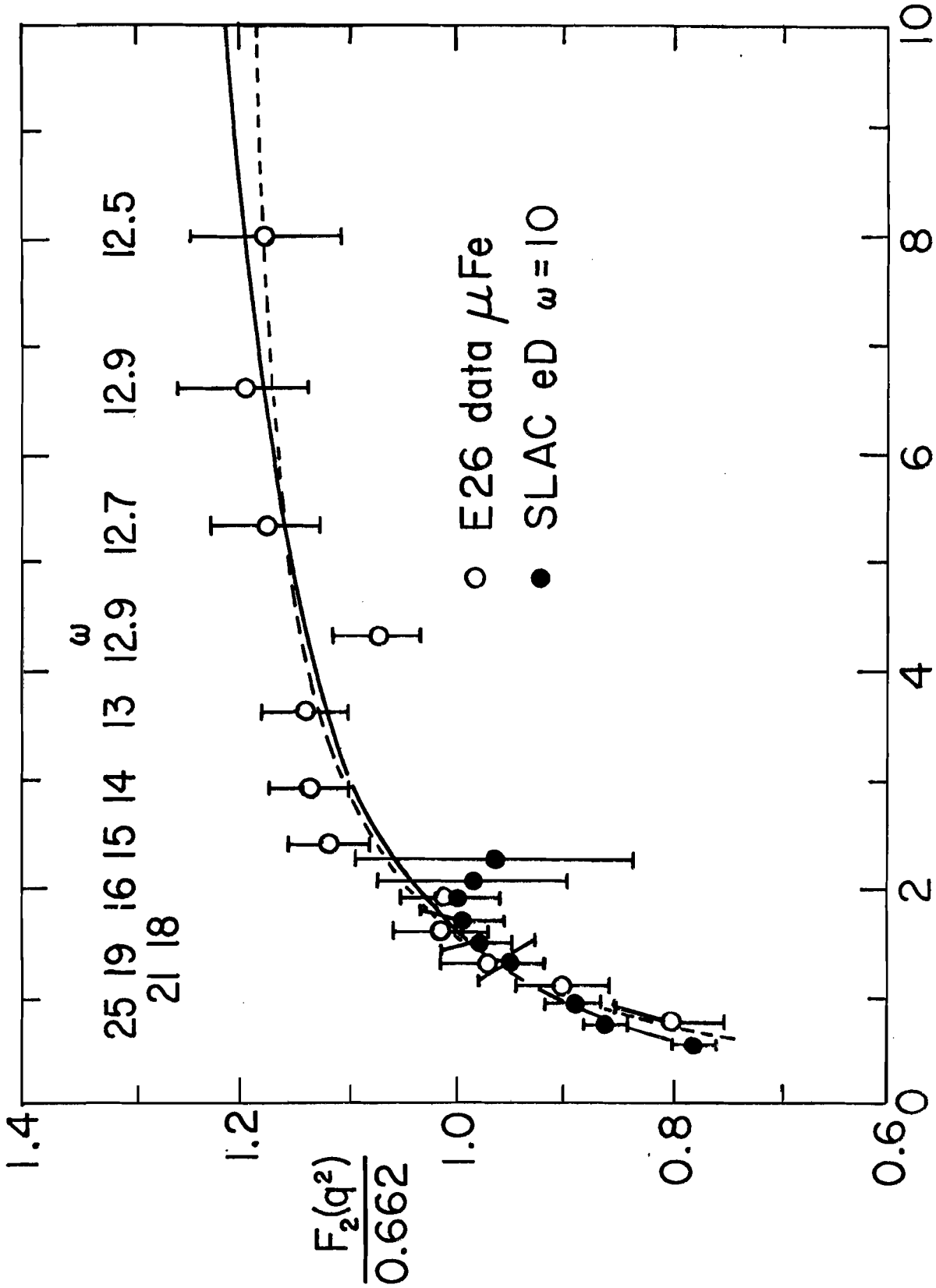
1.4
1.2
1.0
0.8
0.6
0
2
4
6
8
10
q^2 (GeV)^2
$\frac{F_2(q^2)}{0.662}$
ω
25 19 16 15 14 13 12.9 12.7 12.9 12.5
21 18
○ E26 data μFe
● SLAC eD ω=10

Fig. 75.--Comparison of νW_2 with the generalized vector dominance model of Devenish and Schildknecht. The solid line is a fit to the SLAC 4° data of Stein et at.[53]

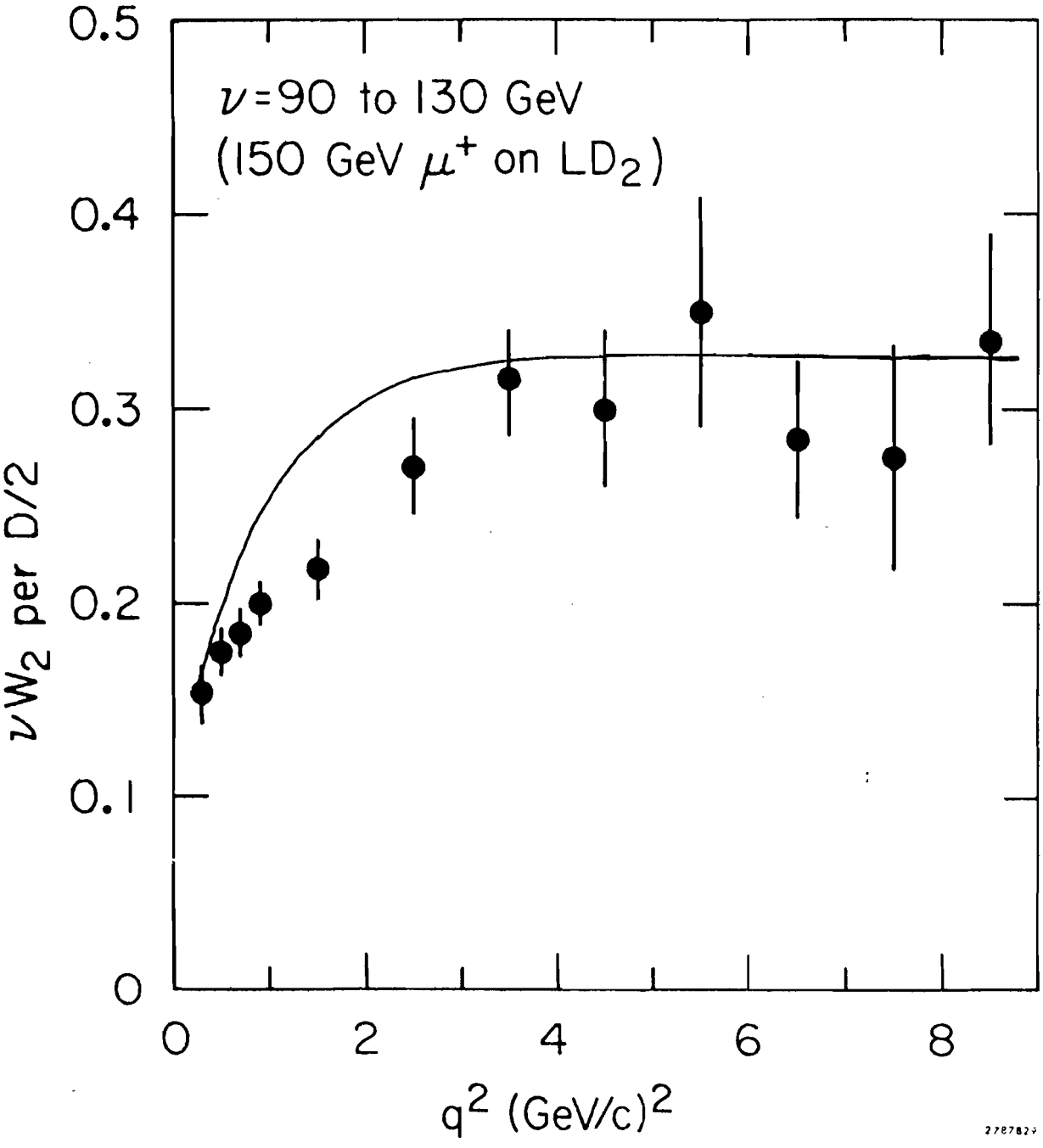
0.5
0.4
0.3
0.2
0.1
0
ν=90 to 130 GeV
(150 GeV μ^+ on LD_2)
νW_2 per D/2
0
2
4
6
8
q^2 (GeV/c)^2

CHAPTER VI

INCLUSIVE HADRON DISTRIBUTIONS

In this chapter we present the results on the inclusive muoproduction of hadrons in scattering 150 GeV μ^+ from a liquid deuterium target.[75] We detect most of the charged hadrons produced in the photon fragmentation region, i.e., hadrons which go forward in the virtual-photon-nucleon center of mass system. Hadrons produced in the target fragmentation region are not detected. The single particle inclusive cross section for producing these hadrons is studied as a function of transverse and longitudinal momentum, rapidity, etc., and as a function of q^2 and ν, the four-momentum transfer-squared and energy of the virtual photon. Results are compared with the distributions of hadrons produced in e^+e^- annihilation and in inelastic neutrino scattering.

As discussed in Chapter V, the observation of large point-like cross sections in inelastic lepton-nucleon scattering experiments and the scaling behavior of the nucleon structure functions has led to the notion that the nucleons are composed of point-like objects called quarks or partons.[19,23] However, attempts to theoretically justify this intuitive picture have been difficult, and many questions remain unanswered. One puzzling result within the framework of this model is that nearly half the energy of the virtual photon must be carried away by neutral constituents of the nucleon. An even more puzzling fact is that these point-like objects have never been observed experimentally. This raises the question of whether they really exist, or

only provide a convenient language to describe the actual processes taking place in lepton-nucleon scattering. One would hope that by studying the final state hadrons that we could gain some insight into the physics underlying the remarkable success of these models.

Besides the above mentioned reasons, interest in the final state hadrons produced in lepton-nucleon scattering has been stimulated by the hypotheses of Feynman scaling[19] and limiting fragmentation[32] in hadron-hadron interactions. This scale invariance says that the invariant cross section $Ed^3\sigma/d^3p$ for the process $a + b \rightarrow c +$ anything, approaches a limit at high energies $\sqrt{s}$, which is finite and independent of s:

$$\lim_{s\to\infty} E\frac{d^3\sigma}{d^3p} = \lim_{s\to\infty} f(p_{\parallel},p_{\perp},s) = f(x_{\parallel},p_{\perp}) \quad . \tag{6.1}$$

Here $x_{\parallel}$ is the reduced longitudinal momentum, $p_{\parallel}^{cm}/p_{max}^{cm}$, with $p_{\parallel}^{cm}$ being the longitudinal momentum of particle c in the center of mass system of particles a and b, $p_{\perp}$ its transverse momentum, and p_{max}^{cm} its maximum possible momentum in the center of mass system. Considerations about fragmentation have led to the picture that the fragmentation products of the projectile should be independent of the target and vice versa. The projectile products would appear at positive values of $x_{\parallel}$, those of the target at negative values. Muon and electron scattering experiments offer the unique opportunity to investigate these theoretical ideas by using the virtual photon as the projectile particle. Very few other particles are as well known.

Invariant Hadron Cross Section

When one is trying to characterize the final hadronic state produced in inelastic muon-nucleon scattering, it is convenient to think in terms of the

corresponding virtual photoproduction process, $\gamma_v + N \rightarrow$ hadrons, as shown in Figure 76. The interaction of the muon with the nucleon is mediated by a single virtual photon.[2] From the incident and final muon momenta, we can determine the mass, $-q^2$, energy, ν, and direction of the virtual photon, and thus regard the muon as defining a beam of virtual photons. The one-photon exchange allows us to view the hadrons as being virtually photoproduced.

The total virtual photoproduction cross section for hadrons, $\sigma_\gamma^{total}(q^2,\nu)$, at a given q^2 and ν can be related to the inelastic muon cross section by assigning a flux, $\Gamma_T(q^2,\nu)$, to the virtual photon:

$$\sigma_\gamma^{total}(q^2,\nu) = \frac{1}{\Gamma_T(q^2,\nu)} \frac{d^2\sigma_\mu(q^2,\nu)}{dq^2 d\nu} \quad , \tag{6.2}$$

where $\Gamma_T(q^2,\nu)$, as defined by Hand,[18] is given by

$$\Gamma_T(q^2,\nu) = \frac{\alpha}{2\pi^2} \left(\frac{K}{q^2}\right)\left(\frac{E'}{E}\right)\frac{1}{1-\varepsilon}\left(\frac{\pi}{PP'}\right) \quad , \tag{6.3}$$

with ε the virtual photon polarization. The invariant cross section for producing a hadron h of momentum $\vec{p}_h$ and energy E_h in the phase space volume $d^3\vec{p}_h$ for the inclusive reaction $\gamma_v + N \rightarrow h + X$ can be written as

$$E_h \frac{d^3\sigma_\gamma(q^2,\nu)}{d^3\vec{p}_h} = \frac{E_h}{\Gamma_T(q^2,\nu)} \frac{d^6\sigma_\mu(q^2,\nu)}{dq^2 d\nu d^3\vec{p}_h} \quad . \tag{6.4}$$

It is convenient to normalize the invariant hadron cross section to the total virtual photoproduction cross section:

$$\frac{1}{\sigma_\gamma^{total}(q^2,\nu)} E_h \frac{d^3\sigma_\gamma(q^2,\nu)}{d^3\vec{p}_h} = \frac{1}{\sigma_\gamma^{total}(q^2,\nu)} \frac{E_h}{\Gamma_T(q^2,\nu)} \frac{d^6\sigma_\mu}{dq^2 d\nu d^3\vec{p}_h} \quad . \tag{6.5}$$

The above expression represents the probability of producing hadrons in the invariant phase space volume $d^3\vec{p}_h/E_h$ per scattered muon.

The virtual photoproduction of hadrons is most easily described in terms of kinematic variables defined relative to the direction of the incident virtual photon, γ_v. The hadron azimuthal angle, ϕ, is measured relative to the muon scattering plane. The transverse momentum of the hadron relative to the virtual photon is denoted by $p_\perp$. The longitudinal component of the hadron momentum is denoted by $p_\parallel$. The square of the total energy, s, in the virtual-photon-nucleon center of mass is given by:

$$s = W^2 = M^2 + 2M\nu - q^2 \quad . \tag{6.6}$$

Using these variables, the invariant hadron cross section takes the form

$$f(q^2,s,p_\parallel,p_\perp,\phi) \equiv 2E_h \frac{d^3\sigma_\gamma(q^2,s)}{dp_\parallel dp_\perp{}^2 d\phi} \quad . \tag{6.7}$$

(f is sometimes called the invariant structure function.) We can also consider the reaction in the virtual-photon-nucleon center of mass. Here it is convenient to use the reduced longitudinal momentum, $x_\parallel$, to express the invariant cross section as:

$$f(q^2,s,x_\parallel,p_\perp,\phi) = \frac{2E_h^{cm}}{p_{max}^{cm}} \frac{d^3\sigma_\gamma(q^2,s)}{dx_\parallel dp_\perp{}^2 d\phi} \quad , \tag{6.8}$$

where E_h^{cm} is the hadron energy in the center of mass. Several other variables and forms of the invariant cross section have also been used. For example, one useful variable is ξ, the reduced rapidity as suggested by Van Hove,[76]

$$\xi = \frac{y - y_{target}}{y_{projectile} - y_{target}} \quad , \tag{6.9}$$

where y is the longitudinal rapidity defined by

$$y = \tfrac{1}{2}\ell n \left[\frac{E_h + p_{\|}}{E_h - p_{\|}}\right] \quad . \tag{6.10}$$

Other commonly used variables and forms of the invariant cross section are listed in Table 3.

As can be seen from the myriad of variables used in parameterizing the invariant cross section, one of the difficulties is how to present the data. The structure function a priori depends on several variables. For this study, we consider only the invariant cross section as a function of one variable at a time, averaging the other variables over their allowable kinematic ranges. For example, averaging over azimuthal angle and integrating over $p_\perp{}^2$ gives the normalized structure function $F(x_{\|})$ often found in the literature:

$$F(x_{\|}) = \int_0^{2\pi} d\phi \int_0^{\infty} dp_\perp{}^2 \frac{1}{\sigma_\gamma^{total}(q^2,s)} \frac{E_h^{cm}}{\pi p_{max}^{cm}} \frac{d^3\sigma_\gamma(q^2,s)}{dx_{\|} dp_\perp{}^2 d\phi} \quad . \tag{6.11}$$

Evaluation of the Invariant Cross Section

In this section we describe the procedures used to evaluate the invariant hadron cross section from the individually detected hadrons in each

inelastic muon scattering event. We only discuss the calculation of the single particle inclusive cross section, as defined in the last section. Two-particle correlations are not considered. Even though there may be several particles in the final state, we treat each hadron separately, summing over all particles, to produce the single particle distributions.

Since there was no means for specific particle identification (we could not identify pions, kaons, etc.) in the muon spectrometer, we have assumed that all hadrons are pions. That is, in calculating a hadron's energy, E_h, from its measured three-momentum, $\vec{p}_h$, we have used the pion mass, m_π. The hadron momentum was calculated by assuming a cylindrically symmetric, hard-edged model for the magnetic field of the Chicago Cyclotron. The calculation is exactly the same as that described for the scattered muon in Chapter IV, and will not be discussed here.

The normalized invariant hadron cross section was evaluated in a specified (q^2,ν) region according to the following formula:

$$\frac{1}{\sigma_\gamma^{total}} E_h \frac{d^3\sigma_\gamma}{d^3\vec{p}_h} = \frac{\sum^{Hadrons} \frac{E_h}{\Gamma_T(q^2,\nu)} \left(\frac{d^6\sigma_\mu}{dq^2 d\nu d^3\vec{p}_h} \right)^{exp} \delta_R^{inelastic}(q^2,\nu)}{\sum_{\mu'} \frac{1}{\Gamma_T(q^2,\nu)} \frac{d^2\sigma}{dq^2 d\nu}} . \quad (6.12)$$

The denominator is simply the total virtual photoabsorption cross section, $\sigma_\gamma^{total}(q^2,\nu)$ evaluated over the specified (q^2,ν) region. The numerator is a sum of the individual hadron contributions to the invariant cross section, including a factor, $\delta_R^{inelastic}(q^2,\nu)$, to take into account the radiative corrections to the inelastic muon scattering cross section. In order to obtain reasonable statistics, the above expression was evaluated over fairly large (q^2,ν) regions.

The contribution of each hadron to the invariant cross section was individually corrected for the acceptance of the spectrometer and for linkage and counter efficiencies. These corrections are discussed below. The inelastic radiative corrections, $\delta_R^{Inelastic}(q^2,\nu)$ were evaluated for the particular (q^2,ν) value of each scattering event. The contribution of each hadron was then binned versus the different kinematic variables to produce the one-dimensional distributions.

Acceptance Corrections

The acceptance correction to the invariant hadron cross section is a product of two terms: the first is the acceptance of the spectrometer for the hadron, the other the acceptance for the scattered muon. Both factors must be taken into account. The invariant cross section, $E_h d^3\sigma_\gamma(q^2,\nu)/d^3\vec{p}_h$, is the cross section for producing a hadron in the invariant phase space volume d^3p_h/E_h, and a scattered muon at the given values of q^2 and ν.

The calculation of the muon acceptance, $A_\mu(q^2,\nu)$, was described in Chapter IV. For each scattering event, $A_\mu(q^2,\nu)$ was evaluated by performing a two-dimensional interpolation on a pre-calculated table of acceptance in q^2 and ν. The acceptance for each hadron was calculated individually in a manner similar to that for the scattered muon, except for two essential modifications. First, the hadrons are treated as being photoproduced by a beam of virtual photons. The momentum vector of each hadron was rotated around the direction of the virtual photon as it was tracked through the magnetic field of the Chicago Cyclotron. Secondly, the hadron acceptance was determined by the G and H hodoscopes located in front of the hadron absorber. The acceptance was calculated as the fraction of the cone which intersected these two hodoscopes and did not pass through the hole in the center for the muon beam.

Linkage and Counter Efficiency Corrections

In addition to acceptance corrections to the invariant hadron cross section, there were also linkage and counter efficiency corrections for the hadron and scattered muon. The scattered muon was required to fire elements of the G, H, M_v, and M_h hodoscopes downstream of the Cyclotron magnet, and to link in both the x- and y-views to tracks in the 1m X 1m MWPC's. Each hadron track was required to link in both the x- and y-views, and to fire elements of the G and H hodoscopes. These restrictions were necessary for several reasons. First, the requirement that the hadron fire elements of both the G and H hodoscopes helped to eliminate stale out-of-time tracks. The H hodoscope requirement was essential since its elements are arranged vertically and the Cyclotron magnet deflects charged particles in the horizontal plane. A simple G or a (G.or.H) requirement was not enough since the central elements of the G hodoscope were fired almost every trigger. The x-y linkage requirement also helped eliminate stale tracks that could be misidentified as in-time hadrons, especially in the central beam region of the downstream wire spark chambers. More importantly, the linkage requirement enabled us to determine the angles of the hadrons using the tracks in the 1m X 1m MWPC's. This gave more reliable measurements of the transverse and longitudinal components of the hadron momentum relative to the direction of the virtual photon.

Radiative Corrections

As discussed in Chapter IV, the muon can radiate a photon before or after scattering from the nucleon. These radiative processes can change the muon cross section considerably and must also be taken into account when evaluating the invariant hadron cross section. The procedure used for

calculating the radiative corrections to the muon inclusive cross section is applicable for the invariant hadron cross section with one minor modification. Since we have detected a hadron, only the radiative corrections to the inelastic muon cross section should be considered. There are no corrections for the radiative tails from elastic and quasi-elastic muon-nucleon scattering. The radiative corrections to the invariant hadron cross section were evaluated by calculating the ratio:

$$\delta_R^{Inelastic}(q^2,\nu) = \frac{\sigma_{Inelastic}(q^2,\nu)}{\sigma_{Inelastic\ Radiated}(q^2,\nu)} \quad , \qquad (6.13)$$

where $\sigma_{Inelastic\ Radiated}(q^2,\nu)$ is the inelastic muon cross section including radiative effects; $\sigma_{Inelastic}(q^2,\nu)$, the theoretical muon scattering cross section. The contribution of each hadron to the invariant cross section was then multiplied by the factor $\delta_R^{Inelastic}(q^2,\nu)$ evaluated at the q^2 and ν values of the scattered muon.

The radiative corrections produce one further complication to the evaluation of the invariant hadron cross section. As shown in Figures 77a and 77b, the emission of a photon before or after scattering from the nucleon changes the four-momentum of the virtual photon from its apparent value $\vec{q}$, as determined by the incident and scattered muon momenta, to $\vec{q}'$. In general, $\vec{q}$ and $\vec{q}'$ are along different directions as indicated in Figure 77c. In order to calculate the components of the hadron momentum with respect to the direction of the virtual photon correctly, this change in angle must be taken into account. This was done, according to a method given by Tsai,[77] by calculating the most probable angle, $\theta_{\vec{q}\vec{q}'}$, between the actual and apparent directions of the virtual photon and relating the hadron momentum to $\vec{q}'$.

Results and Discussion

In this section we present and discuss the results on the single particle inclusive distributions from deuterium. Table 4 summarizes the approximate kinematic ranges of the data for the different variables used to describe the one-dimensional hadron distributions. To study the q^2- and ν-dependence of the invariant hadron cross section, the distributions are presented for the three (q^2,ν) regions given in Table 5.

The $p_\perp{}^2$-Distributions

Figures 78 through 80 show the normalized invariant hadron cross section as a function of $p_\perp{}^2$ for the three different (q^2,ν) regions. We have fitted the data from each region to the form $e^{-bp_\perp{}^2}$. The results are given in Table 6.

Chou and Yang[32] have suggested that as q^2 becomes larger and the virtual photon gets further from the mass shell, we should observe an increase in the average $p_\perp{}^2$, or equivalently, a decrease in the slope of the $p_\perp{}^2$-distribution. For data in the deep inelastic region, $90 \leq \nu \leq 130$ GeV, there is a slight decrease in the value of the slope, b, as the q^2 region is increased from $0.3 \leq q^2 \leq 1.0$ $(GeV/c)^2$ to $1 \leq q^2 \leq 10$ $(GeV/c)^2$. Unfortunately because of limited statistics, the q^2 values are relatively small and the two regions do not have significantly different average q^2 values. Most of the data for $1 \leq q^2 \leq 10$ $(GeV/c)^2$ is clustered at q^2 values near 1.

The $x_\parallel$-Distributions

From the parton model[19] or the hypothesis of limiting fragmentation,[32] we anticipate that the final state hadron distributions should be a universal function of the reduced longitudinal momentum, $x_\parallel = p_\parallel^{cm}/p_{max}^{cm}$; where $p_\parallel^{cm}$ is

the component of hadron momentum parallel to the direction of the virtual photon in the $\gamma_v N$ center-of-mass system; and p^{cm}_{max}, its maximum possible momentum. In our muon experiment we only detect the forward-going charged hadrons with values of $x_{\parallel}$ greater than approximately 0.1. In the fragmentation model, these hadrons are the fragmentation products of the virtual photon. It is extremely interesting to compare the fragmentation of space-like photons in μN scattering with that of time-like photons in high energy e^+e^- annihilation. From the parton model we would expect the $x_{\parallel}$-distributions to be similar.

Figures 81 through 83 show the $x_{\parallel}$-distributions of the sum of positive and negative hadrons in the different (q^2,ν) regions. The solid lines drawn through the data are approximate least-square fits to the form $e^{-bx_{\parallel}}$. The values of the parameter b in the different (q^2,ν) regions are given in Table 7. The slope parameter b does not exhibit any significant q^2-dependence.

In Figure 84 we replot the numerical fit of the $x_{\parallel}$-distribution in the deep inelastic region, $90 \leq \nu \leq 130$ GeV and $1 \leq q^2 \leq 10$ $(GeV/c)^2$, together with the data from the reaction, $e^+ + e^- \rightarrow$ hadrons, measured at SPEAR.[78] It is interesting to observe that the $x_{\parallel}$-distribution of the hadrons produced by time-like photons exhibit somewhat more conspicuous q^2-dependence. However, its limiting distribution at a q^2 value of -25 $(GeV/c)^2$ agrees well with our measurement with space-like photons.

Apparently both space-like and time-like photons exhibit the same limiting fragmentation behavior. Results from a muon scattering experiment at ~14 GeV indicate similar behavior.[79]

The hadrons produced in high energy neutrino scattering at Fermilab[80] also show the same $x_{\parallel}$-distributions as in the reactions induced by virtual photons. Figure 85 shows a comparison of data from neutrino scattering

with that from our muon scattering experiment. The invariant cross sections are again the sum of positive and negative hadrons.

The Rapidity Distributions

One can also plot the invariant hadron cross section as a function of the longitudinal rapidity:

$$y = \tfrac{1}{2}\ell n \left[\frac{E_h + p_{\parallel}}{E_h - p_{\parallel}} \right] \quad . \tag{6.14}$$

The rapidity variable, y, is simply another way to parameterize the longitudinal momentum, and is more or less equivalent to $x_{\parallel}$. It does have the nice feature, however, that under a longitudinal Lorentz boost, $y \rightarrow y +$ constant. The rapidity distribution of hadrons in the $\gamma_v N$ center-of-mass system is identical to the rapidity distribution in the lab system, except for a constant displacement. Figures 86 through 88 show the rapidity distributions for three different (q^2,ν) regions.

There are several theoretical conjectures concerning the rapidity distribution of muoproduced hadrons. The most well known are those given by Feynman[81] and Bjorken.[82] As shown in Figure 89, for large ω values the photon fragmentation region is separated from the target fragmentation region. The width of the photon fragmentation region is proportional to $\ell n\ q^2$. The width of the central region (defined as $x_{\parallel}$ near 0) is proportional to $\ell n\ \omega$. If the scaling hypothesis strictly holds, we expect that the height of the central region, $\frac{d\sigma}{dy}$, to remain constant as s increases. The increase of center-of-mass energy should only make the central region wider, reflecting the increase of longitudinal phase space.

The rapidity distributions of our muoproduced hadrons show approximately

the same amount of variations in the central region (~15%) as that observed in pp collision at ISR.[33] The magnitude is consistent with the scaling violations observed in the muon inclusive cross section.

The Missing Mass and t-Distributions

It is interesting to examine the missing mass distribution and the corresponding t-distribution for the single detected hadron, h, in the reaction $\gamma_v + N \rightarrow h + X$. The missing mass, MM, is defined as the invariant mass of the hadronic state X:

$$\begin{aligned} MM^2 &= (P + q - p_h)^2 \\ &= W^2 + m_\pi{}^2 - 2E_\pi(M + \nu) + 2p_{||}\sqrt{q^2 + \nu^2} \quad . \end{aligned} \tag{6.15}$$

The four-momentum transfer-squared, t, to the state X is given by:

$$t = q^2 + m_\pi{}^2 - 2E_\pi\nu + 2p_{||}\sqrt{q^2 + \nu^2} \quad . \tag{6.16}$$

By considering the virtual photon as the incident beam, we can look at the invariant mass of the final state hadrons produced along with the single detected hadron.

The missing mass spectra for three different (q^2,ν) regions are shown in Figures 90 through 92. For data in the deep inelastic region, $90 \leq \nu \leq 130$ Gev, the distributions show a pronounced peak at high values of the missing mass. To some extent, the shape resembles the effective mass distribution of (n - 1) particles of an n-particle final state ($n \geq 4$), calculated from phase space alone. However, the mass distribution seems to be too sharply peaked at high missing mass to be simply phase space. For lower values of ν, $10 \leq \nu \leq 90$ GeV, (Figure 90) the peak at high missing mass is not so pronounced. Work is in progress to try to fit these distributions to a Triple Regge model proposed by Mueller.[38]

The t-distributions for the three (q^2,ν) regions are shown in Figures 93 through 95. Since the virtual photons cover a wide range of q^2 and ν, the cross sections are plotted against the difference $|t - t_{min}|$, rather than $|t|$, to adjust for the effect due to t_{min}; where t_{min} is the minimum four-momentum transfer-squared corresponding to the case where the hadron h is produced along the direction of the virtual photon:

$$t_{min} = -q^2 + m_\pi^2 - 2E_\pi\nu + 2p_h\sqrt{q^2 + \nu^2} \ . \qquad (6.17)$$

Unless corrected for this kinematic effect of a "broad band" photon beam, the distribution would be curved when plotted against t. The t-distributions in the three (q^2,ν) regions are exponential and can be represented by e^{bt}, with b ~0.8. By comparing the plots for different q^2 ranges, we see a slight decrease in the slope of the distributions as q^2 increases.

In Figure 96, the correlation between $x_\parallel$ of the detected hadron and its missing mass is shown. The large missing mass is strongly connected with detected hadrons which have small values of $x_\parallel$.

The p_n-Distribution

Unlike $p_\parallel$ and $p_\perp$, the component of hadron momentum normal to the scattering plane of the muon, p_n, is not affected by the radiative corrections. As shown in Figure 97, the "radiative correction" photon is always along the direction of the incident or outgoing muon. The virtual photon remains in the scattering plane, leaving p_n unaffected. This distribution is also interesting to look for the production of hadron jets, similar to those observed recently in e^+e^- annihilation at SLAC.[83] One of the predictions of the parton model for e^+e^- annihilation into hadrons is that at high enough

energy the hadrons should be produced in opposite-moving bursts called jets.[84] The annihilation into hadrons occurs through the decay of the virtual photon into a pair of constituent partons which subsequently decay into hadrons. The jet structure results from the final state hadrons maintaining the direction of the elementary constituents. At SLAC, evidence for jet structure was discovered by searching for an axis of hadron production which minimized the sum of squares of transverse momenta. The distribution of transverse momenta relative to this jet axis was found to be more sharply peaked than that expected from phase space alone, thus giving evidence for jets. The p_n-distribution is very similar to the "sphericity" distribution used to discover jets in e^+e^- annihilation. The production of back-to-back hadron jets in muon-nucleon scattering would appear at large positive and negative values of p_n. Figure 98 shows the p_n-distribution in the deep inelastic region, $90 \leq \nu \leq 130$ GeV, and $1 \leq q^2 \leq 10$ $(GeV/c)^2$. The average p_n is fairly small, approximately 250 MeV/c. We do not see any evidence for out-of-plane jet structure. When combined with the fact that there is also no large $p_\perp$ component as shown in Figure 79, we can conclude that there are no jets. Most of the hadrons produced in the photon fragmentation region are produced along the direction of the virtual photon. One can therefore view the virtual photon as the only jet in muon nucleon scattering.

Concluding Remarks

As we have learned during the past three decades, electron (and now muon) scattering experiments have consistently proved to be important sources of information on the structure of the nucleons. The virtual photon has been a powerful tool in unraveling the many complexities. We

used to think that high energy was synonymous with small distance. We have recently come to realize that this is not quite true. Even at the TeV range, the transverse momentum of the final state particles is still quite small. As we increase energy, the transverse distance to which we can probe is not as small as we had hoped. In the meantime, we have increased the longitudinal phase space tremendously. This results in high multiplicities and makes nature most difficult to untangle.

It is becoming apparent that electrons, muons, neutrinos, and virtual photons all behave very much like the bare particles we have indistinghishably named quarks or partons. They should all serve as the simplified tools to probe the nucleons. Hadron production in muon-nucleon scattering adds a new dimension to our study of nucleon structure. The experiment described in this thesis has only signaled its beginning.

TABLE 3

NOTATIONS AND FORMS OF THE INVARIANT HADRON

CROSS SECTION $f \equiv E \frac{d^3\sigma}{d^3\vec{p}}$

Notation	Variable	Definition
$\frac{d\sigma}{dp_\perp^2}$	$p_\perp^2$	$\frac{E}{\pi} \frac{d\sigma}{dp_\perp^2}$
$\frac{d\sigma}{dx_\parallel}$	$x_\parallel = \frac{p_\parallel^{cm}}{p_{max}^{cm}}$	$\frac{E^{cm}}{\pi p_{max}^{cm}} \frac{d\sigma}{dx_\parallel}$
$\frac{d\sigma}{dy}$	$y = \frac{1}{2}\ell n\left[\frac{E + p_\parallel}{E - p_\parallel}\right]$	$\frac{1}{\pi} \frac{d\sigma}{dy}$
$\frac{d\sigma}{d\xi}$	$\xi = \frac{y - y_{target}}{y_{proj} - y_{targ}}$	$\frac{1}{\pi(y_{proj} - y_{targ})} \frac{d\sigma}{d\xi}$
$\frac{d\sigma}{d(MM)}$	MM	$\frac{\sqrt{\Delta(S,-q^2,M^2)}}{\pi} \frac{d\sigma}{2(MM)d(MM)}$
$\frac{d\sigma}{dt}$	t	$\frac{\sqrt{\Delta(S,-q^2,M^2)}}{\pi} \frac{d\sigma}{dt}$
$\frac{d\sigma}{dp_n}$	p_n	$\frac{E}{\pi} \frac{d\sigma}{2p_n dp_n}$

TABLE 4

KINEMATIC RANGES OF THIS EXPERIMENT

Variable	Range
q^2	0.3 to 15.0 $(GeV/c)^2$
ν	10.0 to 130.0 GeV
s	20.0 to 260.0 GeV^2
$p_\perp^2$	0.0 to 1.0 $(GeV/c)^2$
$x_\parallel$	0.1 to 1.0
ϕ	$-\pi$ to π
y	0.0 to 5.0
MM	1.0 to 15.0 GeV
$\lvert t-t_{min} \rvert$	0.0 to 3.0 $(GeV/c)^2$
p_n	-0.6 to 0.6 GeV/c

TABLE 5

(q^2,ν) REGIONS FOR ONE-DIMENSIONAL HADRON DISTRIBUTIONS

Region	q^2	ν
I	0.3 to 1.0 $(GeV/c)^2$	90 to 130 GeV
II	1.0 to 10.0 $(GeV/c)^2$	90 to 130 GeV
III	3.0 to 15.0 $(GeV/c)^2$	10 to 90 GeV

TABLE 6

FITS OF THE INVARIANT HADRON CROSS SECTION

TO THE FORM $e^{-bp_\perp^2}$

q^2	ν	b
0.3 - 1.0 $(GeV/c)^2$	90 - 130 GeV	4.3 $(GeV/c)^{-2}$
1.0 - 10.0 $(GeV/c)^2$	90 - 130 GeV	3.7 $(GeV/c)^{-2}$
3.0 - 15.0 $(GeV/c)^2$	10 - 90 GeV	4.1 $(GeV/c)^{-2}$

TABLE 7

FITS OF THE INVARIANT HADRON CROSS SECTION

TO THE FORM $e^{-bx_{\|}}$

q^2	ν	b
0.3 - 1.0	90 - 130	3.7
1.0 - 10.0	90 - 130	3.7
3.0 - 15.0	10 - 90	3.8

Fig. 76.--Correspondence between muoproduction and virtual photoproduction.

Muoproduction

$\mu + N \rightarrow \mu' + h + x$

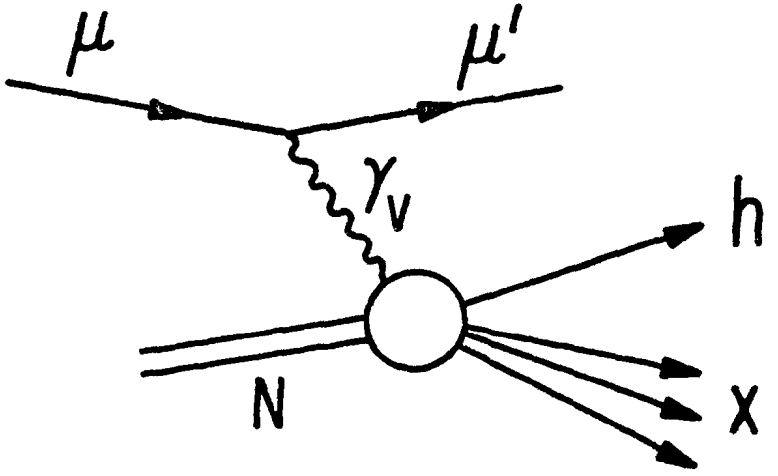

$$\frac{d\sigma}{dq^2 d\nu\, d^3p_h}$$

Virtual Photoproduction

$\gamma_V + N \rightarrow h + x$

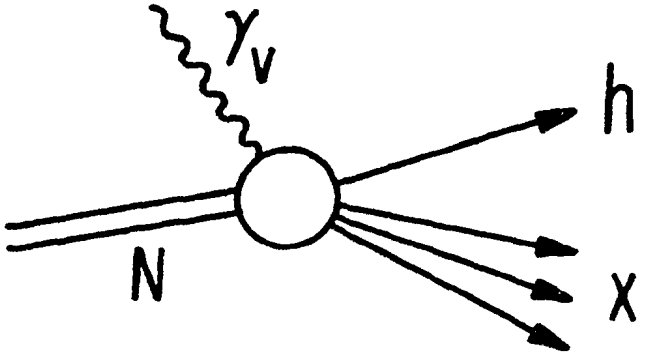

$$\Gamma_T \frac{d\sigma}{d^3p_h}$$

Fig. 77.--(a) When there are radiative corrections, the four-momentum of virtual photon, q', is determined by the unknown quantities, E_s' and E_p'. E_s is the incident muon, and E_p the scattered muon energy.

(b) Without radiative corrections, the four-momentum of the virtual photon, q, is uniquely determined by the momenta of the incident and the scattered muon.

(c) The relationship between $\vec{q}$ and $\vec{q}'$. With the framework of the peaking approximation, $\vec{q}'$ remains in the xz scattering plane.

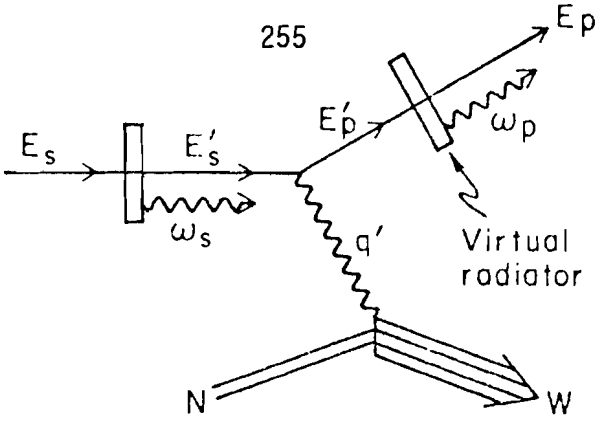
Ep
E's
Es
ω_p
E'p
ω_s
q'
Virtual
radiator
N
W

(a)

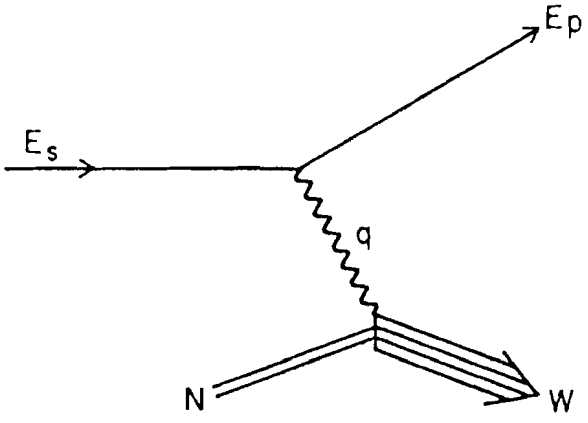
Ep
Es
q
N
W

(b)

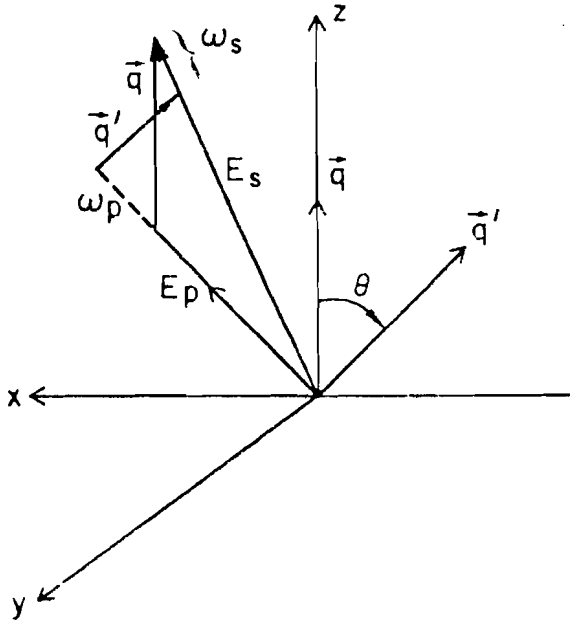
z
ω_s
q
q'
Es
ω_p
q
q'
Ep
θ
x
y

(c)

Fig. 78.--$p_\perp{}^2$-distribution for pions produced in 150 GeV scattering. The (q^2,ν) range is $0.3 \leq q^2 \leq 1.0$ $(GeV/c)^2$ and $90 \leq \nu \leq 130$ GeV.

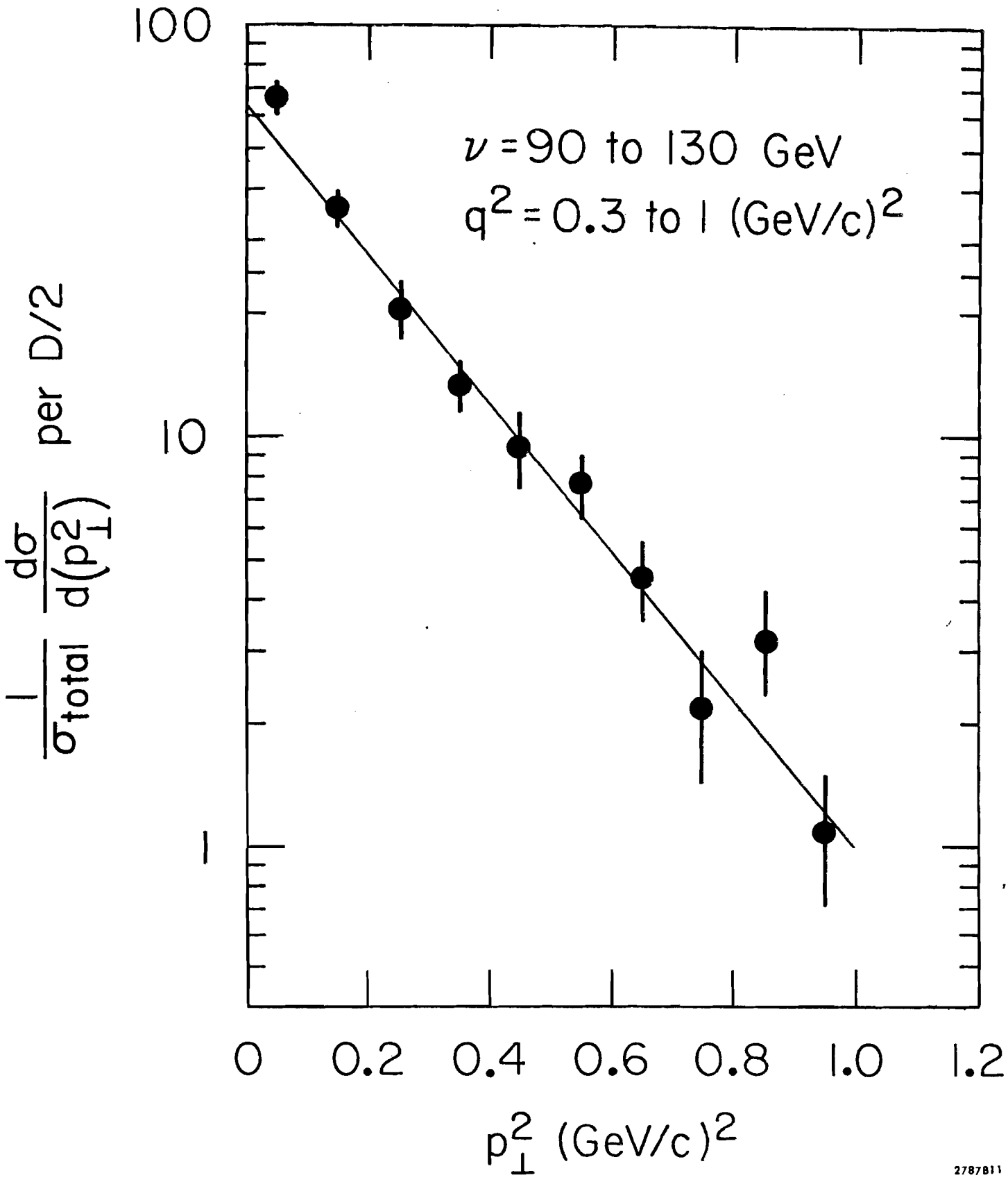
100
10
1
$\frac{1}{\sigma_{total}} \frac{d\sigma}{d(p_\perp^2)}$ per D/2
ν = 90 to 130 GeV
q^2 = 0.3 to 1 (GeV/c)^2
0
0.2
0.4
0.6
0.8
1.0
1.2
$p_\perp^2$ (GeV/c)^2
2787B11

Fig. 79.--$p_\perp{}^2$-distribution for the kinematic region $1 \leq q^2 \leq 10$ $(GeV/c)^2$ and $90 \leq \nu \leq 130$ GeV.

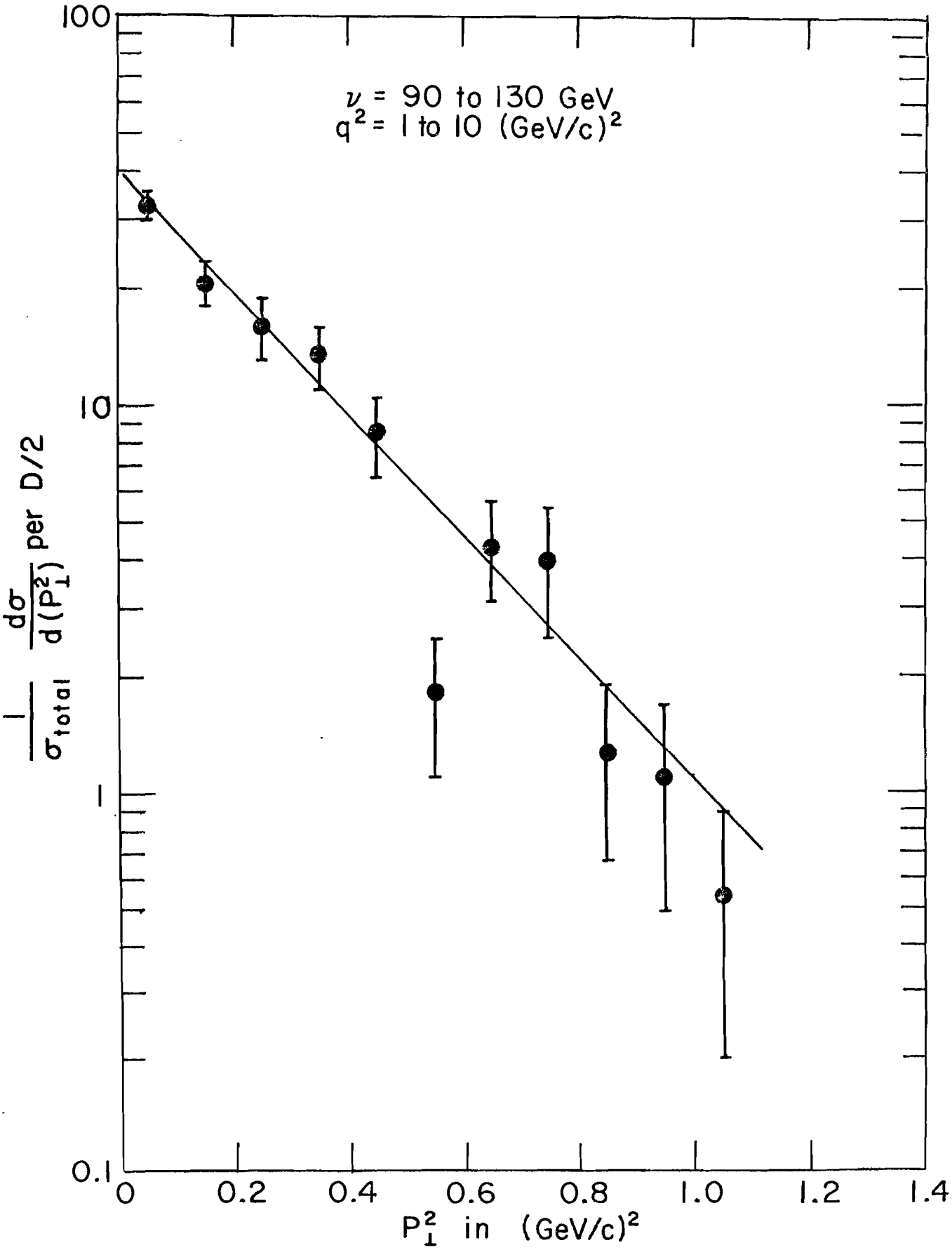
ν = 90 to 130 GeV
q² = 1 to 10 (GeV/c)²
100
10
1
0.1
0
0.2
0.4
0.6
0.8
1.0
1.2
1.4
P²⊥ in (GeV/c)²
1/σtotal dσ/d(P²⊥) per D/2

Fig. 80.--$p_\perp{}^2$-distribution for the kinematic region $3 \leq q^2 \leq 15$ $(GeV/c)^2$ and $90 \leq \nu \leq 130$ GeV.

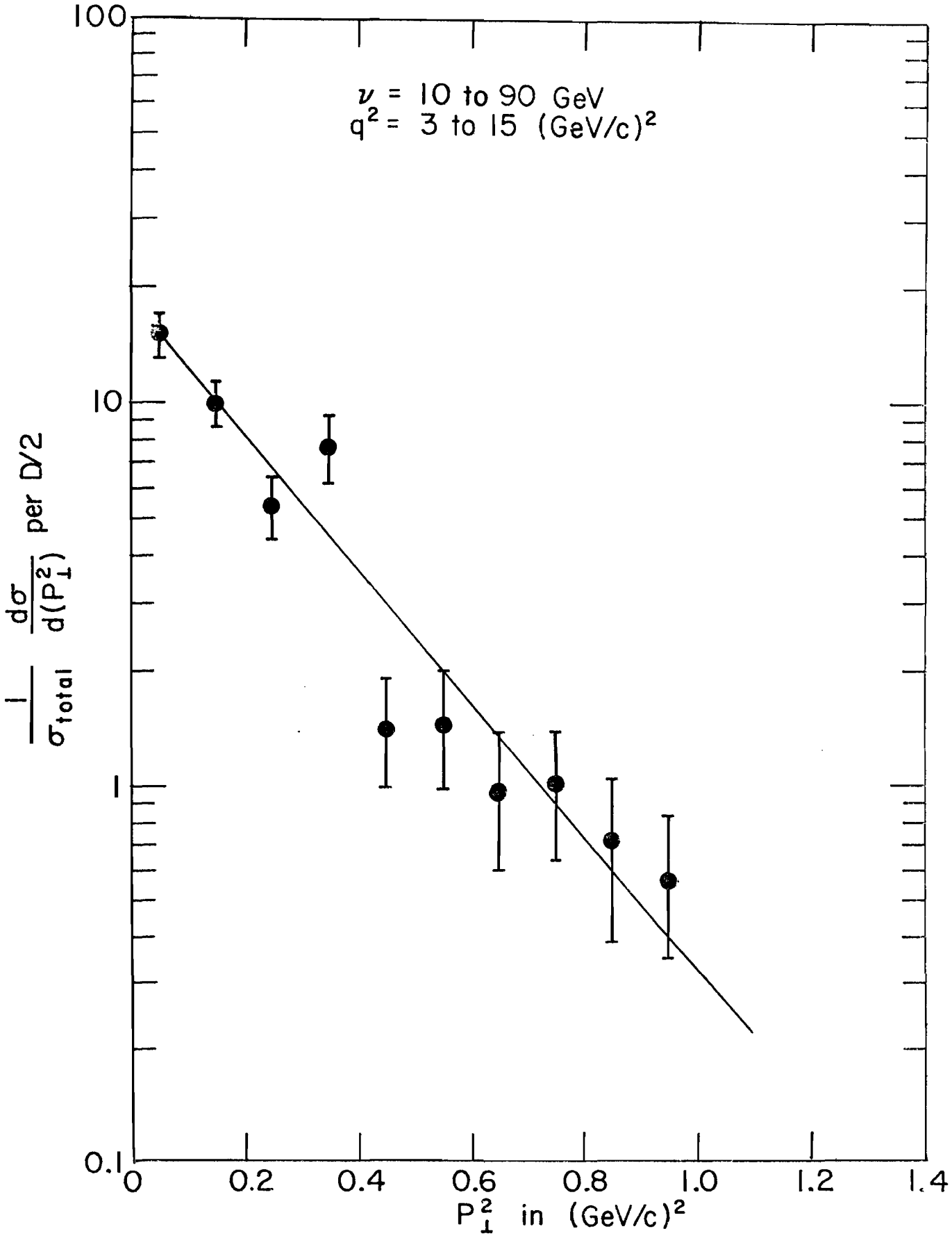
ν = 10 to 90 GeV
q² = 3 to 15 (GeV/c)²
100
10
1
0.1
0
0.2
0.4
0.6
0.8
1.0
1.2
1.4
P²⊥ in (GeV/c)²
1/σtotal dσ/d(P²⊥) per D/2

Fig. 81.--$x_{\parallel}$-distribution for hadrons produced in the kinematic region $0.3 \leq q^2 \leq 1$ $(GeV/c)^2$ and $90 \leq \nu \leq 130$ GeV.

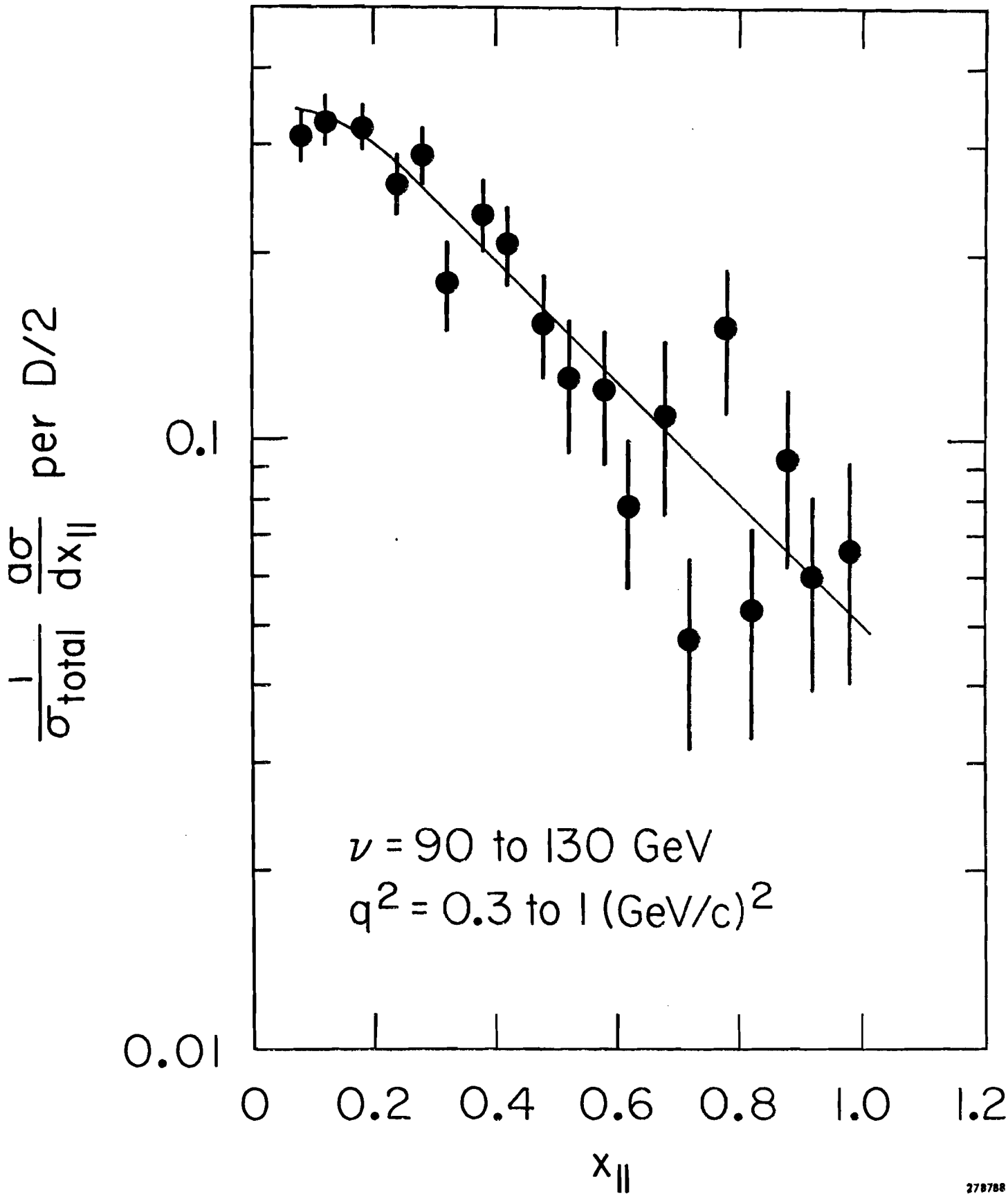
$\frac{1}{\sigma_{total}} \frac{a\sigma}{dx_{||}}$ per D/2
0.1
0.01
ν = 90 to 130 GeV
q^2 = 0.3 to 1 (GeV/c)^2
0
0.2
0.4
0.6
0.8
1.0
1.2
$x_{||}$
278788

Fig. 82.--$x_{\parallel}$-distribution for hadrons produced in the kinematic region $1 \leq q^2 \leq 10$ $(GeV/c)^2$ and $90 \leq \nu \leq 130$ GeV.

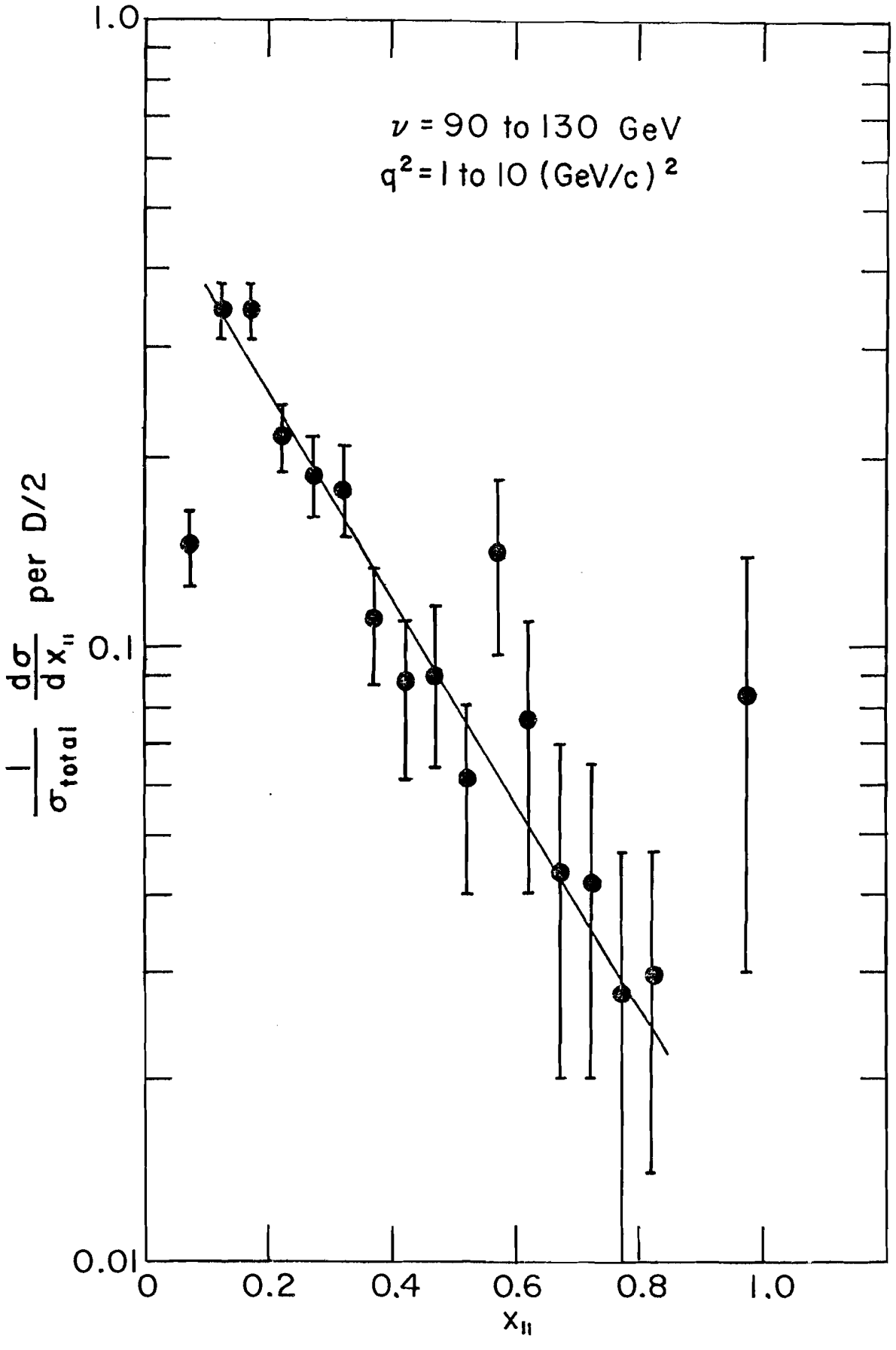
1.0
0.1
0.01
0
0.2
0.4
0.6
0.8
1.0
ν = 90 to 130 GeV
q^2 = 1 to 10 (GeV/c)^2
$\frac{1}{\sigma_{total}} \frac{d\sigma}{dx_{II}}$ per D/2
x_{II}

Fig. 83.--$x_{\parallel}$-distribution for hadrons produced in the kinematic region $3 \leq q^2 \leq 15$ $(GeV/c)^2$ and $10 \leq \nu \leq 90$ GeV.

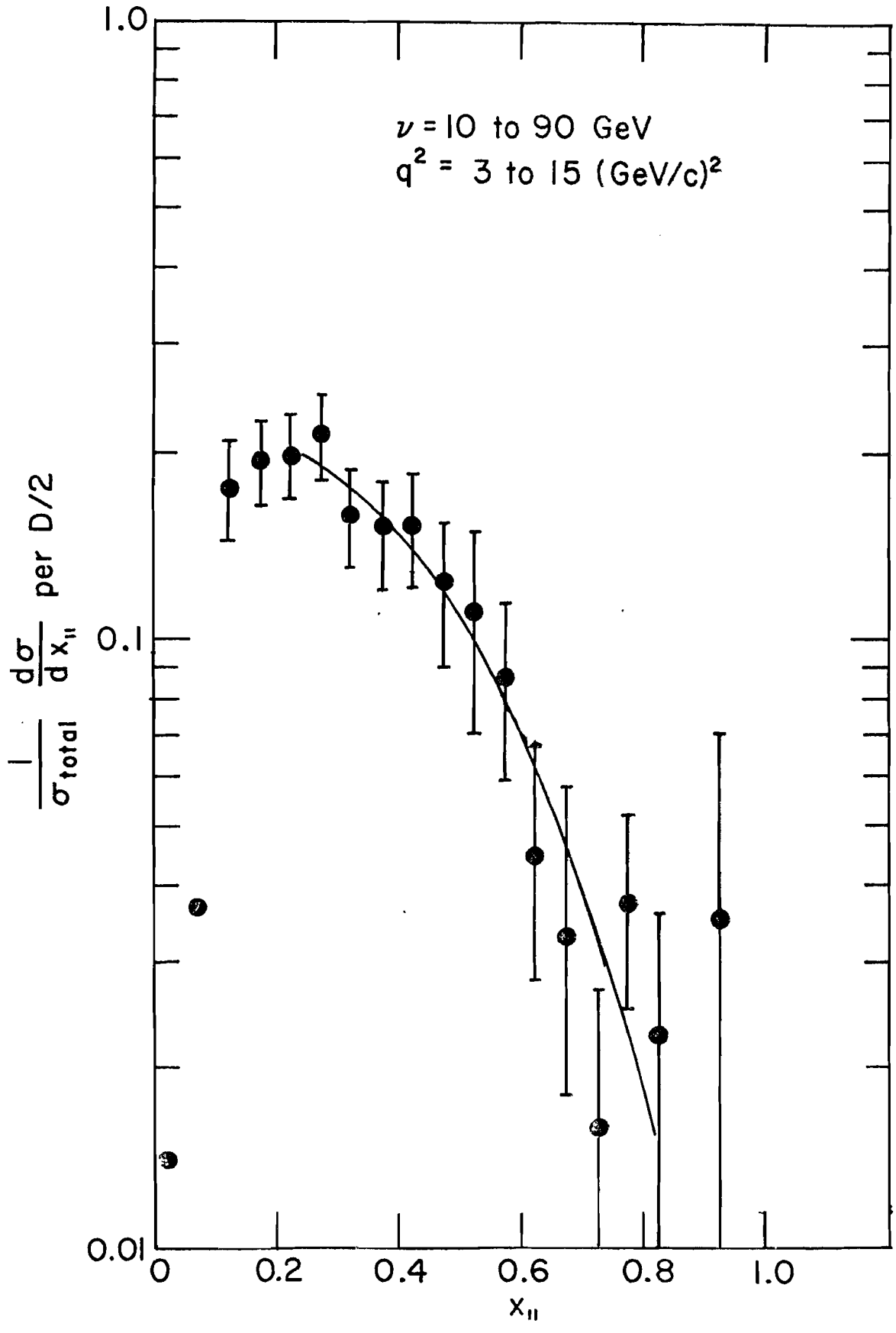
1.0
0.1
0.01
ν = 10 to 90 GeV
q^2 = 3 to 15 (GeV/c)^2
$\frac{1}{\sigma_{total}} \frac{d\sigma}{dx_{\parallel}}$ per D/2
0
0.2
0.4
0.6
0.8
1.0
$x_{\parallel}$

Fig. 84.--$x_{\parallel}$-distribution of hadrons produced in the reaction, $e^+ + e^- \rightarrow$ hadrons, measured at SPEAR. The straight line is the numerical fit of the x -distribution for muoproduced hadrons in the deep inelastic region, $90 \leq \nu \leq 130$ GeV and $1 \leq q^2 \leq 10$ $(GeV/c)^2$.

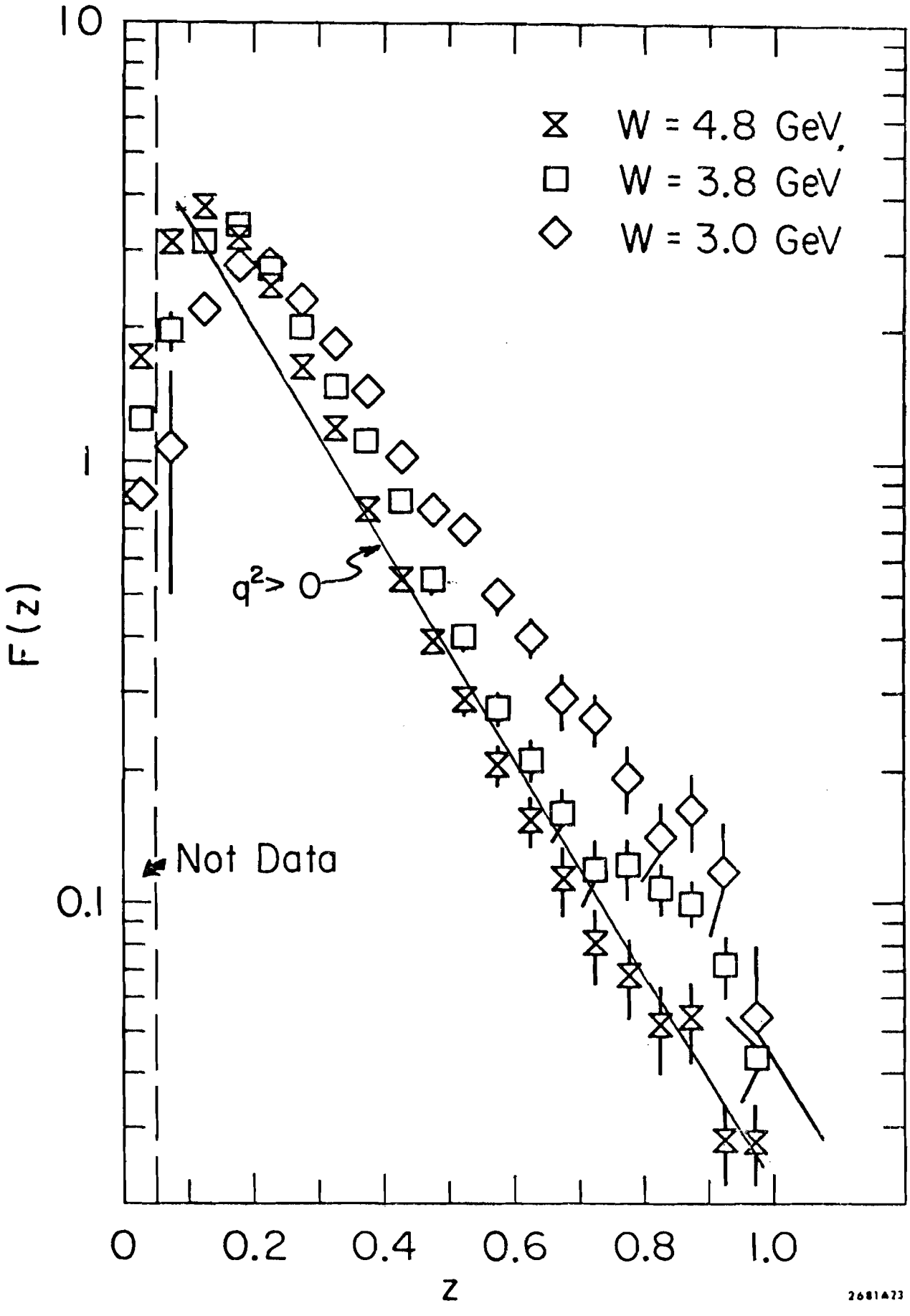
10
1
0.1
F(z)
W = 4.8 GeV
W = 3.8 GeV
W = 3.0 GeV
$q^2 > 0$
Not Data
0
0.2
0.4
0.6
0.8
1.0
z
2681A23

Fig. 85.--Comparison of the $x_{\parallel}$-distribution of hadrons produced in inelastic neutrino scattering at Fermilab with the numerical fit to the $x_{\parallel}$-distribution for muoproduced hadrons in the kinematic region, $90 \leq \nu \leq 130$ GeV and $1 \leq q^2 \leq 10$ $(GeV/c)^2$.

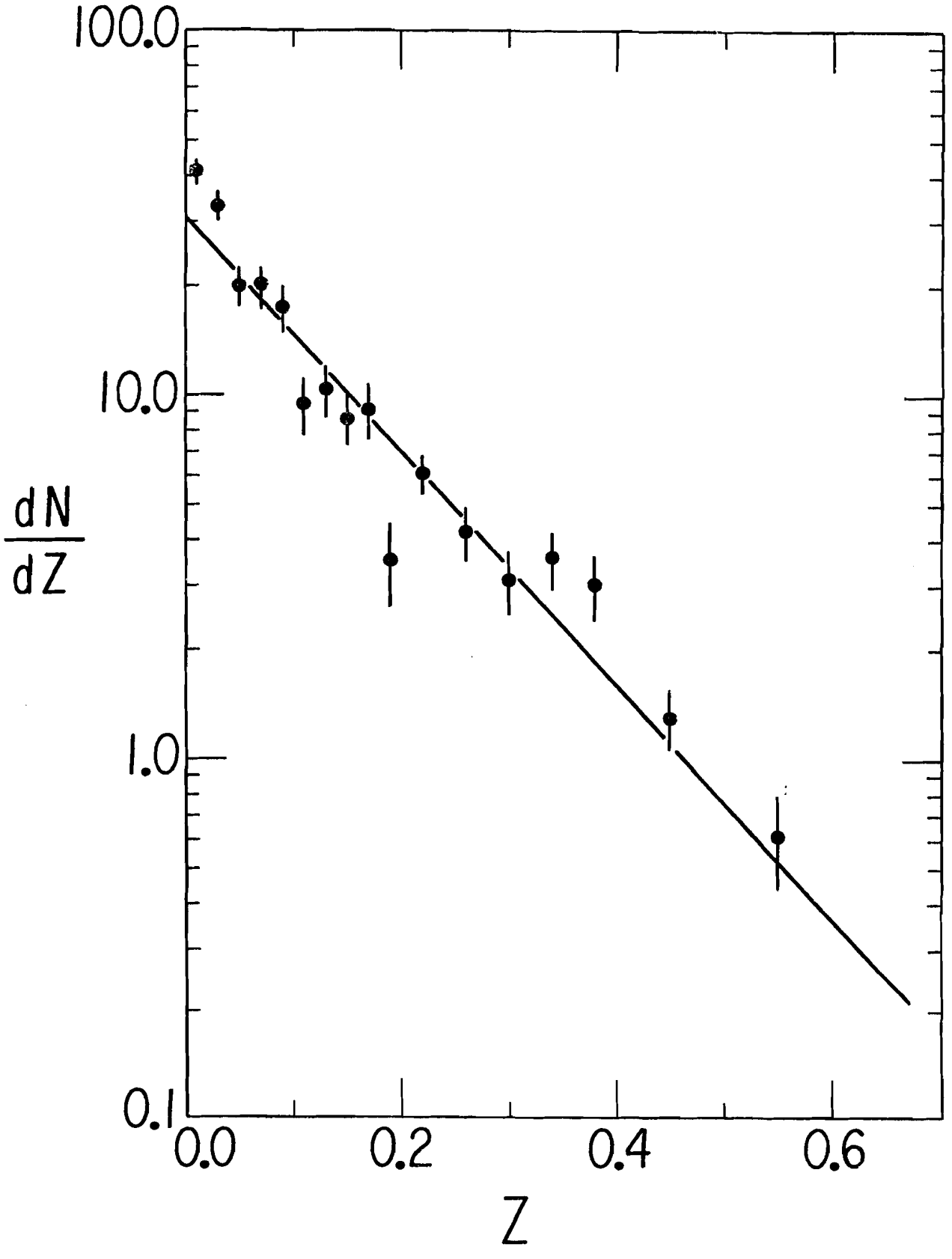
100.0
10.0
1.0
0.1
dN/dZ
0.0
0.2
0.4
0.6
Z

Fig. 86.--Rapidity distribution of muoproduced hadrons in the kinematic region, $90 \leq \nu \leq 130$ GeV and $0.3 \leq q^2 \leq 1.0$ $(\text{GeV}/c)^2$.

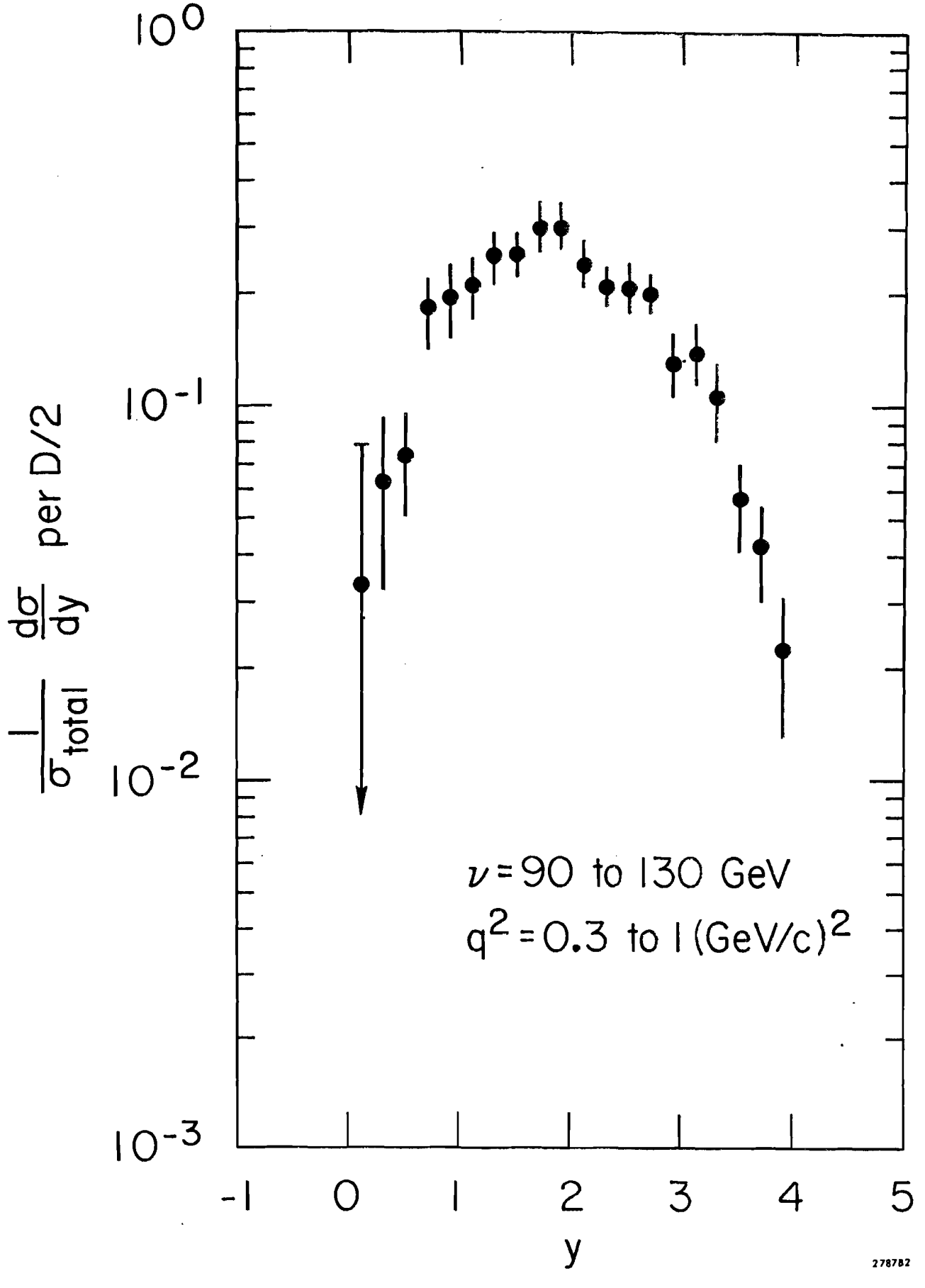
10^0
10^{-1}
10^{-2}
10^{-3}
$\frac{1}{\sigma_{total}} \frac{d\sigma}{dy}$ per D/2
$\nu = 90$ to 130 GeV
$q^2 = 0.3$ to 1 (GeV/c)^2
-1
0
1
2
3
4
5
y
278782

Fig. 87.--Rapidity distribution of muoproduced hadrons in the kinematic region, $90 \leq \nu \leq 130$ GeV and $1.0 \leq q^2 \leq 10.0$ $(GeV/c)^2$.

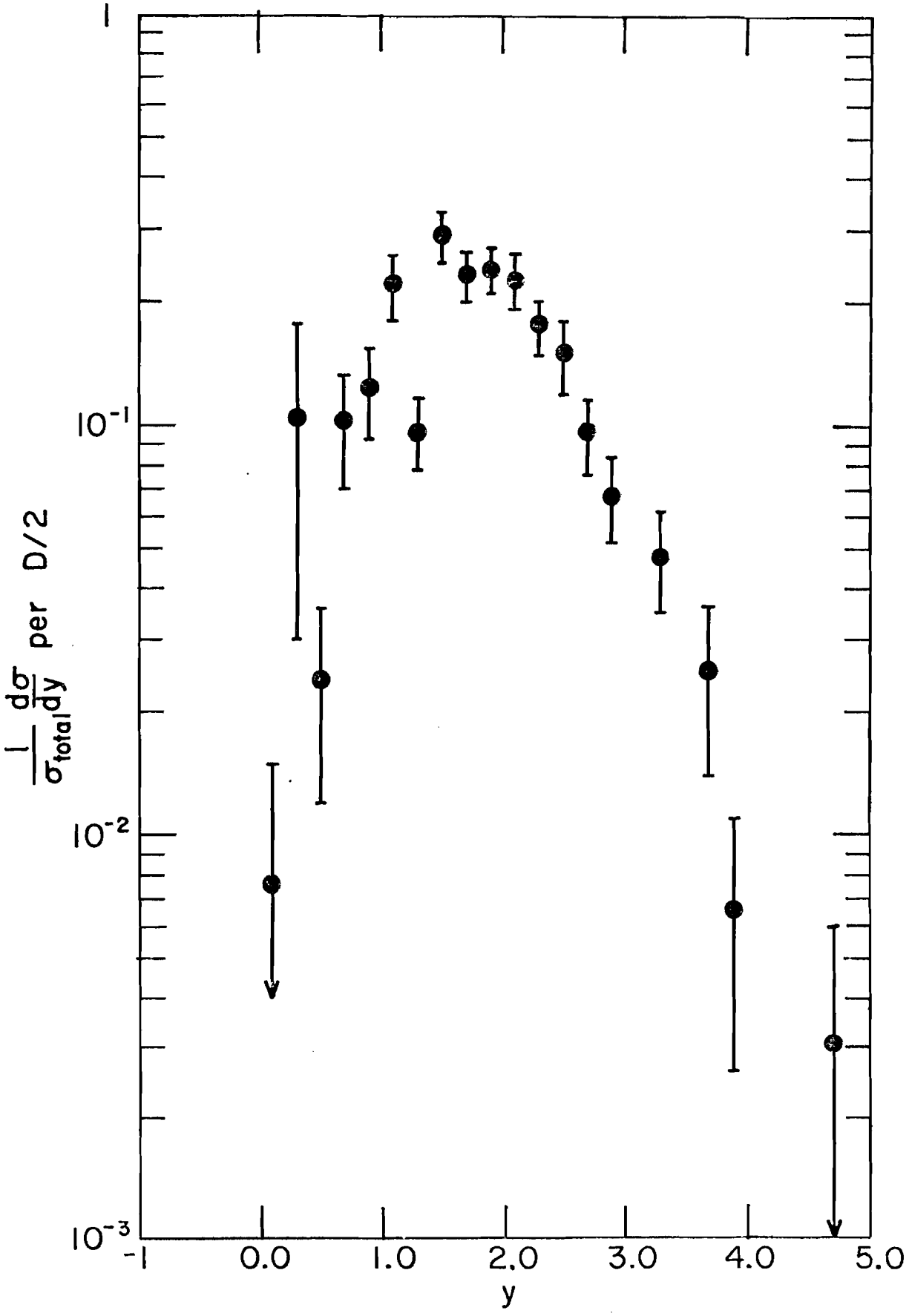
1
10^{-1}
10^{-2}
10^{-3}
$\frac{1}{\sigma_{total}}\frac{d\sigma}{dy}$ per D/2
-1
0.0
1.0
2.0
3.0
4.0
5.0
y

Fig. 88.--Rapidity distribution of muoproduced hadrons in the kinematic region, $10 \leq \nu \leq 90$ GeV and $3.0 \leq q^2 \leq 15$ $(\text{GeV}/c)^2$.

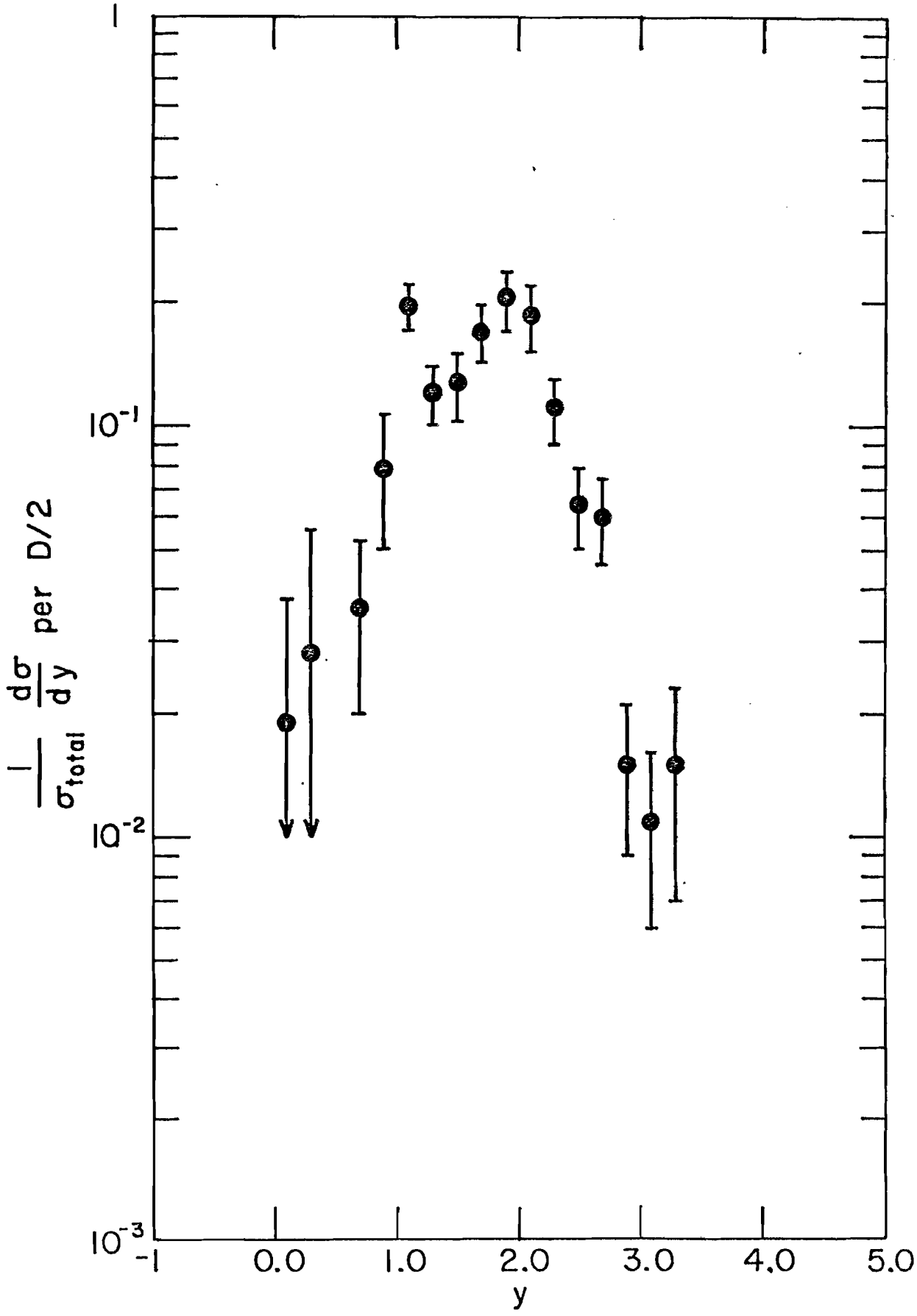
1
10^{-1}
10^{-2}
10^{-3}
$\frac{1}{\sigma_{total}} \frac{d\sigma}{dy}$ per D/2
-1
0.0
1.0
2.0
3.0
4.0
5.0
y

Fig. 89.--Conjectured rapidity distribution for muoproduced hadrons showing the region of target fragmentation, the central plateau, and photon fragmentation region.

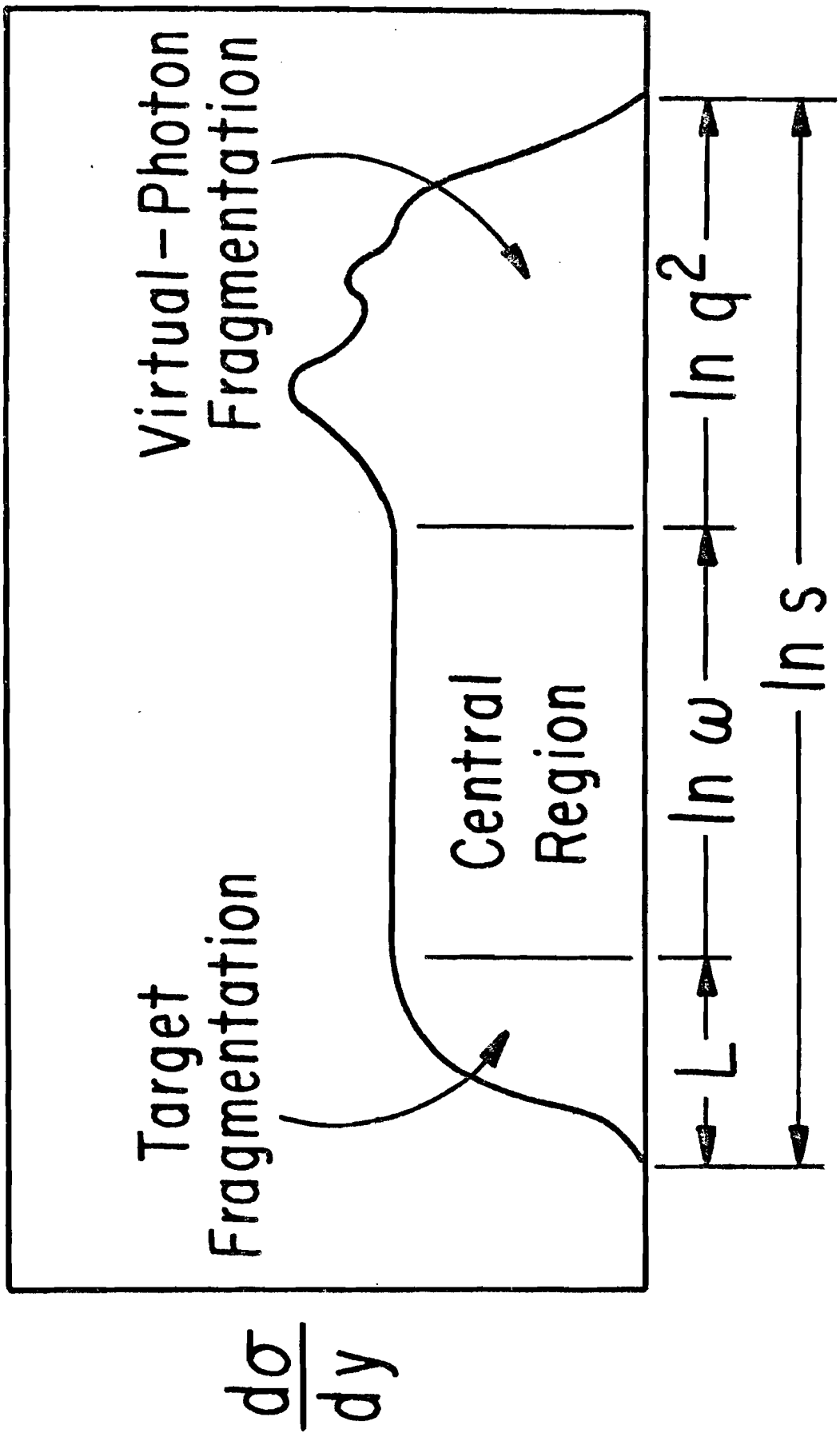
Virtual-Photon Fragmentation
Central Region
Target Fragmentation
L
ln ω
ln q²
ln s
dσ/dy

Fig. 90.--Missing mass spectra of a single detected pion in virtual photoproduction for $90 \leq \nu \leq 130$ GeV and $0.3 \leq q^2 \leq 1.0$ $(GeV/c)^2$.

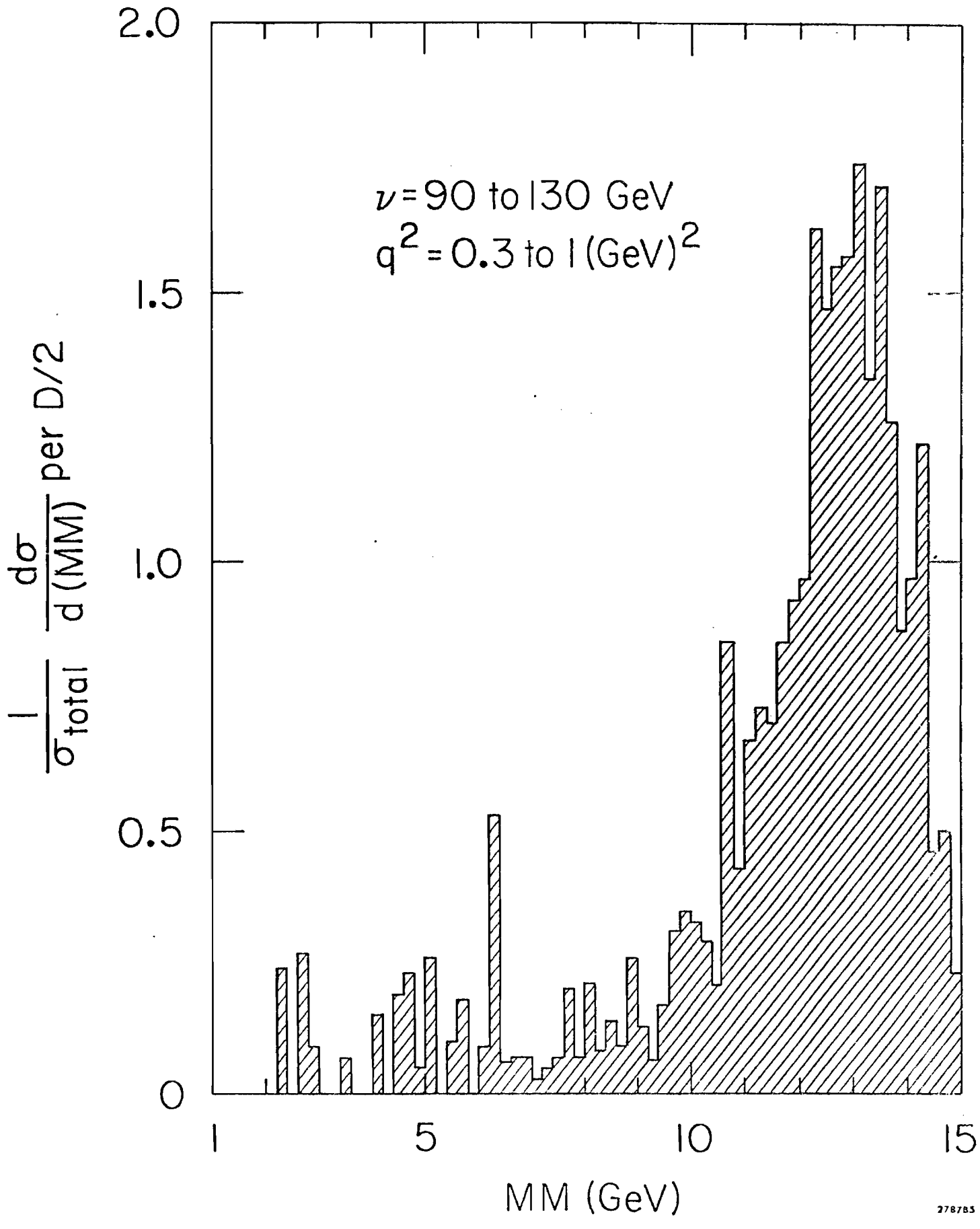
2.0
1.5
1.0
0.5
0
1
5
10
15
ν = 90 to 130 GeV
q² = 0.3 to 1 (GeV)²
1/σ_total dσ/d(MM) per D/2
MM (GeV)
278783

Fig. 91.--Missing mass spectra of a single detected pion in virtual photoproduction for $90 \leq \nu \leq 130$ GeV and $1.0 \leq q^2 \leq 10.0$ $(\text{GeV}/c)^2$.

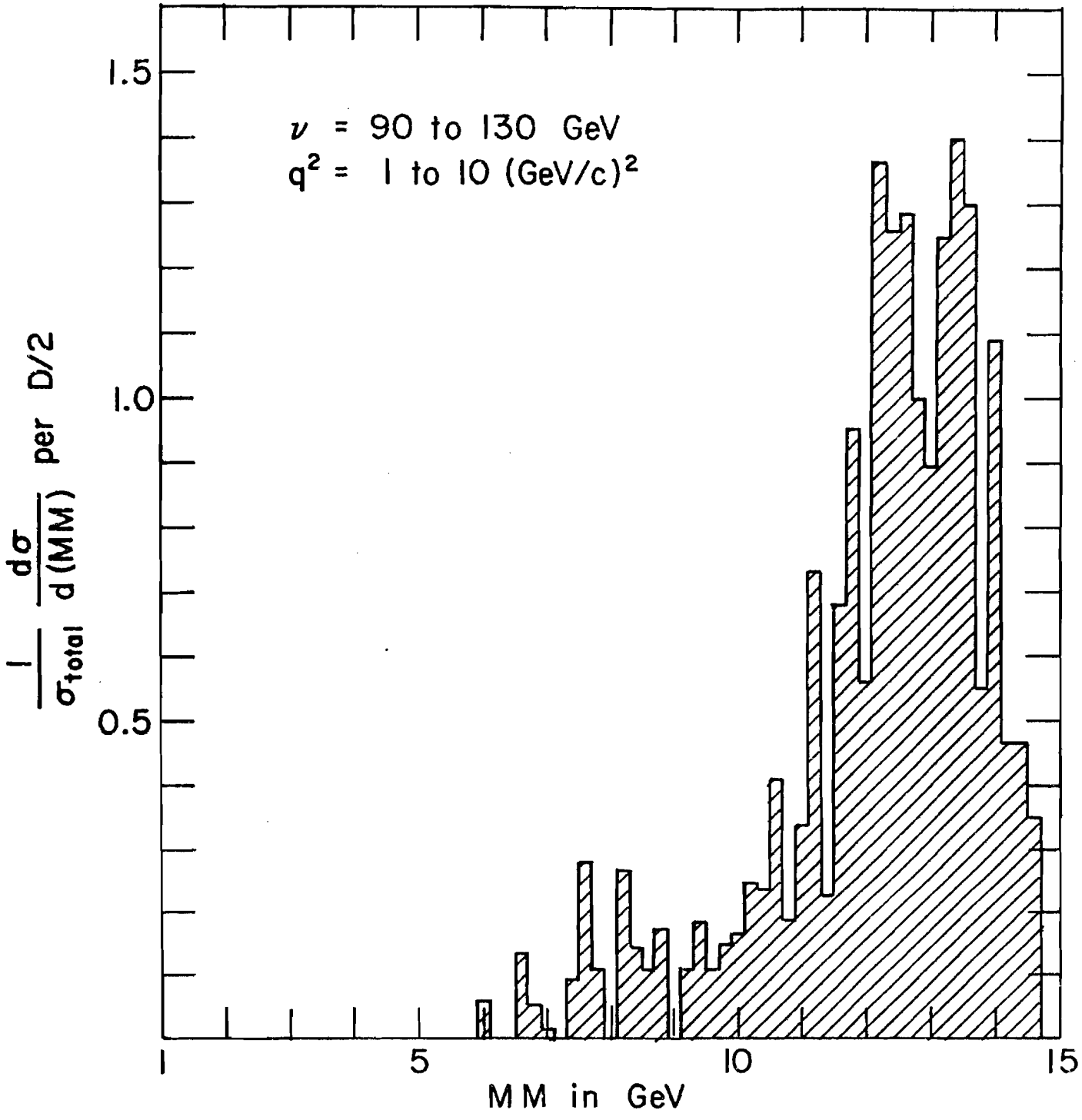
1.5
1.0
0.5
ν = 90 to 130 GeV
q^2 = 1 to 10 (GeV/c)^2
$\frac{1}{\sigma_{total}} \frac{d\sigma}{d(MM)}$ per D/2
1
5
10
15
MM in GeV

Fig. 92.--Missing mass spectra of a single detected pion in virtual photoproduction for $10 \leq \nu \leq 90$ GeV and $3.0 \leq q^2 \leq 15.0$ $(GeV/c)^2$.

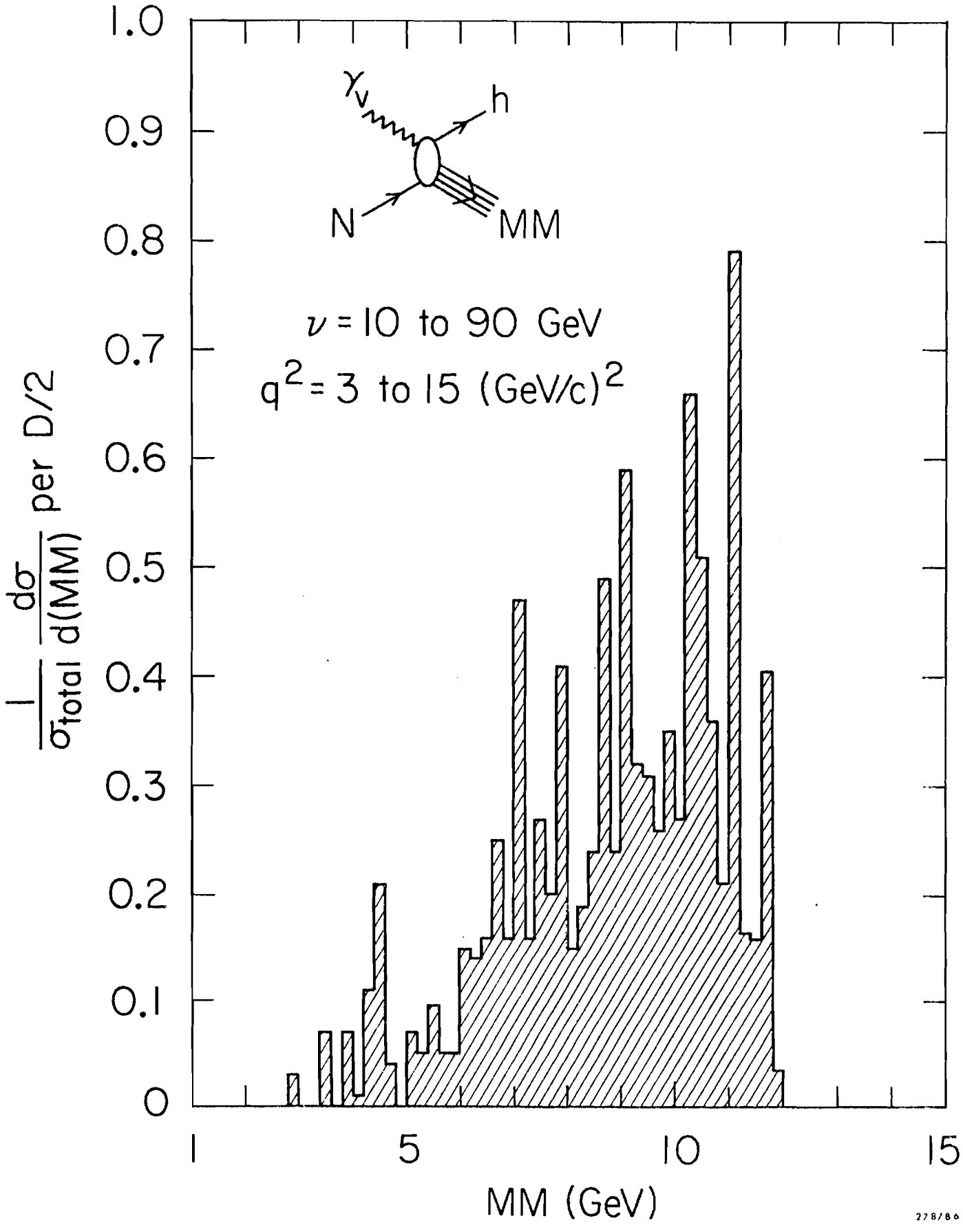
1.0
0.9
0.8
0.7
0.6
0.5
0.4
0.3
0.2
0.1
0
1
5
10
15
MM (GeV)
$\frac{1}{\sigma_{total}} \frac{d\sigma}{d(MM)}$ per D/2
γ_v
h
N
MM
ν = 10 to 90 GeV
q^2 = 3 to 15 (GeV/c)^2
278/86

Fig. 93.--Virtual photoproduction t-distribution for $90 \leq \nu \leq 130$ GeV and $0.3 \leq q^2 \leq 1.0$ $(GeV/c)^2$; where t is the four-momentum transfer-squared between the incident virtual photon and the detected pion, t_{min} is the value of t when the detected pion is produced along the direction of the virtual photon.

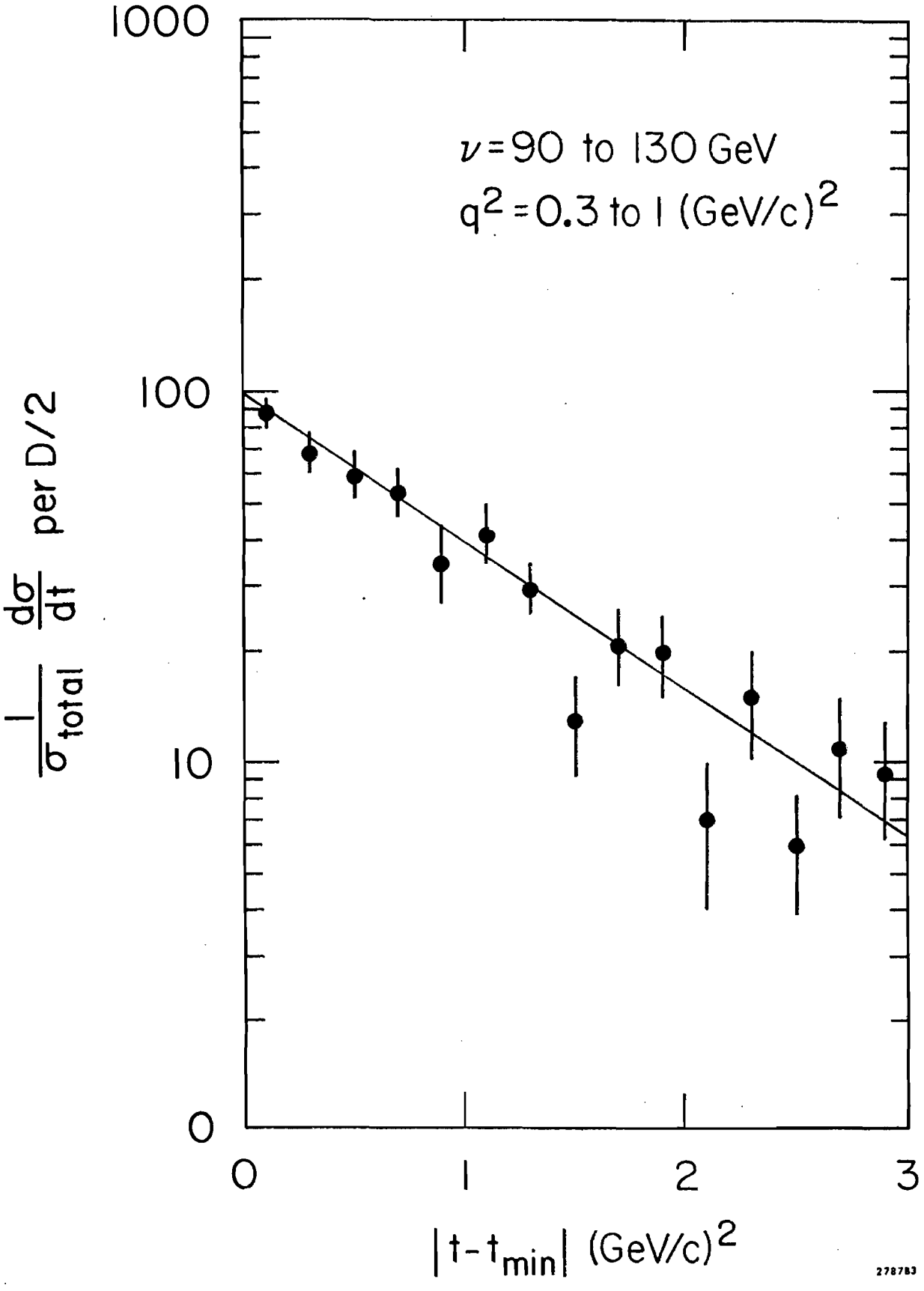
1000
100
10
0
0
1
2
3
ν = 90 to 130 GeV
q^2 = 0.3 to 1 (GeV/c)^2
$\frac{1}{\sigma_{total}} \frac{d\sigma}{dt}$ per D/2
$|t - t_{min}|$ (GeV/c)^2
278783

Fig. 94.--The t-distribution for $90 \leq \nu \leq 130$ GeV and $1.0 \leq q^2 \leq 10.0$ $(\text{GeV}/c)^2$.

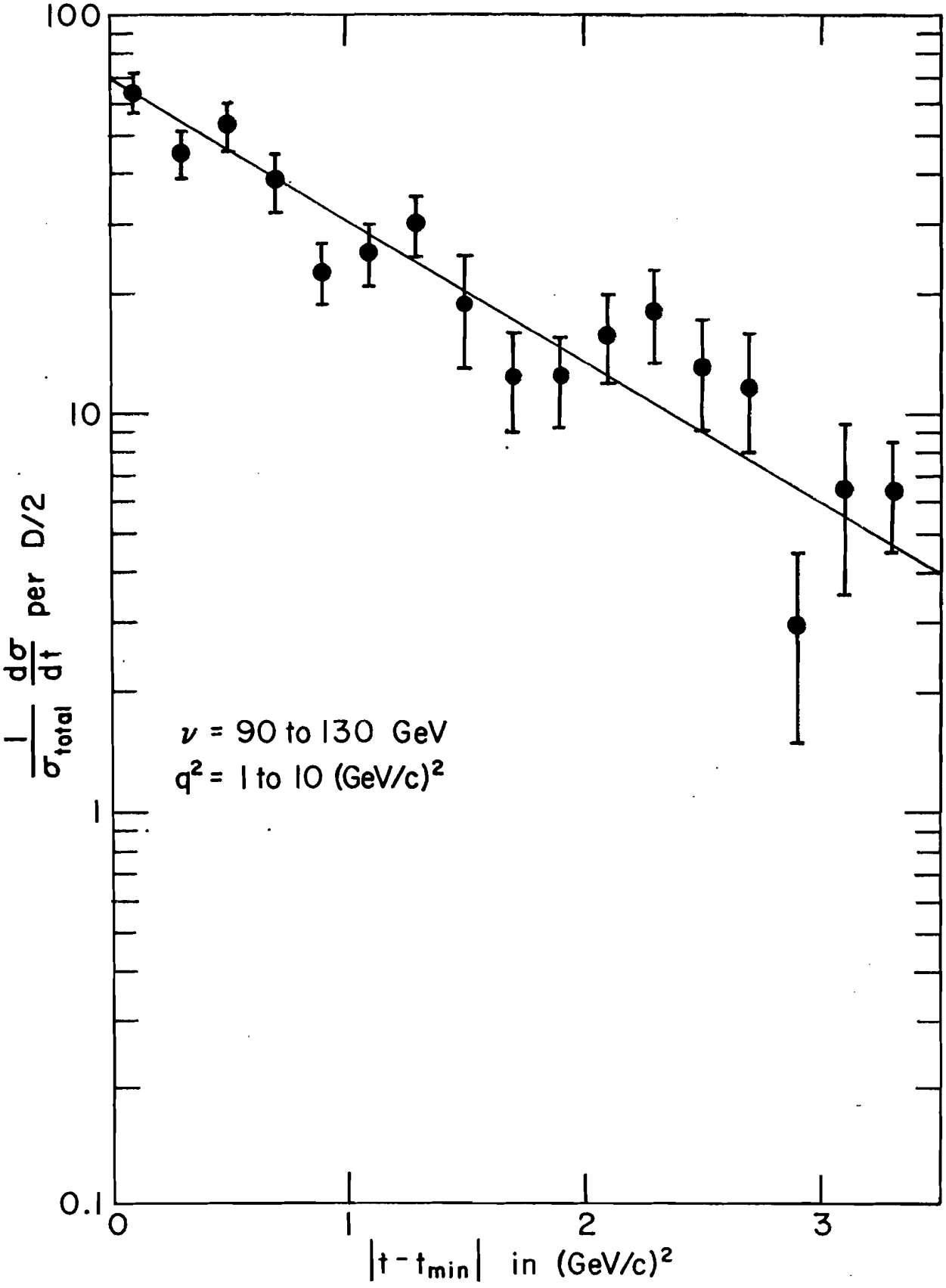
100
10
1
0.1
0
1
2
3
$\frac{1}{\sigma_{total}} \frac{d\sigma}{dt}$ per D/2
$|t - t_{min}|$ in (GeV/c)^2
ν = 90 to 130 GeV
q^2 = 1 to 10 (GeV/c)^2

Fig. 95.--The t-distribution for $10 \leq \nu \leq 90$ GeV and $3.0 \leq q^2 \leq 15.0$ $(\text{GeV}/c)^2$.

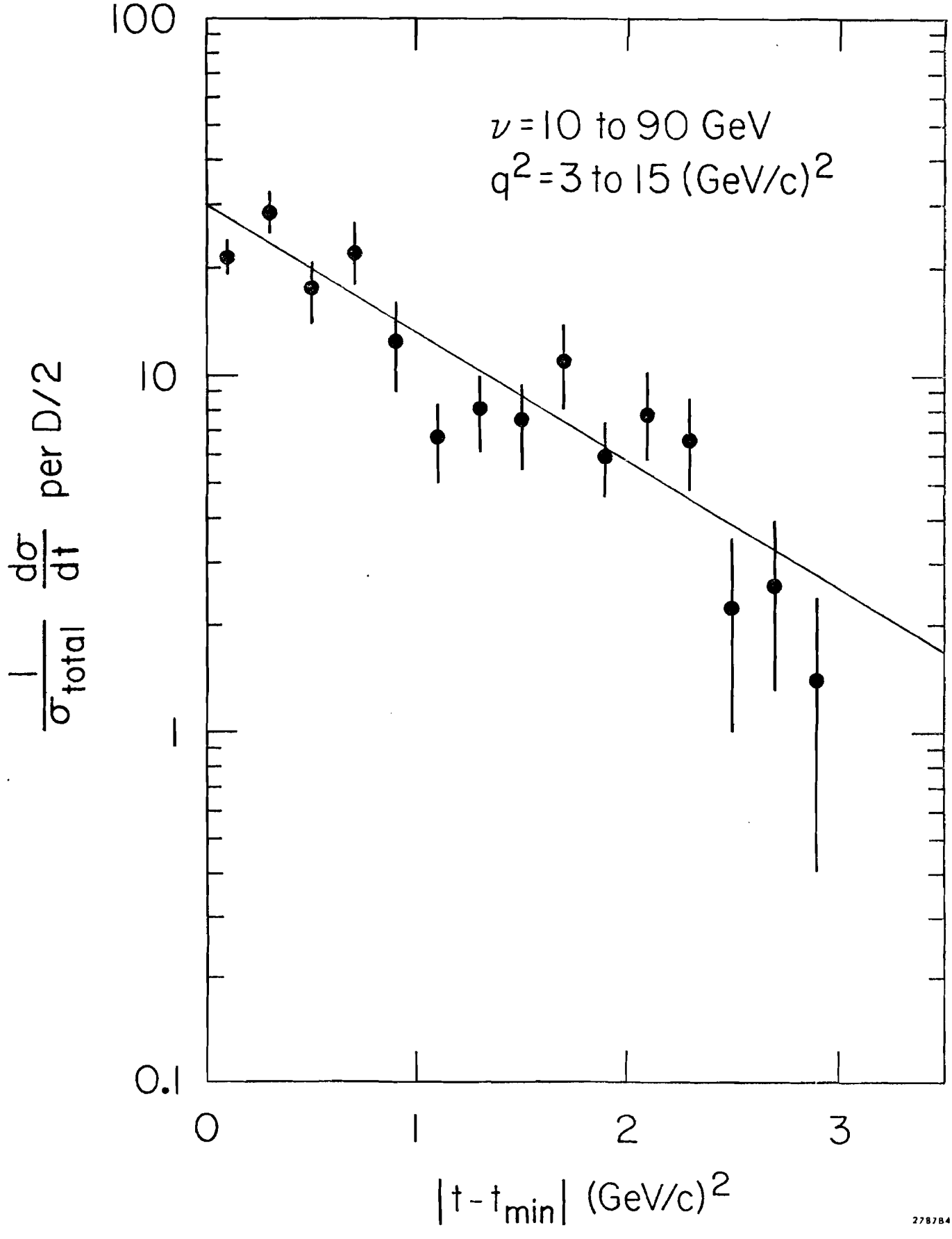
100
10
1
0.1
0
1
2
3
ν = 10 to 90 GeV
q^2 = 3 to 15 (GeV/c)^2
$\frac{1}{\sigma_{total}} \frac{d\sigma}{dt}$ per D/2
$|t - t_{min}|$ (GeV/c)^2
278784

Fig. 96.--The correlation between $x_{\parallel}$ of the detected single hadron and its missing mass for $90 \leq \nu \leq 130$ GeV and $0.3 \leq q^2 \leq 1.0$ $(\text{GeV}/c)^2$.

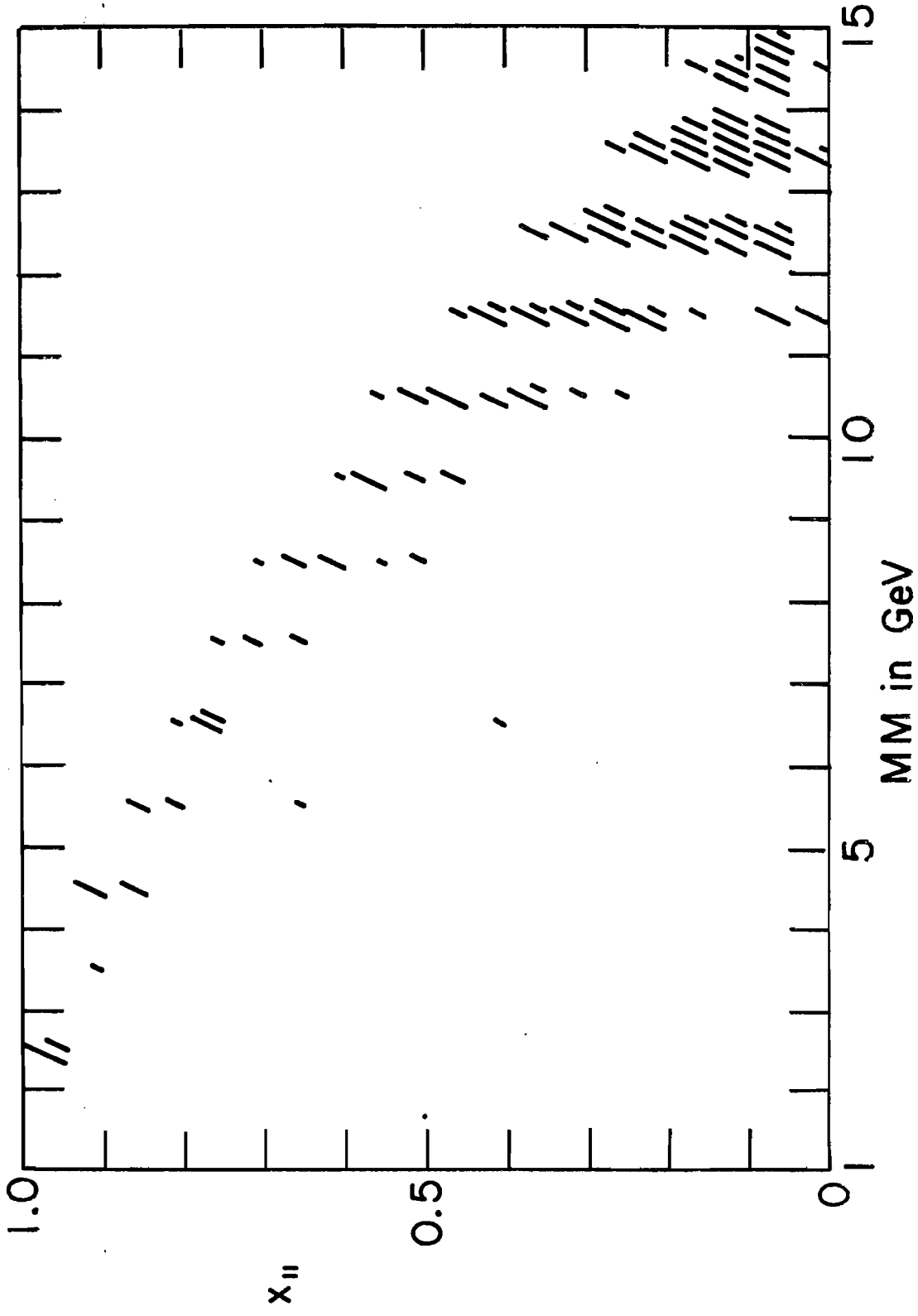
1.0
0.5
0
$x_{\parallel}$
0
5
10
15
MM in GeV

Fig. 97.--Diagram showing p_n, the component of hadron momentum normal to the muon scattering plane.

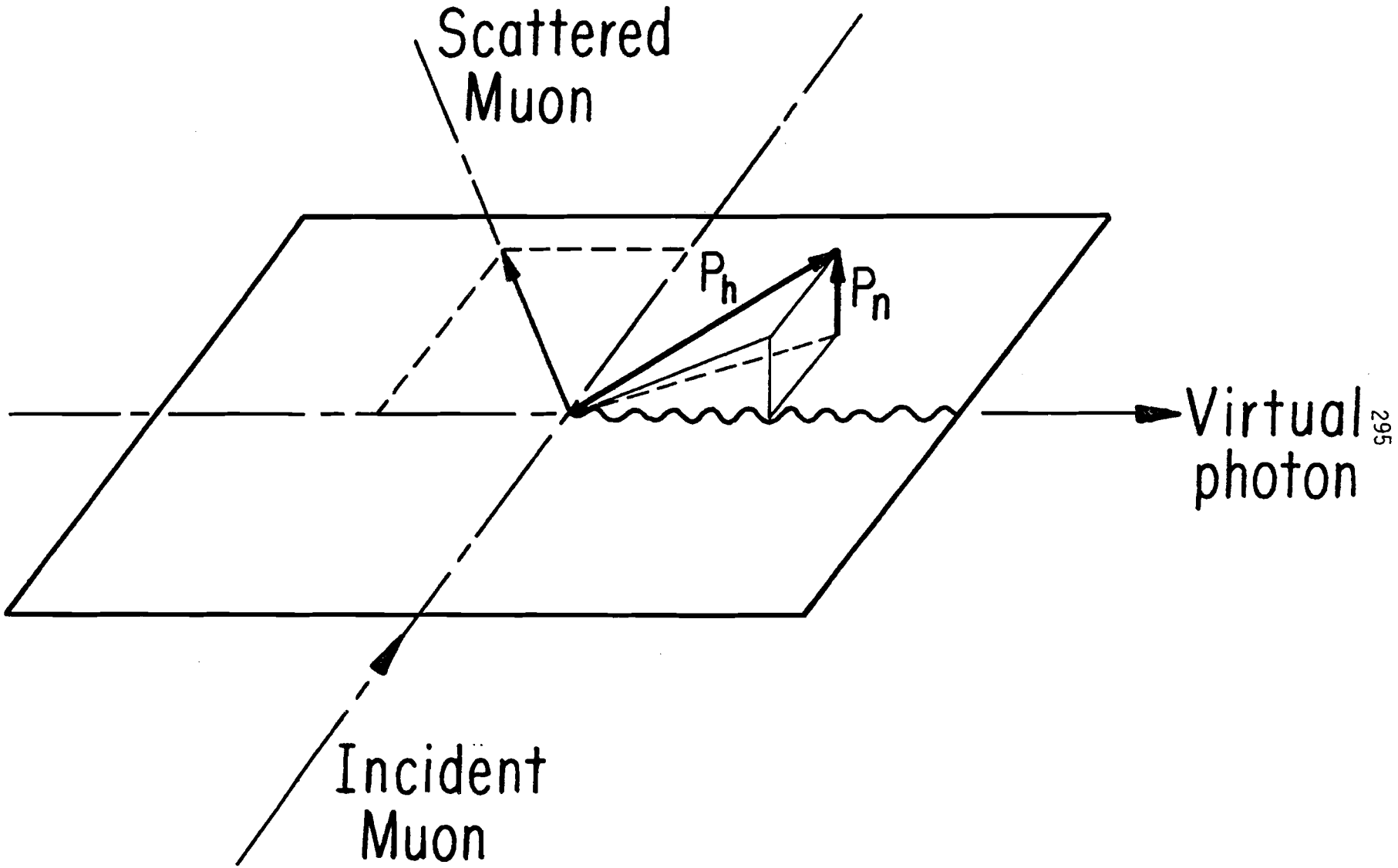
Scattered
Muon
P_h
P_n
Virtual
photon
Incident
Muon

Fig. 98.--p_n-distribution of muoproduced pions from deuterium at 150 GeV. p_n is the component of hadron momentum perpendicular to the muon scattering plane. The plot is for data in the deep inelastic region $90 \leq \nu \leq 130$ GeV and $1 \leq q^2 \leq 10$ $(GeV/c)^2$.

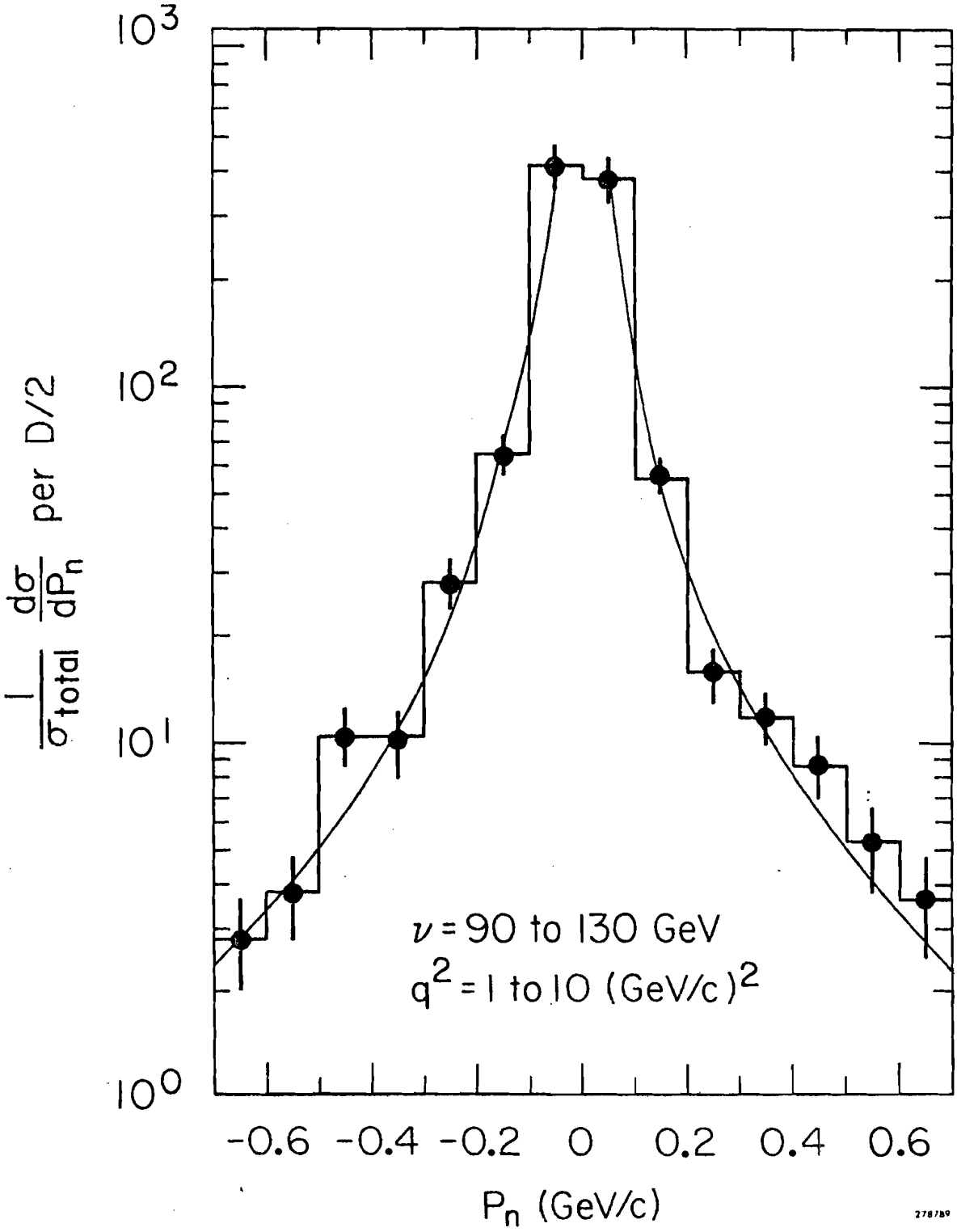
10^3
10^2
10^1
10^0
$\frac{1}{\sigma_{total}} \frac{d\sigma}{dP_n}$ per D/2
ν = 90 to 130 GeV
q^2 = 1 to 10 (GeV/c)^2
-0.6 -0.4 -0.2 0 0.2 0.4 0.6
P_n (GeV/c)
278789

APPENDIX 1

SHIFT REGISTER READOUT

In this appendix we describe the shift register readout electronics for the 1m X 1m MWPC's,[41] the 2m X 4m wire spark chambers,[43] and the associated CAMAC wire chamber scanner.[42] Both the multi-wire proportional chambers and wire spark chambers are read out by means of integrated circuit shift register cards that plug into connectors mounted on the chambers. Shift register couplers on each chamber prepare the shift register output for transmission to the CAMAC scanner, and synchronize the data with the scanner's clock. These couplers can be daisy-chained, so that a number of chambers (up to 8096 wires) can be read out by a single CAMAC scanner module. The data is serially shifted out of the chamber, through the coupler, and into the scanner at a 5 MHz scan rate. A complete scan cycle takes 1.6 msec. The scanner module reformats the shift register data and stores it in its own 64-word buffer memory. After the scan is completed, the contents of the scanner memory is transferred to the computer through the CAMAC dataway.

The 1m X 1m MWPC Shift Register Readout

A schematic of the readout for the 1m X 1m MWPC's is shown in Figure 99. Because the signals from the anode wires of a multi-wire proportional chamber are usually of the order of tens of millivolts, it is necessary to use an amplifier before the discriminator and other stages of readout electronics. The circuitry for eight channels, or anode wires, is contained on one plug-in printed circuit board. The amplifier used for each channel had

a rise time of approximately 40 nsec and a gain of typically 2000. The triggering threshold for the discriminator was set at +1.5 volts, corresponding to 0.8 millivolts at the amplifier input. The output pulse width of the discriminator was used as the electronics delay to meet the experiment triggering requirements. The output of the discriminator was differentiated by an RC network, producing a negative-going spike at the trailing edge of the output pulse. If this negative-going spike was in coincidence with the "load" signal generated by the master event trigger, it set a bit in the shift register. The delay (output pulse width) was set at 580 nsec and could be adjusted over a range of about 10%.

The latched output of the shift registers was then shifted out by a train of clock pulses from the CAMAC scanner. It should be mentioned that the 1m X 1m MWPC's were latched before pulsing the wire spark chambers. To prevent spurious latching or shifting of the MWPC readout by the electrical pulsing noise of the spark chambers, both the "load" and "clock" lines in the MWPC couplers were blocked for a period of approximately 20 μsec when the wire spark chambers were pulsed.

The 2m X 4m Shift Register Readout

The technique used to read out the 2m X 4m wire spark chambers is a simple one: When the chamber is pulsed, the charge from the spark current in a wire is stored on a capacitor until the electrical noise associated with pulsing the chamber has died out; the spark information (stored as charge on individual wire capacitors) is then parallel loaded into shift registers on the chamber, and read out by a CAMAC scanner. The basic circuitry for 32 wires is contained on a printed circuit card that plugs into connectors mounted on the chamber. Each card contains the input storage capacitors,

bias resistors, four 8-bit shift register IC's, and a power gating circuit. The readout connectors are mounted on printed circuit boards built into the chamber which have the power bus and signal lines for the shift register cards and etched printed circuit lands for connection to the spark chamber wires.

A diagram of the shift register card for the 2m X 4m wire spark chambers is shown in Figure 100. When the chamber is pulsed, the spark current in a wire charges capacitors C1 and C2. The input filter network, formed by C1, R1 and C2, not only stores the spark charge but also protects the input of the shift register IC by filtering out high frequency transients. The discharge time constant for the storage capacitors, C1 and C2, is set at 80 μsec by R2. Since the polarity of the spark current in a wire is opposite for low-voltage and high-voltage wire planes, a bias voltage is applied to the input capacitor network: 0 volts on a high-voltage readout plane, and +2.5 volts on a low-voltage readout plane.

The shift registers are powered about 20 μsec after pulsing the chambers; a GATE signal from the scanner turns on transistors Q2 and Q1, applying voltage to the IC's. Under quiescent conditions, the shift registers are not powered; voltage is only applied during the two millisecond readout time. This minimizes the otherwise tremendous power requirements of the readout, and increases the reliability of the IC's by lowering their operating temperature. Once the shift registers are powered, and after a delay of approximately 100 nsec, produced by R3 and C3, the spark information is loaded into the shift registers, and read out by a train of clock pulses from the CAMAC scanner.

Because the shift register electronics on the high-voltage wire planes must float with the high-voltage pulse on the chambers, it is necessary to isolate them from the ground potential of the chamber coupler and CAMAC

scanner lines. This was achieved by using a well-insulated transformer to supply the low-voltage dc power to the shift register cards, and by coupling the signals from the readout plane to the shift register coupler through ferrite core transformers.

As a check on the readout, we permanently set three contiguous shift register bits at the beginning and end of each readout plane. By monitoring these fiducial bits on-line, we could easily detect the failure of a shift register card in the readout plane, and quickly replace it. Also, all the shift register IC's could be tested under computer control by issuing commands to the scanner through the CAMAC system. The first test was to simply execute a normal scan cycle without pulsing the chambers. One expects to find only the permanently set fiducial bits. Any other set bits indicated a faulty shift register card. In the second test, the bias voltage on the input capacitors is reversed, and the output data line of the shift registers is complimented. In this mode only shift register bits in the chambers that fail to set will be read out.

The CAMAC Wire Chamber Scanner

The CAMAC wire chamber scanner is a physically compact module, occupying a single-width slot in a CAMAC crate. Cabling to the wire chambers is very simple: a single cable containing seven shielded twisted pairs. This made the data retrieval from arrays of many chambers a straightforward task. The scanner provides for the complete digital readout of wire chambers using shift register data output, and can also be used to read out magnetostrictive delay line chambers. It has its own 64-word by 16-bit buffer memory and can handle up to 8096 wires. The complete scan cycle takes 1.6 msec. Figure 101 is a block diagram of the scanner. Its function is to

serially shift the data out of the chambers, reformat it, and store it for later transfer to the computer. The format for spark information storage in the scanner's memory is 13 bits for position (wire address) and 3 bits for spread. Spread is the number of adjacent wires set.

A scan sequence is initiated by a NIM level signal generated by the master event trigger. After a delay of 20 μsec to allow the spark chamber noise to die out, a "load" signal is sent to gate on the power and load the shift registers on the wire spark chambers. This delay is utilized to clear the scanner's random access memory (RAM) and all internal registers. The scanner then starts a train of clock pulses to the chamber to shift out the data. In the chamber coupler, the clock pulses are turned around, synchronized with the data, and sent back to the scanner. This makes the operation of the scanner completely independent of cable lengths. The clock and data delay are always the same. When a clock pulse arrives at the scanner, the data line is sampled 50 nsec after the leading edge of the clock. If a data bit is present, a spread scaler is started and incremented for each contiguous data bit. The highest wire address (i.e., the clock count) of this group of set bits is then stored, along with the spread count, in the scanner's 64-word by 16-bit RAM. The spread count occupies the three lowest order bits of a 16-bit word. The wire address occupies the upper 13 bits. If a spark has a spread of more than seven wires, then multiple wire addresses are stored so that no data is lost. Up to 64 wire addresses can be stored.

When handling magnetostrictive delay line signals, the scanner's crystal controlled clock is set to either 20 or 40 MHz, and the magnetostrictive signal must first be squared and converted to NIM level. The scanner records the arrival time (clock count) of the magnetostrictive

signal, and measures the width with its spread circuitry. This allows the scanner to accurately find the center of the magnetostrictive pulse.

At the completion of a scan cycle, a "look-at-me" signal is generated to inform the CAMAC system that the module is ready to transfer data to the computer. The first word read out of the module is the number of wire address stored in the memory, along with an overflow bit. By performing this number of read operations the contents of the scanner memory can be read out for logging on magnetic tape or on-line analysis.

Fig. 99.--Schematic diagram of the readout electronics for the 1m X 1m MWPC's.

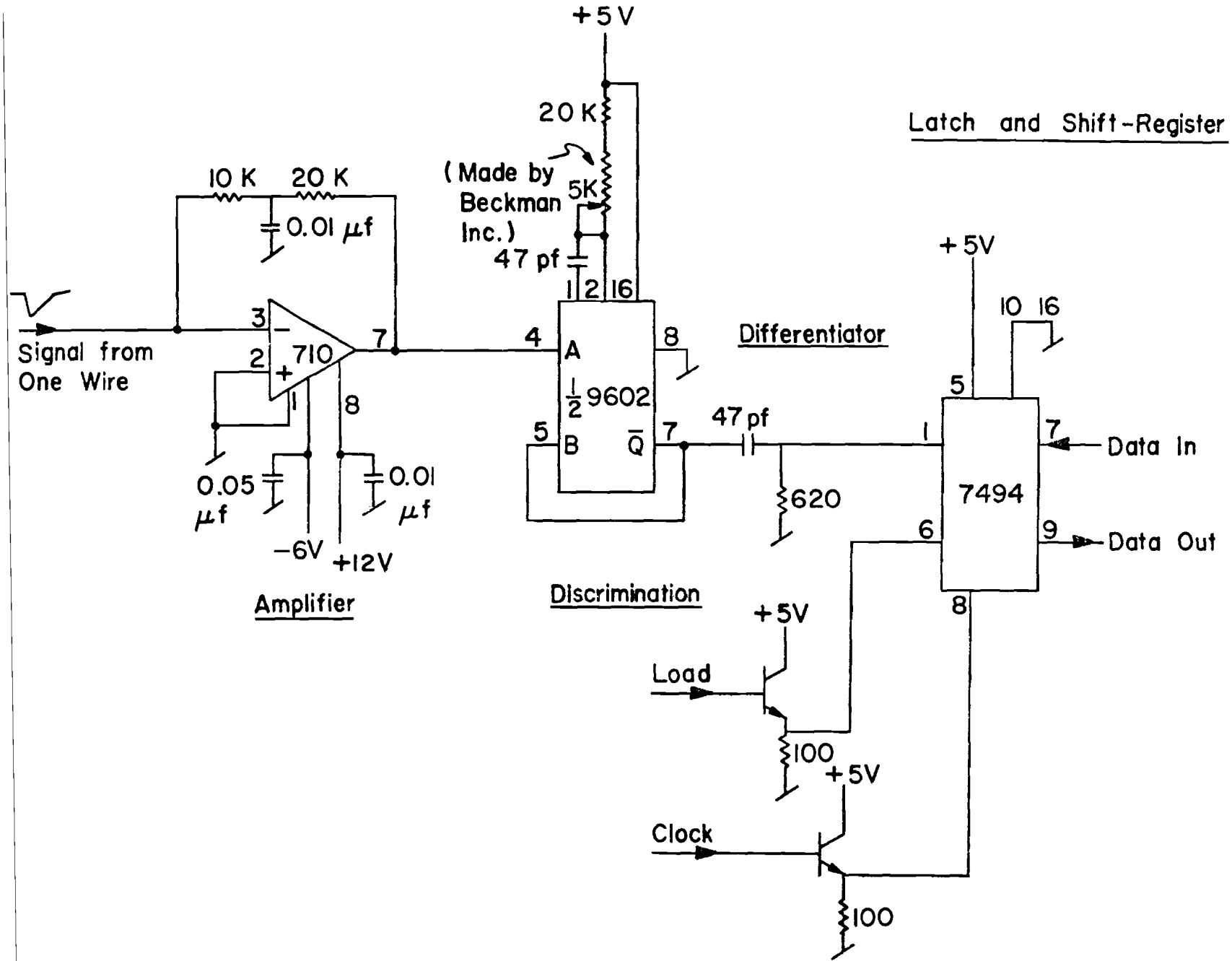
+5V
20 K
(Made by Beckman Inc.)
5K
47 pf
Latch and Shift-Register
10 K
20 K
0.01 μf
Signal from One Wire
3
2
710
7
1
8
4
A
1/2 9602
B
Q̄
5
7
8
1
2
16
Differentiator
47 pf
620
+5V
10
16
5
1
7
Data In
7494
6
9
Data Out
8
0.05 μf
0.01 μf
-6V
+12V
Amplifier
Discrimination
+5V
Load
100
+5V
Clock
100

Fig. 100.--Schematic diagram of the readout electronics for the 2m X 4m shift-register wire spark chambers.

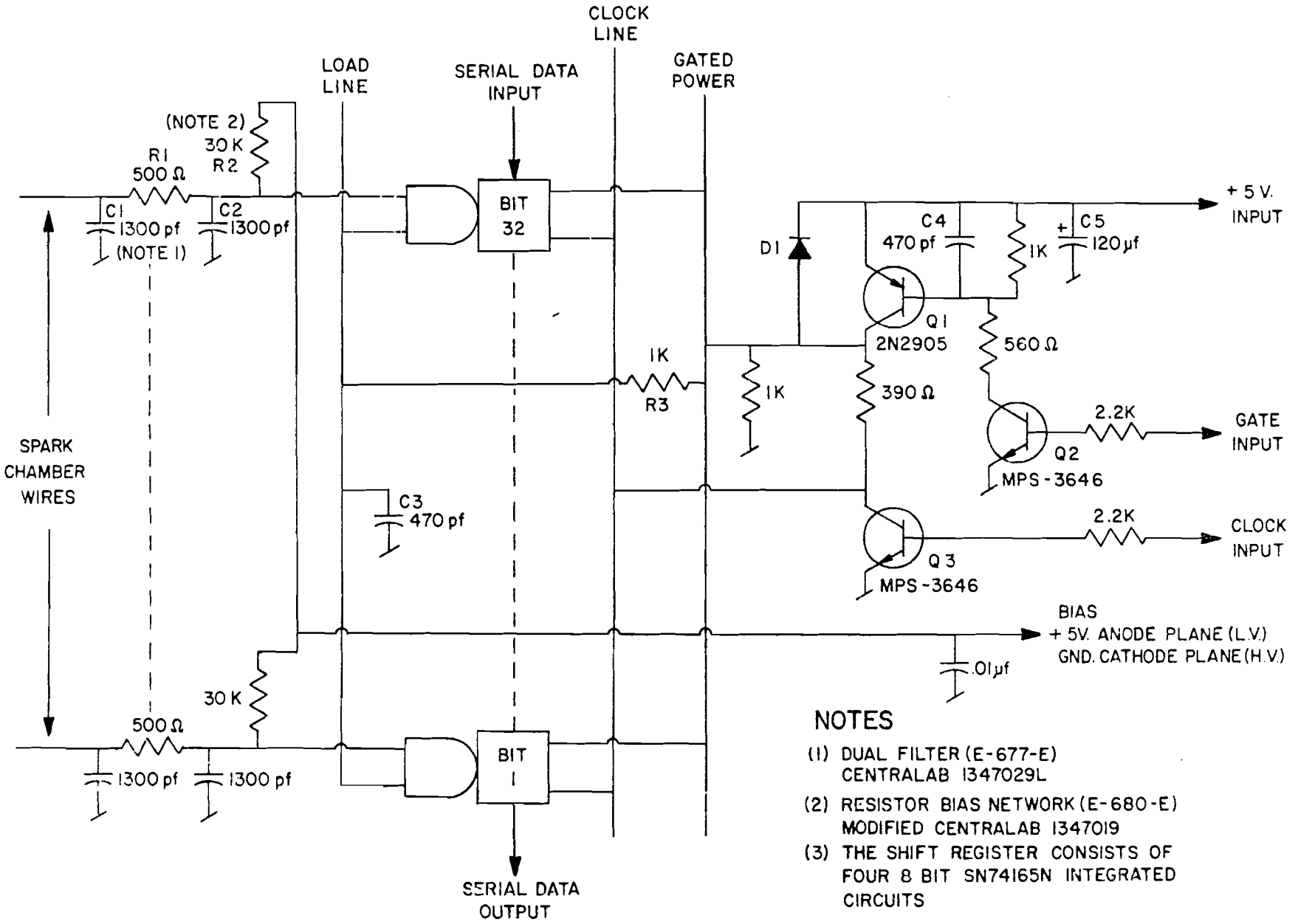

NOTES

(1) DUAL FILTER (E-677-E)
CENTRALAB 1347029L

(2) RESISTOR BIAS NETWORK (E-680-E)
MODIFIED CENTRALAB 1347019

(3) THE SHIFT REGISTER CONSISTS OF FOUR 8 BIT SN74165N INTEGRATED CIRCUITS

Fig. 101.--Block diagram of the CAMAC wire chamber scanner.

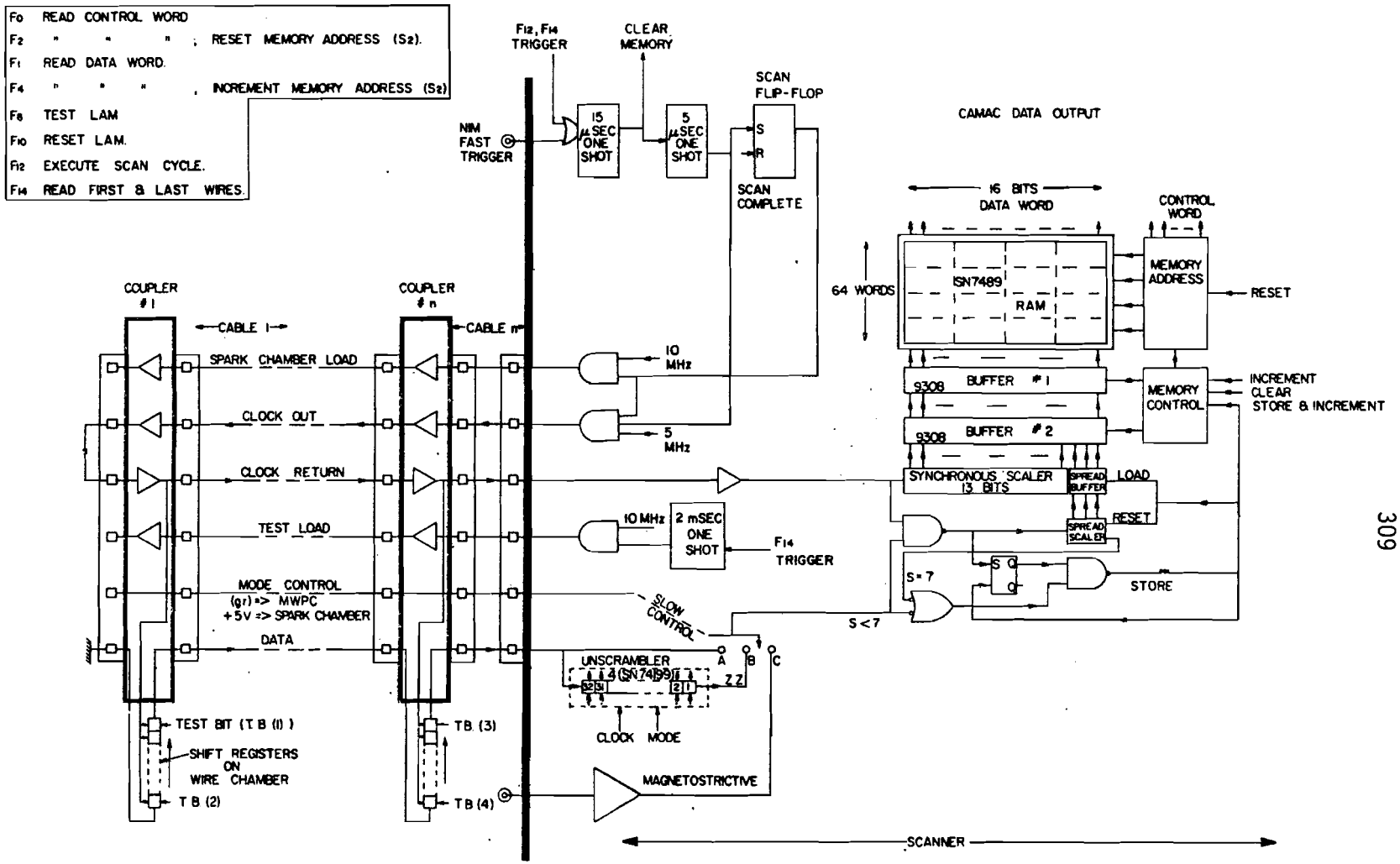
F0 READ CONTROL WORD
F2 " " " ; RESET MEMORY ADDRESS (S2).
F1 READ DATA WORD.
F4 " " " ; INCREMENT MEMORY ADDRESS (S2)
F8 TEST LAM
F10 RESET LAM.
F12 EXECUTE SCAN CYCLE.
F14 READ FIRST & LAST WIRES.
F12, F14 TRIGGER
CLEAR MEMORY
NIM FAST TRIGGER
15 μSEC ONE SHOT
5 μSEC ONE SHOT
SCAN FLIP-FLOP
S
R
SCAN COMPLETE
CAMAC DATA OUTPUT
16 BITS DATA WORD
CONTROL WORD
64 WORDS
SN7489 RAM
MEMORY ADDRESS
RESET
COUPLER #1
COUPLER #n
CABLE 1
CABLE n
SPARK CHAMBER LOAD
CLOCK OUT
CLOCK RETURN
TEST LOAD
MODE CONTROL
(gr) => MWPC
+5V => SPARK CHAMBER
DATA
10 MHz
5 MHz
9308 BUFFER #1
9308 BUFFER #2
MEMORY CONTROL
INCREMENT
CLEAR
STORE & INCREMENT
SYNCHRONOUS SCALER 13 BITS
SPREAD BUFFER
LOAD
RESET
SPREAD SCALER
10 MHz
2 mSEC ONE SHOT
F14 TRIGGER
S=7
S<7
STORE
SLOW CONTROL
UNSCRAMBLER 4 (SN74199)
A
B
C
CLOCK
MODE
TEST BIT (T B (1))
SHIFT REGISTERS ON WIRE CHAMBER
T B (2)
TB (3)
TB (4)
MAGNETOSTRICTIVE
SCANNER

APPENDIX 2

THE ON-LINE CONTROL SYSTEM

The major elements of the on-line control system for the spectrometer were a XDS Sigma-3 computer, an experimental control panel, a CAMAC data acquisition system, and the on-line program. The control system was designed to provide a great deal of flexibility and a minimum of confusion for the experimenter. We aimed for the goal that any physicist be able to run the experiment with almost zero knowledge of details. To keep confusion at a minimum, there were only four buttons to push and simple dialogues with an "English speaking" teletype.

The primary function of the on-line control system was to collect data for the experiment and record it on magnetic tape. In addition, it served to monitor the performance of the spectrometer and provided the basic control for the experiment. The organization is described in the following sections.

The Computer

The XDS Sigma-3 computer had a 64 K word core memory, word length of 16 bits, and a flexible hardware priority-interrupt system for real-time multi-task programming. It was equipped with a 750 K word drum, two 9-track tape drives, a card reader, a teletype, one line printer, and a Tektronix 611 storage display scope.

The prime merit of the Sigma-3 computer was the hardware priority-interrupt system. This hardware interrupt structure allowed the on-line control system to respond to event triggers at the highest priority level,

while performing basic control functions and monitoring the apparatus at lower priority. The computer was equipped with eight external hardware interrupt levels. Each of these levels was protected by two program controlled switches called "Arm" and "Enable," as shown in Figure 102. If a signal triggered a particular interrupt level which was "Armed" and "Enabled," and no higher priority interrupt level was active, then execution of any active lower priority task was suspended, and program control immediately passed to a routine to service this interrupt. At the same time, the protection switches for this interrupt level were opened (i.e., it became "Armed" and "Disabled") to prevent further interrupts at this level. Upon completion of the interrupt service routine, program control was returned to the interrupted task, and the protection switches were placed in an "Armed" and "Enabled" state, ready to receive the next interrupt signal. While the computer was servicing this interrupt level, it could be interrupted by a higher priority level interrupt. Service of this interrupt level could only be resumed after the higher priority task was completed.

Connection of programs to the priority levels was flexible. The highest priority levels were reserved for event triggers and logging the data on magnetic tape. The other levels were assigned to tasks which control and monitor the performance of the apparatus at lower priority as shown in Figure 102.

The Experimental Control Panel

The most important element in the control system was the experimental control panel. It consisted of four interlocked push buttons, labeled Begin Run, Stop, Run, End Run, as shown in Figure 103.

These four push buttons, which could only be operated in a definite sequence, provided the main control for the experiment. Contrary to common practice, the teletype was used only for communication rather than as a control device. (A great many of those colloquially meaningless action control characters often lead the physicist to frustration, and add prestige to the computer as a mysterious black box.) The on-line program was controlled by a set of toggle sense switches. The basic control functions of the experimental control panel are described below.

Begin Run

This push button was the first of the 32 sense switches. When activated, the begin-run sequence was initiated immediately since all interrupt levels were disarmed at this stage.

1) Clear scalers, hardware control flags, and zero regions of core memory for data input.
2) Request information on teletype: date and time, tape number, magnet settings, beam energy, etc. Also record any operator comments.
3) Execute a programmed hardware check of the spectrometer electronics.
4) Log pertinent run information on magnetic tape in a special format record.

Upon completion of the begin-run sequence, the hardware priority levels were "Armed" and "Enabled" and the experimental control panel was advanced to the "Stop" position.

Stop

This push button was an ordinary switch. Its function was to disrupt

the event interrupt chain and inhibit the scalers. It served as an intermediate halt device during the experiment.

Run

This push button was also an ordinary switch. It electrically completed the path leading to the highest priority interrupt level and removed the scaler inhibit. When this button was pushed, data-taking started immediately.

As illustrated in Figure 103, upon the occurrence of an event trigger, the highest priority interrupt was activated and the event data was read into the computer and logged onto magnetic tape. The event interrupt level and the fast electronics were blocked off by a "Rapid Kill" toggle that could only be reset by a programmed signal once the data acquisition and tape logging for the event was completed. The master event trigger was fanned out to activate the MWPC's, wire spark chambers, scintillation counter latches, noise blocking circuits for the MWPC's and scalers, and various CAMAC modules. The interrupt signal to the computer was delayed approximately 2 msec to allow all the CAMAC modules, particularly those which scanned the wire chambers, to get ready to send the data to the computer.

End Run

This push button was the third sense switch. It disrupted the event interrupt chain and inhibited the scalers. Data-taking stopped and the end-run sequence of the on-line program was executed.

1) "Disarm" and "Disable" all interrupt levels.

2) Print out a summary of the run on the line printer.

CAMAC Data Acquisition System

The experimental apparatus consisted of wire chambers of various type, scintillation counters, scalers, DVM, and ADC's, etc. All this equipment, plus electronics for monitoring the accelerator status, was interfaced to the Sigma-3 computer through a CAMAC Branch Highway incorporating up to seven CAMAC crates. Each CAMAC module had a "fast trigger" input which initiated module operations such as scanning a wire chamber, or latching a scintillation counter, etc. Upon completion of its internal cycle, each CAMAC module generated a "look-at-me" signal to inform the computer that it was ready to transfer data.

The data from the CAMAC system was read into the Sigma-3 computer through the DIO (Direct I/O) facility. Each CAMAC module was checked by the on-line program for an appropriate status (e.g., Q-response or look-at-me), and the data read into memory. The readout of the CAMAC system and tape writing took approximately 50 msec per event. The data for each event was packed into two regions of memory; one region for scintillation counter latches, scalers, ADC's, etc., and another for wire chamber data. After writing the event data onto magnetic tape, the on-line program generated a signal to reset the "Rapid Kill" toggle and remove the interrupt and scaler inhibits.

The On-line Program

The main tasks of the on-line computer program were data acquisition and tape logging; these were assigned the two highest priority interrupt levels. The remainder of the time was devoted to performing a simple analysis of a fraction of the event triggers recorded. The on-line analysis consisted of a set of programs (SORT's) and displays to monitor the performance

of the spectrometer. No attempt was made to do any physics calculations on-line.

The on-line analysis program was controlled by the set of thirty-two sense switches interfaced to the Sigma-3 computer. The status of each bit of the two words occupied by these 32 sense switches was scanned by a supervisor routine, SAMPLE, to determine which programs to execute. This offered the experimental physicist a great deal of flexibility in editing the analysis program in residence. Figure 104 shows a typical assignment of the sense switches.

In the on-line sample analysis, the event data was first decoded; the bit patterns of the counter latches and ADC's were unpacked; and the wire chamber data was converted into spatial spark coordinates. Control was then transferred to the SORT analysis routines. Each SORT was controlled (i.e., it could be turned on or off) by a sense switch. By simply flipping the sense switches, the experimenter could select what analysis was performed, and display results on a storage display scope, or direct the output to the line printer.

Fig. 102.--Schematic diagram of the hardware priority interrupt structure for on-line data acquisition.

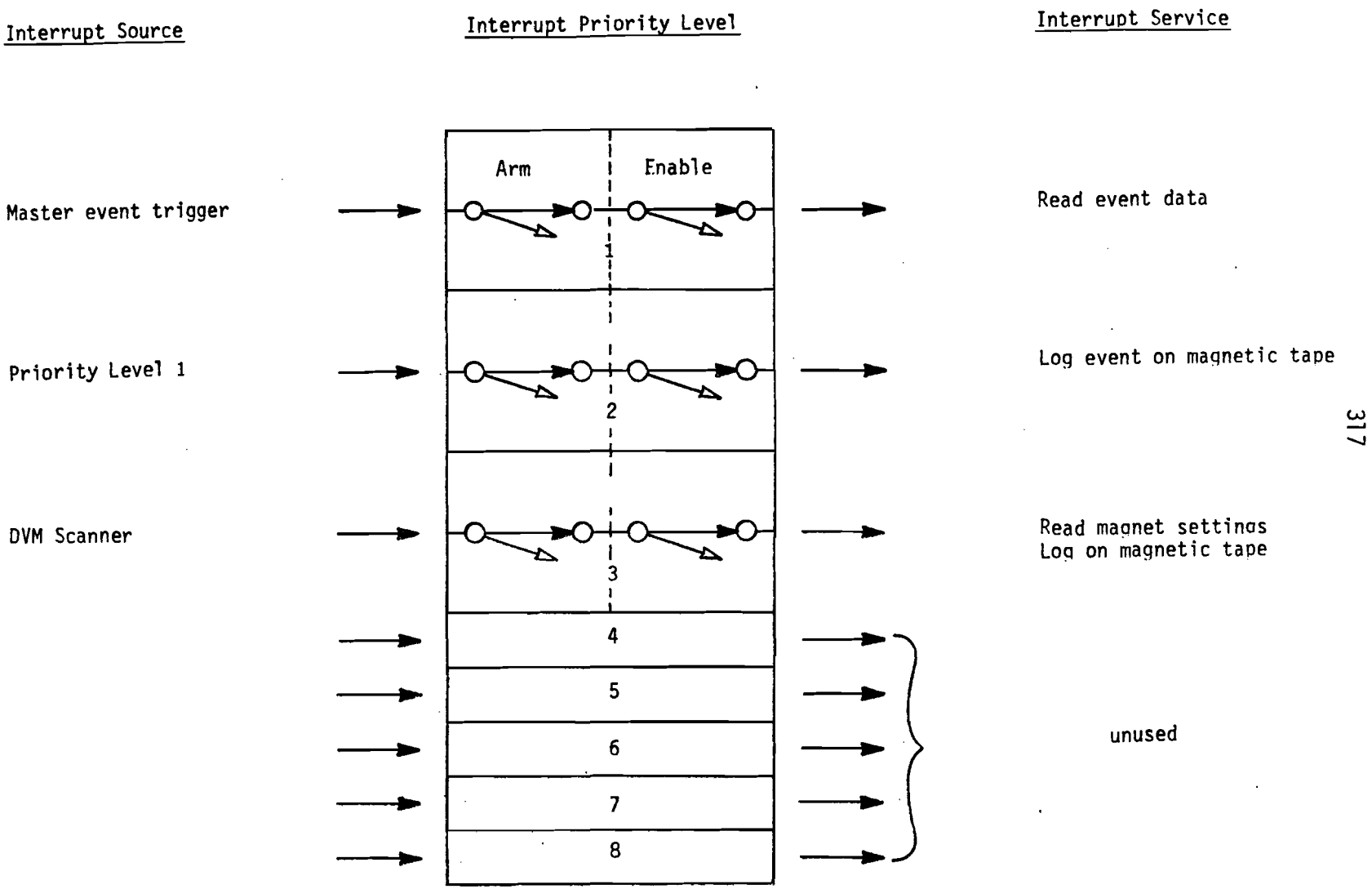
Interrupt Source
Interrupt Priority Level
Interrupt Service
Arm
Enable
Master event trigger
Read event data
1
Priority Level 1
Log event on magnetic tape
2
DVM Scanner
Read magnet settings
Log on magnetic tape
3
4
5
6
7
8
unused

Fig. 103.--Block diagram of the experimental control panel and on-line control system.

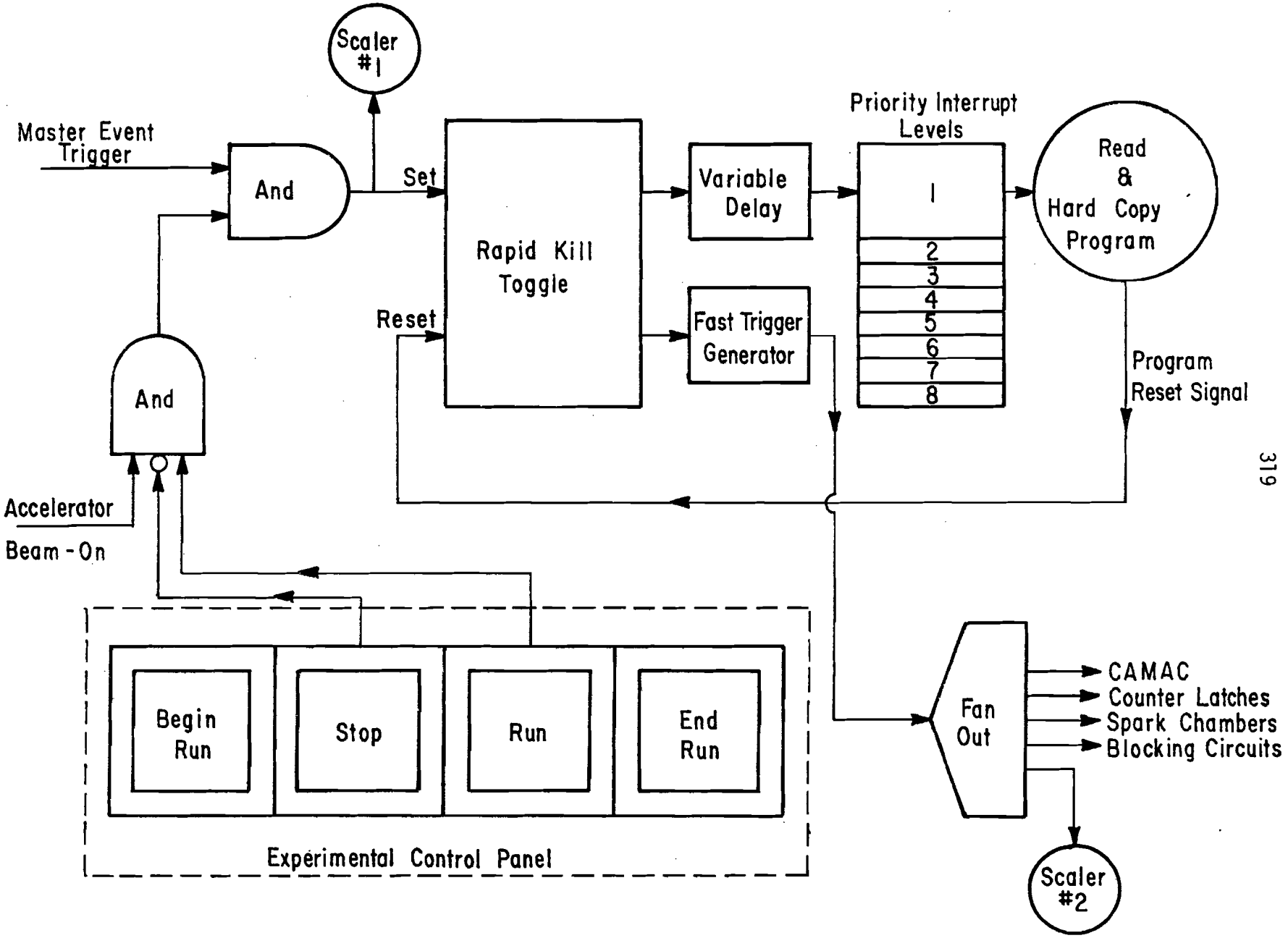
Scaler #1
Master Event Trigger
And
Set
Rapid Kill Toggle
Variable Delay
Priority Interrupt Levels
1
2
3
4
5
6
7
8
Read & Hard Copy Program
Reset
Fast Trigger Generator
Program Reset Signal
And
Accelerator Beam - On
Begin Run
Stop
Run
End Run
Experimental Control Panel
Fan Out
CAMAC
Counter Latches
Spark Chambers
Blocking Circuits
Scaler #2

Fig. 104.--Typical sense switch assignments for control of the on-line data acquisition program.

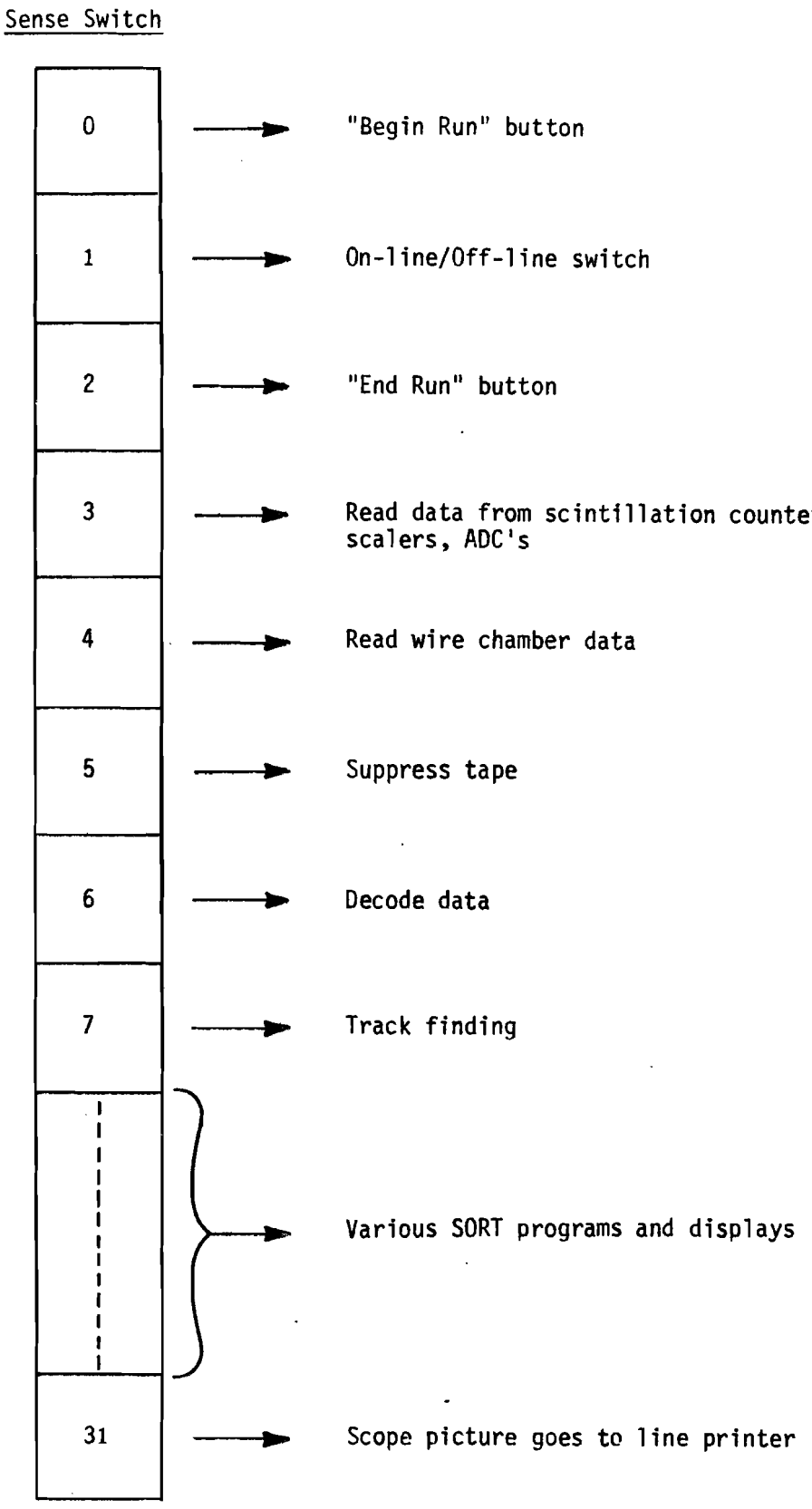
Sense Switch
0
"Begin Run" button
1
On-line/Off-line switch
2
"End Run" button
3
Read data from scintillation counters, scalers, ADC's
4
Read wire chamber data
5
Suppress tape
6
Decode data
7
Track finding
Various SORT programs and displays
31
Scope picture goes to line printer

APPENDIX 3

KINEMATICS

This appendix is intended to provide a convenient reference for the definitions of kinematic variables and formulae used frequently in the text. The first section primarily contains variables and formulae used in the discussion of the muon inclusive cross section and nucleon structure functions. The second section pertains mainly to the analysis of the final state hadrons. We use the convention $\hbar = c = 1$. Energy and mass are expressed in GeV, momentum in GeV/c.

Muon Kinematics

Variables

E = energy of incident muon

P = momentum of incident muon

E' = energy of scattered muon

P' = momentum of scattered muon

θ = angle of scattered muon

q^2 = four-momentum transfer-squared ($q^2 \geq 0$)

ν = energy loss of scattered muon

W = total mass of final hadronic system

M = proton (neutron) mass

M_D = deuteron mass

m_μ = muon mass

m_e = electron mass

m_π = pion mass

$\omega = \frac{2M\nu}{q^2}$ (Bjorken scaling variable)

$x = \frac{1}{\omega}$ (Feynman scaling variable)

Formulae

$$q^2 = 2(EE'-PP'\cos\theta-m_\mu{}^2)$$

$$\nu = E - E'$$

$$W^2 = M^2 + 2M\nu - q^2$$

Cross Sections and Structure Functions

$$\frac{d^2\sigma}{dq^2d\nu} = \left(\frac{\pi}{PP'}\right)\frac{2\alpha^2}{q^4}\left(\frac{P'}{P}\right)\left[(2EE'-q^2/2)W_2(q^2,\nu) + (q^2-2m_\mu{}^2)W_1(q^2,\nu)\right]$$

$$\frac{d^2\sigma}{d\Omega dE'} = \left(\frac{PP'}{\pi}\right)\frac{d^2\sigma}{dq^2d\nu}$$

$$\frac{d^2\sigma}{dq^2d\nu} = \Gamma_T(q^2,\nu)\left[\sigma_T(q^2,\nu) + \varepsilon\sigma_L(q^2,\nu)\right] = \Gamma_T(q^2,\nu)\sigma_{total}(q^2,\nu)$$

$$\Gamma_T(q^2,\nu) = \left(\frac{\pi}{PP'}\right)\frac{\alpha}{2\pi^2}\frac{K}{q^2}\left(\frac{E'}{E}\right)\frac{1}{(1-\varepsilon)}$$

$$K = \frac{W^2 - M^2}{2M}$$

$$\varepsilon = \frac{1}{1 + \frac{2(q^2+\nu^2)\tan^2\theta/2}{q^2(1-q^2_{min}/q^2)^2}}$$

$$q^2_{min} = 2(EE'-PP'-m_\mu{}^2)$$

$$W_1 = \frac{K}{4\pi^2\alpha}\sigma_T$$

$$W_2 = \frac{K}{4\pi^2\alpha}\frac{q^2}{q^2+\nu^2}(\sigma_T + \sigma_L)$$

$$\frac{W_1}{W_2} = (1 + \frac{\nu^2}{q^2})/(1 + R)$$

$$R = \sigma_L/\sigma_T$$

Hadron Kinematics

E_h = energy of hadron (lab)

p_h = momentum of hadron (lab)

$p_\parallel$ = hadron momentum parallel to direction of virtual photon

$p_\perp$ = hadron momentum perpendicular to direction of virtual photon

p_n = hadron momentum normal to the scattering plane of the incoming and and outgoing muon

t = four-momentum transfer-squared between virtual photon and single detected hadron in virtual photoproduction

MM = missing mass of single detected hadron in virtual photoproduction

y = longitudinal rapidity of hadron

$$S = W^2 = 2M\nu + M^2 - q^2$$

$$t = -q^2 + m_\pi^2 - 2E_h\nu + 2p_\parallel\sqrt{q^2 + \nu^2}$$

$$t_{min} = -q^2 + m_\pi^2 - 2E_h\nu + 2p_h\sqrt{q^2 + \nu^2}$$

$$MM^2 = W^2 + m_\pi^2 - 2E_h(\nu+M) + 2p_\parallel\sqrt{q^2 + \nu^2}$$

$$p_{max}^{cm} = \frac{\sqrt{\Delta(W^2, m_\pi^2, (M+m_\pi)^2}}{2W}$$

$$\Delta(x,y,z) = x^2 + y^2 + z^2 - 2xy - 2yz - 2zx$$

$$x_\parallel = \frac{p_\parallel^{cm}}{p_{max}^{cm}}$$

$$x_\perp = \frac{p_\perp}{p_{max}^{cm}}$$

$$y = \tfrac{1}{2}\ell n\left[\frac{E_h + p_\parallel}{E_h - p_\parallel}\right]$$

APPENDIX 4

ELECTROMAGNETIC FORM FACTORS OF THE DEUTERON

The deuteron is the simplest bound state of the nucleus. As such, the understanding of its structure and internal dynamics is of fundamental importance. The deuteron has played a significant role in our study of the strong interactions, and as a weakly bound neutron target has been the primary source of information on the electromagnetic structure of the neutron.

The best measurements of the neutron's electromagnetic form factors have come from the scattering of electrons from deuterons. The analysis of these experiments, however, is considerably complicated by problems related to the deuteron's electromagnetic structure. In order to extract information about the neutron, we must take into account the effects due to the Fermi motion within the nucleus, and be able to subtract the contributions of the proton. For this experiment we must also be able to calculate the radiative corrections from elastic and quasi-elastic deuteron scattering. Both these problems require a detailed knowledge of the electromagnetic structure of the deuteron. Unfortunately, the deuteron wave function is largely unknown at distances smaller than about 0.5 fermi, and we must resort to the use of a phenomenological model to calculate the electromagnetic form factors of the deuteron. Many suggested forms for the deuteron wave function are found in the literature.[85] We have investigated three, which are discussed in the following section.

Deuteron Wave Function

It is well known that the deuteron wave function is primarily an $^3S_1$ wave with a small admixture (~6%) of $^3D_1$:[86]

$$\psi^M(\theta,\phi) = \frac{u(r)}{r}\mathcal{Y}^M_{110}(\theta,\phi) + \frac{w(r)}{r}\mathcal{Y}^M_{112}(\theta,\phi) \quad , \tag{A4.1}$$

where $\mathcal{Y}^M_{JSL}(\theta,\phi)$ are the orthonormal eigenfunctions of total angular momentum J, total spin S, and orbital angular momentum L. The functions u(r) and w(r) are the radial parts of the S and D components of the wave function. The eigenfunctions $\mathcal{Y}^M_{JSL}(\theta,\phi)$ can also be written as a Clebsh-Gordon decomposition into eigenfunctions of orbital angular momentum and intrinsic spin:

$$\mathcal{Y}^M_{JSL}(\theta,\phi) = \sum_{M_s} \langle L,S,M-M_s,M_s|J,M\rangle Y_L^{M-M_s}(\theta,\phi)\chi_s^{M_s} \quad . \tag{A4.2}$$

We have studied the deuteron problem using three different phenomenological wave functions. These non-relative wave functions are solutions of the Schrodinger equation for the two-nucleon problem using various proposed nucleon interaction potentials. The major difference between the models is in the way they treat the nucleon potential at small distances. The Reid Hard Core model[87] incorporates an infinitely repulsive core which produces a sharp cutoff in the wave function at approximately 0.5 fm, and introduces rapid oscillations of the wave function in momentum space. The Reid Soft Core model[87] is similar to the Reid Hard Core except that the wave function continues smoothly to the origin. The Hulthen model[88] is another soft core model which is convenient for calculations since the wave functions have a simple analytic form. The Reid Soft Core wave function was used to calculate

The deuteron form factors since it agrees well with recent elastic eD scattering data.[89] The existing data cannot distinguish between models with hard and soft cores. Figure 105a shows the two radial wave functions, u(r) and w(r), for the Reid Soft Core model. Figure 105b illustrates the differences between the Hulthen and the two Reid wave functions at small distances.

In momentum space, the deuteron wave function is given by

$$\psi^M(\vec{p}) = \frac{1}{(2\pi)^{3/2}} \int d^3r e^{-i\vec{p}\cdot\vec{r}} \psi^M(\vec{r}) \quad . \tag{A4.3}$$

Using the expansion

$$e^{i\vec{p}\cdot\vec{r}} = \sum_{\ell=0}^{\infty} 4\pi i^{\ell} j_{\ell}(pr) \sum_{m=-\ell}^{\ell} Y_{\ell}^{m*}(\theta,\phi) Y_{\ell}^{m}(\theta',\phi') \quad , \tag{A4.4}$$

it can be written as

$$\psi^M(\vec{p}) = u(p)\mathcal{Y}_{110}^{M}(\theta,\phi) + w(p)\mathcal{Y}_{112}^{M}(\theta,\phi) \quad , \tag{A4.5}$$

where

$$u(p) = \frac{1}{\sqrt{2\pi}} \int \frac{u(r)}{r} j_0(pr) r^2 dr$$

$$w(p) = \frac{1}{\sqrt{2\pi}} \int \frac{w(r)}{r} j_2(pr) r^2 dr \quad .$$

The functions u(p) and w(p) are the S and D radial components in momentum space. These are shown in Figure 106a for the Reid Soft Core model.

Averaging over the initial deuteron polarization and doing the angular integration, the probability for finding a nucleon with momentum p is given by:

$$|f(p)|^2 = |u(p)|^2 + |w(p)|^2 \quad .$$

Figure 106b shows f(p) calculated for the three wave functions studied.

Deuteron Elastic Form Factors

The elastic eD cross section can be written as

$$\frac{d\sigma}{d\Omega} = \frac{4\alpha^2 E'}{q^4} \frac{\cos^2\theta/2}{1 + \frac{2E}{M_D}\sin^2\theta/2} \left[G_E(q^2)^2 + G_Q(q^2)^2 + \left[1+2(1+\eta_D)\tan^2\theta/2\right] G_M(q^2)^2 \right]$$

where

$$\eta_D = q^2/4M_D^2 \quad .$$

$G_E(q^2)$, $G_Q(q^2)$, and $G_M(q^2)$ are the charge, quadrupole, and magnetic form factors of the deuteron, respectively. These were calculated in the impulse approximation according to the method of Griffy and Schiff:[90]

$$G_E(q^2) = G_E^{\,s}(q^2)(1 + \eta_D)^{-1} \int_0^\infty (u^2+w^2) j_0(|\vec{q}|r/2)dr \qquad \text{(A4.7)}$$

$$G_Q(q^2) = \left[G_E^{\,s}(q^2)(1 + \eta_D)^{-1} \int_0^\infty 2w(u-w/\sqrt{8}) j_2(|\vec{q}|r/2)dr \right. \qquad \text{(A4.8)}$$

and

$$G_M(q^2) = \sqrt{\frac{2}{3}} \frac{q}{2M} \left[G_M^{\,s}(q^2) \int_0^\infty (u^2 - w^2/2) j_0(|\vec{q}|r/2)dr \right. \qquad \text{(A4.9)}$$

$$+ \frac{G_M^{\,s}(q^2)}{\sqrt{2}} \int_0^\infty w(u+w/\sqrt{2}) j_2(|\vec{q}|r/2)dr$$

$$\left. + \frac{3}{4} G_E^{\,s}(q^2) \int_0^\infty w^2 \left[j_0(|q|r/2) + j_2(|\vec{q}|r/2) \right] dr \right] ,$$

where

$$\begin{aligned} G_E^{\,s}(q^2) &\equiv G_E^{\,p}(q^2) + G_E^{\,n}(q^2) \quad , \\ G_M^{\,s}(q^2) &\equiv G_M^{\,p}(q^2) + G_M^{\,n}(q^2) \quad . \end{aligned} \qquad \text{(A4.10)}$$

The "dipole" form factors were used for the proton and neutron:

$$G_E^n(q^2) = 0$$

$$G_E^p(q^2) = \frac{G_M^p(q^2)}{2.793} = \frac{G_M^n(q^2)}{-1.91} = \frac{1}{(1 + q^2/0.71)^2} \quad . \tag{A4.11}$$

Figure 107 shows the deuteron form factors, G_E, G_Q, and G_M, calculated for the Reid Soft Core wave function. Figure 108 is a plot of the integrals used in their definition.

Fig. 105.--Three phenomenological wave functions for the deuteron. (a) The two radial components, u(r) and w(r), for the Reid Soft Core model. (b) Comparison of the different wave functions at small distances.

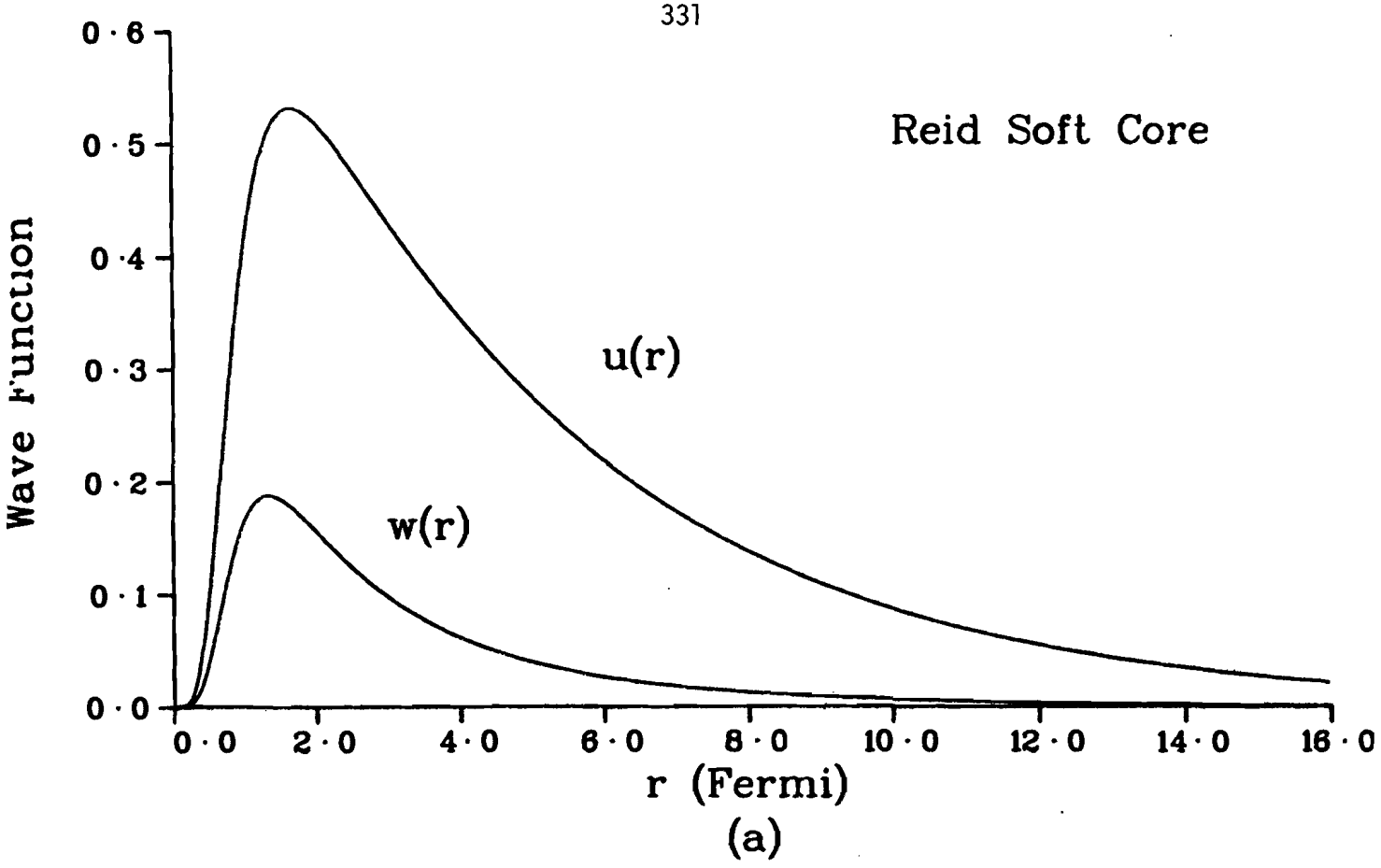
Reid Soft Core
u(r)
w(r)
Wave Function
0·0
0·1
0·2
0·3
0·4
0·5
0·6
0·0
2·0
4·0
6·0
8·0
10·0
12·0
14·0
16·0
r (Fermi)

(a)

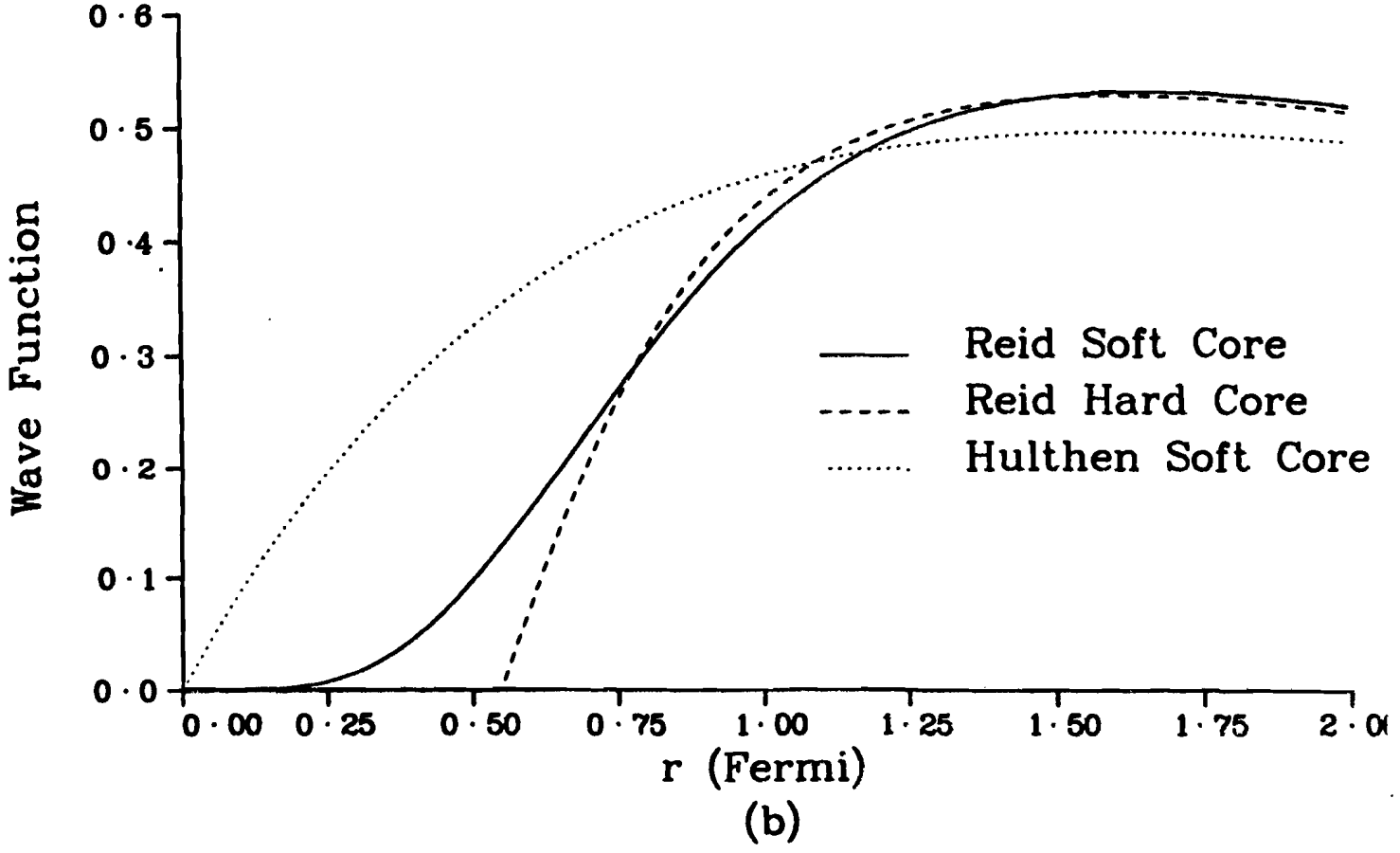
Wave Function
0·0
0·1
0·2
0·3
0·4
0·5
0·6
0·00
0·25
0·50
0·75
1·00
1·25
1·50
1·75
2·0
r (Fermi)
Reid Soft Core
Reid Hard Core
Hulthen Soft Core

(b)

Fig. 106.--Deuteron wave functions in momentum space. (a) The two radial components, u(p) and w(p), for the Reid Soft Core model. (b) f(p) for the Reid Soft Core, Reid Hard Core, and Hulthen wave functions.

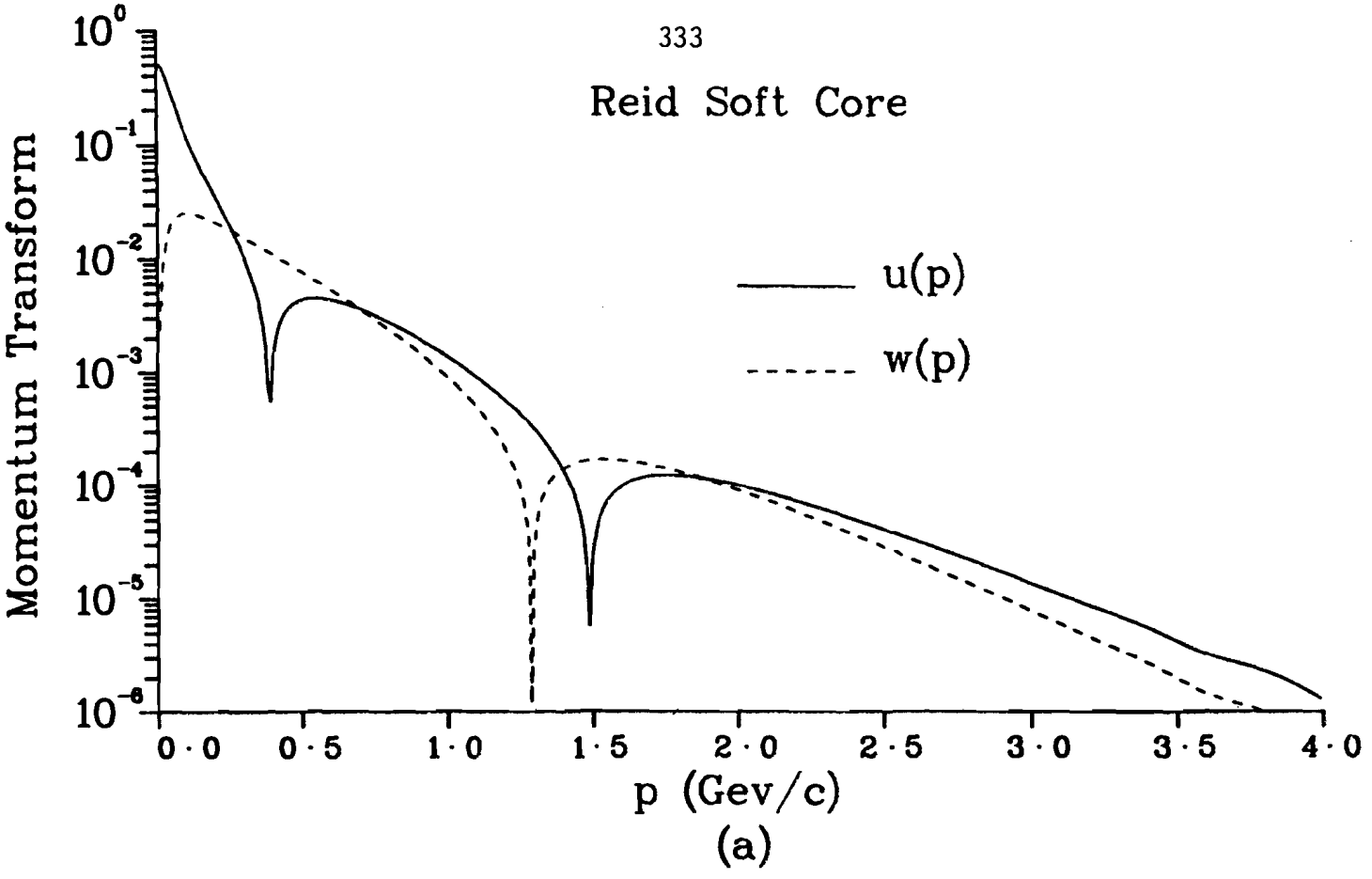
Reid Soft Core
Momentum Transform
u(p)
w(p)
p (Gev/c)

(a)

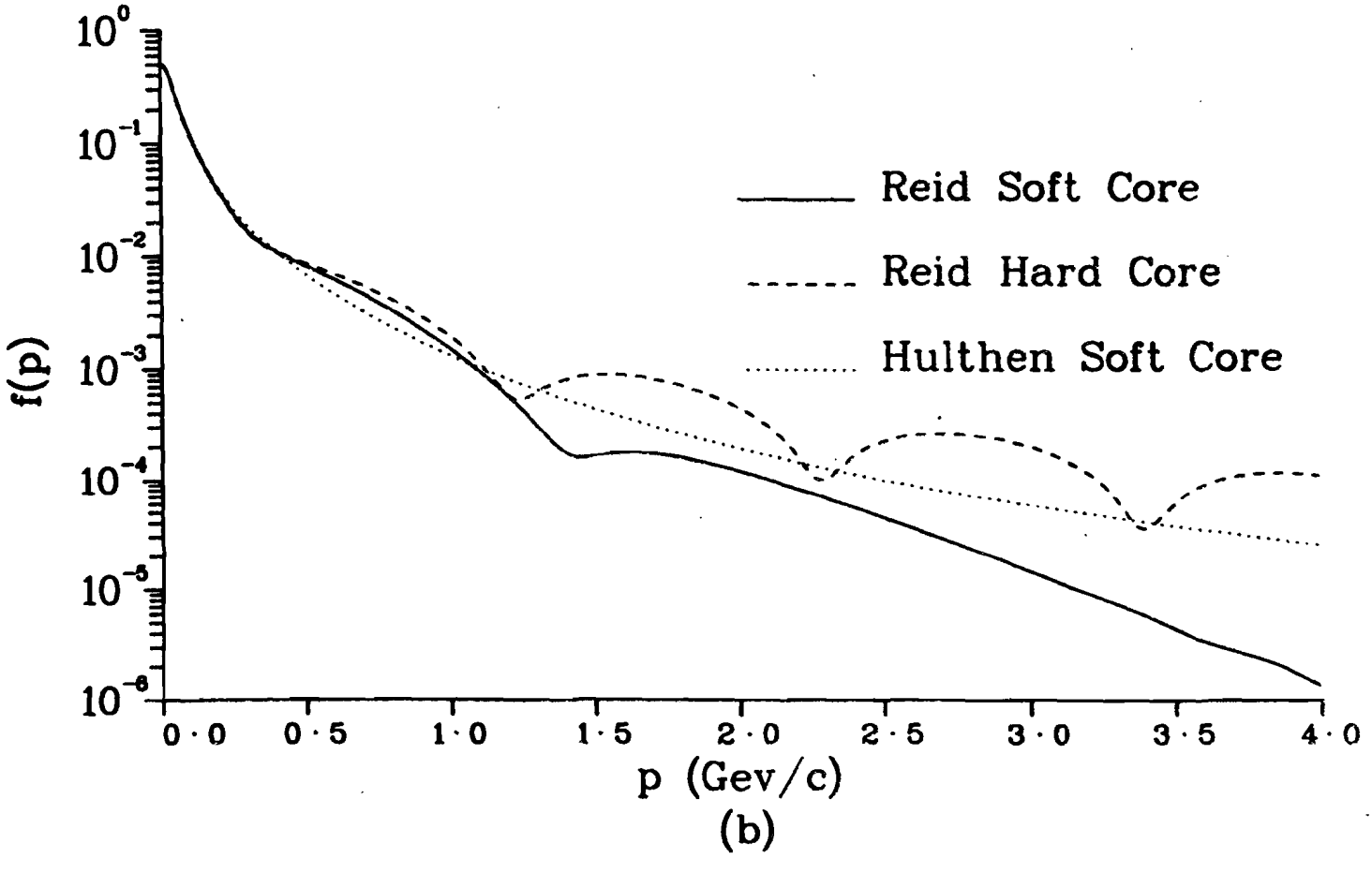
f(p)
Reid Soft Core
Reid Hard Core
Hulthen Soft Core
p (Gev/c)

(b)

Fig. 107.--The electromagnetic form factors of the deuteron, calculated using the Reid Soft Core model. $G_E(q^2)$, $G_Q(q^2)$, and $G_M(q^2)$ are the charge, quadrupole, and magnetic form factors of the deuteron, respectively.

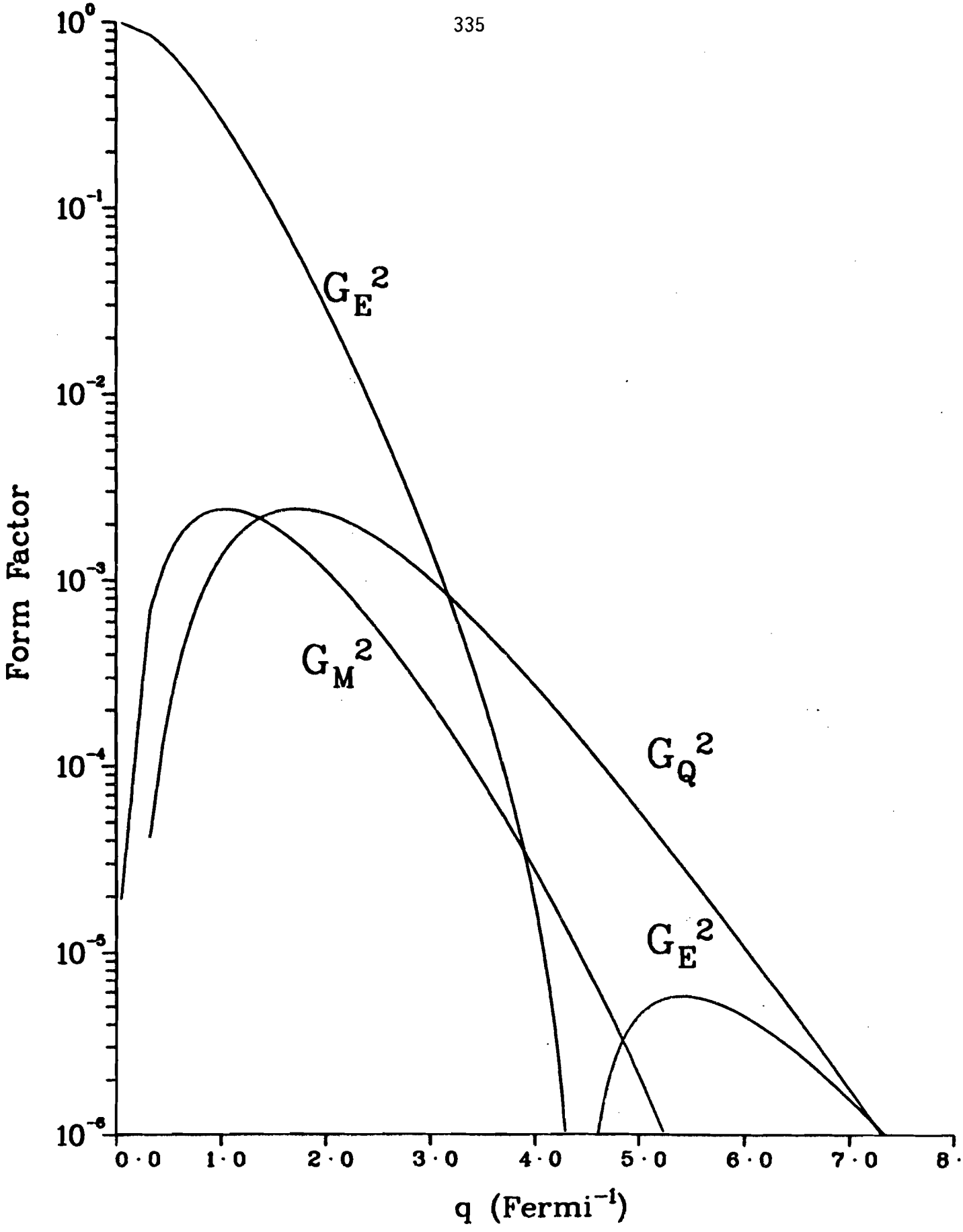
Form Factor
10^{0}
10^{-1}
10^{-2}
10^{-3}
10^{-4}
10^{-5}
10^{-6}
G_E^2
G_M^2
G_Q^2
G_E^2
0·0
1·0
2·0
3·0
4·0
5·0
6·0
7·0
8·
q (Fermi^{-1})

Fig. 108.--Integrals used to calculate the deuteron electromagnetic form factors in the impulse approximation of Griffy and Schiff.[90] The Reid Soft Core wave function was used in the calculation.

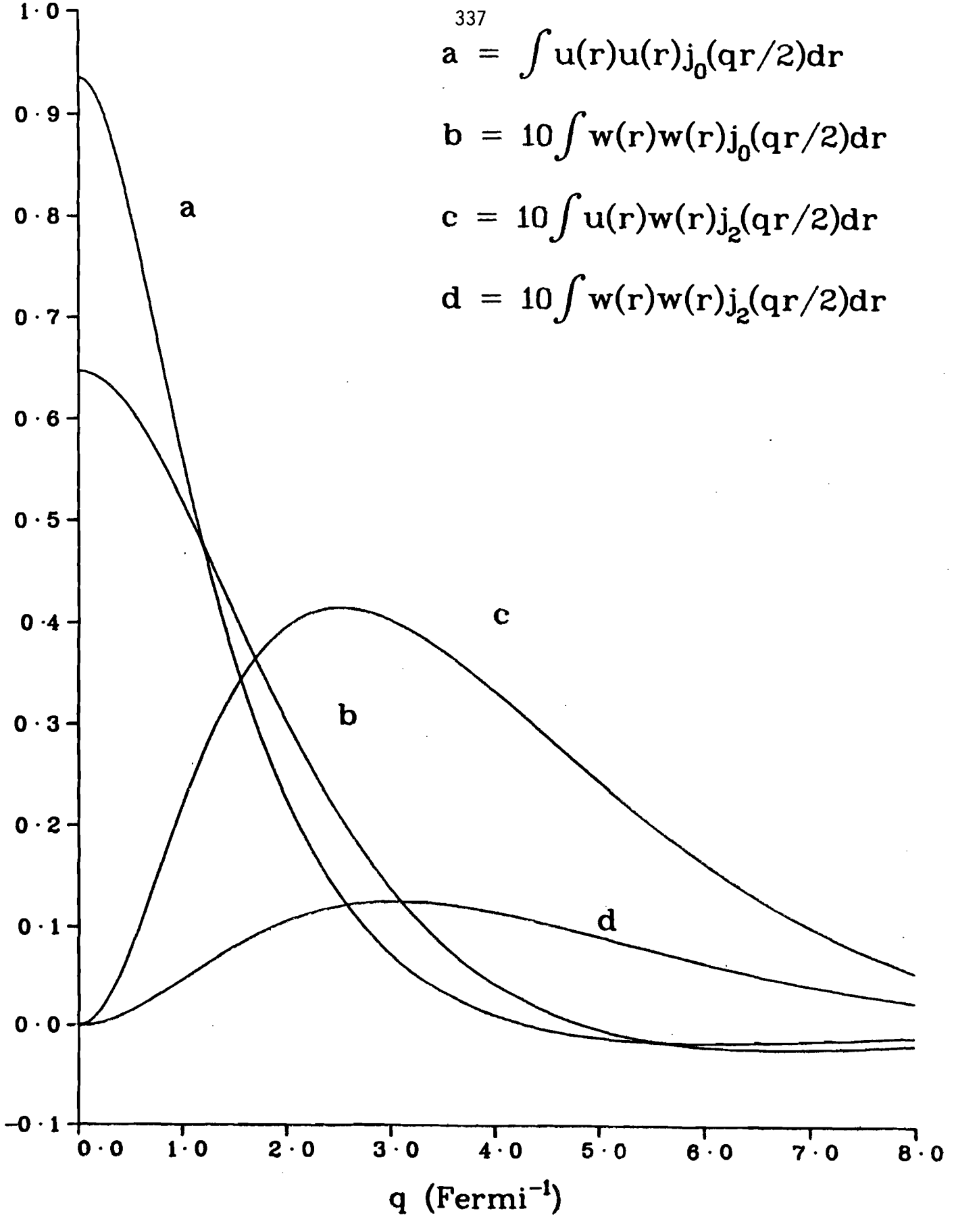
a = ∫u(r)u(r)j0(qr/2)dr
b = 10∫w(r)w(r)j0(qr/2)dr
c = 10∫u(r)w(r)j2(qr/2)dr
d = 10∫w(r)w(r)j2(qr/2)dr
a
b
c
d
1·0
0·9
0·8
0·7
0·6
0·5
0·4
0·3
0·2
0·1
0·0
-0·1
0·0
1·0
2·0
3·0
4·0
5·0
6·0
7·0
8·0
q (Fermi⁻¹)

APPENDIX 5

RADIATIVE CORRECTIONS

This appendix contains a discussion of the procedures used to evaluate the ratio $\delta_R(q^2,\nu)$, defined as

$$\delta_R(q^2,\nu) = \frac{\sigma^{Theory}}{\sigma^{Experimental}} \quad , \tag{A5.1}$$

in applying the radiative corrections to the muon inclusive cross section. As outlined in Chapter IV, the radiative corrections were calculated according to the method of Mo and Tsai.[50] The following discussion is divided into four sections: (1) the elastic radiative tail from elastic μp scattering, (2) the deuteron elastic radiative tail, (3) the radiative tail from quasi-elastic deuteron scattering, and (4) the radiative corrections to the inelastic muon cross section.

Proton Elastic Radiative Tail

The formulation needed for calculating the radiative tail due to the elastic peak in the deep inelastic region is given by:

$$\frac{d\sigma_{t+r}(E_s,E_p,T)}{d\Omega dE_p} = \frac{d\sigma_r(E_s,E_p,T)}{d\Omega dE_p} + \frac{d\sigma_r(E_s,E_p,T)}{d\Omega dE_p} \quad , \tag{A5.2}$$

where the first term on the right-hand side is due to muon straggling in the target, and the second term is due to the internal bremsstrahlung. T is the thickness of the target in radiation lengths. For the elastic scattering of

muons, the effect of straggling in the target can be neglected since the muon bremsstrahlung in the target is reduced by a factor of $(m_e/m_\mu)^2$ ~1/40,000 as compared with that of electrons.

The expression for the radiative tail from the elastic peak is given by

$$\frac{d^2\sigma_r}{d\Omega dp} = \frac{\alpha^3 E_p}{(2\pi)^2 M E_s} \int_{-1}^{1} \frac{\omega d(\cos\theta_k)}{2q^4(u_o - |u|\cos\theta_k)} \; X \int_0^{2\pi} B_{\mu\nu} T_{\mu\nu} d\phi_k \quad , \tag{A5.3}$$

where

$$B_{\mu\nu}T_{\mu\nu} = M^2 F(q^2)\left\{\frac{-m^2}{(pk)^2}\left[2E_s(E_p+\omega)+\tfrac{1}{2}q^2\right] - \frac{m^2}{(sk)^2}\left[2E_p(E_s-\omega)+\tfrac{1}{2}q^2\right] - 2\right.$$

$$+ \frac{2}{(sk)(pk)}\{m^2(sp-\omega^2)+(ps)\left[2E_sE_p-(ps)+\omega(E_s-E_p)\right]\}$$

$$\left. + (pk)^{-1}\left[2(E_sE_p+E_s\omega+E_p^2)+\tfrac{1}{2}q^2-(sp)-m^2\right] - (sk)^{-1}\left[2(E_sE_p-E_p\omega+E_s^2)+\tfrac{1}{2}q^2-(sp)-m^2\right]\right\}$$

$$+ G(q^2)\left(m^2(2m^2+q^2)\{\left[1/(pk)^2\right]+\left[1/(sk)^2\right]\} + 4\right.$$

$$\left. + \frac{4(ps)(ps-2m^2)}{(pk)(sk)} + (2ps+2m^2-q^2)\left[(pk)^{-1}-(sk)^{-1}\right]\right) ,$$

and

$s = (E_s, \vec{s})$ four-momentum of the incident muon,

$p = (E_p, \vec{p})$ four-momentum of the outgoing muon,

$p_i = (M, o)$ four-momentum of the target particle,

$k = (\omega, \vec{k})$ four-momentum of the real photon emitted,

$p_f = s + p_i - p - k$ four-momentum of the final hadronic system,

$u = (u_o, \vec{u}) \equiv s + p_i - p = p_f + k$,

$$\nu = \frac{- p\sin\theta_p}{\omega E_p|s|\sin\theta_s - E_s|p|\sin\theta_p + |s||p|\sin\theta\cos\theta_k} ,$$

$$\nu' = \frac{-|s|\sin\theta_s}{\omega\, E_p|s|\sin\theta_s - E_s|p|\sin\theta_p + |s||p|\sin\theta\cos\theta_k}$$

$a = \omega(E_p - |p|\cos\theta_p\cos\theta_k)$,

$b = -\omega|p|\sin\theta_p\sin\theta_k$,

$a' = \omega(E_s - |s|\sin\theta_s\cos\theta_k)$,

$b' = -\omega|s|\sin\theta_s\sin\theta_k$,

θ_k = angle between k and u,

θ_p = angle between p and u,

θ_s = angle between s and u,

$q^2 = 2m^2 - 2E_sE_p + 2|s||p|\cos\theta - 2\omega(E_s - E_p) + 2\omega|u|\cos\theta_k$,

and ω is the photon energy equal to $\frac{1}{2}(u^2 - M^2)/(u_o - |u|\cos\theta_k)$.

The two form factors for the proton, $F(q^2)$ and $G(q^2)$, are defined as:

$$F(q^2) = \frac{4}{1+\tau}\left[G_E^{\,p}(q^2)^2 + \tau G_M^{\,p}(q^2)^2\right]$$

$$G(q^2) = q^2 G_M^{\,p}(q^2)^2 \qquad \text{(A5.4)}$$

where

$$\tau = q^2/4M^2 \quad .$$

The "dipole" form factors were used:

$$G_E^{\,p}(q^2) = \frac{G_M^{\,p}(q^2)}{2.793} = \frac{1}{(1 + q^2/0.71)^2} \quad . \qquad \text{(A5.5)}$$

The integrated result is given as the following:

$$\frac{d^2\sigma_r}{d\Omega dp} = \frac{\alpha^3}{(2\pi)^2}\left(\frac{E_p}{E_s}\right)M^{-1}\int_{-1}^{1} \frac{d(\cos\theta_k)}{2q^4(u_o - |u|\cos\theta_k)} \qquad \text{(A5.6)}$$

$$X \left(M^2 F(q^2) \left\{ \frac{-2\pi a m^2}{(a^2-b^2)^{3/2}} \left[2E_s(E_p+\omega)+\frac{q^2}{2} \right] - \frac{2\pi a' m^2}{(a'^2-b'^2)^{3/2}} \left[2E_p(E_s-\omega)+\frac{q^2}{2} \right] - 4\pi \right. \right.$$

$$+4\pi \left(\frac{\nu}{(a^2-b^2)^{1/2}} - \frac{\nu'}{(a'^2-b'^2)^{1/2}} \right) \left\{ m^2(sp-\omega^2)+(sp)\left[2E_s E_p-(sp)+\omega(E_s-E_p) \right] \right\}$$

$$+ \frac{2\pi}{(a^2-b^2)^{1/2}} \left[2(E_s E_p+E_s\omega+E_s{}^2)+\frac{q^2}{2}-(sp)-m^2 \right]$$

$$\left. - \frac{2\pi}{(a'^2-b'^2)^{1/2}} \left[2(E_s E_p-E_p\omega+E_s{}^2)+\frac{q^2}{2}-(sp)-m^2 \right] \right\}$$

$$+ G(q^2) \left[\left(\frac{2\pi a}{(a^2-b^2)^{3/2}} + \frac{2\pi a'}{(a'^2-b'^2)^{3/2}} \right) m^2(2m^2+q^2)+8\pi \right.$$

$$\left. \left. + 8\pi \left(\frac{\nu}{(a^2-b^2)^{1/2}} - \frac{\nu'}{(a'^2-b'^2)^{1/2}} \right)(sp)(sp-2m^2)+2\pi \left[(a^2-b^2)^{-1/2}-(a'^2-b'^2)^{-1/2} \right](2sp+2m^2-q^2) \right] \right) .$$

Figure 109 shows the calculated radiative tail for elastic μp scattering with 150 GeV muons.

Deuteron Elastic Radiative Tail

The calculation of the radiative tail from elastic deuteron scattering is identical to the proton case, except that the elastic form factors of the deuteron must be used in evaluating $F(q^2)$ and $G(q^2)$:

$$F(q^2) = 4 \left[G_E{}^D(q^2)^2 + G_M{}^D(q^2)^2 + G_Q{}^D(q^2)^2 \right] ,$$

and

$$G(q^2) = 4M_D{}^2(1+\eta_D)G_M{}^D(q^2)^2 , \qquad \text{(A5.7)}$$

where

$$\eta_D = q^2/4M_D{}^2 .$$

The three form factors $G_E^D(q^2)$, $G_M^D(q^2)$, and $G_Q^D(q^2)$ are the electric, magnetic, and quadrupole form factors for the deuteron, respectively. These form factors were calculated using a method by Griffy and Schiff,[90] with a phenomenological wave function for the deuteron by Reid.[87] This calculation was described in Appendix 4.

Figure 110 shows the calculated μD radiative tail for 150 GeV incident muons.

Deuteron Quasi-elastic Radiative Tail

In calculating the radiative tail from the quasi-elastic peak, we simply added together the elastic radiative tails from the proton and neutron. The quasi-elastic cross section may be written to good approximation as the sum of the proton and neutron cross sections.[91] The form factors used for the neutron are given by

$$G_E^n(q^2) = 0$$
$$G_M^n(q^2) = \frac{-1.91}{(1 + q^2/0.71)^2} \tag{A5.8}$$

One can also do this calculation in a slightly more sophisticated manner, but numerically there is very little difference.[92]

Inelastic Radiative Corrections

The radiative inelastic cross section can be written as:

$$\frac{d^2\sigma\ (E_s,E_p)}{d\Omega dE_p} = \frac{d^2\sigma}{d\Omega dE_p}(E_s,E_p)\exp\delta_r$$
$$+ \left(\frac{\Delta}{E_p}\right)^{(\frac{1}{2})t_p} \int_{E_{s\min}(E_p)}^{E_s-\Delta} \frac{dE_s'}{E_s-E_s'}\, t_s\left[x_s + \frac{3}{4}(1-x_s)^2\right](\ell n x_s^{-1})^{t_s} \frac{d^2\sigma}{d\Omega dE_p}(E_s',E_p) \tag{A5.9}$$

$$+ \left(\frac{\Delta}{E_s}\right)^{(\frac{1}{2})f_s} \int_{E_p+\Delta}^{E_{p\,max}(E_s)} \frac{dE_p'}{E_p'-E_p}\, t_p\left[x_p + \frac{3}{4}(1-x_p)^2\right](\ell n x_p^{-1})^{f_p}\, \frac{d^2\sigma}{d\Omega dE_p'}(E_s, E_p') \quad ,$$

where $\frac{d^2\sigma}{d\Omega dE_p}$ is the non-radiative cross section, and

$$\begin{aligned}
x_s &= E_s'/E_s \quad , \qquad x_p = E_p/E_p' \quad , \\
t_r &= b^{-1}(\alpha/\pi)\, \ell n(2sp/m^2) - 1 \\
f_s &= bt_r \quad , \qquad f_p = bt_r \quad , \\
t_{s,p} &= (\alpha/\pi)\{\tfrac{1}{2}(1 + x_{s,p}^{\,2})\ell n\left[2(sp)/m^2\right] - x_{s,p}\} \quad , \\
E_{s_{min}}(E_p) &= (m_\pi^2 + 2M_p m_\pi + 2M_p E_p)/\left[2M_p - 2E_p(1 - \cos\theta)\right] \quad , \\
E_{p_{max}}(E_s) &= (2M_p E_s - 2M_p m_\pi - m_\pi^2)/\left[2M_p + 2E_s(1 - \cos\theta)\right] \quad .
\end{aligned} \tag{A5.10}$$

The function δ_r is given by:

$$\delta_r = \frac{-\alpha}{\pi}\left[\frac{28}{9} - \frac{13}{6}\,\ell n\,\frac{2(sp)}{m^2} + \left(\ell n\frac{E_s}{\Delta} + \ell n\frac{E_p}{\Delta}\right)\left(\ell n\frac{2(sp)}{m^2} - 1\right) - \Phi\left(-\frac{E_s - E_p}{E_p}\right) - \Phi\left(\frac{E_s - E_p}{E_s}\right)\right],$$

with the Spence function[93] defined as:

$$\Phi(x) = \int_o^x \frac{-\ell n|1 - y|}{y}\, dy \quad . \tag{A5.12}$$

Fig. 109.--The calculated radiative tail for elastic μp scattering with 150 GeV incident muons.

q^2 (Gev/c)^2	$\sigma^P_{\text{elastic tail}}$ (picobarns)												Values x 10^0		
4·8 5·0									1	1	1	2	3	6	
4·6 4·8								1	1	1	1	2	3	7	
4·4 4·6								1	1	1	2	2	4	7	
4·2 4·4							1	1	1	1	2	2	4	8	
4·0 4·2							1	1	1	1	2	3	4	9	
3·8 4·0						1	1	1	1	2	2	3	5	10	
3·6 3·8						1	1	1	1	2	2	4	6	11	
3·4 3·6	1				1	1	1	1	2	2	3	4	7	13	
3·2 3·4	1				1	1	1	1	2	2	3	5	8	15	
3·0 3·2	1			1	1	1	1	2	2	3	4	6	9	17	
2·8 3·0	1			1	1	1	2	2	3	3	5	6	10	20	
2·6 2·8	2	1	1	1	1	1	2	2	3	4	5	8	12	23	
2·4 2·6	2	1	1	1	1	2	2	3	4	5	6	9	14	28	
2·2 2·4	3	1	1	1	2	2	3	4	5	6	8	11	18	33	
2·0 2·2	4	2	1	2	2	3	4	5	6	8	9	14	22	41	
1·8 2·0	6	2	2	2	3	4	5	6	8	10	13	18	27	51	
1·6 1·8	10	3	3	3	4	5	6	8	10	13	17	23	35	65	
1·4 1·6	16	5	5	5	6	7	8	11	13	17	23	30	46	85	
1·2 1·4	27	9	7	7	9	10	12	15	19	24	32	47	63	115	
1·0 1·2	50	17	13	12	14	16	19	23	28	36	47	67	90	163	
0·8 1·0	100	33	24	22	24	27	31	37	45	56	74	105	169	248	
0·6 0·8	227	75	52	46	47	51	57	67	80	99	128	180	289	415	
0·4 0·6	622	204	135	115	111	116	127	144	169	206	264	365	584	1327	
0·2 0·4	2403	784	502	406	376	375	398	439	505	604	764	1048	1671	3552	
0·0 0·2	23828	7835	4963	3957	3586	3525	3666	3984	4507	5336	6699	9086	12624		

ν (Gev)															
	0	10	20	30	40	50	60	70	80	90	100	110	120	130	140
	10	20	30	40	50	60	70	80	90	100	110	120	130	140	150

Fig. 110.--The calculated radiative tail for elastic μD scattering with 150 GeV incident muons.

q^2 (Gev/c)^2	$\sigma^D_{\text{elastic tail}}$ (picobarns)												Values x 10^0		
4·8 5·0											1	1	1	3	
4·6 4·8											1	1	2	3	
4·4 4·6										1	1	1	2	4	
4·2 4·4										1	1	1	2	4	
4·0 4·2										1	1	1	2	5	
3·8 4·0									1	1	1	2	3	5	
3·6 3·8									1	1	1	2	3	6	
3·4 3·6								1	1	1	1	2	3	7	
3·2 3·4								1	1	1	2	2	4	8	
3·0 3·2							1	1	1	1	2	3	5	10	
2·8 3·0							1	1	1	2	2	3	6	11	
2·6 2·8						1	1	1	2	2	3	4	7	14	
2·4 2·6						1	1	1	2	3	3	5	8	16	
2·2 2·4					1	1	1	2	3	3	4	6	10	20	
2·0 2·2				1	1	1	2	2	3	5	5	8	12	25	
1·8 2·0				1	1	2	2	3	4	5	8	10	16	32	
1·6 1·8				1	1	2	3	4	5	7	10	13	21	42	
1·4 1·6			1	1	2	3	4	5	7	10	14	17	28	56	
1·2 1·4			1	2	3	4	6	7	10	14	19	30	39	78	
1·0 1·2		1	2	3	4	6	8	11	15	20	29	44	58	115	
0·8 1·0		1	3	5	7	10	14	18	24	33	46	70	123	182	
0·6 0·8	1	3	6	9	14	19	25	33	44	59	82	124	219	321	
0·4 0·6	3	7	13	22	31	43	56	73	96	128	177	266	465	1177	
0·2 0·4	33	33	53	79	110	145	188	240	309	406	557	825	1421	3264	
0·0 0·2	2910	1269	1191	1349	1602	1921	2309	2794	3431	4335	5746	8161	11723		

ν (Gev)															
	0	10	20	30	40	50	60	70	80	90	100	110	120	130	140
	10	20	30	40	50	60	70	80	90	100	110	120	130	140	150

REFERENCES

1. R. Hofstadter, Electron Scattering and Nuclear and Nucleon Structure, W. A. Benjamin, New York (1963).

2. J. Mar et al., Phys. Rev. Lett. 21, 482 (1968).
   T. Powell et al., Phys. Rev. Lett. 24, 753 (1970).
   L. S. Rochester et al., Phys. Rev. Lett. 36, 1284 (1976).

3. R. Hofstadter, Proceedings of the 1975 International Symposium on Lepton and Photon Interactions at High Energies, W. T. Kirk, ed., Stanford University, Stanford, California (1975), p. 869.

4. F. J. Ernst, R. G. Sachs, and K. Wali, Phys. Rev. 119, 1105 (1960).
   R. G. Sachs, Phys. Rev. 126, 2256 (1962).
   R. G. Sachs, 1962 International Conference on High Energy Physics, R. Armenteros, V. Glaser, R. E. Taylor, eds., CERN, Geneva, Switzerland (1962), p. 197.

5. D. H. Coward et al., Phys. Rev. Lett. 20, 292 (1968).
   P. N. Kirk et al., Phys. Rev. D8, 63 (1973).

6. P. Stein et al., Phys. Rev. Lett. 16, 592 (1966).
   R. H. Budnitz et al., Phys. Rev. 173, 1357 (1968).

7. L. N. Hand, D. G. Miller, and R. Wilson, Rev. Mod. Phys. 35, 335 (1963).

8. D. J. Gross and S. B. Treiman, Phys. Rev. Lett. 32, 1145 (1974).
   A. DeRujula, Phys. Rev. Lett. 32, 1143 (1974).

9. J. G. Rutherglen, Proceedings of the 4th International Symposium on Electron and Photon Interactions at High Energies, D. W. Braben, R. E. Rand, Mrs. S. A. Lowndes, eds., Daresbury Nuclear Physics Laboratory, Liverpool, England (1969), p. 163.

10. W. K. H. Panofsky, C. M. Newton, and G. B. Yodh, Phys. Rev. 98, 751 (1955).
    W. K. H. Panofsky, W. M. Woodward, and G. B. Yodh, Phys. Rev. 102, 1392 (1956).

11. W. K. H. Panofsky and E. A. Allton, Phys. Rev. 110, 1155 (1955).

12. Reviews of resonance electroproduction are given by:

W. K. H. Panofsky, Proceedings of the XIV International Conference on High Energy Physics, J. Prentki and J. Steinberger, eds., CERN, Geneva, Switzerland (1968), p. 23.

A. B. Clegg, Proceedings of the 4th International Symposium on Electron and Photon Interactions at High Energies, D. W. Braben, R. E. Rand, Mrs. S. A. Lowndes, eds., Daresbury Nuclear Physics Laboratory, Liverpool, England (1969), p. 123.

13. R. H. Dalitz and D. R. Yennie, Phys. Rev. 105, 1598 (1957).

S. Fubini, Y. Nambu, and V. Wataghin, Phys. Rev. 111, 329 (1958).

J. D. Walecka and P. A. Zucker, Phys. Rev. 167, 1479 (1968).

14. W. K. H. Panofsky, Proceedings of the XIV International Conference on High Energy Physics, J. Prentki and J. Steinberger, eds, CERN, Geneva, Switzerland (1968), p. 23.

15. M. Breidenbach et al., Phys. Rev. Lett. 23, 935 (1969).

16. J. D. Bjorken, Proceedings of the International School of Physics, "Enrico Fermi" Course XLI, J. Steinberger, ed., Academic Press, New York (1968).

J. D. Bjorken, Phys. Rev. Lett. 16, 408 (1966).

17. S. D. Drell and J. D. Walecka, Ann. Phys. 28, 18 (1964).

18. L. N. Hand, Phys. Rev. 129, 1834 (1963).

19. R. P. Feynman, High Energy Collisions, C. N. Yang, J. A. Cole, M. Good, R. Hwa, J. Lee Franzini, eds., Gordon and Breach, New York (1969), p. 237.

20. J. D. Bjorken and E. A. Paschos, Phys. Rev. 185, 1975 (1969).

21. G. Miller et al., Phys. Rev. D5, 528 (1972).

22. C. G. Callan and D. J. Gross, Phys. Rev. Lett. 21, 311 (1968).

23. M. Gell-Mann, Report CTSL-20, California Institute of Technology (1961), unpublished; also Phys. Rev. 125, 1067 (1962).

G. Zweig, CERN Preprints TH 401, 412 (1964), unpublished.

M. Gell-Mann, Phys. Lett. 8, 214 (1964).

24. B. J. Bjorken and S. L. Glashow, Phys. Lett. 11, 255 (1964).

S. L. Glashow, J. Iliopoulos, and L. Maiani, Phys. Rev. D2, 1285 (1970).

25. O. Greenberg, Phys. Rev. Lett. 13, 122 (1964).
M. Y. Han and Y. Nambu, Phys. Rev. 139, B1006 (1965).

26. J. Kuti and V. F. Weisskopf, Phys. Rev. D4, 3418 (1971).

27. R. P. Feynman, Photon Hadron Interactions, W. A. Benjamin, Inc., Reading, Mass. (1972), p. 150.

28. A. Bodek et al., Phys. Rev. Lett. 30, 1087 (1973).
G. Miller et al., Phys. Rev. D5, 528 (1972).

29. C. H. Llewellyn-Smith, Phys. Rev. D4, 2392 (1971).

30. C. N. Yang and R. Mills, Phys. Rev. 96, 191 (1954).
J. Kuti and V. F. Weisskopf, Phys. Rev. D4, 3418 (1971).

31. T. T. Chou and C. N. Yang, Phys. Rev. D4, 2005 (1971).

32. C. N. Yang, High Energy Collisions, C. N. Yang, J. A. Cole, M. Good, R. Hwa, J. Lee Franzini, eds., Gordon and Breach, New York (1969), p. 509.

33. G. Bellettini et al., Phys. Lett. 45B, 69 (1973).

34. Reviews of recent electroproduction experiments can be found in:
K. Berkelman, Proceedings of the 1971 International Symposium on Electron and Photon Interactions at High Energies, N. B. Mistry, M. E. Nordberg, Jr., G. Grammer, Jr., eds., Cornell University, Ithaca, New York (1971), p. 263.
K. Berkelman, Proceedings of the XVI International Conference on High Energy Physics, J. D. Jackson, A. Roberts, eds., National Accelerator Laboratory, Batavia, Illinois (1972), V. 4, p. 41.
F. Brasse, Proceedings of the VI International Symposium on Electron and Photon Interactions at High Energies, H. Rollnik, W. Pfiel, eds., North Holland, Amsterdam (1974), p. 251.
F. J. Gilman, Proceedings of the XVII International Conference on High Energy Physics, J. R. Smith, ed., Rutherford Laboratory, London, England (1974), p. IV-149.
G. Wolf, Proceedings of the 1975 Symposium on Lepton and Photon Interactions at High Energies, W. T. Kirk, ed., Stanford University, Stanford, California (1975), p. 795.

35. J. J. Sakurai, Phys. Rev. Lett. 22, 981 (1969).

36. K. Fujikawa, Phys. Rev. D9, 2794 (1971).
J. J. Sakurai and D. Schildknecht, Phys. Lett. 40B, 121 (1972); 41B 489 (1972); 42B, 216 (1972).

37. T. D. Lee, Ann. Phys. 66, 857 (1971).

38. A. H. Meuller, Phys. Rev. D2, 2963 (1970).

39. The muon beam at Fermilab was designed by T. Yamanouchi.

40. The following is a list of the people engaged in the muon scattering program:

H. L. Anderson, V. K. Bharadwaj, N. E. Booth, W. R. Francis, R. M. Fine, B. A. Gordon, R. H. Heisterberg, R. G. Hicks, G. I. Kirkbride, T. B. W. Kirk, W. A. Loomis, H. S. Matis, L. W. Mo, L. C. Myrianthopoulos, F. M. Pipkin, S. H. Pordes, T. W. Quirk, W. D. Shambroom, A. Skuja, L. J. Verhey, W. S. C. Williams, Richard Wilson, and S. C. Wright.

41. K. B. Burns et al., Nucl. Instr. and Meth. 106, 171 (1973).

42. T. A. Nunamaker, Nucl. Instr. and Meth. 106, 557 (1973).

43. T. A. Nunamaker, Rev. Sci. Instr. 42, 1701 (1971).

44. T. A. Nunamaker and D. B. Turner, Nucl. Instr. and Meth. 114, 445 (1973).

45. The construction of the magnetostrictive delay line wire spark chambers is described in detail in the thesis of Stephen H. Pordes, Harvard University (1976), unpublished. These chambers are similar to that described by G. Grayer et al., Nucl. Instr. and Meth. 99, 579 (1972).

46. A. Entenberg et al., Phys. Rev. Lett. 32, 486 (1974).

I. Kostoulas et al., Phys. Rev. Lett. 32, 489 (1974).

47. Details of the magnet measurement can be found in the thesis of G. I. Kirkbride, Oxford University, Oxford, England (1976), unpublished.

48. Y. S. Tsai, Phys. Rev. 122, 1898 (1961).

N. T. Meister and D. R. Yennie, Phs. 130, 1210 (1963).

49. L. I. Schiff, Phys. Rev. 87, 750 (1952).

50. L. W. Mo and Y. S. Tsai, Rev. Mod. Phys. 41, 205 (1969).

51. L. W. Mo, Proceedings of the 1975 International Symposium on Lepton and Photon Interactions at High Energies, W. T. Kirk, ed., Stanford University, Stanford, California (1975), p. 651.

52. Y. Watanabe et al., Phys. Rev. Lett. 35, 898 (1975).

C. Chang et al., Phys. Rev. Lett. 35, 901 (1975).

53. A. Bodek, SLAC Report No. SLAC-PUB-1442, Stanford Linear Accelerator Center, Stanford, California (1974).

J. I. Friedman, Proceedings of the XVII International Conference on High Energy Physics, J. R. Smith, ed., Rutherford Laboratory, London, England (1974), p. IV-57.

R. Taylor, Proceedings of the 1975 Symposium on Lepton and Photon Interactions at High Energies, W. R. Kirk, ed., Stanford University, Stanford, California (1975), p. 679.

S. Stein, Phys. Rev. D12, 1884 (1975).

54. G. Miller et al., Phys. Rev. D5, 528 (1972).

E. M. Riordan et al., Phys. Rev. Lett. 33, 561 (1974).

S. Stein, Phys. Rev. D12, 1884 (1975).

R. Taylor, Proceedings of the 1975 Symposium on Lepton and Photon Interactions at High Energies, W. R. Kirk, ed., Stanford University, Stanford, California (1975), p. 679.

55. W. B. Atwood and G. B. West, Phys. Rev. D7, 773 (1973).

56. R. H. Glauber, Phys. Rev. 100, 252 (1955).

57. J. Eickmeyer et al., Phys. Rev. Lett. 36, 289 (1976).

58. Wu-Ki Tung, Phys. Rev. Lett. 35, 490 (1975); also Phys. Rev. D12, 3613 (1975).

R. Carlitz, Phys. Rev. Lett. 36, 1001 (1976).

H. Georgi and H. D. Politzer, Phys. Rev. Lett. 36, 1281 (1976).

59. M. S. Chanowitz and S. D. Drell, Phys. Rev. Lett. 30, 807 (1973); also Phys. Rev. D9, 2078 (1974).

V. Barger, Phys. Lett. 49B, 43 (1974).

G. West and P. Zerwaz, Phys. Rev. D10, 2130 (1974).

60. We list here several scaling variables commonly found in the literature:

1. $\omega' = \omega + \frac{M^2}{q^2}$

E. D. Bloom and F. Gilman, Phys. Rev. Lett. 25, 1140 (1970).

2. $\omega_R = \frac{2M\nu + a^2}{q^2 + b^2}$

V. Rittenberg and H. R. Rubinstein, Phys. Lett. 35B, 50 (1971).

3. $\omega_s = \frac{2M\nu + \frac{2}{3}M^2}{q^2 + \frac{1}{2}M^2}$

J. Schwinger, Proc. Nat. Acad. Sci., Vol. 72, No. 1, January 1975. p. 1.

4. $\omega_s{}^p = \omega + 1.5\ (GeV/c)^2/q^2$ for the proton

$\omega_s{}^n = \omega + 0.6\ (GeV/c)^2/q^2$ for the neutron

R. Taylor, Proceedings of the 1975 International Symposium on Lepton and Photon Interactions at High Energies, W. R. Kirk, ed., Stanford University, Stanford, California (1975), p. 679.

It should be noted that in the deep inelastic region of our muon experiment, the quantity $2M\nu$ is very large. As a consequence, the various scaling variables do not differ significantly from that originally proposed by Bjorken, $\omega = 2M\nu/q^2$.

61. R. McElhaney and S. F. Tuan, Phys. Rev. D7, 2267 (1973); also Nucl. Phys. B72, 487 (1974).

62. G. Altarelli, N. Cabibbo, L. Maiani, and R. Petronzio, Nucl. Phys. B69, 531 (1974).

63. V. Barger and R. J. N. Phillips, Nucl. Phys. B73, 269 (1974).

V. Barger, private communication.

64. V. Barger et al., Report COO-474, University of Wisconsin, Madison, Wisconsin (1974).

B. Aubert et al., Phys. Rev. Lett. 33, 984 (1974).

65. V. Barger and T. Weiler, Nucl. Phys. B102, 493 (1976).

66. F. J. Gilman, SLAC Report No. SLAC-167, Stanford Linear Accelerator Center, Stanford, California (1973), V. 1, p. 82.

K. Wilson, Proceedings of the 1971 International Symposium on Electron and Photon Interactions at High Energies, N. B. Mistry, M.E. Nordberg, Jr., and G. Grammer, Jr., eds., Cornell University, Ithaca, New York (1971), p. 116.

67. E. Gabathuler, Proceedings of the VI International Symposium on Electron and Photon Interactions at High Energies, H. Rollnik and W. Pfiel, eds., North Holland, Amsterdam (1974), p. 299.

68. M. Damashek and F. J. Gilman, Phys. Rev. D5, 1319 (1970).

69. T. P. Cheng and Wu-Ki Tung, Phys. Rev. Lett. D24, 851 (1970).

70. F. E. Close and J. F. Gunion, Phys. Rev. D4, 742 (1971).

71. H. Harari, Phys. Rev. Lett. 22, 1078 (1969); also Phys. Rev. Lett. 24, 286 (1970).

72. Y. Nambu and M. Y. Han, Phys. Rev. D10, 674 (1974).

J. C. Pati and A. Salam, Phys. Rev. Lett. 36, 11 (1976).

G. J. Gounaris, E. K. Manesis, and A. Verganelakis, Phys. Lett. 59B, 391 (1975).

73. L. Hand, private communication.

74. R. Devenish and D. Schildknecht, DESY Report No. DESY 75/18, Deutsches Elektronen-Synchrotron, Hamburg, Germany (1975).

75. L. W. Mo, Proceedings of the 1975 International Symposium on Lepton and Photon Interactions at High Energies, W. R. Kirk, ed., Stanford University, Stanford, California (1975), p. 651.

W. A. Loomis et al., Phys. Rev. Lett. 35, 1483 (1975).

H. L. Anderson et al., Phys. Rev. Lett. 36, 1422 (1976).

76. L. Van Hove, Phys. Reports 1C, 347 (1971).

77. Y. S. Tsai, SLAC Report No. SLAC-PUB-848, Stanford Linear Accelerator Center, Stanford, California (1971).

78. M. L. Perl, SLAC Report No. SLAC-PUB-1614, Stanford Linear Accelerator Center, Stanford, California (1975).

79. K. Bunnell et al., Phys. Rev. Lett. 36, 772 (1976).

80. J. P. Verge et al., Phys. Rev. Lett, (to be published).

81. R. P. Feynman, Photon Hadron Interactions, W. A. Benjamin, Inc., Reading, Mass. (1972), p. 250.

82. J. D. Bjorken, Proceedings of the 1971 International Symposium on Electron and Photon Interactions at High Energies, N. B. Mistry, M. E. Nordberg, Jr., and G. Grammer, Jr., eds., Cornell University, Ithaca, New York (1971), p. 282.

83. G. Hanson et al., Phys. Rev. Lett. 35, 1609 (1975).

84. R. P. Feynman, Photon Hadron Interactions, W. A. Benjamin, Inc., Reading, Mass. (1972), p. 166.

85. M. J. Moravcsik and P. Ghosh, Phys. Rev. Lett. 32, 321 (1974).

86. J. M. Blatt and V. F. Weisskopf, Theoretical Nuclear Physics, Addison-Wesley, Reading, Mass. (1953).

87. R. V. Reid, Jr., Ann. Phys. 50, 411 (1968).

88. L. Hulthen and M. Sugawara, Handbuch der Physik, Vol. 39, S. Flugge, ed., Springer-Verlag, Berlin (1957), p. 1.

89. R. G. Arnold et al., SLAC Report No. SLAC-PUB-1596, Stanford Linear Accelerator Center, Stanford, California (1975).

90. R. A. Griffy and L. I. Schiff, High Energy Physics, Vol. 1, E. H. S. Burhop ed., Academic Press, New York (1967), p. 341.

91. A. Goldberg, Phys. Rev. 112, 618 (1958).

92. Y. S. Tsai, Proceedings of the International Conference on Nuclear Structure, 1963, Stanford University, Stanford, California (1964), p. 221.

93. K. Mitchell, Phil. Mag. 40, 351 (1949).